

2011

3D Imaging for Planning of Minimally Invasive Surgical Procedures

Uma Numburi
Cleveland State University

Follow this and additional works at: <https://engagedscholarship.csuohio.edu/etdarchive>



Part of the [Biomedical Engineering and Bioengineering Commons](#)

How does access to this work benefit you? Let us know!

Recommended Citation

Numburi, Uma, "3D Imaging for Planning of Minimally Invasive Surgical Procedures" (2011). *ETD Archive*. 226.
<https://engagedscholarship.csuohio.edu/etdarchive/226>

This Dissertation is brought to you for free and open access by EngagedScholarship@CSU. It has been accepted for inclusion in ETD Archive by an authorized administrator of EngagedScholarship@CSU. For more information, please contact library.es@csuohio.edu.

**3D IMAGING FOR PLANNING OF MINIMALLY INVASIVE
SURGICAL PROCEDURES**

UMA NUMBURI

Bachelor of Technology in Chemical Engineering

Jawaharlal Nehru Technological University

May, 2002

Master of Science in Chemical Engineering

Cleveland State University

May, 2005

submitted in partial fulfillment of requirements for the degree

DOCTOR OF ENGINEERING IN APPLIED BIOMEDICAL ENGINEERING

at the

CLEVELAND STATE UNIVERSITY

May, 2011

This dissertation has been approved
for the Department of Chemical and Biomedical Engineering
and the College of Graduate Studies by

Dissertation Committee Chairperson, Sandra S. Halliburton, Ph.D.
Department of Chemical and Biomedical Engineering

Date

George P. Chatzimavroudis, Ph.D.
Department of Chemical and Biomedical Engineering

Date

Paul Schoenhagen, M.D., FAHA
Department of Chemical and Biomedical Engineering

Date

Miron Kaufman, Ph.D.
Department of Physics

Date

Frank Dong, Ph.D.
Department of Chemical and Biomedical Engineering

Date

ACKNOWLEDGEMENTS

First, I would like to express my deepest gratitude to my advisor Dr. Sandra Halliburton for her continuous support, patience, motivation and enthusiasm for my research. Her constant encouragement and immense knowledge has inspired me to achieve my goal and complete this research. I will never forget her unfailing support as I hurdle the obstacles during the course of this thesis. I am grateful to her for believing in me and giving me this opportunity.

I would also like to thank my committee members, Dr. Paul Schoenhagen, Dr. Frank Dong, Dr. George Chatzimavroudis and Dr. Miron Kaufman for helping me with their encouragement, insightful comments and guidance. I would like to express my gratitude to Dr. Schoenhagen for his valuable insights, patience and encouragement all through my research. I would also like to specially thank Dr. Dong and Mr. Paul Johnson from Cleveland Clinic for their immense help in designing phantom experiments for dose measurements in this thesis.

I would like to thank Siemens AX, Forchheim, Germany for providing financial assistance to this project. I am grateful to Dr. Andrew Primak and Mr. Martin von Roden from Siemens for their support and suggestions all through the project. I am thankful to the CT technologists: Stacie Kuzmiak, Lindsay Oppman, Mike Kral and Julia Hart for their patience in answering my innumerable questions and helping me with patient scans.

I thank my fellow labmates: Mitya Barreto, Carla Thompson and Xiaopeng Zhou for all the stimulating discussions, help and motivation to complete the dissertation, and for all the fun. I would also like to thank my friends, Vidya and Chaitu who have been there to help me and guide me when ever I needed them.

I would like to thank my parents, Ramachandra Raju and Satya Sri Namburi, my grandmother Lakshmi Namburi and my sister Hema for their unconditional love, support and help all throughout my life. Lastly, I would like to thank my dearest husband Aditya for his unwavering love, support and motivation to help me complete this thesis. This dissertation would not have been possible without him.

3D IMAGING FOR PLANNING OF MINIMALLY INVASIVE SURGICAL PROCEDURES

UMA NUMBURI

ABSTRACT

Novel minimally invasive surgeries are used for treating cardiovascular diseases and are performed under 2D fluoroscopic guidance with a C-arm system. 3D multi-detector row computed tomography (MDCT) images are routinely used for preprocedural planning and postprocedural follow-up.

For preprocedural planning, the ability to integrate the MDCT with fluoroscopic images for intraprocedural guidance is of clinical interest. Registration may be facilitated by rotating the C-arm to acquire 3D C-arm CT images. This dissertation describes the development of optimal scan and contrast parameters for C-arm CT in 6 swine. A 5-s ungated C-arm CT acquisition during rapid ventricular pacing with aortic root injection using minimal contrast (36 mL), producing high attenuation (1226), few artifacts (2.0), and measurements similar to those from MDCT ($p > 0.05$) was determined optimal. 3D MDCT and C-arm CT images were registered to overlay the aortic structures from MDCT onto fluoroscopic images for guidance in placing the prosthesis. This work also describes the development of a methodology to develop power equation ($R^2 > 0.998$) for estimating dose with C-arm CT based on applied tube voltage. Application in 10 patients yielded 5.48 ± 2.02 mGy indicating minimal radiation burden.

For postprocedural follow-up, combinations of non-contrast, arterial, venous single energy CT (SECT) scans are used to monitor patients at multiple time intervals resulting in high cumulative radiation dose. Employing a single dual-energy CT (DECT) scan to replace two SECT scans can reduce dose. This work focuses on evaluating the feasibility of DECT imaging in the arterial phase. The replacement of non-contrast and arterial SECT acquisitions with one arterial DECT acquisition in 30 patients allowed generation of virtual non-contrast (VNC) images with 31% dose savings. Aortic luminal attenuation in VNC (32 ± 2 HU) was similar to true non-contrast images (35 ± 4 HU) indicating presence of unattenuated blood. To improve discrimination between calcium and iodine, a combined basis spectral and material analysis was developed. The algorithm differentiated calcium and iodinated pixels in phantom experiments and measured the mass fraction within 3%. Application in a patient resulted in VNC images with luminal attenuation of 57 HU indicating removal of contrast. However, high attenuating pixels with low density values appeared with decreased intensity in VNC images.

TABLE OF CONTENTS

ABSTRACT.....	v
LIST OF TABLES.....	xiii
LIST OF FIGURES.....	xv
CHAPTER	Page
I. INTRODUCTION	1
II. THE HEART AND GREAT VESSELS.....	7
III. MINIMALLY INVASIVE CARDIOVASCULAR SURGERIES.....	12
3.1 EVAR.....	13
3.1.1 Thoracoabdominal Aneurysm.....	13
3.1.2 Management of Thoracoabdominal Aneurysm.....	13
3.2 TAVI.....	14
3.2.1 Aortic Stenosis.....	14
3.2.2 Management of Aortic Stenosis.....	15
IV. X-RAY BASED IMAGING	17
4.1 X-ray Physics.....	18
4.1.1 X-ray Tube.....	18
4.1.1.1 Tube Voltage.....	19
4.1.1.2 Tube Current.....	19
4.1.2 X-ray Generation.....	20
4.1.2.1 Bremsstrahlung Radiation.....	20
4.1.2.2 Characteristic Radiation.....	22
4.1.3 X-ray Interaction with Matter	24
4.1.3.1 Rayleigh Scattering.....	25

4.1.3.2	Compton Scattering.....	25
4.1.3.3	Photoelectric Effect.....	27
4.1.4	Attenuation.....	28
4.1.4.1	Linear Attenuation Coefficient.....	29
4.1.4.2	Mass Attenuation Coefficient.....	29
4.1.4.3	Factors Affecting Attenuation.....	30
4.2	X-ray Based Imaging.....	30
4.2.1	Fluoroscopy.....	30
4.2.2	Computed Tomography (CT).....	32
4.2.2.1	Data Acquisition.....	33
4.2.2.2	Image Reconstruction.....	35
4.2.2.3	Image Display.....	37
4.2.3	Dual Energy Computed Tomography (DECT).....	38
4.2.4	Cardiac CT.....	41
4.2.4.1	ECG synchronization.....	42
4.2.5	C-arm Computed Tomography (C-arm CT).....	43
4.2.6	Contrast Administration with X-ray Based Imaging.....	45
4.2.6.1	Considerations for Fluoroscopy.....	45
4.2.6.2	Considerations for CT.....	46
4.2.6.3	Considerations for C-arm CT.....	49
4.2.7	Dose.....	50
4.2.7.1	Considerations for Fluoroscopy.....	50
4.2.7.2	Considerations for CT.....	51
4.2.7.3	Considerations for C-arm CT.....	53
4.2.8	Image Quality for X-ray based modalities.....	54

V.	LITERATURE REVIEW.....	56
5.1	DECT.....	56
5.2	C-arm CT.....	62
VI.	HYPOTHESIS AND SPECIFIC AIMS.....	67
6.1	Specific Aim 1.....	67
6.2	Specific Aim 2.....	68
6.3	Specific Aim 3.....	69
VII.	PRELIMINARY DATA.....	70
7.1	Specific Aim 1.....	70
7.1.1	Description of Standard SECT Contrast and Scan Protocol for Aortic Imaging.....	71
7.1.2	Development of DECT Imaging Protocol.....	72
7.1.3	Development of DECT Contrast Injection Protocol.....	75
7.1.4	VNC generation.....	75
7.2	Specific Aim 2.....	76
7.2.1	Development of DECT Imaging Protocol on Flash.....	77
7.2.2	Development of LTI Modeling in Time Domain.....	77
7.2.2.1	Impact of Saline on LTI Modeling.....	79
7.2.2.2	Modeling of Contrast Injection.....	84
VIII.	FEASIBILITY OF DUAL-ENERGY COMPUTED TOMOGRAPHY IN THE ARTERIAL PHASE: IMAGING AFTER ENDOVASCULAR ANEURYSM REPAIR.....	88
8.1	Introduction.....	88
8.2	Material and Methods.....	90
8.2.1	Patients.....	90
8.2.2	Data Acquisition and Image Reconstruction.....	90

8.2.3	Dual-Energy Image Processing.....	92
8.2.4	Radiation Dose Measurements.....	93
8.2.5	Clinical Evaluation.....	94
8.2.6	Tissue Attenuation and Image Noise.....	94
8.3	Results.....	96
8.3.1	Clinical Evaluation.....	96
8.3.2	Radiation and Contrast Dose Measurements.....	99
8.3.3	Tissue Attenuation.....	100
8.3.4	Image Noise.....	103
8.4	Discussion.....	104
8.4.1	Technical Considerations.....	105
8.4.2	Limitations.....	108
8.5	Conclusion.....	109
IX.	IMPROVED DIFFERENTIATION OF CALCIUM AND IODINE WITH DECT IMAGING	110
9.1	Introduction.....	110
9.2	Material and Methods.....	112
9.2.1	Contrast Injection Optimization Algorithm.....	112
9.2.2	VNC Theory And Algorithm Development.....	113
9.2.3	In-Vitro Study.....	116
9.2.4	In-Vivo Study.....	119
9.3	Results.....	123
9.3.1	In-Vitro Study.....	123
9.3.2	In-Vivo Study.....	126
9.4	Discussion.....	127

9.5 Conclusion.....	130
X. OPTIMIZATION OF ACQUISITION AND CONTRAST-INJECTION PROTOCOL FOR C-ARM CT IMAGING IN TRANSCATHETER AORTIC VALVE IMPLANTATION: INITIAL EXPERIENCE IN A SWINE MODEL	131
10.1 Introduction.....	131
10.2 Materials and Methods.....	133
10.2.1 Animal Preparation.....	133
10.2.2 Image Acquisition.....	134
10.2.2.1 Pre-TAVI.....	134
10.2.2.2 TAVI procedure.....	139
10.2.2.3 Post-TAVI.....	139
10.2.3 Image Analysis.....	140
10.2.3.1 Pre-TAVI.....	140
10.2.3.2 Post-TAVI.....	142
10.3 Results.....	142
10.3.1 Pre-TAVI.....	142
10.3.2 TAVI Procedure.....	151
10.3.3 Post-TAVI.....	152
10.4 Discussion.....	153
10.4.1 Limitations.....	155
10.5 Conclusion.....	156
XI. DOSE ASSESSMENT WITH C-ARM CT.....	157
11.1 Introduction.....	157
11.2 Materials and Methods.....	159
11.2.1 C-arm CT System.....	159
11.2.2 Phantom Imaging.....	160

11.2.3 Patient Imaging.....	162
11.3 Results.....	162
11.4 Discussion.....	166
XII. DISCUSSION AND CONCLUSION	170
REFERENCES.....	181
APPENDICES.....	209
APPENDIX 1.....	209
APPENDIX 2.....	209
APPENDIX 3.....	209
APPENDIX 4.....	209
A4.1 Introduction.....	226
A4.2 Materials and Methods.....	227
A4.2.1 Test Bolus Contrast Injection.....	229
A4.2.2 Test Bolus Attenuation Curve Characteristics.....	230
A4.2.3 Prediction of Contrast Injection for Short Scan Time Cardiac Imaging.....	230
A4.3 Results.....	231
A4.3.1 Test Bolus Contrast Injection.....	232
A4.3.2 Test Bolus Attenuation Curve Characteristics.....	233
A4.3.3 Prediction of Contrast Injection for Short Scan Time Cardiac Imaging.....	235
A4.4 Discussion.....	242
A4.5 References.....	246

LIST OF TABLES

Table	Page
4.1: CT number of various clinical tissues.....	38
7.1: Impact of saline on contrast volume and flow rate and comparison with values programmed in the injector.....	84
8.1: Patient demographics.....	96
8.2: Tissue attenuation measurements in various image sets.....	102
8.3: Comparison of noise measurements on DECT and SECT Images.....	104
9.1: Composition of the ten inserts composed of aqueous contrast mixtures.....	118
9.2: Comparison between theoretical and calculated mass fractions of aqueous contrast mixtures.....	125
10.1: Contrast injection parameters and cardiac rhythm status during ECG-gated MDCT and ECG-gated and ungated C-arm CT Imaging.....	138
10.2: Analysis of images obtained from ECG-gated MDCT and C-arm CT methods....	144
10.3: Pre-TAVI aortic root measurements from MDCT reference images and C-arm CT images.....	148
10.4: Total injection volume, contrast volume, saline volume, and injection flow rate for C-arm CT methods.....	149
10.5: Comparison of aortic root diameters and angiographic projections from optimal C-arm CT (Method 3) with MDCT.....	150
11.1: X-ray imaging parameters used for ungated C-arm CT scan.....	159

11.2: Highest system entrance dose required to maintain corresponding tube voltage constant during the C-arm CT acquisition.....	163
11.3: CTDI _w dose values measured at different tube voltages using 300 mm ionization chamber and 470 mm body phantom.....	165
A4.1: Patient characteristics.....	231
A4.2: Impact of saline on contrast volume and flow rate and comparison with values programmed in the injector.....	233
A4.3: Impact of saline (60/80 mL) on test bolus attenuation curve characteristics in the ascending aorta.....	235
A4.4: Average contrast injection parameters for 6-, 4-, 2-, and 1-s Scan.....	239

LIST OF FIGURES

Figure	Page
2-1: Schematic of the aorta.....	9
2-2: Schematic of the heart.....	11
4-1: Components of an x-ray tube required for x-ray production.	18
4-2: Production of bremsstrahlung spectrum and impact of subatomic distance between the nucleus and electrons on the production of the energy of x-rays. Adapted from Bushberg et al [69].	21
4-3: The bremsstrahlung spectrum for a 90 kVp peak voltage. The unfiltered spectrum shows the linear decrease of x-rays with energy up to the maximum energy of 90 keV. The filtered spectrum shows the preferential absorption of x-rays below 10 keV. Adapted from Bushberg et al [69].	21
4-4: Generation of characteristic x-rays. (1) The incident electron with energy greater than the binding energy of the electron in the K-shell ejects the electron from the shell. (2) This creates an unstable positive ion. (3) The electron from the adjacent L-shell fills in the vacancy in the K-shell. (4) The electron transition causes the emission of characteristic x-ray with energy equivalent to the difference between the binding energies of K and L shells. Adapted from Bushberg et al [69].	23
4-5: The filtered bremsstrahlung and characteristic x-ray spectrum of tungsten material obtained at 90 kVp tube voltage. The curve shows the filtering of low-energy photons below 10 keV in the bremsstrahlung spectrum superimposed with the characteristic x-rays from $K_{\alpha 1}$, $K_{\alpha 2}$, and $K_{\beta 1}$ transitions at 59.3, 57.9 and 67.2 keV. Adapted from Bushberg et al [69].	24
4-6: Rayleigh scattering where the incident photon at low energy strikes the atom causing the electrons of the atom to oscillate and finally ejecting a photon at the same incident energy, but in a different direction. Adapted from Bushberg et al [69].	25

4-7: Compton scattering showing the incident photon ejecting a valence electron and a Compton scattered photon at an angle θ relative to the incident photon. The energy E_0 is split into E_{SC} and E_e . Adapted from Bushberg et al [69].	26
4-8: Photoelectric absorption showing interaction of a 100 keV photon with an iodine atom. The incident photon interacts with the K shell having binding energy (34 keV) closest to the incident photon and yields a 66 keV photoelectron. The removal of the electron from K shell triggers a cascade of electron transitions from L to K, M to L, and N to L resulting in characteristic x-rays with 29, 4.4 and 0.6 keV respectively as well as positive iodine ion without an electron in the N shell. Adapted from Bushberg et al [69].	27
4-9: Graph showing the occurrence of Rayleigh scatter, Compton scatter, photoelectric effect, pair production as function of incident x-ray energies when they interact with soft tissue. Adapted from Bushberg et al [69].	28
4-10: Schematic illustrating the key components of a fluoroscopic system.	31
4-11: Illustration showing multiple detectors in the longitudinal direction in the MDCT scanners.	32
4-12: Schematic showing conversion of x-rays in the flat detectors using CsI scintillator and photodiodes.	44
7-1: Alderson Phantom mimicking human body.	71
7-2: Optimal beam collimation, rotation time, pitch, reconstructed slice thickness and tube current values resulting in minimum noise and dose values developed for imaging on a dual-source DECT scanner (Definition, Siemens).	74
7-3: Optimization technique used to estimate the effective test injection profiles with and without saline along with the patient's impulse response.	81

7-4: Effective contrast flow with test injections A (—) and B (—) along with impulse response (—), measured (●) and convolved (---) test bolus attenuation curves from test injection A, and measured (■) and convolved (---) test bolus attenuation curves from test injection B. Graphs from a 67-year-old man weighing 88 kg showing **(a)** administration of 13 mL of contrast at a maximum flow rate of 2.0 mL/s without use of saline (test injection A) and the entire 20 mL of contrast at a flow rate of 4.5 mL/s with the use of a 60-mL saline chaser (test injection B), and **(b)** the resulting measured and convolved test attenuation bolus curves plus the patient's impulse response. Graphs from a 52-year-old woman weighing 115 kg showing **(c)** administration of 9 mL of contrast at a maximum flow rate of 0.7 mL/s without use of saline (test injection A) and the entire 20 mL of contrast at a flow rate of 4.5 mL/s with the use of a 80-mL saline chaser (test injection B), and **(d)** the resulting measured and convolved test attenuation bolus curves plus the patient's impulse response. 82

7-5: Optimization technique for computing patient-specific injection profiles to achieve uniform enhancement during a short duration cardiac scan..... 85

7-6: Patient-specific injection predicted using LTI modeling to achieve 300 HU (●) during a 6-s cardiac scan. A biphasic injection profile in a 60-year-old, 123-kg man (BMI = 37.9 kg/m²) using a total of 52 mL of contrast (—) was required to achieve uniform contrast enhancement of approximately 300 HU (----)..... 87

8-1: 87-year-old 74-kg man after endovascular aneurysm repair for abdominal aortic aneurysm. **(A)** Axial dual-energy VNC CT image shows non-contrast blood (33 HU) in aorta. Axial arterial phase **(B)** weighted-average, **(C)** 80-kVp, and **(D)** 140-kVP images show high-attenuation contrast material (342 HU, 526 HU, and 263 HU, respectively) in aorta..... 97

8-2: 76-year-old 52-kg woman with CT evidence of endoleak after endovascular aortic repair. A, DECT VNC image (A) shows no contrast material outside the stent in the aneurysm sac (*arrow*). (B) Weighted-average arterial phase DECT and (C) venous phase SECT images show contrast enhancement..... 98

8-3: Graph shows replacing two (non-contrast [<i>light gray</i>] and arterial phase [<i>dark gray</i>]) of three SECT acquisitions in standard triple-phase protocol with single arterial phase DECT acquisition in study protocol while retaining SECT venous phase (<i>white</i>) acquisition in both protocols results in significant 31% dose	99
8-4: 57-year-old 74-kg man after endovascular stenting of descending thoracic aorta. Comparison of (A) VNC CT image generated from DECT data obtained during current examination with (B) true non-contrast image acquired at 120 kVp during previous examination. Mean attenuation values of 28 HU and 31 HU were measured in aorta on A and B, indicating presence of blood in lumen. Noise (SD of mean attenuation in aorta) from VNC CT images (11 HU) was lower than noise from true non-contrast images (24 HU). Stent (<i>arrow</i>) in A appears with lower attenuation than B.	100
8-5: Images from a 79-year-old 81-kg man show effect of DECT on tissue attenuation. (A) Axial VNC CT DECT, (B) weighted-average arterial phase DECT, and (C) venous phase SECT images show stent (<i>arrow</i>) and thrombus in excluded aneurysm sac (<i>star</i>). Thrombus attenuation measures 24 HU in A, 26 HU in B, and 25 HU in C, showing that low-attenuation tissues such as thrombus have similar attenuation in all three phases. High-attenuation materials such as stent, however, have low attenuation on VNC images.	101
8-6: 76-year-old 103-kg man with stable endovascular stent-graft in abdominal aorta. (A) Axial VNC DECT image shows decreased calcium attenuation (<i>arrow</i>) in wall of aneurysm sac than in (B) venous phase SECT image.	103
8-7: 76-year-old woman with weight of 52 kg who presented for follow-up of endovascular stent for thoracoabdominal aortic rupture. Images show misregistration artifacts (<i>arrows</i>) as result of ungated and low-temporal-resolution data acquisition. Arterial phase DECT image obtained at (A) 80 kVp, (B) 140 kVp. (C) VNC DECT image.	108

9-1: Weighting factor $w(E)$ at 80 and 140 kVp for DECT scanner (Flash, Siemens Medical Systems, Forchheim, Germany).....	114
9-2: Plot of $F_n(Z)$ as function of atomic number (Z).....	115
9-3: Plot of weighting function of x-ray spectrum at 80 kVp, 140 kVp and 140 kVp with tin filter as a function of energy. The tin filter applied to the 140 kVp spectrum filtered lower energies allowing better separation between the 80 and 140 kVp energies.....	117
9-4: Plot of enhancement vs. time showing uniform contrast enhancement (415 ± 10 HU) in a patient imaged with a uniphasic contrast protocol and DECT scan protocol on a second generation dual-source DECT scanner.....	120
9-5: Flow chart of three-material decomposition in patients.	122
9-6: Axial images of phantom with HA cylinders and aqueous iodinated mixtures at (A) 80 kVp and (B) 140 kVp with additional tin filter.....	124
9-7: Axial images of phantom showing identification of only (A) iodine pixels in contrast agent and (B) calcium pixels in HA.	125
9-8: Axial images in a patient showing aortic luminal attenuation in the aorta (A) 57 HU in VNC, (B) 222 HU in arterial 140 kVp, and (C) 61 HU in true non-contrast images.	126
9-9: Axial images in a patient showing calcium (white arrow) in (A) VNC and (B) true non-contrast images. Calcium appeared with decreased attenuation in VNC images.	127
10-1: Ungated and ECG-gated C-arm CT Imaging	136
10-2: Sagittal Images Obtained From MDCT and C-arm CT Methods. (A) Multidetector row computed tomography (MDCT) image acquired with peripheral injection showing no artifacts. C-arm CT image acquired from (B) Method 1 showing moderate artifacts, (C) Method 3 showing mild artifacts, (D) Method 4 showing moderate artifacts, and (E) Method 5 showing mild artifacts.....	145

10-3: Comparison of Axial C-arm CT Images at the Level of the Aortic Annulus.....	146
10-4: Images From Ungated C-arm CT During Rapid Pacing With Aortic Root Injection. (A) Volume-rendered computed tomography (CT) image of aortic root showing the coronary arteries. Multiplanar reformatted images of well-enhanced aortic root showing (B) vertical distance from aortic annulus (AN) to right coronary artery (RCA) along with minimum AN diameter, and (C) distance from AN to left coronary artery (LCA) along with maximum AN diameter.....	147
10-5: Images from MDCT Fused With Fluoroscopy. (A) 3-dimensional (3D) multidetector row computed tomography (MDCT) image with coronary ostia (yellow lines) and aortic annulus (AN) (white line) marked. (B) Overlay of 3D MDCT images on 2-dimensional (2D) fluoroscopy image showing the catheter in the aortic root. (C) 2D image with contrast injected in the aortic root showing the AN and coronary arteries. .	151
Figure 10-6: Images From Ungated C-arm CT. (A) Multiplanar reformat (MPR) C-arm CT image showing the valve and catheter before valve deployment. (B) MPR image showing the placement of the valve without any coronary occlusions. (C) Volume- rendered image showing the valve after deployment.....	152
11-1: Schematic showing the center and periphery locations in a PMMA phantom.....	160
11-2: Normalized Peak Dose as a function of phantom length at center and periphery locations for the body phantom at 125 kVp. Peak dose did not vary by more than 3% when phantom length was increased from 320 to 470 mm either at the center or peripheral locations.	164
11-3: Longitudinal dose profiles using 300 mm TLDs in the body phantom at the center. Dose profiles are measured using 470 mm phantom and simulated using 900 mm phantom.....	164

11-4: Longitudinal dose profiles using 300 mm TLDs in the body phantom at the periphery (average of four peripheral locations). Dose profiles are measured using 470 mm phantom and simulated using 900 mm phantom.	165
11-5: CTDI _w values calculated from weighted average of center and periphery locations for an ungated C-arm CT protocol. The power equation fit with correlation coefficient $R^2=0.99$ was used for calculating dose in patients.	166
A4-1: Effective flow profile of contrast agent injected with test injections A (20 mL contrast only) and B (20 mL contrast followed by saline) in 71-year-old man weighing 74 kg. Use of 60 mL saline chaser resulted in injection of the entire 20 mL of contrast at an effective rate of 4.5 mL/s; without saline, only 13 mL of contrast was delivered at a rate of 2.4 mL/s.	232
A4-2: Patient-specific contrast profiles predicted to achieve a constant attenuation of 300 HU during a 6-s cardiac scan. Injections were computed for 25 patients from LTI modeling.	236
A4-3: Patient-specific contrast profiles predicted to achieve a constant attenuation of 300 HU during a 4-s cardiac scan. Injections were computed for 25 patients from LTI modeling.	236
A4-4: Patient-specific contrast profiles predicted to achieve a constant attenuation of 300 HU during a 2-s cardiac scan. Injections were computed for 25 patients from LTI modeling.	237
A4-5: Patient-specific contrast profiles predicted to achieve a constant attenuation of 300 HU during a 1-s cardiac scan. Injections were computed for 25 patients from LTI modeling.	238
A4-6: Biphasic contrast profiles obtained by averaging data from 25 patient-specific injection profiles for 6-, 4-, 2-, and 1-s cardiac scans.	240

A4-7: Average total contrast volumes computed from 25 patient-specific injections. Contrast volumes of 64, 55, 46, and 40 mL were required for 6-, 4-, 2-, and 1-s scans. Paired Student *t* tests with Bonferroni adjustments were used to compare average contrast volumes for 6- and 4-s scans, 4- and 2-s scans, and 2- and 1-s scans ; a *P* value < .017 indicated statistical significance. * and † indicate difference between contrast volumes was statistically significant..... 241

A4-8: Total contrast volumes required in two sample patients for different scan durations. For 6-, 4-, 2-, and 1-s cardiac scans, a 62-year-old man 122-kg man (—●—) required 94, 78, 64, and 63 mL of contrast, whereas a 67-year-old 85-kg man (—◆—) required 58, 48, 36, and 35 mL of contrast, respectively. 241

CHAPTER I

INTRODUCTION

Diseases of the aorta such as aneurysm, dissections, ruptures, atherosclerotic ulcers, and degenerative valvular stenosis are a major problem in industrialized nations [1-3]. Visualization of the cardiac anatomy is critical for diagnosis, treatment planning and follow-up in these cases. Traditionally, chest radiography, echocardiography and X-ray angiography (using C-arm system) have been used as primary imaging modalities in the evaluation of these patients. However, these imaging techniques allow only two-dimensional (2D) viewing, thus limiting visualization of the lumen and changes in the vessel wall. Three-dimensional (3D) imaging provides not only precise visualization of the complex anatomy in physiological conditions, but also allows the measurement of critical structural and functional parameters. Typically, 3D images are acquired using multi-detector-row computed tomography (MDCT), magnetic resonance imaging (MRI) and ultrasound (US). Short examination times, ease of scanning and minimum dependence on the technologist, along with rapid developments in technology allow MDCT imaging from pre-operative planning to intra-operative guidance to post-operative evaluation. Intravenous injection of iodinated contrast medium is required with MDCT to

opacify the blood pool and visualize the chambers of the heart, great vessels, and coronary arteries as well as distinguish different parts of cardiac anatomy.

Preprocedural imaging with contrast-enhanced single-energy MDCT plays a vital role in planning for novel transcatheter and minimally invasive procedures like percutaneous coronary interventions (PCI), aortic endovascular aneurysm repair (EVAR), and transcatheter aortic valve implantation (TAVI) by identifying optimal anigographic views required for the procedure and optimal device size required for the patient [1-10]. Integration of this 3D data into the procedure and overlaying these 3D MDCT images with the two-dimensional (2D) fluoroscopy images obtained from a C-arm system allows real-time guidance for more accurate and safer interventions. The use of MDCT data further enables new approaches for development of devices [11]. However, the direct use of MDCT images in this way has been limited because of registration challenges between 3D MDCT and 2D fluoroscopic images. By rotating a C-arm system around the patient, 3D images (aka, C-arm CT images) can be acquired in the catheterization laboratory. The 3D images from C-arm CT and preprocedural MDCT can then be registered to facilitate overlay of the MDCT images onto the live 2D fluoroscopic images for guidance.

In this thesis, optimal contrast and scan protocols for obtaining C-arm CT images in the context of TAVI were systematically determined in a swine model and image measurements were compared with those obtained from MDCT. Then, the utility of overlaying 3D preprocedural MDCT images onto real-time 2D fluoroscopy images for intraprocedural guidance during TAVI was evaluated, and the feasibility of making post-TAVI measurements from C-arm CT images assessed. Finally, a procedure was developed to obtain a C-arm CT dose metric to estimate the radiation burden with 3D C-

arm acquisition.

MDCT is also routinely used for follow-up of patients after the interventional procedure to insure accurate placement of the prosthetic valves/stents and their long-term results [2, 3, 12-14]. In the context of EVAR, triple phase single-energy CT (SECT) is often used to evaluate patients 1 month, 6 months, and yearly after such repairs [13]. The combination of non-contrast, arterial phase, and venous phase SECT images is used to evaluate aneurysm size, stent-graft position and patency, perigraft flow (endoleaks), graft fractures and kinks, and the patency of native vessels near the graft [2, 3, 12-14]. Of concern is the high cumulative radiation dose to the patient resulting from three-phase imaging in multiple follow-up examinations [15-17].

In an attempt to decrease radiation dose, two SECT acquisitions can be replaced with one dual-energy CT (DECT) acquisition [18, 19]. At DECT, data acquisition at two x-ray energies is followed by the reconstruction of corresponding image sets with different attenuation properties [20-23]. DECT data obtained during or after contrast injection can be used to generate not only arterial and venous phase images but also virtual non-contrast (VNC) images [18, 19, 22, 24]. Hence, another objective of this study was to evaluate the feasibility of using arterial DECT imaging to generate VNC images. However, the presence of high-density iodinated contrast medium adjacent to other high-density materials, such as a stent and calcium, and, in many cases, the lack of uniformity of contrast attenuation along the length of the aorta increase the challenge of generating VNC CT images from arterial DECT data.

During arterial phase contrast medium protocol, which is defined by the volume, flow rate, iodine concentration, and injection timing (relative to the start of the scan) of

contrast, can be controlled to influence contrast enhancement. The same contrast injection protocol is used for all patients undergoing CT for a particular clinical indication. However, the patient response to the contrast injection and the resulting enhancement of the vessel of interest is affected by a multitude of patient specific parameters, such as weight, height, gender and cardiac condition [4]. Consequently, cardiac enhancement can vary widely within patients with a standardized protocol and can result in non-uniform enhancement, which causes problems in the generation of VNC CT images with DECT imaging. Therefore, an advanced injection protocol may be required to consistently achieve prolonged, uniform vascular enhancement. Although various modeling techniques have been used to develop contrast injection protocols for SECT cardiovascular imaging [25-27], these advanced profiles focused on imaging with single or 16- detector row CT imaging. With rapid improvements in scanner technology, the scan acquisition time for the latest generation MDCT scanners has decreased drastically [28]. Moreover, no studies to date have investigated the impact of contrast optimization during arterial phase DECT imaging. A part of the evaluation of the feasibility of using arterial DECT to generate VNC images included development of an algorithm to determine contrast protocols for achieving uniform enhancement during DECT imaging to improve VNC generation.

This dissertation is organized as background (chapters II-V), hypothesis and specific aims of the thesis (chapter VI), pilot studies performed for the specific aims (chapter VII) and implementation of each specific aim (chapters VIII-XI). Chapter II describes the structure of the heart and its functions. Chapter III explains the cardiovascular diseases and the paradigm shift in treating patients with safe and efficient

minimally invasive surgeries. Chapter IV focuses on the basic principles of x-ray based imaging modalities that are routinely used for planning, guidance and follow-up of the minimally invasive surgeries. Chapter V shows a thorough literature review of the extensive work done so far in the use of the imaging modalities for different minimally invasive surgeries along with the limitations of the studies. Chapter VI describes the hypothesis and specific aims of this thesis and chapter VII describes the preliminary studies done in order to develop the imaging and contrast protocols for the specific aims.

Chapter VIII describes specific aim 1 showing the feasibility of arterial phase DECT imaging to generate VNC images using three-material decomposition algorithm for follow-up of 30 patients post-EVAR. The study also shows the limitations in VNC generation due to non-uniform arterial enhancement, false identification of high-density substances like iodine and stent as contrast agent with the three-material decomposition. This chapter has been published as “Feasibility of dual-energy CT in the arterial phase: Imaging after endovascular aortic repair” in American Journal of Roentgenology in 2010. Chapter IX describes specific aim 2, suggesting improvements in VNC image generation with use of optimized contrast protocols developed using linear-time invariant modeling in time domain, three-material decomposition algorithm using basis spectral and basis material analysis, and employing spectrally well separated x-ray tube voltages for DECT imaging.

Chapter X, in fulfillment of specific aim 3, focuses on the determination of optimal contrast and imaging protocols for obtaining C-arm CT images before TAVI in a swine model and the comparison of the resulting image measurements with those obtained from MDCT. The study shows that an ungated C-arm CT acquisition during

rapid pacing with aortic root injection is optimal for evaluation and measurement pre-TAVI in swine and allows overlaying MDCT on fluoroscopic images for intraprocedural guidance and finally the assessment of valve position post-TAVI in the interventional suite. The contents of this chapter has been submitted as a manuscript titled “Optimization of Acquisition and Contrast-Injection Protocol for C-arm CT Imaging in Transcatheter Aortic Valve Implantation: Initial Experience in a Swine Model” to Journal of the American College of Cardiology: Cardiovascular Imaging and is currently under review. Chapter XI describes development of a procedure to obtain a C-arm CT dose metric to estimate the radiation burden with 3D C-arm acquisition along with implementation in patients for dose measurement.

This dissertation concludes with a brief summary of the findings of the research and its relevance followed by possible future studies. The appendices include the Matlab programs for patient-specific contrast agent optimization, combined basis spectral and basis material algorithm for VNC generation, implementation of Savitzky-Golay filter for simulating dose measurements with C-arm CT experiments, and a potential manuscript describing development of linear-time invariant modeling for contrast agent optimization in time domain and predictions of contrast protocols for fast MDCT scans.

CHAPTER II

THE HEART AND GREAT VESSELS

2.1 Anatomy

The heart is a hollow, conically shaped muscular organ located between the lungs and enclosed in the cavity of pericardium. The pericardium is a conical membranous sac in which the heart and the origin of the great vessels are contained [29]. The heart is subdivided by a muscular septum into right and left lateral halves. A transverse constriction subdivides each half of the organ into two cavities; the upper cavity on each side being the atrium and the lower, the ventricle [29].

Three heart is composed of three layers namely, the epicardium or external layer, the myocardium or middle layer and the endocardium or inner layer. The myocardium comprises of cardiac muscle tissues and causes the contraction of the heart [29].

Aorta is the largest artery that channels the oxygenated blood to other arterial branches for supplying nutrients to the tissues of the body. It originates at the upper part of the left ventricle with a diameter of approximately 3 cm, continues in cranial direction for a short distance, arches backward to the left side, descends within the thorax to pass into the abdominal cavity and finally ends near the fourth lumbar vertebra with

approximately 1.75 cm diameter by dividing into the right and left common iliac arteries [29].

The aorta can be described based on the location. The portion of the aorta from the left ventricle extending in the cranial direction is termed as the ascending aorta (AA) and is approximately 5 cm in length [29]. The three aortic sinuses are present as small dilatations at the origin of AA opposite to the segments of the aortic valve (Figure 2-1). Additionally, the two coronary arteries that provide blood supply to the heart also arise near the commencement of the AA above the margins of the valves. The arch of aorta, also known as the transverse aorta is the portion that begins after the ascending aorta and runs cranially and then moves caudally eventually becoming the descending aorta [29]. The descending aorta is further divided into the thoracic and abdominal aorta depending on its location in the trunk cavity.

The aorta is composed of three layers of tissue: intima, media and adventitia. The intima is the innermost thin layer lined with endothelial cells. The media is the middle and thickest layer and consists of layers of elastic tissue. This composition provides the tensile strength to the aorta. The adventitia is the outermost layer and is composed of collagen material. This layer contains a network of small blood vessels that supply blood to the aortic wall.

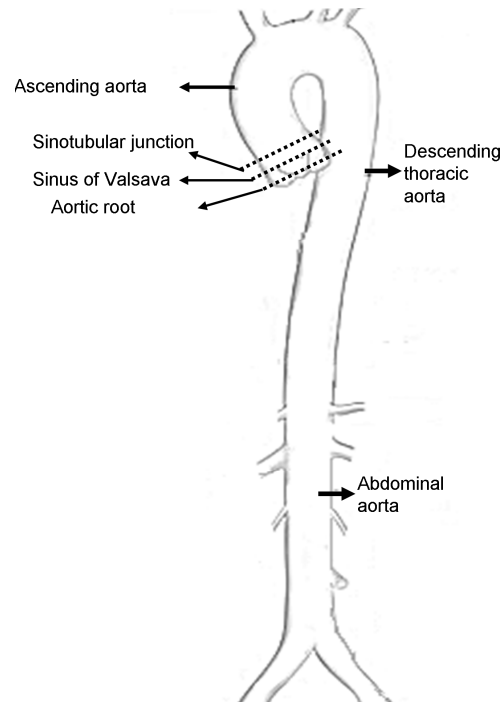


Figure 2-1: Schematic of the aorta.

The aortic valve consists of three thin, crescent-shaped cusps, and lies between the left ventricle and aorta. The three cusps move outwards toward aorta in their open position and come together to shut the aortic orifice in their closed position. The cusps are controlled by the pouches of the aortic root called the sinus of Valsalva that are located behind the cusps.

2.2 Function

The heart is a positive displacement pump responsible for blood circulation to the various organs in the body. The left side of the heart pumps oxygenated blood to the body, while the right side of the heart pumps deoxygenated blood to the lungs. The supply of blood to the heart and the body constitutes the systemic circulatory system; the

blood flow to the lungs comprises the pulmonary circulatory system. The cardiac cycle consists of two major functional periods: diastole (ventricular relaxation and filling) and systole (ventricular contraction and ejection) [29]. In diastole, blood from the right and left atria enters the right and left ventricles, respectively. In systole, the ventricles contract and blood is ejected from the right ventricle into the main pulmonary artery and from the left ventricle into the aorta.

Deoxygenated blood from the body enters the right atrium (RA) through the superior vena cava (SVC) and inferior vena cava (IVC) (Figure 2-2). The RA contracts to fill the right ventricle, which then ejects the blood into the lungs. The oxygenated blood from the lungs enters the left atrium (LA). The LA contracts to fill the left ventricle, which then pumps blood to the rest of the body through the aorta. Four one-way valves regulate flow through the heart. Two of these valves, the mitral valve on the left side and the tricuspid valve on the right side, are located between the atria and the ventricles. The aortic valve is located between the left ventricle and the aorta, while the pulmonary valve is located between the right ventricle and the pulmonary artery. With the exception of the mitral valve, which is a bileaflet valve, the other heart valves are trileaflet valves.

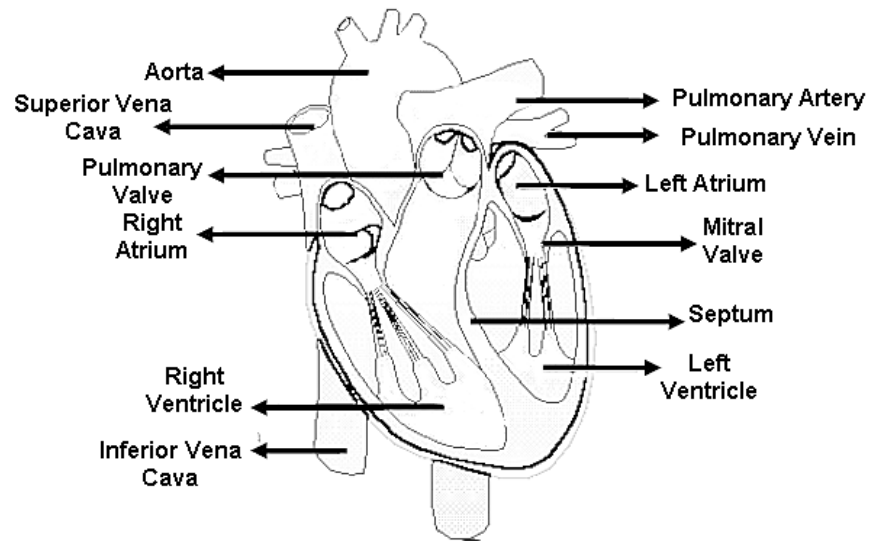


Figure 2-2: Schematic of the heart.

CHAPTER III

MINIMALLY INVASIVE CARDIOVASCULAR SURGERIES

Minimally invasive cardiovascular surgeries represent a paradigm shift in treating patients with cardiovascular diseases. With the rapid development of technology and improvements in techniques, minimally invasive surgeries have evolved into an alternative treatment option to traditional open surgery in suitable patients. Minimally invasive procedures like percutaneous coronary interventions (PCI), endovascular aneurysm repair (EVAR), transcatheter aortic valve implantation (TAVI) are few techniques currently used for treating specific cardiovascular diseases like coronary artery aneurysms, aortic aneurysms and valve repairs by providing greater patient comfort and recovery with fewer complications. Some of the cardiovascular diseases and the minimally invasive surgical procedures used for treatment of these diseases are discussed in this chapter.

3.1 EVAR

3.1.1 Thoracoabdominal Aneurysm

Thoracoabdominal aortic aneurysms are frequently caused by atherosclerosis [30, 31]. The aneurysms are typically categorized as true or false depending on their pathologic features [30]. In true aneurysms, all three layers of the aortic wall (intima, media and adventitia) form the aneurysm, while in false aneurysm, the intima and/or media may be disrupted leaving the blood in the adventitia layer [32]. Thoracoabdominal aneurysms have been classified into four types on the basis of their anatomic location [33]. Type I aneurysm includes the descending thoracic aorta and the upper abdominal aorta; type II involves both the descending thoracic and abdominal aorta. Type III aneurysm occurs only in the lower portion of the thoracic aorta and type IV aneurysm starts at the diaphragm and continues in the caudal direction. MDCT is the most commonly used modality for diagnosis and treatment planning of aortic aneurysms followed by transesophageal echocardiography (TEE), MRI and aortography [34].

3.1.2 Management of Thoracoabdominal Aneurysm

Traditionally, surgical intervention was required for treatment of aortic aneurysms [34]. The choice of surgical techniques depends on the extent of disease, patient age, long-term anticoagulation therapy, state of the native aortic tissues, status of the aortic valve, prior aortic surgeries [1, 3]. However, a paradigm shift has occurred with the emergence of aortic endovascular stent procedures. EVAR has become a reliable alternative to open surgery for thoracic, thoracoabdominal and abdominal aortic

aneurysm treatment [35-37]. During EVAR, an endograft, or stent is placed in the aneurysm of the aorta. Preprocedural arterial 3D imaging is required to ensure fitting of the stent in the aneurysm, without blocking flow in the branching vessels. This requires accurate details of the size, length, wall characteristics of the aneurysm along with location and rotation angle of the visceral arteries relative to the aorta and other branches. In addition to device placement, the 3D images are also used for optimizing device selection specific to a patient using computational modeling. EVAR is associated with lower morbidity and mortality rates than open surgical repair, along with reduced stay in the hospital after the procedure [38]. After stent placement, triple-phase SECT is often used to monitor patients 1 month, 6 months, and yearly [13]. Combinations of the three phases, namely the pre-contrast (non-contrast), contrast-enhanced (arterial) and post-contrast (venous) SECT images is used to evaluate aneurysm size, stent-graft position and patency, perigraft flow (endoleaks), graft fractures/kinks, and the patency of native vessels near the graft [2, 3, 12-14].

3.2 TAVI

3.2.1 Aortic Stenosis

Aortic stenosis is the most frequent native valvular heart disease [39-42] with a significant impact on cardiovascular mortality and morbidity [40, 41, 43]. Degenerative aortic valve calcification is an active process similar to atherosclerosis [44-46].

3.2.2 Management of Aortic Stenosis

Due to the lack of any pharmacological therapy for treating the stenosis [47-50], traditional open-heart surgical aortic valve replacement (SAVR) is considered as an effective treatment for advanced disease state in suitable patients [51]. However, for high-risk patients with unstable hemodynamics or multiple co-morbidities [52-55], less-invasive interventional procedures like balloon aortic valvuloplasty (BAV) may be performed. Even though BAV provides temporary relief to patients, restenosis develops within 6-12 months after the procedure [56, 57]. TAVI is considered a viable option in these patients, where valve prosthesis is implanted on the existing native valve using transfemoral, transapical or transseptal methods [58-64]. Current results from clinical trials show a high success rate and clinical improvement in patients after the procedure [65-67].

To eliminate complications like vascular injury during device positioning, coronary artery occlusion, arrhythmias, prosthetic embolization, and imprecise positioning of the prosthesis (currently available valves cannot be repositioned), it is critical to perform preprocedural imaging for accurate knowledge of the anatomy and functionality of the cardiovascular structures and valves. Currently, TEE and cardiac catheterization are used for image guidance during TAVI. However, these are limited to 2D views of the anatomy. Recently, MDCT has been used routinely to image patients before TAVI to provide three-dimensional (3D) information on valve morphology, function, and the extent and location of aortic valve calcifications, in addition to the vascular access, including calcifications and tortuosity of the aorta and ilio-femoral arteries, used for the delivery of the prosthesis in these patients. Preprocedural MDCT

images also help to accurately determine the relationship between the aortic annulus and the ostium to avoid complications of TAVI and plan for the procedures [10, 68].

CHAPTER IV

X-RAY BASED IMAGING

Visualization of the cardiovascular anatomy is critical for planning and follow-up of minimally invasive surgeries. Traditionally, chest radiography, echocardiography and X-ray angiography (using C-arm system) have been used as primary imaging modalities in these procedures. However, these techniques allow only two-dimensional (2D) viewing, thus limiting visualization of the lumen and changes in the vessel wall. In these cases, three-dimensional (3D) imaging provides not only precise visualization of the complex anatomy in physiological conditions, but also allows the measurements of critical structural and functional parameters. Typically, 3D images are acquired using multi-detector-row computed tomography (MDCT), magnetic resonance imaging (MRI) and ultrasound (US). Minimally invasive surgeries rely on using X-ray based imaging for planning, guidance and follow-up. The technique and basic principles of X-ray based 2D and 3D imaging modalities are discussed in this chapter.

4.1 X-ray Physics

4.1.1 X-ray Tube

X-rays are a form of electromagnetic radiation, produced when a fast moving stream of highly energetic electrons collide with a target metal to convert their kinetic energy into electromagnetic radiation. The basic elements of an x-ray tube are shown in Figure 4-1. The x-ray tube consists of a glass tube with two electrodes (the cathode and the anode) enclosed in vacuum.

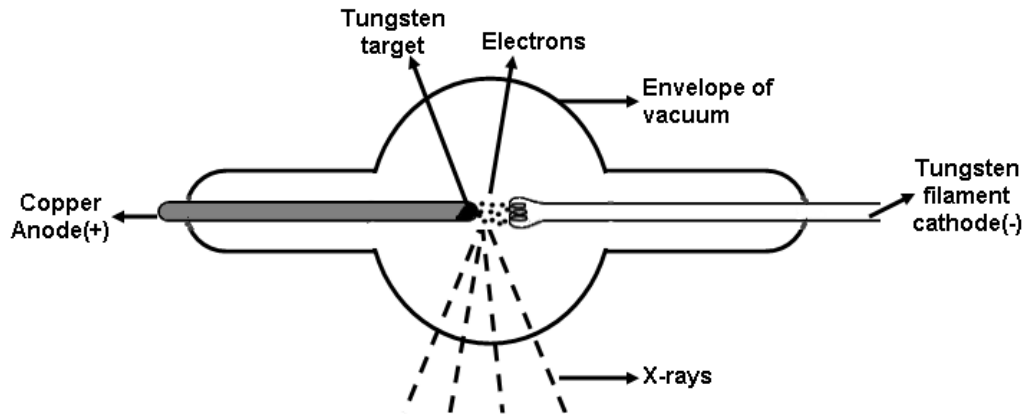


Figure 4-1: Components of an x-ray tube required for x-ray production.

The cathode is the negative terminal of the x-ray tube consisting of a helical filament, which is the source of electrons surrounded by a focusing cup. It also contains two wires that heat the filament. The heated filament releases electrons by thermionic emission (emission of electrons due to absorption of thermal energy). The anode is the positive metal target electrode of the tube. Tungsten is typically used as the anode material because of the high atomic number and high melting point that allow efficient production of x-rays and high absorption of heat, respectively. With the application of a high potential difference (or voltage) between the two electrodes, electrons produced at

the cathode accelerate towards the anode. Once the electrons strike the target anode, 99% of the kinetic energy of the electrons gets converted into heat and the remaining 1% gets transformed into x-rays. The presence of vacuum in the x-ray tube allows independent control of the number and speed of the accelerated electrons. Critical modifiable parameters associated with x-ray production include tube voltage and tube current.

4.1.1.1 Tube Voltage

Tube voltage is defined as the potential difference applied between the cathode and the anode in the x-ray tube to allow the flow of electrons from the former to the latter [69]. It is typically expressed as the peak voltage applied across the x-ray tube. For example, 100 kVp indicates that a maximum voltage of 100,000 V is applied across the tube to accelerate the electrons and the applied voltage fluctuates between some lower value and the maximum value. An increase in the tube voltage improves the quality of the x-rays and enables them to penetrate tissue more easily and reach the detector, thus increasing the signal to noise ratio (SNR) [69]. However, this also increases the radiation dose proportional to square of the increase in tube voltage [69].

4.1.1.2 Tube Current

Tube current refers to the number of electrons flowing from the cathode to the target anode per second and is measured in milliamperes (mA) [69]. An increase in the tube current proportionally increases the number of electrons (quantity) in the x-ray tube and enables more x-rays to penetrate tissue and reach the detector. This results in an improvement in SNR and a directly proportional increase in radiation dose [69].

4.1.2 X-ray Generation

X-rays are generated through two electronic processes: bremsstrahlung and characteristic x-ray spectrum.

4.1.2.1 Bremsstrahlung Radiation

The Bremsstrahlung radiation is produced when the electrons from the cathode interact with the nucleus of the target anode. The coulombic forces attract the electron towards the positively charged nucleus of the target. The electron gets decelerated and changes in its trajectory. This results in the loss of a part or all of the electron's kinetic energy along with the production of an x-ray photon with equivalent energy. The distance between the electron and nucleus determines the energy of the x-ray. When the distance is the largest, the coulombic forces of attraction are the weakest resulting in the production of the lowest energy x-rays. As the distance decreases, the x-ray energy increases (Figure 4-2) and the highest energy x-rays are produced when the electron directly impacts the nucleus.

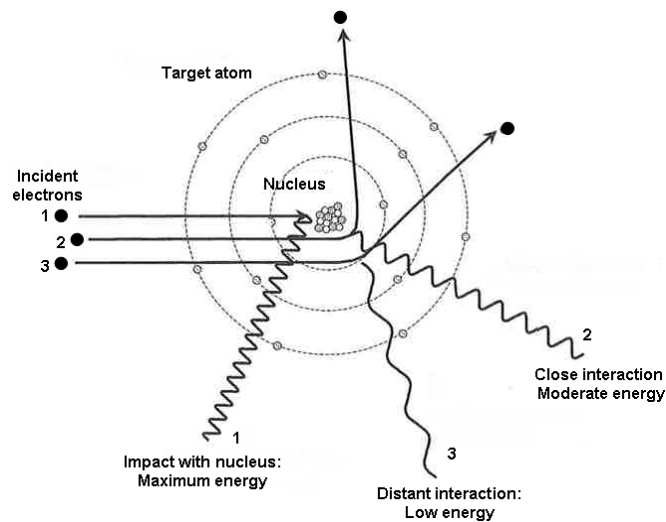


Figure 4-2: Production of bremsstrahlung spectrum and impact of subatomic distance between the nucleus and electrons on the production of the energy of x-rays. Adapted from Bushberg et al [69].

Due to the relatively empty space and the small subatomic distances in the atom, the probability of a direct interaction between the electron and nucleus is extremely low. Hence, a greater number of low-energy x-rays are produced as compared to high-energy x-rays in a bremsstrahlung spectrum (distribution of x-ray photons with respect to energy) [69]. The unfiltered spectrum shows a linear decrease in the production of x-rays with energy up to the highest energy determined by the peak tube voltage applied between the electrodes in the x-ray tube (Figure 4-3) [69]. With the filtered bremsstrahlung spectrum, the lower-energy x-rays are removed and the average x-ray energy varies between one third to one half of the maximum x-ray energy (Figure 4-3).

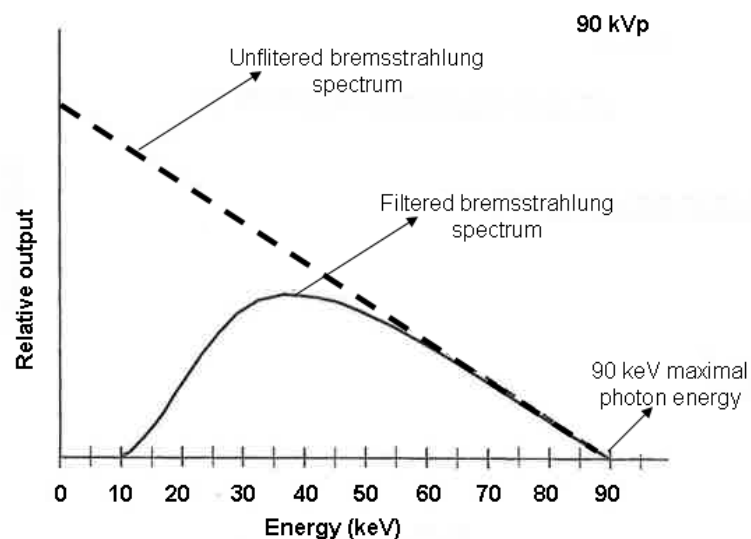


Figure 4-3: The bremsstrahlung spectrum for a 90 kVp peak voltage. The unfiltered spectrum shows the linear decrease of x-rays with energy up to the maximum energy of

90 keV. The filtered spectrum shows the preferential absorption of x-rays below 10 keV. Adapted from Bushberg et al [69].

4.1.2.2 Characteristic Radiation

Characteristic radiation occurs when an electron strikes the target and releases electrons from the inner orbitals of the target atoms. The ejection of the electron creates a positively ionized target atom, which subsequently releases the excess energy to return to its original state either by removing an additional electron called Auger electron, or by emitting an x-ray with the excess energy. The characteristic radiation contains only x-rays at discrete energies uniquely associated with the binding energy of the ionized atom of the target material.

Each atom has different shells (K, L, M etc) with distinct binding energies. When an electron strikes the target anode with energy greater than the binding energy of a shell in the target atom, the electron from the shell gets ejected resulting in an unstable ionized atom. An electron from a higher level with lower binding energy fills the vacant orbital releasing a characteristic x-ray with energy equivalent to the difference between the binding energies of the two shells (Figure 4-4).

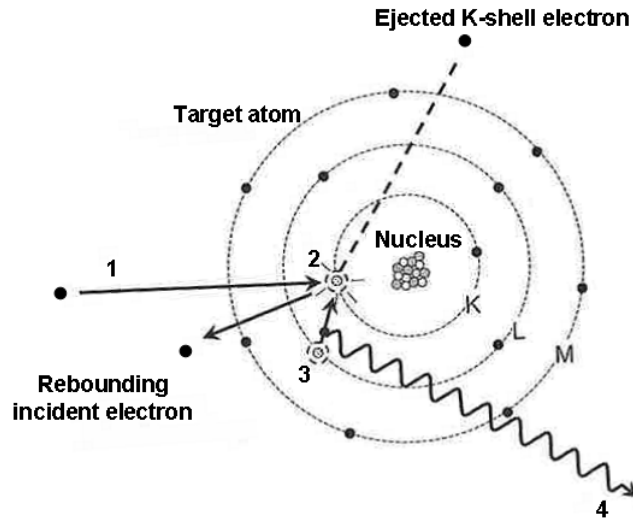


Figure 4-4: Generation of characteristic x-rays. (1) The incident electron with energy greater than the binding energy of the electron in the K-shell ejects the electron from the shell. (2) This creates an unstable positive ion. (3) The electron from the adjacent L-shell fills in the vacancy in the K-shell. (4) The electron transition causes the emission of characteristic x-ray with energy equivalent to the difference between the binding energies of K and L shells. Adapted from Bushberg et al [69].

This can also lead to a cascade of electron transitions producing x-rays at discrete energies (depending on the difference of the binding energies of the shells) that are characteristic of the target material. The characteristic x-rays produced in the diagnostic imaging range are primarily due to vacancies in the K-shell. For example, in the filtered spectrum from a tungsten target, a K_{α} characteristic x-ray at 59.3 keV is seen that corresponds to the difference between the binding energies of the K and L shells (Figure 4-5).

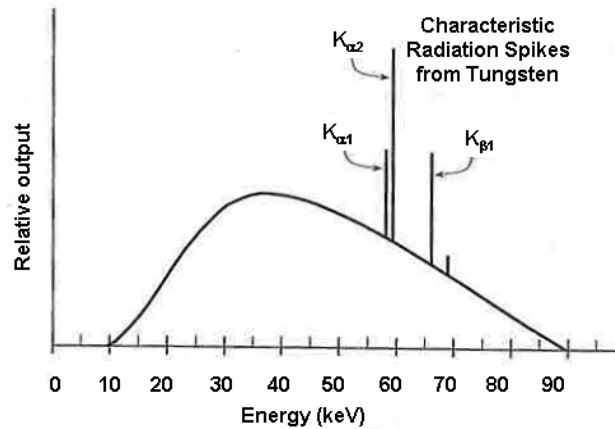


Figure 4-5: The filtered bremsstrahlung and characteristic x-ray spectrum of tungsten material obtained at 90 kVp tube voltage. The curve shows the filtering of low-energy photons below 10 keV in the bremsstrahlung spectrum superimposed with the characteristic x-rays from $K_{\alpha 1}$, $K_{\alpha 2}$, and $K_{\beta 1}$ transitions at 59.3, 57.9 and 67.2 keV. Adapted from Bushberg et al [69].

4.1.3 X-ray Interaction with Matter

X-rays interact with matter in different ways: Rayleigh scattering, Compton scattering, photoelectric absorption, pair production, or photodisintegration. In the range of diagnostic energy (< 150 keV), x-rays primarily interact with the orbital electrons of the atoms and can cause disruption of the atomic structure of the tissue. Rayleigh scattering and Compton scattering and photoelectric interactions dominate in the diagnostic x-ray range.

4.1.3.1 Rayleigh Scattering

Rayleigh scattering occurs when a low energy diagnostic x-ray excites the electrons of an atom and causes them to vibrate in phase. The atom returns to its stable state by emitting radiation of the same energy in a different direction (Figure 4-6). This interaction however does not cause ionization, as the atom does not eject electrons during this process. However, scatter radiation can contribute to image noise and degrade image quality. Scatter radiation has a low incidence (less than 5%) as compared to other interactions in diagnostic energy range.

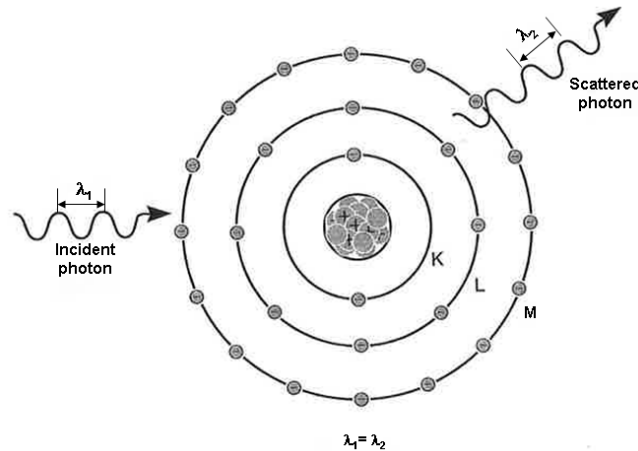


Figure 4-6: Rayleigh scattering where the incident photon at low energy strikes the atom causing the electrons of the atom to oscillate and finally ejecting a photon at the same incident energy, but in a different direction. Adapted from Bushberg et al [69].

4.1.3.2 Compton Scattering

Compton scattering occurs when a high energy incident photon (E_0) interacts with a valence electron to eject the outer orbital electron from the atom with some kinetic energy (E_{e-}). Additionally, a scattered photon with reduced energy (E_{sc}) as compared to

incident energy is produced (Figure 4-7). According to conservation of energy, the energy of the incident photon is distributed as the sum of the kinetic energy of the recoiled electron and the energy of the scattered photon.

$$E_0 = E_{e^-} + E_{SC} \quad (4-1)$$

Due to the production of scattered photon, Compton scatter results in ionization and may cause subsequent interactions with matter. The incident energy of the photon and the angle of the scattered photon determine the energy of the scattered photon. As E_0 increases, amount of energy transfer to the scattered photon increases and hence, the probability of Compton scattering interaction is dominant at higher energies.

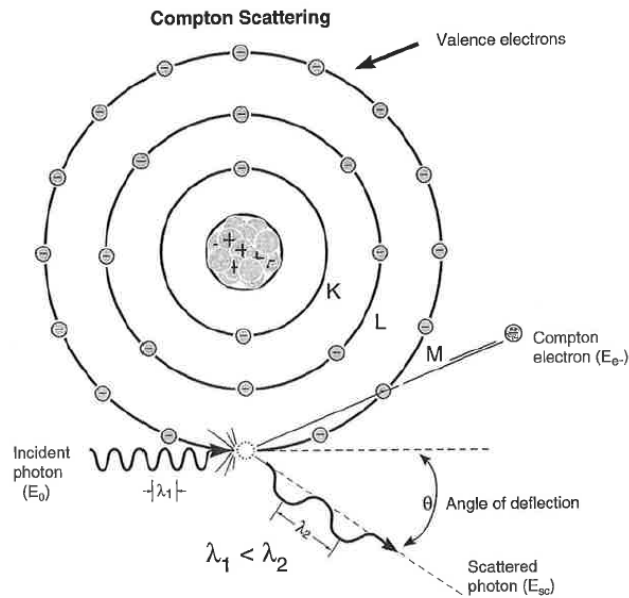


Figure 4-7: Compton scattering showing the incident photon ejecting a valence electron and a Compton scattered photon at an angle θ relative to the incident photon. The energy E_0 is split into E_{SC} and E_{e^-} . Adapted from Bushberg et al [69].

4.1.3.3 Photoelectric Effect

Photoelectric effect occurs when an incident photon (energy E_0) interacts with an electron with binding energy (E_b) close to but slightly lower than E_0 . The entire energy of the photon is used to overcome the binding energy of the electron and eject it from the orbit to produce a photoelectron (negative ion) with kinetic energy (E_e). The atom left with a void in the shell allows transition of electron from an adjacent shell yielding the emission of a characteristic x-ray photon with energy equal to the difference between the binding energy of the two shells. This leads to a cascade of electron transitions between the different shells and production of characteristic x-rays of lower energies leaving a positive ion (atom lacking an electron) at the end. Hence, photoelectric effect produces a photoelectron, positive ion and characteristic x-rays (Figure 4-8).

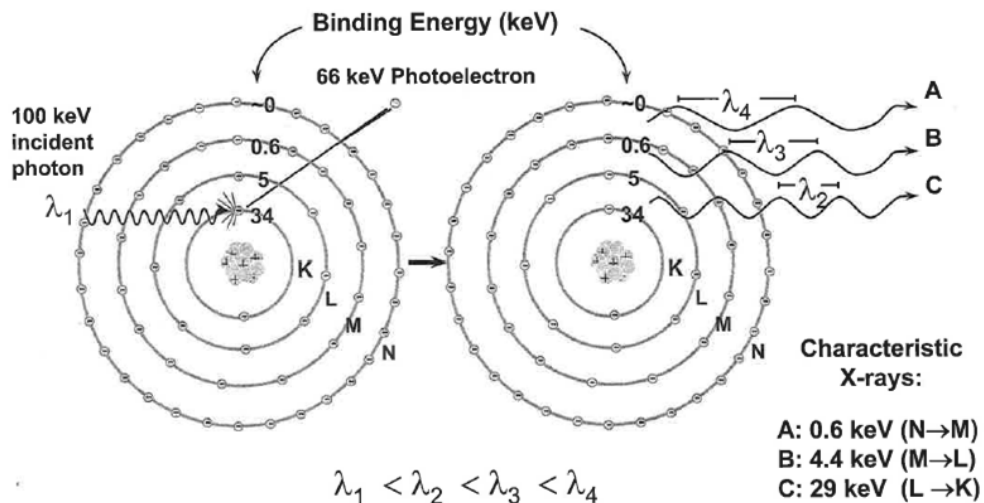


Figure 4-8: Photoelectric absorption showing interaction of a 100 keV photon with an iodine atom. The incident photon interacts with the K shell having binding energy (34 keV) closest to the incident photon and yields a 66 keV photoelectron. The removal of the electron from K shell triggers a cascade of electron transitions from L to K, M to L, and N to L resulting in characteristic x-rays with 29, 4.4 and 0.6 keV respectively as well

as positive iodine ion without an electron in the N shell. Adapted from Bushberg et al [69].

As E_0 increases, the occurrence of photoelectric effect decreases and hence photoelectric effect is the dominant interaction with low energy radiation. Moreover, photoelectric effect produces high contrast in the images. The important interactions of x-rays with soft tissue in the diagnostic x-ray energy range are shown in Figure 4-9.

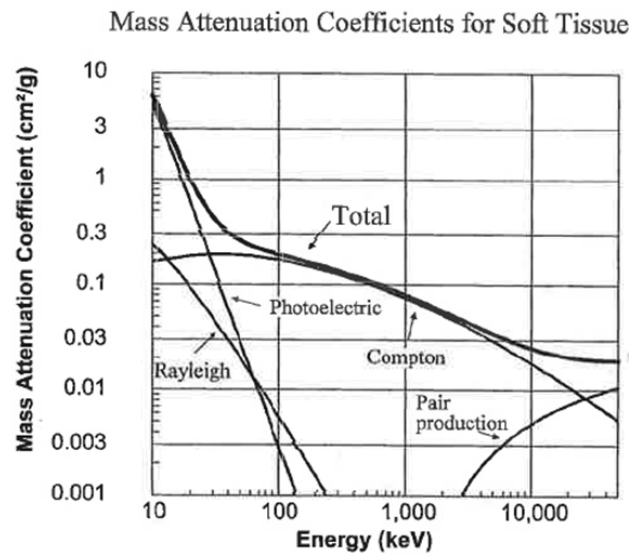


Figure 4-9: Graph showing the occurrence of Rayleigh scatter, Compton scatter, photoelectric effect, pair production as function of incident x-ray energies when they interact with soft tissue. Adapted from Bushberg et al [69].

4.1.4 Attenuation

Attenuation is the process of reducing the intensity from a beam of x-rays either due to absorption or scattering of photons when the beam travels through matter. Attenuation measures the change in the intensity of the photon and depends both on the quality and quantity of the x-ray beam. Attenuation also depends on the type of

interaction of x-ray photons with matter. The attenuation coefficient is used to measure the amount of x-ray beam attenuation by a substance.

4.1.4.1 Linear Attenuation Coefficient

Linear attenuation coefficient is defined as the fraction of photons removed from a monoenergetic beam of x-rays per unit thickness of material. It indicates the amount of attenuation or decrease in intensity of x-ray beam that can occur with a certain amount of material. It is represented by μ and the units are cm^{-1} . The μ of a substance can be calculated using the exponential relationship shown below between the number of incident photons (N_0), number of transmitted photons (N) through the substance of thickness x (in cm).

$$N = N_0 e^{(-\mu x)} \quad (4-2)$$

The linear attenuation coefficient can also be described as the sum of individual linear attenuation coefficients from the different interactions between x-rays and matter.

$$\mu = \mu_{\text{Rayleigh}} + \mu_{\text{Compton}} + \mu_{\text{Photoelectric}} + \mu_{\text{Pair Production}} + \mu_{\text{Photodisintegration}} \quad (4-3)$$

The linear attenuation coefficient depends on the number of atoms of the substance the x-rays need to pass through per unit distance. Hence, μ is proportional to the density of the material and is greater for highly dense substances.

4.1.4.2 Mass Attenuation Coefficient

Mass attenuation coefficient is defined as the linear attenuation coefficient per unit density. It is expressed as μ/ρ and the units are cm^2/g . The mass attenuation

coefficient is independent of the density of the substance. Hence, for a given photon energy, a substance has the same mass attenuation coefficient in different states. For example, water, ice and watervapor have the same mass attenuation coefficient ($0.214 \text{ cm}^2/\text{g}$) even though the linear attenuation coefficients and densities are different in each state.

4.1.4.3 Factors Affecting Attenuation

Energy (E) of the incident x-rays along with density (ρ), atomic number (Z) and electrons per gram of the material influence the degree of attenuation of the x-ray beam as it passes through matter. Increasing the radiation energy decreases attenuation, while increasing density, atomic number or electrons per gram of the material increases attenuation. Apart from the individual influence, energy and atomic number together influence the type of interaction of x-ray with matter. For example, as energy or atomic number increases, the photoelectric effect dominates. Moreover, with the knowledge of the percentage of each type of interaction, the total attenuation coefficient can be calculated as the weighted sum of the individual attenuation coefficients from each interaction.

4.2 X-ray Based Imaging

4.2.1 Fluoroscopy

Fluoroscopy is a 2D imaging procedure that allows visualization of the anatomy of the patient in real-time with high temporal resolution. The standard components of fluoroscopic imaging system contain x-ray tube, filters, collimator to control the x-ray

beam, anti-scatter grid to eliminate scatter, image intensifier and a video camera. The image intensifier distinguishes the fluoroscopy equipment from the other x-ray equipment (Figure 4-10). The image intensifier tube shows the image to the observer by converting the x-ray photons in light photons, then converting light photons into electrons and finally into light photons as described below.

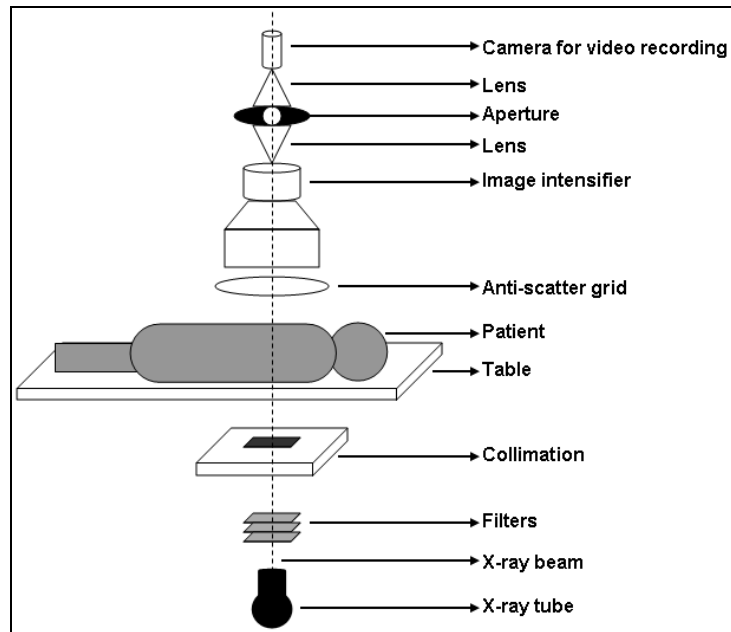


Figure 4-10: Schematic illustrating the key components of a fluoroscopic system.

When the x-ray beam travels from the x-ray tube through the patient, it enters the image intensifier tube which is a vacuum glass tube consisting of input phosphor, photocathode, electrostatic focusing lens, accelerating anode and output phosphor. The x-rays are absorbed by the input fluorescent screens and convert the x-ray photons into light photons. As these light photons interact with the cathode, they emit photoelectrons which travel towards the accelerating anode from the photocathode due to the potential difference between the two electrodes. The electrons are focused by the electrostatic lens

strike the fluorescent screen and emit light photons carrying the fluoroscopic image to the human eye. Fluoroscopic systems are heavily used during minimally invasive surgical procedures for guidance during the procedure. However, the inability to obtain 3D information in the images is a limitation with this technology.

4.2.2 Computed Tomography (CT)

CT is a tomographic imaging technique, which generates cross-sectional images of the patient by rotating an x-ray source and detector array around the patient. Both the x-ray source and the detector array are housed inside a gantry. Multiple x-ray projections at different angulations are obtained with every rotation of the gantry. These projections are preprocessed to calculate the average linear attenuation coefficients within a cross-section of the body and reconstruct the CT image.

Multi-detector row CT (MDCT) scanners consist of multiple detectors in the longitudinal (z-axis) direction, which enable acquisition of multiple images with a single gantry rotation (Figure 4-11). Scanners typically used for cardiovascular imaging acquire 64, 128, 256 or 320 images per gantry rotation depending on specific scanner.

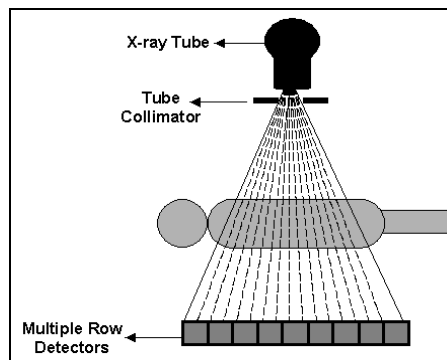


Figure 4-11: Illustration showing multiple detectors in the longitudinal direction in the MDCT scanners.

4.2.2.1 Data Acquisition

During data acquisition, a series of x-ray beams with intensity (I_0) are projected from an x-ray source through a patient. The x-rays are differentially absorbed by the tissue along the path of the x-ray and the beam gets attenuated. The transmitted radiation is then measured by a detector array lying opposite to the x-ray tube in the gantry. The intensity of an x-ray which passes through the patient is measured by the detectors as I_t . A reference detector measures the intensity of the unattenuated x-ray beam as I_0 . I_0 and I are related by the following equation.

$$I = I_0 e^{(-\mu x)} \quad (4-4)$$

where, x is the thickness of the tissue along the ray (in centimeters), and μ is the average linear attenuation coefficient along the ray (in cm^{-1}) [69]. The intensity values measured from each ray at the detectors are collected at many orientations as the gantry is rotated around the patient. This data is then used to calculate the projection data, $P(x)$, which is independent of the intensity of the x-ray beam.

$$P(x) = \ln\left(\frac{I_0}{I}\right) \quad (4-5)$$

Combining equations 4-4 and 4-5 results in

$$P(x) = \mu x \quad (4-6)$$

MDCT imaging is performed using either the sequential (also known as axial or step and shoot) or spiral (also known as helical) scanning mode. In the sequential mode, the gantry rotates around the patient in a circular path to obtain a set of cross-sectional images, and then the patient table is incremented to the next position. This procedure of

rotating the gantry 360° around the patient and then incrementing the patient table is repeated until the entire anatomy of interest is covered.

In the spiral mode, both the gantry and the patient table move continuously and trace a helical path of data acquisition around the patient. This is possible due to the development of slip ring technology that allows the tube and detectors to move continuously. With spiral MDCT, acquired projection data are interpolated to reconstruct images of each axial position.

The ratio of the table translation per gantry rotation (d) to the nominal beam width (NT) is defined as pitch. This is also known as beam pitch (p) and given as:

$$p = \frac{d}{NT} \quad (4-7)$$

where, N is the number of rows and T is the thickness of each row. For single-row detector CT scanners, $NT=1$ and pitch can be inferred as the table movement per row. Hence, pitch is a dimensionless quantity and indicates the overlap in data acquisition. A pitch value of ≥ 1 indicates no overlap in data, and a value < 1 indicates overlap. In general, increasing the pitch results in decrease in scan time, linear reduction in radiation dose and an increase in noise.

MDCT scanners have anatomically adapted tube current modulation, in which the x-ray tube current is continuously modulated online on the basis of the tissue attenuation measurements of the patient [70]. The tube current is lowered as the x-rays pass through thinner sections of the body and increased as they pass through thicker parts. Although anatomy based modulation decreased radiation dose significantly, same noise levels were observed with and without modulation [70, 71]

4.2.2.2 Image Reconstruction

In the image reconstruction process, the acquired projection data (from equation 4-6) are used to produce a reconstructed image of the scanned volume of the patient. Every picture element (pixel) in the digital image corresponds to a volume element (voxel) in a cross-section of the patient. The average linear attenuation coefficient for each voxel is calculated from the projection data, and reflects the degree to which the x-ray intensity is reduced by a tissue within the voxel. The total attenuation coefficient along the ray can be simplified as:

$$\mu x = \mu_1 \Delta x + \mu_2 \Delta x + \mu_3 \Delta x + \dots + \mu_n \Delta x \quad (4-8)$$

where, Δx is the small path length, which factors out from the above equation resulting in

$$\mu = \mu_1 + \mu_2 + \mu_3 + \dots + \mu_n \quad (4-9)$$

Specific attenuation values are then assigned to each individual voxel. After this preprocessing step, a reconstruction algorithm is used to produce the CT image.

Filtered back-projection is the most commonly used reconstruction algorithm. Back-projection is a mathematical process of reversing the image acquisition or the measurement of projection data to reconstruct an image. The image is reconstructed from the given projection data by performing 2-D inverse Fourier transforms. According to this method, the projection data are transferred into the frequency domain using the Fourier transform, then multiplied with a mathematical filter $K(f)$, and finally transformed back to the space domain using the Inverse Fourier transform [69]. This can be mathematically described as

$$p'(x) = FT^{-1} \{FT[p(x) * K(f)]\} \quad (4-10)$$

where, $p'(x)$ is the filtered data in the space domain.

A filter in the frequency domain is equivalent to a kernel in the spatial domain. Hence, the multiplication operation of the projection data with the filter in the frequency domain is the same as the convolution operation between the projection data and kernel in the spatial domain. However, due to the simplicity associated with multiplication, frequency domain is used for filtering the image before backprojection. A filter is applied to the projection data to minimize blurring and artifacts, and to typically obtain a more precise image of the scanned object. Different filters can be applied to the projection data to highlight certain features depending on the desired image appearance in the CT image. For example, the Ram-Lak filter allows high frequency data to pass yielding high-resolution images at the expense of increased noise [69]. Filters such as the Shepp-Logan and Hamming window allow passage of data at low frequencies and yield images with lower noise but decreased image resolution.

Once the raw data are mathematically filtered, they are back-projected into the spatial domain to obtain the image matrix of the scanned volume. After image reconstruction, a numerical gray value between 0 and 1 is assigned to each pixel in the image. This value indicates the average of all the attenuation values contained within the corresponding voxel.

An alternative to filtered back projection is iterative reconstruction using a maximum likelihood algorithm [72]. Iterative reconstruction algorithms were used with early CT scanners but soon replaced as the standard for CT image reconstruction in favor of faster, less computationally intensive filtered backprojection techniques. Iterative reconstruction algorithms assume initial attenuation coefficients for all voxels and use these coefficients to predict projection data. Predicted projection data are compared with

actual, measured projection data and voxel attenuations are modified until the error between estimated and measured projection data is acceptable. Compared to standard analytical reconstruction methods based on filtered back projections, statistical iterative reconstruction produces equivalent SNRs at lower radiation doses without a loss in spatial resolution [73, 74]. Recent advances in computer processing hardware and the increased efficiency of new iterative reconstruction algorithms have sparked the commercial introduction of these algorithms as an option for CT image reconstruction.

4.2.2.3 Image Display

In order to store these numbers in a computer for image display, pixel values are scaled up to an integer value and compared to the attenuation coefficient of water. The resulting number is called the CT number. When the scaling factor equals 1000, the CT number is described as a Hounsfield Unit (HU) [75]

$$\text{CT number} = \frac{(\mu_{\text{voxel}} - \mu_{\text{water}})}{\mu_{\text{water}}} \times \text{scaling factor} \quad (4-11)$$

CT numbers indicate the brightness of the pixels in the final image [69]. On the Hounsfield Unit scale, water has an attenuation value of zero. Air and tissues that are less dense than water, such as fat, have lower attenuation values (Table 4.1) than water and appear dark on the final image [76]. Tissues denser than water, such as bone and dense soft tissues have higher attenuation values (Table 4.1) than water and appear bright on the final CT image [76].

TISSUE	CT NUMBER (HU)
Bone	50 to 1000
Soft Tissue	40 to 80
Blood	50 to 60
Water	0
Fat	-80 to -100
Lung	-550 to -950
Air	-1000

Table 4.1: CT number of various clinical tissues.

To visualize, distinguish and interpret the different pixels in a CT image with the human eye, the image is displayed using a gray scale range. The gray scale range is assigned only to the set of CT values that need to be displayed in the image and is known as windowing. All the pixels above and below the window level are displayed as white and black respectively in the CT images [75].

4.2.3 Dual Energy Computed Tomography (DECT)

SECT allows measurement of the linear attenuation coefficient of a tissue at a given energy and may not be able to uniquely identify a tissue. DECT utilizes the energy dependence of attenuation properties of tissues. DECT imaging can be used to acquire two sets of data with two x-ray energy spectra to provide two independent measurements of linear attenuation coefficient of the tissues for characterizing properties of a given material. The linear attenuation coefficients can be defined as a product of the density (ρ) and the mass attenuation coefficient (μ/ρ) of each material.

$$\mu = \left(\frac{\mu}{\rho} \right) (E, Z) \bullet \rho \quad (4-12)$$

And the mass attenuation coefficient in turn depends on the energy (E) of the x-rays and the atomic number (Z) of the material. Therefore, tissues with different Z, ρ and E can be differentiated using DECT quantitative analysis. Basis spectral method and basis material decomposition are two approaches for quantitative based tissue characterization.

With the basis spectral method, DECT can provide material-specific information based on the assumption that the attenuation coefficient of any material in the diagnostic x-ray energy range can be described as a linear combination of Compton and photoelectric interactions. The linear equations can be solved to obtain the effective atomic number and density of the mixture [77]. The photoelectric effect is inversely proportional to E^3 , and Compton scattering is modeled by the Klein-Nishina formula (f_{KN}). Hence, Compton scattering dominates at higher energies due to density differences while photoelectric absorption dominates at lower energies due to differences in effective atomic numbers [78].

$$\mu(x, y, E) = \mu_P + \mu_C = A_1 \frac{1}{E^3} + A_2 f_{KN}(E) \quad (4-13)$$

The above equation can be solved for A_1 and A_2 using DECT measurements and further used to estimate the coefficients $a_1(x, y)$ and $a_2(x, y)$ representing the atomic number and physical density of the material where

$$A_1 = \int a_1(x, y) ds \text{ and } A_2 = \int a_2(x, y) ds \quad (4-14)$$

With basis material decomposition, the principle is that mass attenuation coefficient of a material can be expressed as a linear combination of the mass fractions of

the basis materials [79]. The composition of a mixture can be solved using this approach to obtain the mass fraction of the individual constituent elements present in the mixture.

DECT quantification with both basis spectral and basis material methods can be performed either in the pre- or post-reconstruction space. In the raw data or pre-reconstruction domain, energy dependent analysis can be applied to the measured projection data at the two energies prior to reconstruction. In the image or post-reconstruction domain analysis, images from the two x-ray energy spectrum are first reconstructed and then processed to characterize tissue. Although the latter approach is simpler and easier to implement, the former approach may allow benefits like beam hardening correction.

DECT imaging requires CT scanners capable of acquiring projection data at two different energies. There are four methods that are commonly used for DECT imaging. With the first and the simplest approach, CT data is first acquired using one x-ray energy spectrum and then data is acquired from the same region using a different energy spectrum [80]. Although this method allows adjustment of the tube-current for both energy spectrums independently and noise matching between the two image sets, it results in misregistration in the DECT image sets. The second technique for DECT imaging can be performed using dual-source method, where low and high-energy projections are acquired using two x-ray tube/detector pairs operating simultaneously during one acquisition [22, 28]. The advantage of this method is simultaneous acquisition of low and high energy data sets and improved spatial and temporal registration. However with the existing scanner design, only truncated data is acquired at one energy due to the limited field of view with the second x-ray tube/detector pair [81].

A third method employs a single x-ray tube that rapidly switches tube voltage from low to high values at different projection angles to acquire DECT data with good spatial and temporal registration. However, as the same x-ray tube is used for low and high energy, the tube current cannot be modulated separately and may result in more noise in low energy images [82-84].

With the fourth method, imaging is performed with a single-energy spectra and the energy separation is performed at the detector level using either dual-layer detectors [85, 86] or photon counting detectors [87]. The dual layer detector contains of a thin first layer of scintillator resting on a photodiode placed over a thicker layer of scintillator resting on a photodiode. While the low energy x-rays are detected in the first layer, the high energy x-rays are detected in the second layer. Although this approach offers simultaneous acquisition of low and high energy data sets optimizing spatial and temporal registration, the energy resolving capabilities of the detectors are limited due to the overlap in the energy spectrums. With photon counting detectors, the detector response can be split into energy bins and the attenuated x-rays within each energy bin used to generate energy-specific images. This technique provides good temporal and spatial registration between the DECT data sets but prevents adjustment in tube current with changes in tube voltage.

4.2.4 Cardiac CT

With the advent of MDCT in 1999 [88-90], faster gantry rotations and multisegment reconstruction algorithms, CT has been used in combination with intravenous contrast agent injection in routine clinical cardiac imaging [91-98] for

reliable visualization and analysis of the heart and the great vessels, as well as coronary circulation. Various clinical applications include evaluating the pericardium, the myocardium, the coronary arteries, the pulmonary veins, the thoracic and abdominal aorta, right ventricular dysplasia, stent visualization, graft patency, and to detect anomaly, malignancy, pericardial lesions and cardiac masses.

4.2.4.1 ECG synchronization

Cardiac CT imaging requires synchronization of data acquisition to the cardiac cycle for minimizing motion artifacts due to cardiac activity [99]. In cardiac CT, it is important to synchronize data acquisition with the electrical activity of the heart in order to obtain images within a specified time-window during the cardiac cycle. It is usually preferable to obtain data during diastole when the least cardiac motion occurs in order to avoid motion artifacts. This can be accomplished by using the electrocardiographic (ECG) signal to either prospectively acquire or retrospectively reconstruct data during the desired cardiac cycle. Prospective ECG triggering is typically used with sequential data acquisition while retrospective ECG-gating is typically used with spiral acquisition.

With prospective ECG trigger sequential imaging the patient is scanned at a predetermined time period of the cardiac cycle [99]. If necessary, the patient table is incremented and the process is repeated until desired anatomy is covered. All of the data obtained during the acquisition are used for the image reconstruction. With retrospective ECG gated, spiral imaging data are acquired continuously along with the recording of the ECG signal. Data necessary for image reconstruction during one or more cardiac phases are extracted retrospectively with reference to the ECG signal [100].

Advantages of the retrospective ECG gated spiral over prospective ECG trigger sequential include higher spatial and temporal resolutions, because of the retrospective reconstruction of thinner slices from the acquired data. In addition, retrospective ECG gated spiral is less sensitive to arrhythmia. The disadvantage of this technique is that it requires higher radiation than prospective ECG triggered sequential imaging, thereby increasing the radiation dose to the patient. To minimize this disadvantage, ECG-based tube current modulation can be employed with spiral imaging, in which maximum tube current is used to acquire data during the diastolic phase in order to eliminate motion artifacts, and reduced tube current is used outside diastole. Although retrospective ECG-gating with spiral MDCT reduces cardiac motion artifacts, it does not completely eliminate them. For patients with high heart rate, controlling of this high heart rate with beta-blocking agents may be necessary to prolong diastole in order to reduce cardiac motion during scanning.

4.2.5 C-arm Computed Tomography (C-arm CT)

A new approach to acquire 3D CT like images uses a C-arm system. A C-arm system consists of an x-ray source and a flat-panel detector system mounted parallel to each other via a C-arm. 3D C-arm CT is a new and innovative imaging technique that acquires 2D projection data sets at various angular positions by a single rotation of C-arm system over $180^{\circ} + 2 \times \text{fan-angle}$ at a constant angular frequency. Several projection data are acquired depending on the acquisition protocol and reconstructed using a 3D cone-beam reconstruction algorithm to generate 3D data sets [101-104].

The x-ray tube, generator and control system regulate the tube voltage, tube current and time of irradiation in a C-arm system. Typically, C-arm systems are operated at lower tube voltages (compared to CT systems) to allow better image contrast in the presence of iodinated contrast dye. However, this may also result in higher noise in images. Hence, C-arm systems use automatic exposure control (AEC) to regulated x-ray output and maintain constant dose at the detector to optimize image quality. AEC regulates x-ray output first, by increasing the tube current-time product and then by increasing the tube voltage.

The flat detectors used in C-arm systems allow conversion of x-rays into electrical charge into steps [105]. In the first step, x-rays are absorbed by a scintillating screen, where they are converted into visible light. In the second step, the visible light is absorbed by a photodiode array and converted into electrical charge (Figure 4-12).

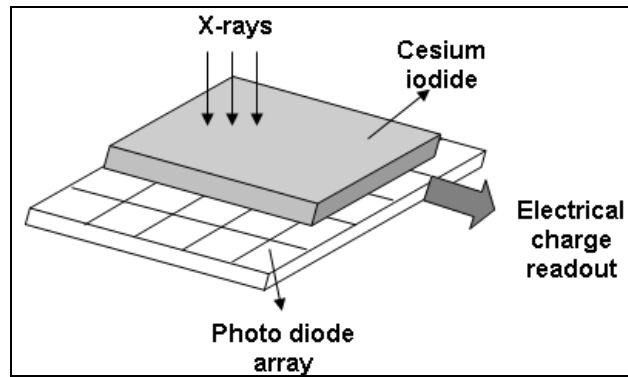


Figure 4-12: Schematic showing conversion of x-rays in the flat detectors using CsI scintillator and photodiodes.

The scintillating screen improves both energy absorption and x-ray sensitivity, but decreases the spatial resolution. Hence, an optimum balance between absorption properties (x-ray sensitivity) and spatial resolution is critical to choose the thickness and

type of scintillator material. Cesium iodide (CsI) enables high spatial resolution even at larger thickness and is typically used as scintillator material [105]. Flat panel detectors have advantages like homogeneous image quality with good soft-tissue resolution. Technological developments like use of miniature electronics may allow improvement of low-contrast resolution of C-arm CT and bring it closer to MDCT.

C-arm CT has initially been used for interventional neuro-radiological applications. More recently, C-arm CT has been proposed for use during minimally invasive cardiovascular procedures like PCI and EVAR.

4.2.6 Contrast Administration with X-ray Based Imaging

Contrast agents are water-soluble iodine-based compounds, which are either ionic or non-ionic compounds. The iodine component in the contrast agent attenuates x-rays and the absorption is proportional to the concentration of iodine present in the contrast agent [106]. Owing to similar densities and average atomic numbers, blood vessels cannot be identified from surrounding heart tissue on x-ray based images without administration of contrast agent to increase the attenuation coefficient of blood. Contrast agent opacifies the blood pool and enables visualization and distinction of cardiac anatomy.

4.2.6.1 Considerations for Fluoroscopy

Contrast agent is routinely used during fluoroscopic imaging to facilitate guidance and placement of equipment during an interventional procedure. Contrast can be injected

arterially either with an automated power injector or using hand injectors directly. Hand injection is fast and can be used to guide advancement of catheters in small vessels. However, power injection may be required to opacify large vessels like the aorta. High flow rates ranging from 10 to 20 mL/s are employed during direct injection into the vessel of interest while acquiring fluoroscopic images. As the contrast is injected directly into the vessel, fluoroscopic images can be acquired without any delay after contrast injection. Large volumes of contrast are typically used for guidance and ensuring accurate placement of prosthesis with fluoroscopy.

4.2.6.2 Considerations for CT

The delivery of contrast agent remains one of the most challenging aspects of cardiac imaging with MDCT. Peripherally injected contrast agent reaches the heart through the inferior or superior vena cava. The blood mixes with contrast here, passes through the pulmonary circulation and reaches the left heart to flow to the rest of the body through systemic circulation. The contrast agent mixed with blood diffuses through capillaries primarily into the extracellular space with minor intracellular distribution due to the lower binding to plasma proteins. Contrast agent is then reabsorbed or excreted by the tubular cells to a very small extent and mostly removed from the blood stream by excretion through kidneys [106]. For this reason, contrast agent cannot be administered to patients with renal disorders. Understanding of pharmacokinetics and physiology of contrast enhancement, especially during early arterial enhancement is critical to adapt contrast protocols for state-of-the-art cardiac MDCT scanners. Arterial enhancement is a function of the administered iodine dose and injection duration. With peripheral injection

of contrast, it is crucial to determine the transit time of the contrast agent from the site of injection to the organ of interest being imaged. This transit time varies for patients depending on individual physiologic parameters, such as the cardiac output, weight, body mass index (BMI) and used to determine the scan delay or time between the start of injection and the start of the CT scan. Currently, two techniques are used clinically to determine the scan delay:

- 1) Timing Bolus Method
- 2) Bolus Monitoring Method

With the timing bolus method, a small amount of contrast medium or a “timing bolus” is injected intravenously at a particular flow rate. Typically, high flow rates are used with cardiac imaging to achieve high attenuation of cardiac structures in MDCT images. The organ of interest is imaged repeatedly at a certain level with a low dose protocol following contrast injection. A region of interest (ROI) is drawn and the attenuation is measured over time to determine the time to peak enhancement, which defines the scan delay for the patient. For example, an ROI is placed in a cross-section of the ascending aorta to obtain the time to peak enhancement for performing imaging of the coronary arteries. A larger diagnostic or main bolus of contrast material is then injected intravenously at the same flow rate as the timing bolus. The diagnostic or main scan of the entire organ of interest (example: heart) is performed after the scan delay determined from the timing bolus. For cardiac scans, patients are instructed to hold their breath for the duration of the scan to reduce the movement of the chest and, thus, avoid respiratory motion artifacts. Timing bolus data can also be used for modeling individual patient’s

cardiovascular and contrast pharmacokinetic response to optimize main bolus injections [27, 107-109].

With the bolus monitoring method, a large diagnostic bolus of contrast material is injected intravenously at a given flow rate. Contrast flow through the organ of interest is monitored by drawing an ROI and scanning repeatedly with low dose scan after a time lag following contrast injection. A threshold value of attenuation is predefined. As soon as this threshold is reached, breathing instructions are given to the patient and the organ of interest is scanned.

Injection of the entire contrast bolus at a single flow rate, or a uniphasic injection, results in a steadily increasing enhancement profile with a single peak of enhancement shortly after completion of injection followed by a rapid decline in enhancement. However, uniform enhancement during the scan is desired. The shape of the contrast injection profile can be modified to achieve a more uniform enhancement profile. One approach is biphasic injection where a portion of the contrast agent volume is injected at an initial high flow rate for a short duration and the remaining volume is injected at a lower rate for a long duration without increasing the overall contrast volume [110-112]. The biphasic profile typically results in a relatively flat enhancement profile with two peaks indicating the end of the two injection phases. Another approach is the use of a multiphasic, exponentially decaying injection profile, where the contrast agent volume is injected at an initially high flow rate followed by exponentially decreasing flow rates [25, 113]. The contrast injection profile can also be customized for each patient based on data obtained from a timing (test) bolus [27, 107, 114].

Timing and main bolus injections may be followed by injection of saline, referred to as saline flush or saline chaser. The use of saline flush has several potential advantages. It creates a tight bolus by reducing intravascular contrast dispersion and optimizes the delivery of the contrast agent to the vessel of interest by eliminating any wasted contrast material from the connector tubing and peripheral veins. In fact, it is estimated that 10 to 12 mL of contrast given to a patient could be replaced by saline flush with no effect on image quality [115]. Thus, reducing the amount of contrast given to the patient may reduce some adverse reactions, such as renal toxicity, particularly in patients with renal insufficiency.

In addition, when saline flush is used without any change in contrast volume, it results in an increase in peak arterial enhancement with prolonged time to peak enhancement [116-118]. Saline chase also reduces the streak artifacts arising from accumulation of contrast in brachiocephalic vein and superior vena cava in thoracic CT images [119, 120].

4.2.6.3 Considerations for C-arm CT

C-arm CT is a relatively new imaging technique and contrast protocols are still emerging. Typically, C-arm CT images can be acquired either with peripheral or direct arterial injections. However, contrast administration needs to be customized depending on the scan duration of C-arm CT and the clinical application. For example in the context of using C-arm CT for ablation procedures, 20 mL of contrast agent is injected at a high flow rate of 20 mL/s into the pulmonary artery and the transit time for the test bolus to appear in the left atrium is obtained using fluoroscopy. This is followed by a large

injection of 84 mL of contrast again into the pulmonary artery and images of the left atrium and pulmonary veins are acquired [121]. In another application, 60 mL of diluted contrast agent (30 mL contrast mixed with 30 mL of saline) was injected at 6 mL/s at level of renal ostia for detection and correction of endoleaks [122]

4.2.7 Dose

X-ray photons in the diagnostic energy range interact with a medium by Compton and photoelectric interactions resulting in a free electron. This high velocity electron ionizes molecules as it loses its kinetic energy and can cause a cascade of ionization reactions that are not desirable. With the increasing use of x-ray based modalities, it is critical to understand the concepts of radiation dose measurement and estimation.

Radiation exposure describes the quantity of x-ray ionization events produced in air. It is usually expressed in units of roentgen (R) or C/kg. It describes the amount of ionization present in a given volume of air, but does not indicate the amount absorbed in the tissue that has been irradiated. Absorbed radiation dose describes the quantity of radiation deposited per unit mass in a body due to exposure and is calculated using the exposure and energy absorption estimates. It is expressed in units of rad or gray (Gy). It describes the amount of energy absorbed in a small volume due to ionizing radiation.

4.2.7.1 Considerations for Fluoroscopy

Fluoroscopic guidance during interventional procedures may result in high patient radiation doses. The radiation dose depends on the type of imaging (dynamic vs. static) and imaging modes (normal, high-dose, conventional, digital cine). The receptor entrance

exposure and skin entrance exposure determine are important factors that affect radiation dose with fluoroscopic imaging. A patient dose monitoring system during the fluoroscopic procedures is highly desirable. Currently, patient skin dose can be measured either using small dosimeters like thermoluminescent dosimeters (TLDs) or photographic films directly on the patient's skin [123]. Clinical C-arm systems are equipped with a dose-area product (DAP) meter, which uses a transmission type air-ionization chamber placed on the collimator of the x-ray tube. This DAP meter integrates exposure over the entire field of view and expressed in units of $\text{mGy}\cdot\text{cm}^2$. Skin entrance dose can be estimated from the DAP meter reading [123].

4.2.7.2 Considerations for CT

With CT type imaging, the distribution of dose in the scan plane (x-y direction), perpendicular to scan plane (z-direction) [referred to as the dose profile], and in 3D space (xyz) [referred as scatter radiation] are important for physical measurement of dose. The dose profiles in the z-direction indicate the distribution of absorbed dose along the z-axis of the patient, and can be measured using TLDs. The dose profile includes the impact of the primary beam, scatter of photons from the object being irradiated and also the collimation source irregularities.

CT dose index (CTDI) is the fundamental unit for measuring radiation dose with CT [124]. CTDI represents the integral dose profile measured in the z-axis derived from measuring dose from a single slice. The maximum value of the dose profile is termed as peak dose value.

Typically CTDI measurements are made with ionization chambers or TLDs. CTDI₁₀₀ measurements are made with 10 cm ionization chambers to measure the radiation exposure integrated for a length of 100 mm

$$CTDI_{100,x} = \frac{1}{NT} \int_{-50mm}^{+50mm} D(z) \cdot dz \quad (4-15)$$

where, x=air for air measurement; c for center, p for periphery, and w for weighted in phantom measurements and NT reflects the nominal width of the x-ray beam during acquisition. CTDI₁₀₀ can be calculated by performing a single 360° rotation CT scan with a beam collimation of NT and measuring the exposure E with a pencil ionization chamber of length L:

$$CTDI_{100,x} = \frac{f \cdot C \cdot E \cdot L}{NT} \quad (4-16)$$

where, f is the conversion factor from exposure to a dose in air (0.87 rad/R) and C is the calibration factor for the electrometer used for measuring the exposure. CTDI₁₀₀ is measured in Gy or rad using 100 mm of TLDs or ionization chamber in a plexiglass (polymethyl methacrylate or PMMA) phantom with 16 or 32 cm diameter to simulate head and body measurements at the center and four different peripheral positions to calculate CTDI_{100,w} in units of mGy

$$CTDI_{100,w} = \frac{1}{3} CTDI_{100,c} + \frac{2}{3} CTDI_{100,p-average} \quad (4-17)$$

where, p-average is the average measurement obtained from the four peripheral locations. CTDI_{100,vol}, also expressed in units of mGy, is typically used as the dose indicator and calculated from CTDI_{100,w} as

$$CTDI_{100,vol} = \frac{CTDI_{100,w}}{pitch} \quad (4-18)$$

To describe the overall energy deposited by a scan protocol, the absorbed dose is integrated over the length of region imaged (scan length) to calculate dose-length product (DLP) in units of mGy-cm.

$$DLP = CTDI_{100,vol} \cdot \text{scan length} \quad (4-19)$$

These CTDI descriptors are considered as parameters to estimate dose, but cannot determine the exact dose for a specific patient. Effective dose values can be used to express the biological effect of radiation on the tissue imaged. Effective dose describes partial body irradiation in terms of equivalent dose to the whole body using weighting factors based on tissue radiosensitivity. DLP values can be used to estimate effective dose (E) in milliSieverts (mSv) using appropriate conversion factors depending on the region imaged.

$$E = DLP \cdot k \quad (4-20)$$

where, k is a conversion factor in mSv/(mGy-cm) obtained from experimental results.

4.2.7.3 Considerations for C-arm CT

The use of C-arm CT results in radiation dose to the patient due to the use of x-ray photons. As traditional C-arm systems are associated with 2D imaging, they use dose area product (DAP) meter to calculate the integral of radiation exposure across the imaging field. However, these DAP meters do not provide an estimate of the dose delivered to the patient due to the 3D acquisition. The resulting dose from a 3D C-arm

CT acquisition is not well established and there is no consensus on estimating the patient dose.

4.2.8 Image Quality for X-ray based modalities

Spatial and contrast resolution are the major factors that determine the quality of the x-ray images. Spatial resolution is the ability to distinctly represent two different objects very close to each other (in proximity) in an image [75]. Contrast resolution is the ability to display two similar density materials distinctly in the images [75]. Contrast and spatial resolutions are interrelated and also associated with the radiation dose absorbed by the detectors (noise). Improving spatial resolution results in an increase in noise, which reduces the contrast resolution. On the other hand, improving contrast resolution requires an increase in scan time, which in turn decreases spatial resolution. Hence, it is desirable to have an adequately high spatial and contrast resolution with a trade-off between them [75].

Noise and blurring are artifacts that affect the image quality. Blurring refers to an indistinct appearance of any discrete object in a CT image. This occurs mainly due to the size of the X-ray source and detectors. Blurring is introduced during the data acquisition and image reconstruction phases [75]. During data acquisition, an x-ray with a certain width is projected through a slice of tissue. All the anatomical details within this width of the x-ray are processed together. Any object that is smaller than the x-ray source or detector width, or lies in the distance between adjacent x-rays or detectors appears blurred in the final image. Thus, a smaller voxel size is desirable to reduce blurring. This can be achieved by using detectors with narrow widths, yielding to images with higher

spatial resolution. Using sharp filters allows retaining details of the image even at high frequency, resulting in reduced blurring but increased noise.

Noise also impacts the image quality. It results from either electronic noise from the electronic components like the detectors or due to quantum random variations in the number of x-rays absorbed within an individual voxel. While the former cannot be controlled, the later can be minimized using various approaches during image acquisition or reconstruction. Radiation absorbed in each voxel affects the noise in the final image. Increasing voxel size can reduce noise but causes image blurring. Certain filters like the Hamming window can be applied to reduce noise, but with an increase in blurring because of the roll-off at high frequencies. Increasing the radiation dose to the patient would also reduce noise, but is undesirable. Hence, there is always a trade-off between radiation dose, noise and spatial resolution in x-ray based images.

CHAPTER V

LITERATURE REVIEW

3D contrast-enhanced x-ray based acquisitions have been increasingly used for imaging patients pre- and post-minimally invasive cardiovascular interventional procedures. The goal of this chapter is to provide an extensive overview of the clinical applications of DECT and C-arm CT technologies in the context of cardiovascular imaging.

5.1 DECT

The basic principle of DECT is the acquisition of datasets covering the same anatomical range by employing two different tube voltages. Although DECT has been extensively studied using two separate scans since the late 1970s [77, 78, 80, 125-129], technical challenges like unstable CT density values, limited spatial resolution and temporal resolution, and limitations on power output of the x-ray tubes did not allow extensive use for clinical applications. With continuous improvements in scanner technology, DECT measurements can commercially be obtained using simultaneous image acquisition at two different energies with two sources [21] (Definition and Flash;

Siemens Medical Systems, Erlangen, Germany), using rapid tube voltage switching between two energies with a single source [23, 84] (Discovery 750 HD; GE Healthcare, Milwaukee, Wisconsin, USA), or using energy selective dual-layer detector technology to filter lower energy radiation in the top layer, leaving higher energy photons in the bottom layer [20, 85, 86] (Brilliance 64 MultiEnergy; Philips Medical Systems, Cleveland, Ohio, USA).

DECT data acquired using good separation between low and high-energy spectra has the ability to discriminate between two materials with differences in effective atomic numbers or density values. Quantification of material composition can be performed using either basis spectral analysis or basis material decomposition either in the pre-reconstruction or post-reconstruction space in CT. While basis spectral analysis results in the identification of effective atomic number and density from CT images using the photoelectric effect and Compton scattering, basis material decomposition results in quantifying mass or volume fraction of the components present in a mixture. Both the methods have been implemented in both pre-reconstruction [77, 79, 130] and post-reconstruction (or image) domain [131, 132]. However, no studies to date have investigated combined use of these two approaches for quantification of substances with calcium, iodine and blood as basis materials in the image domain. One approach to perform basis material decomposition for a three-component mixture is by employing triple energy CT measurements to get three unique equations correlating mass attenuation coefficients with amount of components present in the mixture. However, as attenuation coefficient is a function of only two x-ray interaction mechanisms (photoelectric effect and Compton scatter) in the x-ray energies used for CT, three equations may not have

unique data to solve for the three materials. Alternatively, applying law of conservation of mass (the sum of the total mass fractions of a mixture can be assumed to be equal to one), a third equation can be generated to solve for the composition of the three-component mixture.

DECT has been used in many clinical applications such as bone removal [22], measurement of bone mineral density [133], identification of nodules in lungs and liver [134], characterization of urinary stones [135-137], computing tophus volume in peripheral joints of patients with tophaceous gout [138, 139], quantification of calcified plaque [86]. For cardiovascular applications, DECT has the potential to differentiate contrast agent from high density objects like stent or calcium due to the differences in density and atomic number. This may allow identification of iodine pixels in contrast-enhanced cardiac images, which can be eliminated to create VNC images. This application may particularly decrease radiation dose burden in patients imaged post-EVAR, where the high cumulative radiation dose from triple phase (non-contrast, arterial and venous phase) multiple follow-up examinations is of concern [15-17]. The radiation exposure can be reduced by replacing two SECT acquisitions with a single DECT acquisition [18, 19]. DECT data obtained during or after contrast agent injection can be used to create not only arterial or venous phase images, respectively, but also VNC (VNC) images [18, 19, 22, 24]. Previous studies [18, 19] have acquired DECT data during the venous phase, but no studies to date have evaluated the feasibility of arterial phase DECT acquisition. The presence of high density iodinated contrast adjacent to other high density materials like stent or calcium and, in many cases, the non-uniformity

of contrast attenuation along the length of the aorta make generation of VNC images from arterial DECT data more challenging.

Good spectral separation between the high and low- energy x-rays allows improved discrimination of materials with less difference in atomic numbers like calcium vs. iodine, and ensure better identification of iodine pixels for generating reliable VNC images. Spectral separation can be improved by adding filters to both the lower and higher energies to improve DECT imaging for material discrimination. Kelcz et al [80] performed the first study using additional filtration for two different tube voltages to improve DECT imaging. Rutt et al [140] used a split filter for DECT imaging on a single source scanner. Marshall et al [141] employed a pre-reconstruction technique to change beam filtration manually for DECT scans. All these studies emphasized the importance of additional filtration for DECT to enhance differentiation and quantification of substances. Recent study by Primak et al [142] on a commercially available dual-source CT scanner (Flash, Siemens) showed that 100/140 kVp acquisition with additional filtration decreased noise and increased contrast in images as compared to those obtained from the previous generation scanner with 80/140 kVp with no additional filtration for large patients.

Contrast-enhanced CT imaging is critical to visualize and evaluate the cardiac anatomy, and luminal details. Various cardiovascular indications like evaluation of aortic dissections, aneurysms, intramural hematoma, atherosclerotic disease, coronary arteries or bypass grafts, cardiac valves, pericardium, congenital anomalies, mass, or post-operative changes require arterial phase images. With the commercial availability of dual-energy capable CT scanners, DECT arterial phase imaging is expected to be used for

many clinical applications. In the context of EVAR, arterial images are important for the evaluation of luminal details, in particular of smaller branch vessels. With other indications for aortic imaging (aneurysm, dissection, aortitis, pre- and post- operative imaging), arterial phase acquisition is the clinical standard. Reliable reconstruction of VNC images from arterial DECT images could provide information about tissue characteristics (e.g. intramural hematoma, surgical material, low-density calcium versus contrast) in these situations. As VNC image generation largely relies on the accurate identification of contrast pixels using data from the two different energies, uniform enhancement in the arterial phase DECT images will result in a constant ratio of contrast attenuation at the two energies in all images. Uniform enhancement also ensures that the mass fraction of contrast agent mixed with blood will be constant so that contrast pixels can be easily identified. Thus, differentiation of iodine pixels from blood can be more robust and contrast agent can be removed more accurately from arterial DECT images to generate VNC images.

Various modeling techniques have been used to develop contrast injection protocols for SECT cardiovascular imaging [25-27]. Prolonged uniform aortic enhancement has been achieved with both biphasic [107] and multiphasic [113] injection protocols. Bae et al used pharmacokinetic modeling to develop exponentially decreasing multiphasic injections yielding prolonged, uniform enhancement for single detector-row cardiac CT [25]. Fleischmann et al developed a “black-box” mathematical approach to determine individual biphasic protocols for each patient necessary to achieve desired cardiac enhancement in the aorta with single detector-row CT [26]. However, these

advanced profiles focused on imaging with single detector row CT with prospective ECG-triggered sequential techniques and have not been evaluated in cardiac CT imaging.

Numburi et al utilized a “grey-box” modeling approach to obtain multiphasic patient-specific injections with ≤ 6 phases developed in the Fourier domain yielding uniform enhancement of the left heart on ECG-gated spiral MDCT acquired at single-energy MDCT [27]. With the mathematical modeling approaches [26, 27], a transfer function was developed using the input (injection) and output (enhancement) of the patient in the Fourier domain. The patient transfer function was further used to compute an “ideal” injection necessary to achieve “ideal” uniform enhancement during the scan. The ideal injection was then modified into a realistic injection protocol by eliminating negative flow rates. However, the algorithm could not predict injection in one patient due to problems in computation of transform of the patient in the Fourier domain. The calculation of the transfer function in the Fourier domain (division of output by input) required use of 2^n numbers in an array (with zero padding where data was not available), sometimes resulting in division errors and thus unable to achieve a realistic patient-specific injection protocol [27]. Also, this study was developed for a 16 detector-row CT scanners with average scan time of 20 s.

However, with the latest technological advances, state-of-the-art MDCT scanners employing dual-source x-ray tube technology [28, 143] and/or an increased number of detector-rows [144-147] allow DECT aortic and cardiac imaging with short scan times. No studies to date have evaluated systematic optimization of contrast administration for these short duration scans, in particular for DECT imaging to insure uniform contrast enhancement during data acquisition resulting in a constant mass fraction of iodinated

contrast agent mixed with blood. This requires an adequate understanding of the pharmacokinetics of contrast medium injection in the human circulatory system to achieve homogeneous enhancement synchronized with image acquisition. The contrast enhancement depends on various patient physiological factors (eg, cardiac output, blood volume, height, weight, body mass index [BMI], and body surface area), contrast agent characteristics (concentration, density, viscosity) and contrast injection properties (flow rate, volume, duration). One approach for developing contrast protocols with DECT imaging is to use linear time invariant (LTI) modeling in the time domain using non-linear optimization. This method considers the patient as an LTI system with contrast injection as input and enhancement as output [26]. The output can be modeled as the convolution integral of the input and impulse response of the patient. The advantage of this approach is that the impulse response considers the contrast injection and patient characteristics as part of the system and predicts patient-specific injection protocols without the limitations of the Fourier domain.

5.2 C-arm CT

Minimally invasive surgical procedures primarily rely on 2D x-ray C-arm angiography and transesophageal echocardiography (TEE) in the catheterization lab. Typically, 3D MDCT images are acquired prior to the procedure to provide visualization of cardiovascular anatomy and detailed information for accurate planning during the intervention. However, the direct use of the MDCT images in the cardiac catheterization lab is limited due to challenges involved in the direct integrating of the 3D information onto the 2D fluoroscopy images. With recent technical advances in flat-panel detector

technology and improvements in gantry rotations, traditional C-arm systems are capable of providing 3D C-arm CT images with CT-like soft-tissue image quality. These C-arm CT images can be used for planning, guidance and evaluate the procedural outcome in the interventional suite. C-arm CT is commercially available as Axiom Artis with syngo DynaCT (Siemens AG, Healthcare Sector, Forchheim, Germany), XperCT (Philips Healthcare, Andover, MA, USA) and Innova CT (GE Healthcare, Chalfont St. Giles, UK).

C-arm CT has been initially used for neuro-interventional procedures for assessing cerebral vasculature and hemodynamics [148-156]. Its use has been extended into other interventional radiology applications like abdominal [122, 157-160], spine [161] and hepatic [162-166] imaging. Cardiac C-arm CT requires rapid image acquisition during a single heartbeat to minimize motion artifacts, which is not feasible with the current C-arm system. However, with improvements in image reconstruction and image correction algorithms, cardiac C-arm CT may be possible [167, 168]. For cardiac applications like ablation for atrial fibrillation, C-arm CT images [121] were helpful despite motion blur. Left atrium and pulmonary veins from C-arm CT were marked and registered with the electroanatomic mapping system for guidance. In some cases, adenosine was used to reduce cardiac motion during imaging [169]. A report by Kempfert et al [170] suggested use of rapid pacing to freeze cardiac motion during C-arm CT acquisition. ECG-gated cardiac C-arm CT images can also be acquired with ECG synchronization and images can be reconstructed at a preferred cardiac phase to minimize motion of the heart [167, 168]. Acquiring images with optimal image quality, minimum artifacts, contrast and radiation dose in the context of TAVI will help for anatomical

assessment, quantitative evaluation, procedural guidance or postprocedural follow-up in patients. A systematic study exploring various C-arm CT imaging protocols in the context of TAVI has not yet been performed. Proper application of C-arm CT images for TAVI will facilitate accurate catheter guidance and device positioning to minimize complications and enable safer procedural outcomes in patients.

Typically during the TAVI procedure, 2D fluoroscopy with C-arm system is routinely used to visualize the 2D plane of the aortic annulus, sinuses and aortic valve cusps. In these situations, the overlay of detailed 3D C-arm CT or preprocedural 3D MDCT images onto the 2D fluoroscopy images from the C-arm system may help to determine if the three aortic sinuses and valve cusps are in the same plane so that proper valve position is achieved. In situations where preprocedural 3D MDCT needs to be overlaid on 2D fluoroscopy images, an intermediate step by rotating the C-arm during the procedure to acquire 3D images that will help. First, 3D C-arm CT images can be fused with the 3D MDCT images by registering the center of volumes from the two image sets, thus allowing the preprocedural MDCT images to be integrated with the 2D fluoroscopic images for guidance with C-arm system during the interventional procedure. The availability of the latest 3D anatomical information from the patient along with the ability to use this information for real-time guidance during intervention is of clinical interest.

The use of C-arm CT results in radiation dose to the patient due to the use of x-ray photons. As traditional C-arm systems are associated with 2D imaging, they use dose area product (DAP) meter to calculate the integral of radiation exposure across the x-ray beam. These DAP meters provide measure of dose which is an indicator of risk to skin, but not overall dose delivered to the patient due to the 3D acquisition. The resulting dose

from C-arm CT imaging is not well established and there is no consensus on estimating the patient dose. One approach to estimate the dose resulting from the 3D C-arm CT acquisition is to utilize an MDCT dose metric like $CTDI_{100}$ using a 150 mm phantom and 100 mm ionization chamber.

$$CTDI_{100} = \frac{1}{C_z} \int_{-50}^{+50} D(z) dz \quad (5-1)$$

where, C_z is the collimation used in z-direction. The ionization chamber is placed in the center and four peripheral locations (12, 3, 6, and 9-o'clock positions) of a 150 mm long CT phantom to measure the radiation exposure at different locations in the phantom. This measured exposure is multiplied with weighting functions for the center and the peripheral locations to convert into averaged absorbed dose in a cross-section of a patient's body. $CTDI_w$ is calculated using

$$CTDI_w = \left(\frac{1}{3} CTDI_{100,c} + \frac{2}{3} CTDI_{100,p} \right) \cdot f \quad (5-2)$$

where, f is the difference between the absorption of radiation in air and tissue, c and p indicate center and peripheral locations in the phantom. Fahrig et al [171] estimated $CTDI_w$ for C-arm CT imaging similar to that with MDCT by measuring $CTDI_c$ and $CTDI_p$ at the center and average of the periphery of a 160 mm diameter head and 150 mm length phantom. However, as the beam collimation with C-arm CT (~200 mm) is larger than the phantom and integration length, $CTDI_{100}$ may underestimate dose [172-176]. Hence, there is a need to adapt the CTDI concepts for C-arm CT and develop a procedure to obtain a C-arm CT dose metric to estimate the radiation burden with 3D C-arm acquisition.

Kyriakou et al estimated dose using a 250 mm ionization chamber and 300 mm long body phantom (320 mm) to calculate $CTDI_{w,250}$ for C-arm CT imaging [177]. However, as the C-arm system employs AEC technique to modulate the x-ray exposure depending on the DED settings, varying tube voltage and tube current-time product are employed during each projection of the 3D acquisition [103]. With their experiment set up, Kyriakou et al obtained dose values with varying tube voltage and tube current-time product, but assumed them as constant. Since dose is proportional to the (tube voltage)ⁿ where n=2.5 to 3, the dose measurements obtained from the experiments cannot be translated to patients. For example, dose measured at a constant 90 kVp assumed during their phantom experiment may actually employ tube voltages between 90 to 125 kVp for each projection. This does not reflect the actual dose measured if the phantom was imaged at 90 kVp in all the projections. Hence, there is a need to develop a procedure to obtain a C-arm CT dose metric to estimate the radiation burden with 3D C-arm CT acquisition. It is also required to estimate the necessary phantom and integration length to include complete scatter radiation tails and estimate C-arm CT dose metric accurately. This information can be further used to develop empirical equations to estimate dose in a patient using the individual tube voltage and tube current time-product values from each projection during 3D C-arm CT imaging.

CHAPTER VI

HYPOTHESIS AND SPECIFIC AIMS

The objective of the research is to develop strategies for employing novel x-ray based technologies to improve planning, guidance and follow-up of minimally invasive surgeries in patients with aortic diseases. The central hypothesis is that novel x-ray based technologies can be used to acquire preprocedural images for interventional guidance and obtain post- procedural images for patient follow-up. The central hypothesis was tested and the objectives of this proposal were achieved using the following specific aims:

6.1 Specific Aim 1

Hypothesis: VNC images can be generated using arterial dual-energy computed tomography (DECT) data and can replace true non-contrast (TNC) SECT images, thus reducing radiation dose.

The hypothesis was tested by imaging 30 patients on a first generation dual-source DECT scanner with an arterial DECT protocol developed for imaging patients post-endovascular aneurysm repair (EVAR). The DECT arterial images were processed using three-material decomposition algorithm to eliminate contrast and generate VNC

images. Noise and attenuation of tissues of interest post-EVAR were compared between VNC images and TNC images acquired from a previous exam in the same patient. Finally, radiation dose savings resulting from the omission of TNC imaging were estimated.

6.2 Specific Aim 2

Hypothesis: VNC image generation can be improved by (a) achieving uniform arterial enhancement during DECT data acquisition using patient-specific contrast injection protocols and by (b) applying basis spectral and basis material decomposition to resulting DECT images.

The hypothesis was tested by performing in-vitro and in-vivo experiments on a second generation dual-source DECT scanner. With phantom experiments, samples using varying concentrations of contrast and water, or calcium and water were imaged with DECT. The resulting images were processed using a customized algorithm based on basis spectral and basis material decomposition in the post-processing domain. The algorithm assumes that each pixels is a mixture of water, calcium hydroxyapatite and iodinated contrast agent and differentiates calcium and iodine pixels. Further, the mass fractions of the iodine solutions was quantified and compared with theoretical values.

An algorithm for generating patient-specific contrast injection was developed. However, its clinical use (and therefore in-vivo validation) was deemed unnecessary because of significant improvements in the uniformity of arterial enhancement using standard contrast protocols with shorter scan duration second generation dual-source DECT techniques. One patient post-EVAR was imaged with non-contrast SECT,

arterial DECT (using standard contrast injection protocols), and venous SECT. The resulting arterial DECT images were processed using customized basis spectral and basis material decomposition algorithm. To evaluate the efficiency of customized basis spectral and material decomposition algorithm, aortic luminal attenuation in VNC images was compared with those from TNC images.

6.3 Specific Aim 3

Hypothesis: Three-dimensional (3D) images similar to 3D MDCT images can be obtained by rotating the X-ray source/detector system of a traditional C-arm machine over a wide circular angle ($>180^\circ$) and facilitate the registration of preprocedural 3D MDCT images with real-time 2D fluoroscopic images from the C-arm system for guidance during an interventional procedure.

The hypothesis was tested by imaging 6 pigs with C-arm CT and MDCT. Various scan and contrast protocols were systematically evaluated to acquire optimal C-arm CT images. Aortic root measurements critical for TAVI procedure were obtained from 3D C-arm CT images and compared with those from 3D MDCT images. The 3D images from the MDCT and C-arm CT were also fused by registering the center of volumes from the two image sets to allow integration of 3D MDCT images with the 2D fluoroscopic images for real-time guidance during interventional procedures. Finally, a procedure to obtain a C-arm CT dose metric that can be compared to MDCT was developed to estimate the radiation burden with C-arm CT acquisition.

CHAPTER VII

PRELIMINARY DATA

Preliminary studies were performed to develop contrast injection and imaging protocols for the x-ray based imaging modalities used for minimally invasive surgeries. Specific patient populations were selected to develop the protocols. Specific aims 1 and 2 were evaluated in post-EVAR population and specific aim 3 was evaluated in the context of TAVI. Pilot studies were performed using phantom experiments for developing imaging protocols that can be used to image the aforementioned patient populations. Preliminary data acquired for the specific aims are described in the current chapter.

7.1 Specific Aim 1

Preliminary phantom experiments were performed to determine optimal imaging and contrast injection protocols for arterial DECT imaging. Additionally, parameters required for customizing existing algorithms were investigated to optimize VNC generation in patients for post-EVAR application. Preliminary DECT and SECT imaging were performed using a dual-source MDCT scanner (Somatom Definition, Siemens Healthcare, Forchheim, Germany). The scanner is equipped with two x-ray tubes and corresponding detector sets each with 32 detector-rows, mounted at a 90-degree angle in

one gantry. While the detector for tube A has a field of view (FOV) of 50 cm, tube B has a smaller FOV of only 26 cm. The two tubes can be operated independently at different voltages (kVp) and tube currents (mA). Imaging was performed on an Alderson anthropomorphic thorax phantom (Figure 7-1) with internal organs (heart, lungs and liver) inserted in the volume of the thoracic cavity.



Figure 7-1: Alderson Phantom mimicking human body.

7.1.1 Description of Standard SECT Contrast and Scan Protocol for Aortic Imaging

For routine triple-phase SECT imaging post-EVAR, non-contrast, arterial and venous phase SECT scans are acquired. For the arterial SECT scan, a total of 120 ml of contrast (Ultravist 370, Berlex, Montville, NJ) is typically injected at a flow rate of 3.5 ml/sec and the descending aorta (DA) is monitored at 120 kVp. Once sufficient threshold (~120 HU) is reached in the DA, a non-ECG gated helical scan covering the entire chest, abdomen and pelvis regions is performed using a standard SECT protocol: tube voltage, 120 kVp (Tube A); effective tube current-time product, 270 mAs (Tube A) with anatomic-based modulation; rotation time, 0.5 sec; beam collimation, 24 x 1.2 mm; pitch, 0.8. Images are reconstructed with 3.0 mm slice thickness and 3.0 mm slice increment

using a medium-smooth kernel (B31f). This SECT protocol was used to image the Alderson phantom and the resulting scan time, dose was recorded.

7.1.2 Development of DECT Imaging Protocol

A design of experiment (DOE) was performed on an Alderson phantom to develop an optimal dual-energy scanning protocol using the dual-source MDCT scanner (Definition, Siemens). Two spectrally separate energies available on the scanner (80 and 140 kVp) were used with tube A and tube B respectively, for ungated spiral DECT imaging. Various options available for the acquisition and reconstruction parameters for DECT imaging were selected:

1. Beam collimation: 64 x 0.6 mm; 14 x 1.2 mm
2. Rotation time: 0.5 sec; 0.33 sec
3. Pitch: 0.8; 0.7; 0.6
4. Tube current modulation (CareDose) with the maximum allowed effective tube-current product (eff mAs): Yes; No
5. Reconstructed slice thickness: 0.6 mm; 1.5 mm; 3.0 mm

A factorial design was developed with all the aforementioned parameters and image acquisition was performed on the Alderson phantom. With each scan, data at 80 and 140 kVp was acquired. Two image sets were reconstructed from the raw spiral projection data using a soft convolution kernel (D30f). The individual data sets were then linearly mixed (30% of 80 kVp data with 70% of 140 kVp data) to generate a weighted-average image. Noise was defined as standard deviation (SD) measured in the individual 80 and 140 kVp images, and calculated as $\sqrt[2]{(0.7^2 \times SD_{140}^2 + 0.3^2 \times SD_{80}^2)}$ in

weighted-average images. Dose from the DECT acquisition ($CTDI_{vol}$) reported at the end of each scan was noted. The impact of the various acquisition and reconstruction parameters on noise and dose was evaluated in all DECT image sets. The impact of the following scan parameters on noise and dose was evaluated:

- **Effect of beam collimation:** With constant pitch, rotation time, tube current modulation, and reconstructed slice thickness, 64 x 0.6 mm beam collimation resulted in lower dose and similar noise as compared to 14 x 1.2 mm beam collimation.
- **Effect of rotation time:** Using constant beam collimation, pitch, tube current, reconstructed slice thickness, a decrease in rotation time (0.5 to 0.33 sec) resulted in a decrease in dose and increase in noise.
- **Effect of pitch:** Employing a constant beam collimation, rotation time, tube current, and reconstructed slice thickness, a decrease in pitch resulted in an increase in dose, but similar noise values.
- **Effect of tube current modulation:** With a constant beam collimation, rotation time, pitch, and reconstructed slice thickness, use of tube current modulation did not impact noise.
- **Effect of reconstructed slice thickness:** Reconstruction of thicker slices resulted in decreased noise, with no impact on dose.

Noise measurements from the image sets were plotted against corresponding dose measurements for all acquisition and reconstruction parameters to find the optimal protocol resulting in minimum noise and dose values (Figure 7-2).

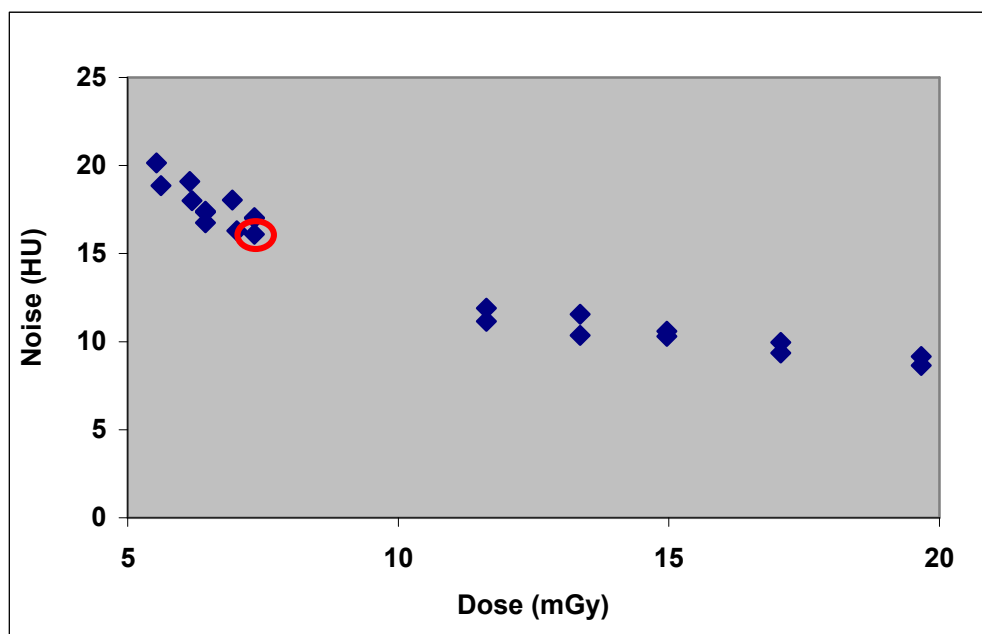


Figure 7-2: Optimal beam collimation, rotation time, pitch, reconstructed slice thickness and tube current values resulting in minimum noise and dose values developed for imaging on a dual-source DECT scanner (Definition, Siemens).

The optimal protocol achieving these values required DECT scanning of the chest, abdomen and pelvis to be performed using a non-ECG gated helical technique with tube voltage, 140 kVp (Tube A), 80 kVp (Tube B); effective tube current-time product, 110 mAs (Tube A), 467 mAs (Tube B) with anatomic-based tube current modulation employed for each tube; rotation time, 0.5 sec; beam collimation, 14 x 1.2 mm; pitch, 0.6. Both 80 and 140 kVp image sets need to be reconstructed with 3.0 mm slice thickness and 3.0 mm slice increment using a medium-smooth kernel (D30f).

7.1.3 Development of DECT Contrast Injection Protocol

With the optimal DECT protocol identified above, the scan duration was almost doubled as compared to the standard SECT protocol (12 sec with SECT and 26 sec with DECT). Therefore, the contrast protocol typically used for aortic imaging was adjusted. The iodine dose and input rate were calculated for the arterial SECT protocol using the following equations:

$$\text{Iodine Dose (gI)} = \text{contrast concentration (gI/ml)} * \text{contrast volume (ml)} \quad (7-1)$$

$$\text{Iodine Rate (gI/sec)} = \text{contrast concentration (gI/ml)} * \text{flow rate (ml/sec)} \quad (7-2)$$

The iodine dose was calculated as 44.4 gI and the input rate as 1.3 gI/sec. In order to inject the same iodine dose and rate for DECT imaging in patients, the contrast injection flow rate was decreased to 3.0 ml/sec while maintaining the total injected volume to that used with SECT.

7.1.4 VNC generation

VNC images were generated using DECT three-material decomposition post-processing algorithm, where each voxel was assumed as a mixture of fat, soft tissue and iodine. The known attenuation of these materials at 80 and 140 kVp was used to calculate their relative contributions to the voxel and to generate an iodine distribution image. VNC image was obtained by subtracting the iodine distribution image from the contrast-enhanced DECT image. Key parameters that need to be input into the algorithm include the average attenuation values for fat and soft tissue, the ratio of contrast attenuation (luminal attenuation at 80 kVp/luminal attenuation at 140 kVp), and a maximum

attenuation value or threshold above which voxels are excluded from processing. Average attenuation values for fat and soft tissue at 80 and 140 kVp were determined from our preliminary studies with patients. In these patients, a circular region of interest of approximately 100 pixels was drawn in fat and subcutaneous (or soft) tissue on both 80- and 140-kVp axial images. Multiple measurements were made at different locations within and across patients. Average attenuation values of -115 and -94 HU were noted for fat and 75 and 61 HU for soft tissue on both 80-and 140-kVp images. In order to avoid processing of inhomogeneous high density stent placed in EVAR patients, the attenuation of stent material was obtained by measuring CT attenuation from multiple circular regions of interest (25 pixels) in the DECT images. Stent attenuation was used to compute the maximum threshold value and only pixels below the maximum value were processed using the three-material decomposition algorithm.

7.2 Specific Aim 2

For specific aim 2, preliminary phantom studies were performed to develop imaging protocol on the DECT scanner (Flash, Siemens) employing additional spectral filtration. To achieve uniform enhancement during rapid aortic DECT imaging, patient based modeling was performed in the time domain. As time domain modeling has not been used for developing contrast injections, our preliminary work focused on implementation of modeling test injection (use of saline as chase after contrast injection) and enhancement data to accurately calculate impulse response, and further using the data to calculate patient-specific contrast protocols in the time domain. Additionally, we

developed an approach for implementing both basis spectral and basis material decomposition for differentiating iodine and calcium.

7.2.1 Development of DECT Imaging Protocol on Flash

The DOE as described in 7.1.2 was repeated on an Alderson phantom imaged with the second generation dual-source DECT scanner (Flash, Siemens). Images were acquired at 80/140 kVp and 100/140 kVp with additional tin filtering applied to the 140 kVp tube. DECT protocol with the following scan parameters resulted in optimal noise and dose values and was selected for imaging patients: non-ECG gated helical technique with tube voltage, 100 kVp (Tube A), 140 kVp with tin filter (Tube B); quality reference tube current-time product, 195 mAs (Tube A), 151 mAs (Tube B) with anatomic-based tube current modulation employed for each tube; rotation time, 0.28 sec; beam collimation, 64 x 0.6 mm; pitch, 0.65. Both 100 and 140 kVp image sets can be reconstructed with 3.0 mm slice thickness and 3.0 mm slice increment using a medium-smooth kernel (B31f).

7.2.2 Development of LTI Modeling in Time Domain

From tracer kinetics, we need to input a tracer into a system and measure the output concentration to model the system. This is feasible in patients by injecting a small bolus (10-20 ml) of contrast and measuring the resulting enhancement in a region of interest. In fact, administration of small bolus (test bolus) is routinely used clinically for determination of the appropriate scan delay (time between contrast injection and start of the scan) used with the larger, diagnostic bolus. The contrast bolus is typically injected

with a specified volume, flow rate, and injection duration and followed by saline using a power injector. However, little is known about the utility of saline on the injection of contrast into the venous system and the resulting measured enhancement curve, which are critical for modeling patients as LTI system. So, the aim of this preliminary study was to: (1) quantitatively evaluate the need for saline with the test injection for LTI modeling, and (2) assess the feasibility of using the test injection and enhancement data to develop modeling for patient-specific injections in the time domain for short duration imaging.

Applying tracer kinetics for contrast medium injection, patient can be considered as a linear time-invariant (LTI) system [26]. The arterial enhancement (*enh*) could be modeled as the convolution integral of the contrast agent flow rate (*inj*) and impulse response of the patient (response to a Dirac impulse input, *imp_resp*)

$$enh(t) = \int_0^t imp_resp(\tau) \cdot inj(t - \tau) \cdot d\tau \quad (7-3)$$

In the discrete domain, this can be approximated as

$$enh(n) = \sum_m imp_resp(m) \cdot inj(n - m) \quad (7-4)$$

where *m* is the number of data points of the test bolus attenuation curve. For each patient in this study, the two test bolus attenuation curves were used to estimate the effective contrast profile (volumes and flow rates) of both test injections using customized software (Excel Solver; Microsoft Corporation, Redmond, Wash). The mean differences between the programmed and effective values of contrast volume and flow rate, as well as 95% confidence intervals and Bland-Altman limits of agreement, were calculated for both test injections.

A total of 25 patients were included in the study. A single low-dose image was obtained near the carina, and a circular region-of-interest (ROI) was drawn in the ascending aorta (AA) to determine a baseline intensity value (attenuation without contrast agent). This was followed by the administration of 2 test bolus injections: test injection A, which consisted of 20 mL of contrast injected at 4.5 mL/s, and test injection B, which consisted of 20 mL of contrast followed by 60 mL (for patients weighing < 90 kg) or 80 mL (for patients weighing \geq 90 kg) of saline administered at 4.5 mL/s. The order of the test injections was randomized, and an average of 4 minutes was allowed between injections to eliminate any potential bias resulting from residual contrast from the previous injection. From 10 s through 44 s after each injection, a test scan was performed every 2 s at the same level (near the carina), with scan parameters as follows: number of images, 18; tube voltage, 120 kVp; and tube current-time product, 40-60 mAs. Relative time-attenuation curves (indicating enhancement due to contrast agent injection) were obtained by subtracting the baseline intensity measured in the AA (prior to the injection of contrast) from the absolute values measured from each test bolus method.

7.2.2.1 Impact of Saline on LTI Modeling

Each patient was considered as an LTI system characterized by an impulse response (imp_resp). Using commercially available software (Excel Solver; Microsoft Corporation, Redmond, Wash), the two effective inputs with test injections A and B (inj_A and inj_B) were estimated by simultaneously using data from the two measured outputs of test bolus attenuation curves (enh_{A-meas} , enh_{B-meas}) as described below (Figure 7-3):

Algorithm

1. Assumed initial values for the unknowns (inj_A , inj_B , and imp_resp).
2. Computed the two convolved test enhancement curves by additive convolution of impulse response with the corresponding inputs.

$$enh_{A-conv}(n) = \sum_m imp_resp(m) \cdot inj_A(n - m) \quad (7-5)$$

$$enh_{B-conv}(n) = \sum_m imp_resp(m) \cdot inj_B(n - m) \quad (7-6)$$

3. Computed sum of squared difference (error) between the measured and convolved test bolus attenuation curves.

$$error = \sum_m (enh_{A-meas} - enh_{A-conv})^2 + (enh_{B-meas} - enh_{B-conv})^2 \quad (7-7)$$

4. Minimized error while satisfying boundary conditions:
 - a. Impulse response must be non-negative.
 - b. Flow rate of contrast agent in both test injections must be non-negative
 - c. Flow rate of contrast agent in both test injections must be less than or equal to the injected flow rate programmed in the injector (4.5 mL/s)
 - d. Total volume of contrast agent in each test injection must be less than or equal to the injected volume programmed in the injector (20 mL).

Initial values of the two inputs and impulse response were modified with each iteration. Iterations were converged by the program when a minimum error was obtained along with feasible boundary conditions.

5. Obtained values for effective test injection profiles (inj_A , inj_B) along with patient impulse response (imp_res).

The volumes and flow rates of effective test injection profiles were compared with programmed values (20 ml of contrast at 4.5 ml/s) using paired t-test with $p < 0.05$ indicating difference was statistically significant.

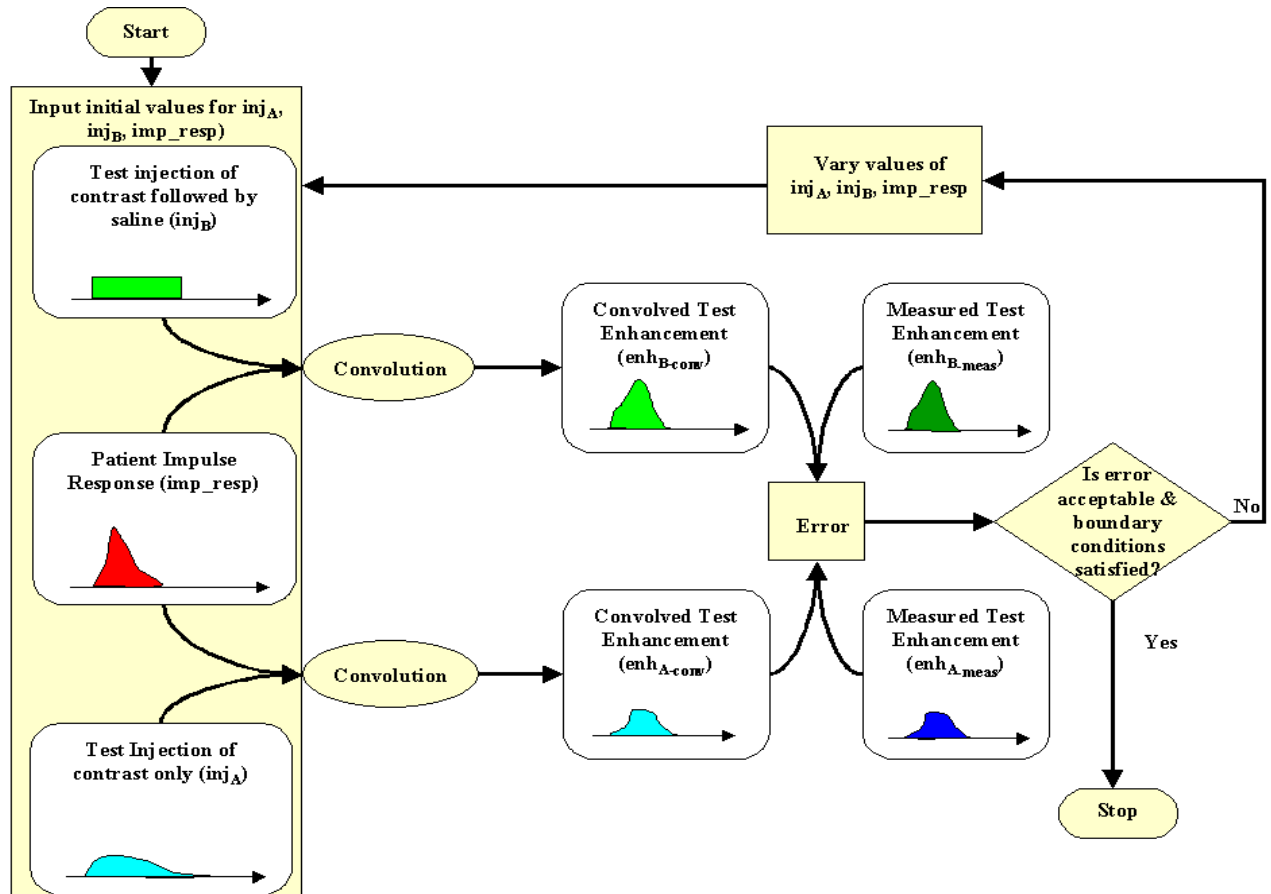


Figure 7-3: Optimization technique used to estimate the effective test injection profiles with and without saline along with the patient’s impulse response.

The results from the preliminary analysis showed that LTI modeling can be used to determine the effective flow of contrast agent resulting from the injection of a contrast only bolus and a contrast followed by saline bolus without any programming errors in all 25 patients (Figure 7-4).

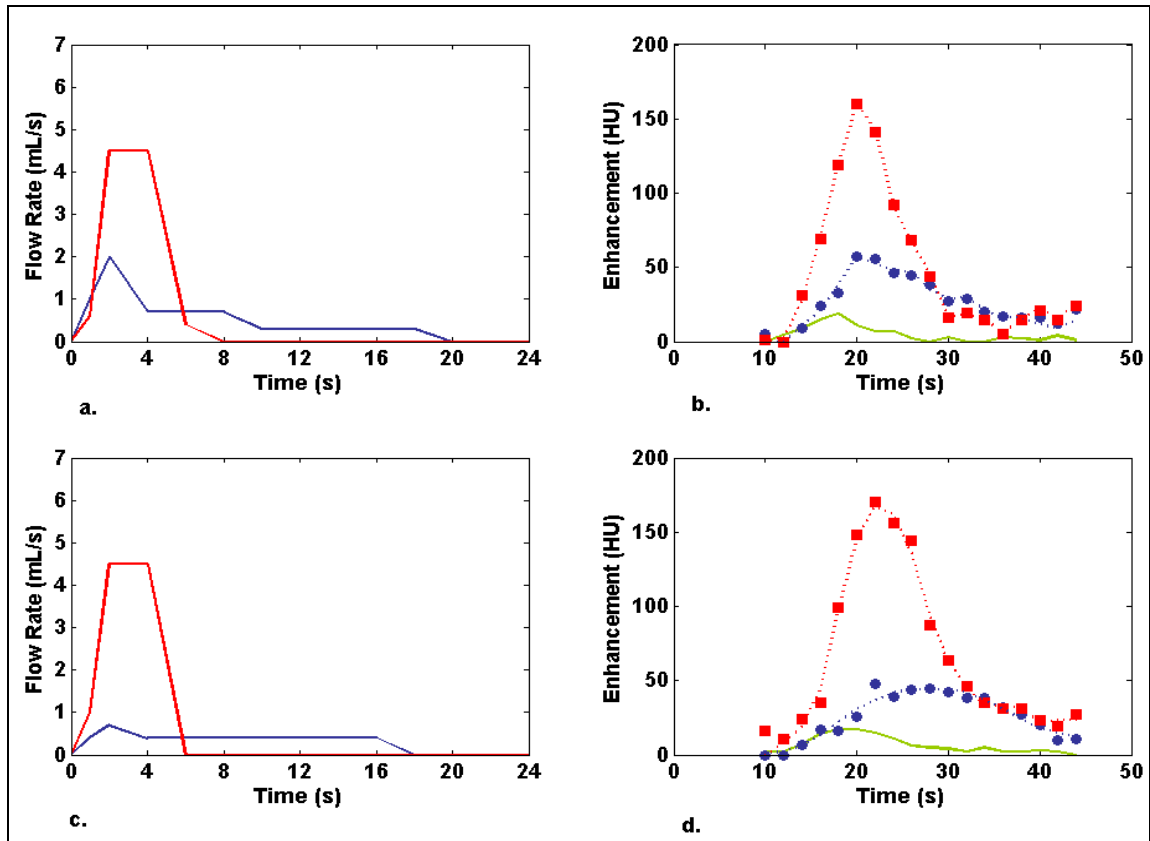


Figure 7-4: Effective contrast flow with test injections A (—) and B (—) along with impulse response (—), measured (•) and convolved (---) test bolus attenuation curves from test injection A, and measured (■) and convolved (---) test bolus attenuation curves from test injection B. Graphs from a 67-year-old man weighing 88 kg showing (a) administration of 13 mL of contrast at a maximum flow rate of 2.0 mL/s without use of saline (test injection A) and the entire 20 mL of contrast at a flow rate of 4.5 mL/s with the use of a 60-mL saline chaser (test injection B), and (b) the resulting measured and convolved test attenuation bolus curves plus the patient's impulse response. Graphs from a 52-year-old woman weighing 115 kg showing (c) administration of 9 mL of contrast at a maximum flow rate of 0.7 mL/s without use of saline (test injection A) and the entire 20 mL of contrast at a flow rate of 4.5 mL/s with the use of a 80-mL saline chaser (test

injection B), and **(d)** the resulting measured and convolved test attenuation bolus curves plus the patient's impulse response.

The injector administered 20 mL of contrast at 4.5 mL/s for both test injections. On average, however, only 13 mL of contrast was effectively delivered at 2.2 mL/s with test injection A. With the use of saline after test injection B, the entire 20 mL of contrast was injected at an effective rate of 4.4 mL/s. The mean difference, 95% confidence interval for the mean difference, and Bland-Altman limits of agreement for volume and flow rate were smaller for test injection B than for test injection A (Table 7.1), indicating that programmed values were closer to being realized when saline was used after contrast agent in a test bolus. These results demonstrate that saline flush is required to ensure the programmed injection profile matches the effective injection profile and accurately model the patient as an LTI system.

	Programmed Value	Effective Value	Mean Difference	95% CI	Limits of Agreement
Average volume of contrast (mL)					
20 mL contrast	20 ± 0	13 ± 3	7.2 ± 3.4	5.8, 8.6	0.5, 13.9
20 mL contrast followed by 60/80 mL saline		20 ± 1	0.4 ± 1.3	0, 0.9	0, 2.9
Average flow rate of contrast (mL/s)					
20 mL contrast	4.5 ± 0	2.2 ± 0.8	2.4 ± 0.8	2.0, 2.7	0.7, 4.0
20 mL contrast followed by 60/80 mL saline		4.4 ± 0.2	0.0 ± 0.2	0, 0.1	0, 0.4
<p>Note.— Data are mean ± standard deviation for programmed, effective, and mean difference values.</p> <p>CI indicates the 95% confidence intervals for mean difference. Limits of agreement are the Bland-Altman limits, indicating that 95% of all individual differences in patients lie within these limits.</p>					

Table 7.1: Impact of Saline on Contrast Volume and Flow Rate and Comparison with Values Programmed in the Injector

7.2.2.2 Modeling of Contrast Injection

Using test bolus data, we performed LTI modeling in time domain and predicted patient-specific contrast injection profiles that would achieve uniform enhancement in the heart during fast cardiac MDCT scans. Hypothesizing that saline chase would impact

tPME, scan delay was determined as $2\text{ s} + \text{tPME}$ from test injection B in each patient. Further, a desired diagnostic enhancement of 300 HU in the heart [115] was defined for a duration of 6 s after scan delay. Optimal patient-specific contrast injection protocols were computed using the patient's impulse response (described in section 7.2.2.1) and the target diagnostic enhancement using non-linear optimization using the algorithm described below (Figure 7-5).

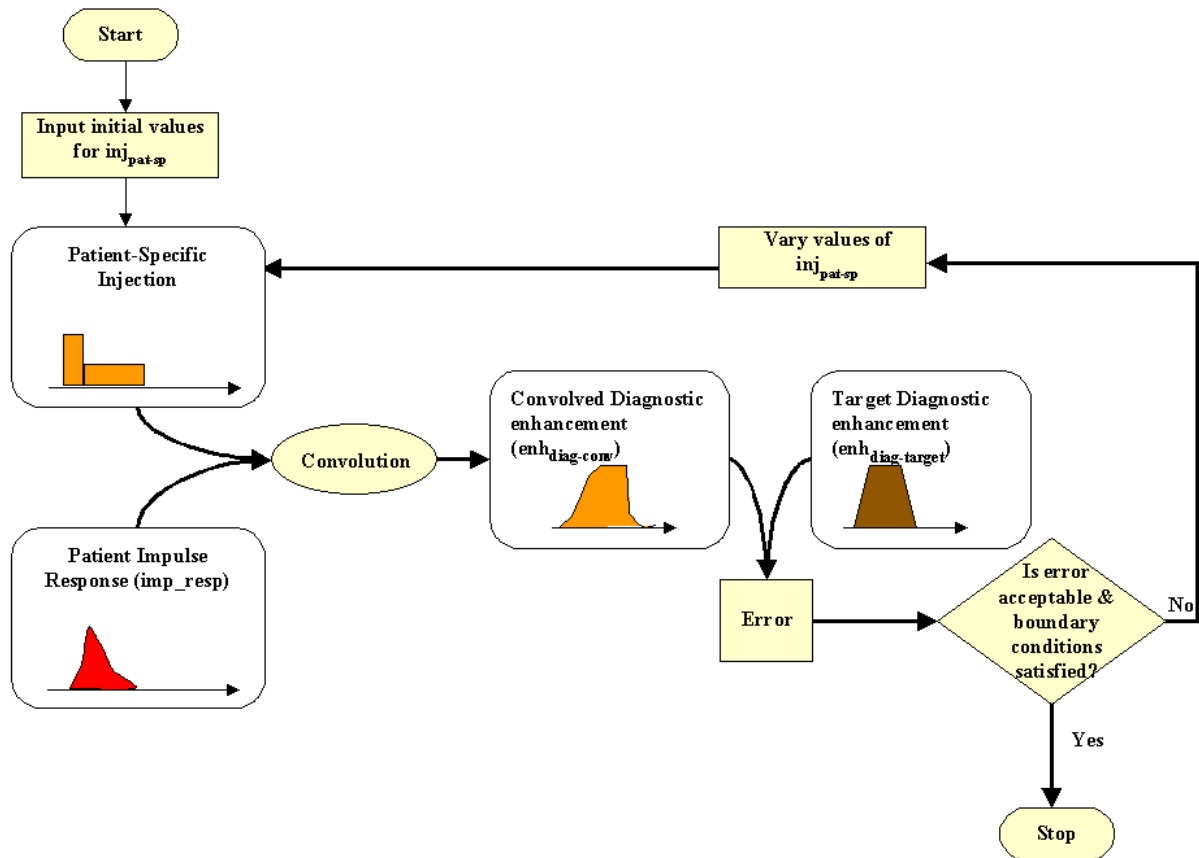


Figure 7-5: Optimization technique for computing patient-specific injection profiles to achieve uniform enhancement during a short duration cardiac scan.

Algorithm

The impulse response of each patient was obtained as shown in section 7.2.2.1. Using commercially available software (Excel Solver; Microsoft Corporation, Redmond, Wash), a target diagnostic enhancement of 300 HU ($enh_{diag-target}$) was defined in the heart for a 6-s scan (starting 2 s after tPME of the test bolus attenuation curve obtained from test injection with saline) for each patient. An optimal patient-specific injection (inj_{pat-sp}) was computed by minimizing the difference between the convolved diagnostic enhancement ($enh_{diag-conv}$) and the desired target enhancement as described below:

1. Assumed initial values for the unknowns (inj_{pat-sp}).
2. Computed the convolved diagnostic enhancement curve by additive convolution of impulse response with the patient-specific injection.

$$enh_{diag-conv}(n) = \sum_m imp_resp(n) \cdot inj_{pat-sp}(n - m) \quad (7-8)$$

3. Computed sum of squared difference (error) between the convolved and targeted diagnostic enhancement curves during a 6-s scan duration.

$$error = \sum_n (enh_{diag-conv} - enh_{diag-target})^2 \quad (7-9)$$

4. Minimized error while satisfying following boundary conditions:
 - a. Flow rate of contrast agent must be non-negative.
 - b. Flow rate of contrast agent must be less than or equal to 7 mL/s (physiologic limitations).

Initial values of patient-specific injection were modified with every iteration until a minimum error was obtained along with feasible boundary conditions.

5. Obtained an optimal patient-specific injection (inj_{pat-sp}).

Preliminary result in a sample patient showed that patient-specific injection could be predicted by performing LTI modeling in time domain to achieve the desired target enhancement during a short duration cardiac MDCT scan (Figure 7-6).

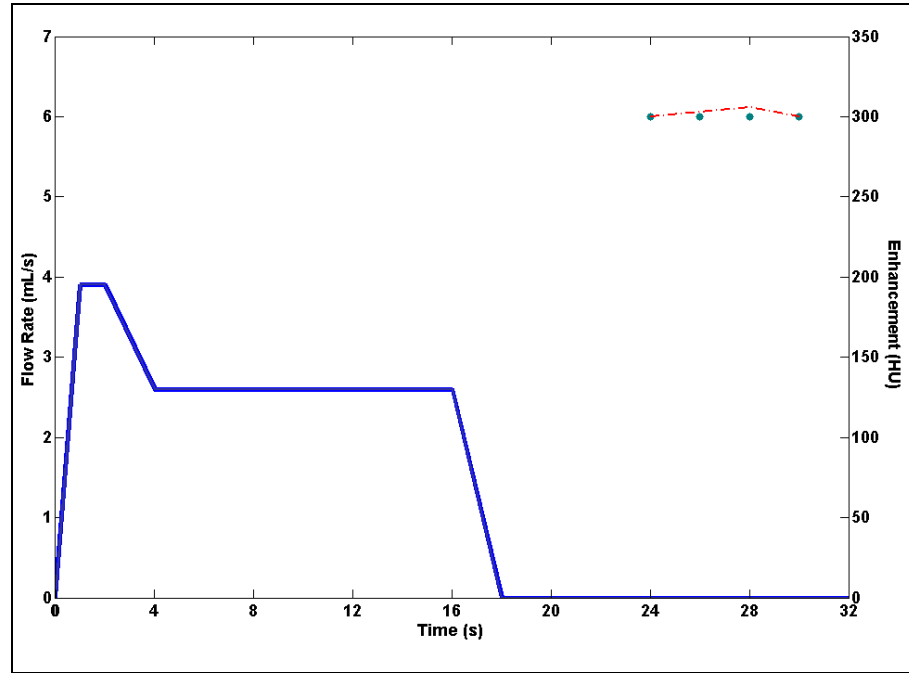


Figure 7-6: Patient-specific injection predicted using LTI modeling to achieve 300 HU (●) during a 6-s cardiac scan. A biphasic injection profile in a 60-year-old, 123-kg man (BMI = 37.9 kg/m^2) using a total of 52 mL of contrast (—) was required to achieve uniform contrast enhancement of approximately 300 HU (-----).

The results demonstrated that patient-specific contrast injection protocols could be calculated in the time domain with convolution techniques and non-linear optimization using data from test injection of contrast (followed by saline) and the resulting test enhancement curve.

CHAPTER VIII

FEASIBILITY OF DUAL-ENERGY COMPUTED TOMOGRAPHY IN THE ARTERIAL PHASE: IMAGING AFTER ENDOVASCULAR ANEURYSM REPAIR

The current chapter investigates the use of dual-energy CT (DECT) imaging during arterial phase to generate virtual non-contrast (VNC) images. The VNC images were compared to “true” non-contrast images routinely acquired using a single energy CT scan. The feasibility of the study was evaluated by imaging 30 patients with an arterial phase DECT protocol after endovascular aneurysm repair (EVAR) and described here.

8.1 Introduction

Endovascular aneurysm repair (EVAR) has become a reliable alternative to open surgery for thoracic, thoracoabdominal, and abdominal aortic aneurysms [35, 37, 178]. Triple phase SECT is often used to evaluate patients 1 month, 6 months, and yearly after such repairs [13]. The combination of non-contrast, arterial phase, and venous phase SECT images is used to evaluate aneurysm size, stent-graft position and patency,

perigraft flow (endoleaks), graft fractures and kinks, and the patency of native vessels near the graft [2, 3, 12-14]. Of concern is the high cumulative radiation dose to the patient resulting from three-phase imaging in multiple follow-up examinations [15-17].

In an attempt to decrease radiation dose, studies have been conducted to investigate eliminating one or more SECT acquisitions [179, 180] or limiting the coverage of these acquisitions to stented segments. An emerging approach to reducing radiation exposure is to replace two SECT acquisitions with one DECT acquisition [18, 19]. At DECT, data acquisition at two x-ray energies is followed by the reconstruction of corresponding image sets with different attenuation properties [20-23]. DECT data obtained during or after contrast injection can be used to generate not only arterial and venous phase images but also VNC images [18, 19, 22, 24]. In studies of endoleak detection [18, 19], DECT data have been acquired during the venous phase, but in no studies to date, to our knowledge, has the feasibility of arterial phase DECT acquisition been evaluated. The presence of high-density iodinated contrast medium adjacent to other high-density materials, such as a stent and calcium, and, in many cases, the lack of uniformity of contrast attenuation along the length of the aorta increase the challenge of generating VNC CT images from arterial DECT data.

Our rationale for investigating the utility of arterial phase DECT is based on considerations for EVAR and for future clinical applications of DECT. In the context of EVAR, arterial images are important for the evaluation of luminal details, in particular smaller branch vessels. In other indications for aortic imaging (aneurysm, dissection, aortitis, preoperative and postoperative evaluation), arterial phase acquisition is the clinical standard. Reliable reconstruction of VNC CT images from arterial DECT scans

may yield information about tissue characteristics (e.g., intramural hematoma, surgical material, low-density calcium versus contrast medium) in these situations.

The purpose of this study was to test the feasibility of replacing routine non-contrast and arterial phase SECT images with VNC and dual-energy arterial phase images obtained in one arterial DECT acquisition and to estimate the resulting radiation dose (single-energy venous phase acquisition was included in both the standard and the study protocols). A secondary purpose was to describe the effect of dual-energy acquisition on the attenuation of tissues of interest for overall assessment of anatomic features after EVAR.

8.2 Material and Methods

8.2.1 Patients

This study was approved by the local institutional review board with waiver of consent and was compliant with HIPAA. Only patients without standard contraindications to contrast-enhanced CT undergoing follow-up after EVAR and at least one standard triple-phase SECT examination after EVAR were included in the study. A total of 30 patients were prospectively identified. Patient characteristics, including age, sex, weight, and body mass index (weight in kilograms divided by height squared in meters), were noted.

8.2.2 Data Acquisition and Image Reconstruction

A dual-source CT scanner (Definition, Siemens Healthcare) with two x-ray tubes (tubes A and B) was used to acquire data [21]. On the basis of preliminary phantom data

and data on five patients not described in this report but supporting the suitability of VNC CT for evaluation after EVAR, we decided to spare the patients radiation exposure and to forgo acquisition of true non-contrast data. Hence, with our study protocol, each patient was imaged only with arterial phase DECT followed by venous phase SECT, and image-processing techniques were used to generate non-contrast images from arterial phase DECT data. The resulting scan time and dose-length product (DLP) were recorded. Patient size indexes (maximum lateral width in the thorax and abdomen) were measured from the anteroposterior radiograph acquired at the start of the examination.

Arterial phase DECT—The optimized contrast injection and scan protocol developed for arterial phase DECT was based on preliminary data. In this protocol, 120–150 mL of contrast medium (iopromide, Ultravist 370, Bayer HealthCare Pharmaceuticals) was injected at a flow rate of 3.0 mL/s, and the descending aorta was monitored at 140 kVp. Once a 120-HU threshold was reached, breathing instructions were given, and DECT scanning of the chest, abdomen, and pelvis was performed with non-ECG-gated helical technique (tube voltage, 140 kVp tube A, 80 kVp tube B; effective tube current–time product, 110 mAs tube A, 467 mAs tube B, anatomy based tube current modulation for each tube; rotation time, 500 milliseconds; beam collimation, 14×1.2 mm; pitch, 0.6). Both 80-kVp and 140-kVp image sets were reconstructed with 3.0-mm slice thickness and 3.0-mm slice increment with a medium-smooth kernel (D30f).

Venous phase SECT—A second non-ECG-gated helical scan covering the same anatomic region was obtained 60 seconds after contrast injection according to our standard SECT protocol (tube voltage, 120 kVp tube A; effective tube current–time product, 270 mAs tube A with anatomy-based modulation; rotation time, 500

milliseconds; beam collimation, 24×1.2 mm; pitch, 0.8). Images were reconstructed with 3.0-mm slice thickness and 3.0-mm slice increment with a medium-smooth kernel (B31f) and used without further modifications for venous phase analysis.

True non-contrast SECT from previous examination—True non-contrast images acquired with the same CT scanner, scan acquisition, and reconstruction parameters used for venous phase SECT were obtained from our archiving system. Anteroposterior topographic images also were retrieved, and the maximum lateral width in the thorax and abdomen was measured.

8.2.3 Dual-Energy Image Processing

Weighted-average arterial images—A weighted-average arterial image set was obtained by linear combination of 80- and 140-kVp attenuation values (30%/70%) for all pixels.

VNC CT images—VNC CT images were generated with dual-energy postprocessing software (Liver VNC, Syngo DE, Siemens Healthcare) on the basis of three-material decomposition. In the algorithm, it is assumed that each voxel is composed of three materials (fat, soft tissue, and iodine), and the known attenuation of these materials at 80 and 140 kVp is used to calculate their relative contributions to the voxel and to generate an iodine distribution image. A VNC CT image is obtained by subtracting the iodine distribution image from a weighted-average arterial image.

Important input parameters for the commercial software include the average attenuation values for fat and soft tissue, the ratio of contrast attenuation (luminal attenuation at 80 kVp/luminal attenuation at 140 kVp), and a maximum attenuation value or threshold above which voxels are excluded from processing. These parameters were

modified from default settings to customize postprocessing for follow-up after EVAR. The manufacturer default values for fat and soft tissue at 80 and 140 kVp were replaced with average attenuation values determined from our preliminary studies with five patients. In these patients, a circular region of interest of approximately 100 pixels was drawn in fat and subcutaneous (or soft) tissue on both 80- and 140-kVp axial images. Multiple measurements were made at different locations within and across patients. Average attenuation values of –115 and –94 HU were noted for fat and 75 and 61 HU for soft tissue on both 80-and 140-kVp images. The default ratio of contrast attenuation in the software was replaced with two custom values measured separately in the thoracic and abdominal aorta to generate VNC CT images of the two regions separately. Finally, the maximum threshold for each patient was reset to the attenuation of stent material obtained by measuring CT attenuation from multiple circular regions of interest (25 pixels) in the weighted-average arterial images.

8.2.4 Radiation Dose Measurements

The effective dose in millisieverts was estimated as the product of the DLP in milligray · centimeters and a conversion coefficient, k , in mSv/(mGy · cm) [20]. The value of k is 0.014 for the chest and 0.015 for the abdomen and pelvis; the average k for a single scan encompassing all three regions is 0.015. The total effective dose (ED_{Total}) for each patient in our study was estimated with the DLPs from arterial DECT arterial ($DLP_{DECT\ Arterial}$) and venous SECT ($DLP_{SECT\ Venous}$) acquisitions, as follows:

$$ED_{Total} = k \cdot (DLP_{DECT\ Arterial} + DLP_{SECT\ Venous}) \quad (8-1)$$

Because the venous SECT acquisition parameters are typically used for all three phases of a standard imaging protocol, the total effective dose was estimated as:

$$ED'_{Total} = k \cdot (3 \cdot DLP_{SECT\ Venous}) \quad (8-2)$$

8.2.5 Clinical Evaluation

Without blinding, a radiologist (8 or 16 years of experience in cardiovascular CT) and a vascular surgeon independently, subjectively evaluated the images in routine clinical follow-up to detect the presence of endoleaks and to evaluate the appearance of stents and calcium. Endoleaks were defined as the presence of contrast material within the aneurysm sac beyond the stent on weighted-average arterial phase DECT images and/or venous phase SECT images and the absence in the corresponding location on VNC CT images. Stents and calcium were visually assessed on virtual image non-contrast, weighted-average arterial and venous images.

8.2.6 Tissue Attenuation and Image Noise

A circular region of interest encompassing approximately 300 pixels was drawn at multiple locations in the lumen of the thoracic aorta beginning at the level of the pulmonary artery bifurcation and in the abdominal aorta starting at the level of the celiac artery. Regions of interest were placed at the same z-axis locations based on anatomic landmarks on VNC CT, arterial phase DECT (80 kVp, 140 kVp, weighted-average), and venous phase SECT images from the study examination and on true non-contrast SECT images acquired from the preceding triple-phase CT examination of each patient. The average attenuation and SD were recorded at all locations.

The attenuation of thrombus present outside the stent was identified and measured at the same locations in image sets from all three phases. Image noise was defined as the SD in the aortic lumen on true non-contrast, VNC, arterial 80-kVp (SD_{80}), arterial 140-kVp (SD_{140}), and venous images and calculated as follows on weighted-average arterial images:

$$\sqrt[2]{(0.7^2 \cdot SD_{140}^2 + 0.3^2 \cdot SD_{80}^2)} \quad (8-3)$$

Statistical Analysis: A paired Student's t test was used to compare total effective dose for the standard and study protocols. The scan times for dual-energy and SECT acquisitions also were compared by use of paired Student's t tests. To evaluate the ability of three-material decomposition to remove iodine from arterial images, luminal attenuation on VNC CT images was compared with that on previously acquired true non-contrast images by use of a paired Student's t test. Mixed-model one-way analysis of variance was used to compare the attenuation of thrombus on VNC CT, weighted-average arterial, and venous phase images. If the overall F -test value was significant, Tukey-Kramer adjustments were used to make pairwise comparisons between image sets.

To analyze the effect of DECT acquisition on image quality, noise on DECT arterial and SECT venous images acquired during the study examination was compared in both the thoracic and abdominal regions by use of paired Student's t tests. Furthermore, noise on VNC CT images derived from DECT images and previously acquired true non-contrast images were compared in both regions, again by use of a paired Student's t test. Because of the time lapse between the acquisitions of virtual and true non-contrast images, patient size indexes obtained from the anteroposterior radiograph acquired at the start of each examination were compared by use of a paired

Student's t test to determine whether a change in patient size had occurred that could compromise noise comparisons. For all statistical analyses, $p \leq 0.05$ was considered significant.

8.3 Results

8.3.1 Clinical Evaluation

All patients underwent imaging with the study protocol (arterial phase DECT followed by venous phase SECT) (Table 8.1); images of the chest, abdomen, and pelvis were obtained.

Characteristic	Value
No. of patients	30
Male/female ratio	21/9
Age (y)	72 (35-88)
Weight (kg)	82 (45-116) *
Body mass index (kg/m ²)	27 (18-38) †
Note— Data are mean with range in parenthesis. * Data obtained from 28 patients. † Data obtained from 27 patients.	

Table 8.1: Patient Demographics.

VNC CT and weighted-average arterial DECT images were generated from 80- and 140-kVp arterial data (Figure 8-1) with a processing time of less than 5 minutes for each patient. All images were deemed diagnostic by the radiologist and vascular surgeon

and satisfied clinical requirements. Repetition of imaging (according to our standard protocol) was not necessary for any patient.

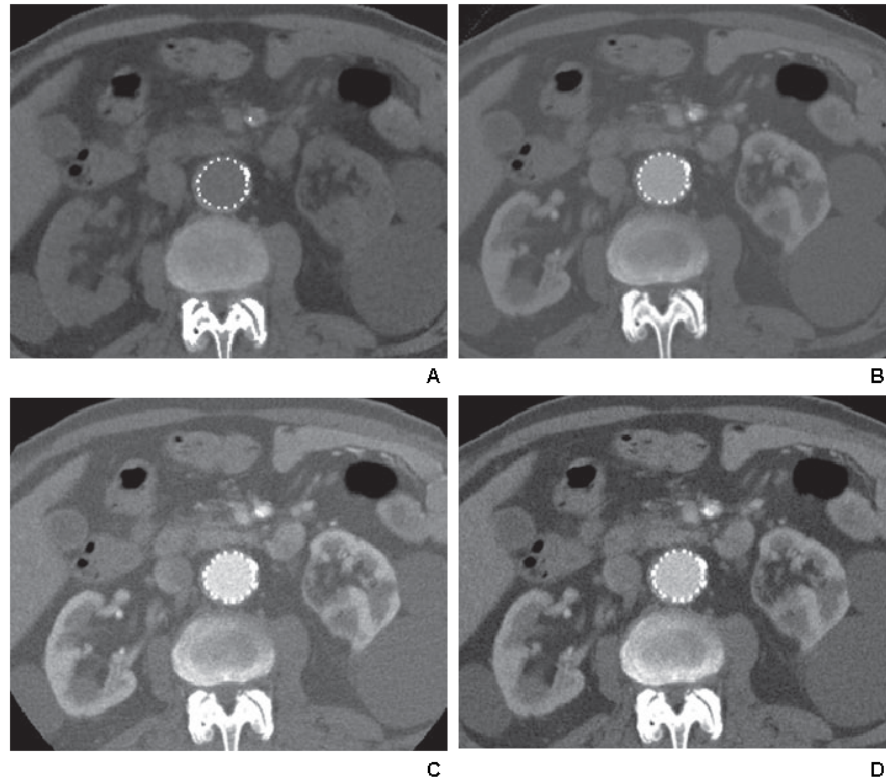


Figure 8-1: 87-year-old 74-kg man after endovascular aneurysm repair for abdominal aortic aneurysm. (A) Axial dual-energy VNC CT image shows non-contrast blood (33 HU) in aorta. Axial arterial phase (B) weighted-average, (C) 80-kVp, and (D) 140-kVP images show high-attenuation contrast material (342 HU, 526 HU, and 263 HU, respectively) in aorta.

Endoleaks (Figure 8-2) were detected in seven patients on the arterial phase images and in one patient on the venous phase images. Thrombus was detected and measured outside the stent in 28 of 30 patients. Thrombus was identified within the stented lumen in one of the other two patients and was not present in the other; both

patients were excluded from thrombus analysis. Previously acquired true non-contrast images of the chest were not available for five patients and of the abdomen for one patient. Hence, luminal attenuation and noise comparisons were performed only for the thoracic aorta in 25 patients and the abdominal aorta in 29 patients.

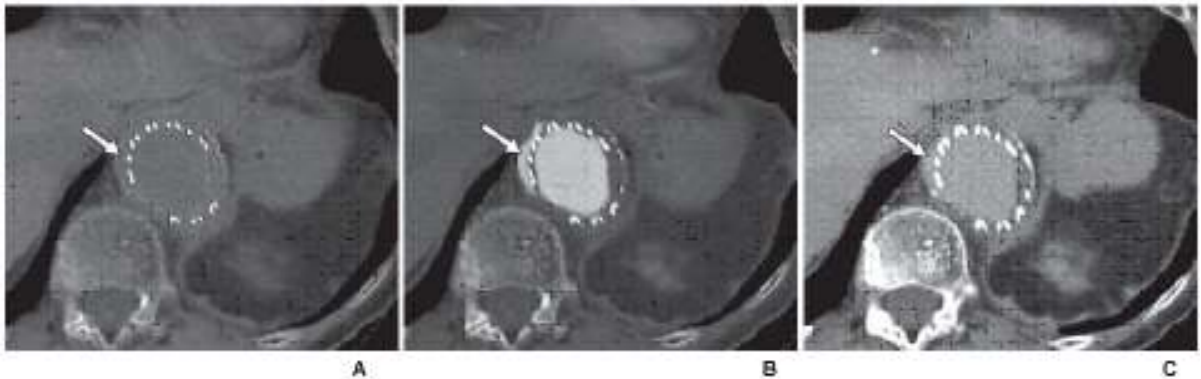


Figure 8-2: 76-year-old 52-kg woman with CT evidence of endoleak after endovascular aortic repair. A, DECT VNC image (A) shows no contrast material outside the stent in the aneurysm sac (*arrow*). (B) Weighted-average arterial phase DECT and (C) venous phase SECT images show contrast enhancement.

In these patients, true non-contrast scans preceded the study examination by an average of 7 months (range, 1–15 months) without interval acute events. Comparison of patient size indexes measured from the topograms acquired in the previous and current examinations (maximum thoracic width, 37.9 vs 39.6 cm; maximum abdominal width, 37.4 vs 38.9 cm) showed no significant difference ($p > 0.1$, paired Student's t test), indicating there was no change in patient body habitus within the scanned region between CT time points.

8.3.2 Radiation and Contrast Dose Measurements

The total effective radiation dose was significantly lower with the study (ED_{Total} , 26 mSv) than with the standard protocol (ED'_{Total} , 37.5 mSv). An average radiation dose reduction of 31% (range, 26.5%–34.2%) was realized for each patient examination through elimination of the non-contrast acquisition (Figure 8-3). The dose reduction for a given patient depended on the patient's anatomic features and the subsequent efficiency of anatomy-based tube current modulation during both dual-energy and SECT acquisitions. Although DECT required a longer scan time (34 seconds) than SECT (15 seconds), the contrast injection flow rate for DECT (3.0 mL/s in the study protocol) was lower than that for SECT (3.5 mL/s with our routine arterial protocol), yielding equivalent contrast volumes for the single and dual-energy protocols.

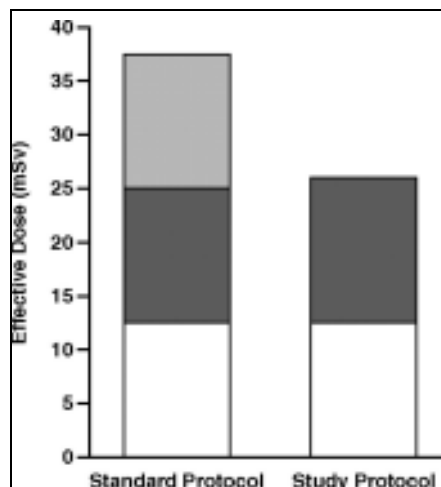


Figure 8-3: Graph shows replacing two (non-contrast [*light gray*] and arterial phase [*dark gray*]) of three SECT acquisitions in standard triple-phase protocol with single arterial phase DECT acquisition in study protocol while retaining SECT venous phase (*white*) acquisition in both protocols results in significant 31% dose reduction.

8.3.3 Tissue Attenuation

Average luminal attenuation in the thoracic and abdominal aorta on VNC CT images was 32 HU and 30 HU, respectively, indicating the presence of non-contrast blood [181]. Although the attenuation of blood on true non-contrast images was slightly higher than on VNC CT images (Table 8.2), the magnitude of the difference was small (mean difference, 3 HU in the thorax and 5 HU in the abdomen), indicating sufficient removal of iodine from arterial DECT images by means of three-material decomposition (Figure 8-4).

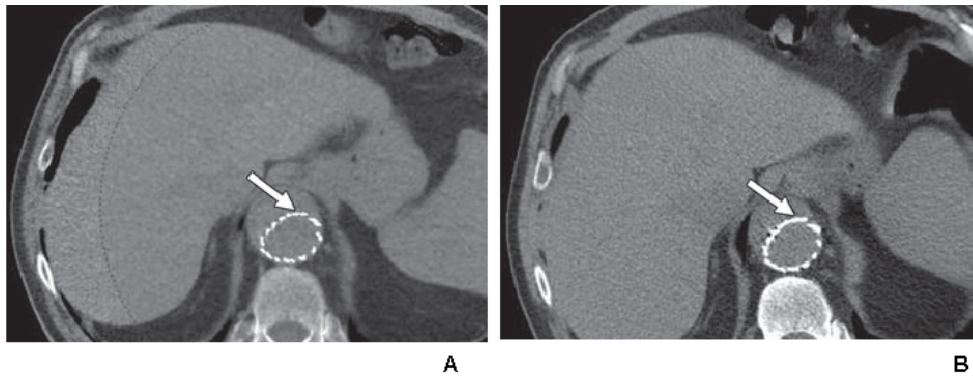


Figure 8-4: 57-year-old 74-kg man after endovascular stenting of descending thoracic aorta. Comparison of (A) VNC CT image generated from DECT data obtained during current examination with (B) true non-contrast image acquired at 120 kVp during previous examination. Mean attenuation values of 28 HU and 31 HU were measured in aorta on A and B, indicating presence of blood in lumen. Noise (SD of mean attenuation in aorta) from VNC CT images (11 HU) was lower than noise from true non-contrast images (24 HU). Stent (*arrow*) in A appears with lower attenuation than B.

For low-attenuation tissue such as thrombus (Figure 8-5), measurements on VNC CT images were similar to measurements on weighted-average arterial but lower than

those on venous images (Table 8.2). However, the attenuation measured on VNC (18–47 HU) and weighted-average arterial (18–47 HU) and venous (22–46 HU) images indicates a range of thrombus attenuation values typically observed on SECT images [181, 182]. This finding shows that neither DECT acquisition nor VNC generation significantly alters the attenuation of low-density tissue. For high-attenuation objects such as stents and calcium, attenuation values varied significantly across images sets. At some locations, some stent struts (Figure 8-5) and calcium (Figure 8-6) had lower attenuation on VNC CT images than on weighted-average arterial and venous images, indicating that some voxels of high-attenuation material were still below the user-defined threshold and were processed during generation of VNC images.

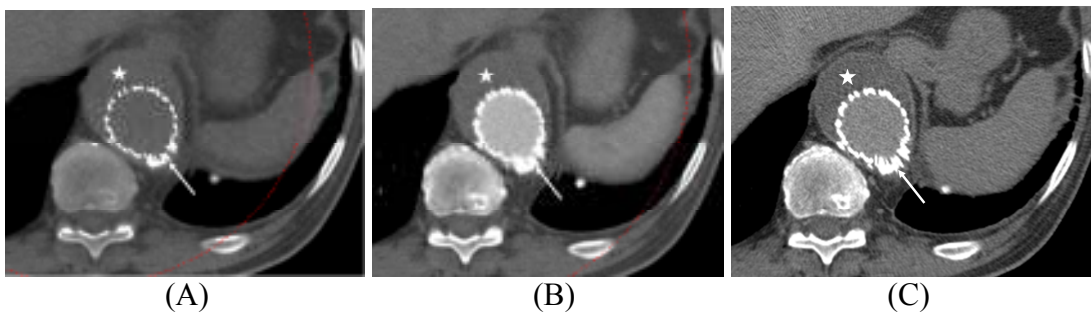


Figure 8-5: Images from a 79-year-old 81-kg man show effect of DECT on tissue attenuation. (A) Axial VNC CT DECT, (B) weighted-average arterial phase DECT, and (C) venous phase SECT images show stent (*arrow*) and thrombus in excluded aneurysm sac (*star*). Thrombus attenuation measures 24 HU in A, 26 HU in B, and 25 HU in C, showing that low-attenuation tissues such as thrombus have similar attenuation in all three phases. High-attenuation materials such as stent, however, have low attenuation on VNC images.

Tissue Type	n	Attenuation (HU)	p
<u>Blood in Thoracic Aorta</u>			
Virtual non-contrast	25	32 ± 2	
True non-contrast		35 ± 4	< 0.05
<u>Blood in Abdominal Aorta</u>			
Virtual non-contrast	29	30 ± 3	
True non-contrast		35 ± 5	< 0.05
<u>Thrombus</u>			
Virtual non-contrast	28	32 ± 6	
Weighted-average arterial		33 ± 7	0.07
Venous		34 ± 6	< 0.05
<p>Note— <i>n</i> indicates number of patients contributing to average values. Attenuation values are mean ± SD. Virtual non-contrast images were generated from arterial DECT data from current exam. True non-contrast images were obtained from a previous clinical examination. Values of <i>p</i> were obtained by paired Student's <i>t</i> test (for blood attenuation) or Tukey-Kramer test (for thrombus attenuation) in comparison with virtual non-contrast images. All <i>p</i> < 0.05 were considered statistically significant.</p>			

Table 8.2: Tissue Attenuation Measurements in Various Image Sets

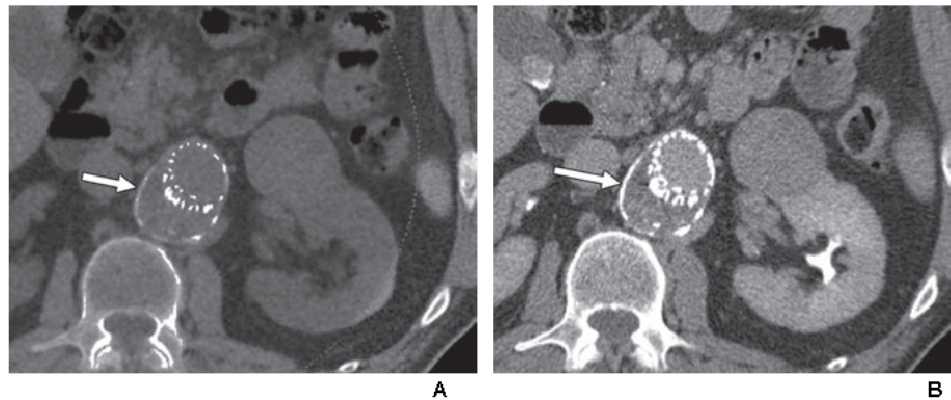


Figure 8-6: 76-year-old 103-kg man with stable endovascular stent-graft in abdominal aorta. (A) Axial VNC DECT image shows decreased calcium attenuation (*arrow*) in wall of aneurysm sac than in (B) venous phase SECT image.

8.3.4 Image Noise

VNC CT images were less noisy than routinely used true non-contrast images in both the thoracic and abdominal aorta (Table 8.3) ($p < 0.05$). Therefore, noise on VNC images was considered acceptable for clinical review. Noise was lower on weighted-average arterial DECT images than on venous SECT images of the abdominal aorta (Table 8.3) ($p = 0.05$), indicating an acceptable noise level for this image type in the abdomen. Although noise on arterial DECT images of the thoracic aorta was slightly greater than that on venous SECT images (Table 8.3) ($p < 0.05$), the magnitude of the average difference (3 HU) was considered negligible by our readers because it did not interfere with clinical interpretation. Therefore, the image noise for arterial phase DECT of the thorax was considered acceptable.

Location	n	Noise (HU)	p
<u>Thoracic Aorta</u>			
Virtual non-contrast	25	10 ± 1	
True non-contrast		13 ± 4	< 0.05
Weighted-average arterial	25	16 ± 2	
Venous		13 ± 2	< 0.05
<u>Abdominal Aorta</u>			
Virtual non-contrast	29	12 ± 2	
True non-contrast		19 ± 5	< 0.05
Weighted-average arterial	29	21 ± 3	
Venous		23 ± 5	0.05
<p>Note— <i>n</i> indicates number of patients contributing to average values. Attenuation values are mean ± SD. Virtual non-contrast images were generated from arterial phase DECT data from current examination. True non-contrast images were obtained from a previous clinical examination. Values of <i>p</i> were obtained by paired Student's <i>t</i> test. All <i>p</i> < 0.05 were considered statistically significant</p>			

Table 8.3: Comparison of Noise Measurements on DECT and SECT Images.

8.4 Discussion

The results of our study show the feasibility of using arterial DECT acquisition to obtain both VNC and arterial phase CT images. In combination with venous SECT acquisition, substitution of one arterial phase DECT acquisition for both non-contrast and arterial phase single-energy acquisitions led to an overall 31% average dose savings with

no significant loss of diagnostic information in follow-up after EVAR. Virtual and true non-contrast images had similar aortic luminal attenuation.

Thrombus attenuation values on VNC, arterial, and venous images were similar. High-attenuation materials in the aneurysm sac, such as endoleak and calcium were appropriately differentiated on VNC CT images. Although iodine in endoleaks on arterial and/or venous images was removed at the corresponding locations on VNC CT images, calcium was present on images from all three phases. However, stent and calcium had decreased attenuation at some locations on VNC images, indicating improper identification of these materials as iodine with the three-material decomposition algorithm. Noise from DECT was considered similar to noise from SECT.

8.4.1 Technical Considerations

Commercially available three-material decomposition software is designed to operate with a single contrast ratio for iodine removal from the entire set of VNC CT images. Results of our preliminary studies indicated this approach can result in very small or even negative aortic luminal attenuation on VNC CT images of patients with inhomogeneous enhancement along the length of the aorta. Therefore, each DECT arterial phase image set was processed twice with two different contrast ratios computed separately for the thoracic and abdominal aorta. Use of this procedure resulted in luminal attenuation on VNC images similar to that on true non-contrast images.

The significant decrease in the attenuation of high-density materials observed at some locations on VNC images compared with weighted-average arterial and venous images in both the current and previous studies [18, 19] was a limitation of the three-

material decomposition algorithm, in which it is assumed that each voxel is a combination of only fat, tissue, and iodine. A voxel containing any other material was still decomposed into a mixture of these three basis materials, and in the case of high-density materials, the voxels were assumed by the algorithm to contain iodine. This improperly identified material was then removed by the software, resulting in reduced attenuation of the voxel. In an attempt to preserve the attenuation values of stent material in this study, only voxels below a threshold equal to the weighted-average stent attenuation were processed for each patient. Even with this approach, however, the attenuation of some stent and even some calcium voxels on VNC CT images appeared with reduced attenuation, indicating that these voxels were below the threshold (Figure 8-5).

A significant increase in the attenuation of high-density materials was observed at some locations on both VNC and weighted-average arterial images compared with venous images. When calcium and stent voxels were above the threshold, attenuation values at 80 and 140 kVp were combined in a 30%/70% ratio, resulting in higher attenuation values than those obtained at the same location with 120 kVp. These observations indicate that this linear mixing ratio may not be optimal for maintaining attenuation of high-density materials on DECT images that is similar to the attenuation on SECT images obtained at 120 kVp.

Another technical consideration with DECT is the high noise associated with 80 kVp, particularly in imaging of large patients. In their study of venous phase DECT, Chandarana et al. [18] excluded heavy patients (≥ 90 kg) with a large abdominal diameter (>35 cm) to avoid poor image quality. In a similar study, Stolzmann et al. [19] reported a

false prediction of endoleak in a patient with a body mass index of 36.5. In our study, no patients were excluded on the basis of size. Yet noise did not affect clinical interpretation even in six obese patients (102–116 kg; body mass index, 29.9–37.7). Moreover, in contrast to the observation by Chandarana et al., with our approach, VNC CT images were less noisy than true non-contrast images (Table 8.3). We also observed in our study that, on average, noise from the weighted-average arterial DECT image set was similar to that on venous phase SECT images, indicating that mixing 30% 80-kVp data with 70% 140-kVp data did not exact a noise penalty.

For both single- and dual-energy CT, dose requirements for the long-scan-range aortic studies necessitated ungated data acquisition with slow gantry rotation times. Inevitable misregistration artifacts present on the original 80- and 140-kVp images of some patients were amplified on VNC CT images (Figure 8-7). These artifacts can be reduced by use of either faster rotation times (0.33 vs 0.5 second) or ECG-referenced techniques. However, the improved temporal resolution would further limit the maximum power available for the lower-energy images and might result in increased noise. In addition, the use of an ECG-referenced technique would require a substantial increase in radiation dose, which does not seem justified, because the observed artifacts were not found to interfere with clinical evaluation. Use of a new dual-source CT system (Flash, Siemens Healthcare) with very high pitch ECG-referenced helical data acquisition [28] may significantly reduce radiation exposure, allowing lower-dose ECG-gated single- or dual-energy CT of the aorta.



Figure 8-7: 76-year-old woman with weight of 52 kg who presented for follow-up of endovascular stent for thoracoabdominal aortic rupture. Images show misregistration artifacts (*arrows*) as result of ungated and low-temporal-resolution data acquisition. Arterial phase DECT image obtained at (A) 80 kVp, (B) 140 kVp. (C) VNC DECT image.

8.4.2 Limitations

Because of radiation exposure concerns, acquisition of true non-contrast data was not included in our study protocol, preventing direct comparison of VNC and true non-contrast images obtained at the same time. We relied on previously acquired true non-contrast data to illustrate two main points: iodine was sufficiently removed from the vessel lumen on VNC images and noise was sufficiently low on VNC images. Because both true and VNC image sets were obtained with the same scanner and because patient size in the scanned region was unchanged in the interval between examinations, we believe the use of current VNC and previously acquired true non-contrast image sets to establish these points was valid.

Reliance on VNC images may not be appropriate for follow-up imaging soon after EVAR because residual contrast material in the excluded aneurysm sac likely would

be removed and not visible on VNC images [19]. Hence, patients in the immediately post-EVAR period were excluded from our study to avoid misdiagnosis. Images from different phases were qualitatively assessed for the presence of endoleaks; quantification and classification were considered outside the focus of this study. Similarly, the presence of calcium in the aneurysm sac was assessed visually but not quantified. Because some voxels containing stent metal and calcium (attenuation below threshold) were processed with the three-material decomposition algorithm and some voxels (above the threshold) were not, a quantitative evaluation of stent and calcified regions was not appropriate.

8.5 Conclusion

We conclude that both VNC and arterial phase images can be obtained from a single arterial DECT acquisition rather than from two separate SECT acquisitions. The attenuation of low-density tissues was similar on the dual-energy and standard SECT images, but the attenuation values of high-density materials differed significantly. Nevertheless, VNC and weighted-average arterial images from DECT can replace true non-contrast and arterial phase SECT images, respectively, in the follow-up of patients who have undergone EVAR (except immediately after the procedure) to provide comparable diagnostic information with an average dose savings of 31%.

CHAPTER IX

IMPROVED DIFFERENTIATION OF CALCIUM AND IODINE WITH DECT IMAGING

This chapter focuses on developing new approaches to address the limitations of the three-material decomposition algorithm and non-uniform enhancement during generation of virtual non-contrast (VNC) images described in the previous chapter. A linear-time invariant based mathematical modeling approach for developing patient-specific contrast protocols for achieving uniform enhancement during the scan was described in this chapter. Also a three-material decomposition algorithm based on a combined basis spectral and basis material approach developed to improve VNC image generation is explained here. Finally, the feasibility of applying the algorithm in both in-vitro and in-vivo studies was demonstrated.

9.1 Introduction

DECT has the ability to identify iodine from its surrounding tissues based on differences in atomic number, density and energy of the x-ray spectrums employed [22, 183, 184]. A recent study by Numburi et al [183] evaluated the feasibility of generating

VNC images using dual-energy technique on a first generation dual-source CT scanner (Definition, Siemens) in arterial phase. But, due to limitations of the three-material decomposition algorithm provided by the manufacturer, spectral overlap of the two energy spectra employed (80 and 140 kVp) and non-uniform contrast enhancement, calcium and iodine were not discriminated well resulting in removal of calcium in the VNC images [183].

The manufacturer implementation of the basis three-material decomposition algorithm assumes that each voxel is composed of fat, soft tissue and iodine, and the attenuation of these materials is solved to identify and eliminate contrast pixels during VNC generation. However, as calcium is not considered as one of the three basis materials, discrimination between contrast material and calcium is challenging. The three material decomposition algorithm can be improved by assuming calcium, blood and contrast as the basis materials present in each pixel and employing a combined basis spectral [77] and basis material analysis [79] to the DECT images to differentiate the components of the mixture.

Spectral overlap of the two x-ray energies used for dual-energy imaging on the first-generation dual-source DECT scanner (Definition, Siemens) also hampers separation of calcium and iodine. Smaller spectral separation pose a challenge for separating materials with similar atomic numbers [142]. Hence, improving spectral separation between the two tube voltages has the potential to better differentiate and quantify tissue like calcium and iodine. A recent study by Primak et al [142] on second generation dual-source CT scanner (Flash, Siemens) showed that additional filtration of the low energies in the 140 kVp spectrum increased the difference of dual-energy ratio

(DE_{ratio} , defined as the ratio of CT numbers of the material and high and low energy) between tissues with similar atomic numbers (like calcium and iodine).

In this study, the potential improvement in VNC generation from DECT was explored by employing (1) an additional filter to separate the x-ray spectra for DECT imaging, (2) a customized basis spectral and basis material decomposition algorithm, and (3) an optimization algorithm for administrating patient-specific contrast protocols.

9.2 Material and Methods

9.2.1 Contrast Injection Optimization Algorithm

Using tracer kinetics, the effective flow profile of contrast in the venous system with the test injections can be estimated. Fleischmann et al suggested that a patient could be assumed as a linear time-invariant (LTI) system and arterial enhancement (*enh*) could be modeled as the convolution integral of the contrast agent flow rate (*inj*) and impulse response of the patient (*imp_resp*)

$$enh(n) = \sum_m imp_resp(m) \cdot inj(n - m) \quad (9-1)$$

A test bolus of 20 mL of contrast agent followed by saline should be administered to a patient and the resulting test bolus attenuation curve can be measured. Using the test bolus data, LTI modeling can be performed in the time domain to predict patient-specific contrast injection profiles that would achieve uniform enhancement in the CT images. The target enhancement and scan duration desired during the diagnostic scan can be defined and optimal patient-specific contrast injection protocols can be computed using non-linear optimization algorithm as explained in section 7.2.2.2. A paper describing

modeling of the contrast injections for short duration CT scans in explained in detail in Appendix 4.

9.2.2 VNC Theory And Algorithm Development

Basis spectral method can provide the effective atomic number and density of the mixture [77] and basis material analysis can identify the mass fraction of the individual elements of the mixture [79]. Assuming, that each pixel consists of calcium, iodine and blood, the combined spectral and material approach can be implemented as described:

Step 1: Find effective density and atomic number of the mixture in each pixel

- Perform DECT measurements using spectrally separate 80 and 140 kVp acquisition with additional filtration.
- Measure CT number of the tissue from both 80 and 140 kVp images.
- Compute the linear attenuation coefficient at both energies from definition of CT number using linear attenuation of water at 80 and 140 kVp.

$$\mu_{80} = \left(\frac{HU_{80}}{1000} + 1 \right) \bullet \mu_{water, 100} \quad (9-2)$$

$$\mu_{140} = \left(\frac{HU_{140}}{1000} + 1 \right) \bullet \mu_{water, 140} \quad (9-3)$$

- Model the linear attenuation coefficient using the continuous x-ray spectrum $S(E)$ and detector sensitivity $D(E)$ of the CT scanner

$$\mu = C \bullet \rho_{eff} \int w(E) \bullet \left(\frac{\mu}{\rho} \right) (E, Z_{eff}) \bullet dE \quad (9-4)$$

where, $w(E)$ is the weighting function calculated from $S(E)$ and $D(E)$ for 80 and 140 kVp data (Figure 9-1), and C is an empirical value [$C=1$ for $Z_{eff}<10$ and $C=1.45 \cdot (0.05 \cdot Z_{eff})$ for $Z_{eff} \geq 10$].

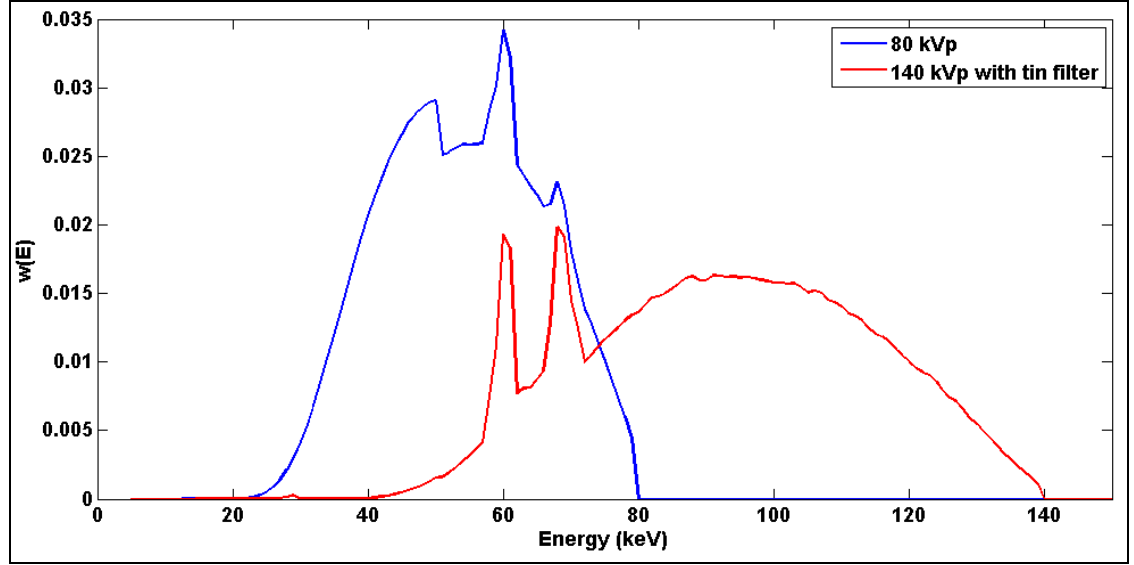


Figure 9-1: Weighting factor $w(E)$ at 80 and 140 kVp for DECT scanner (Flash, Siemens Medical Systems, Forchheim, Germany).

- Compute the functions (f_{80} and f_{140}) using $w(E)$ for 80 and 140 kVp spectrum, and mass attenuation coefficient of elements ($Z=1$ to 30) from National Institute of Standards and Technology database [185]. Plot the ratio of the functions for all the elements (Figure 9-2).

$$f_{80} = \int w_{80}(E) \cdot \left(\frac{\mu}{\rho} \right) (E, Z_{eff}) \cdot dE \quad (9-5)$$

$$f_{140} = \int w_{140}(E) \cdot \left(\frac{\mu}{\rho} \right) (E, Z_{eff}) \cdot dE \quad (9-6)$$

$$\frac{f_{80}(Z)}{f_{140}(Z)} = Fn(Z) \quad (9-7)$$

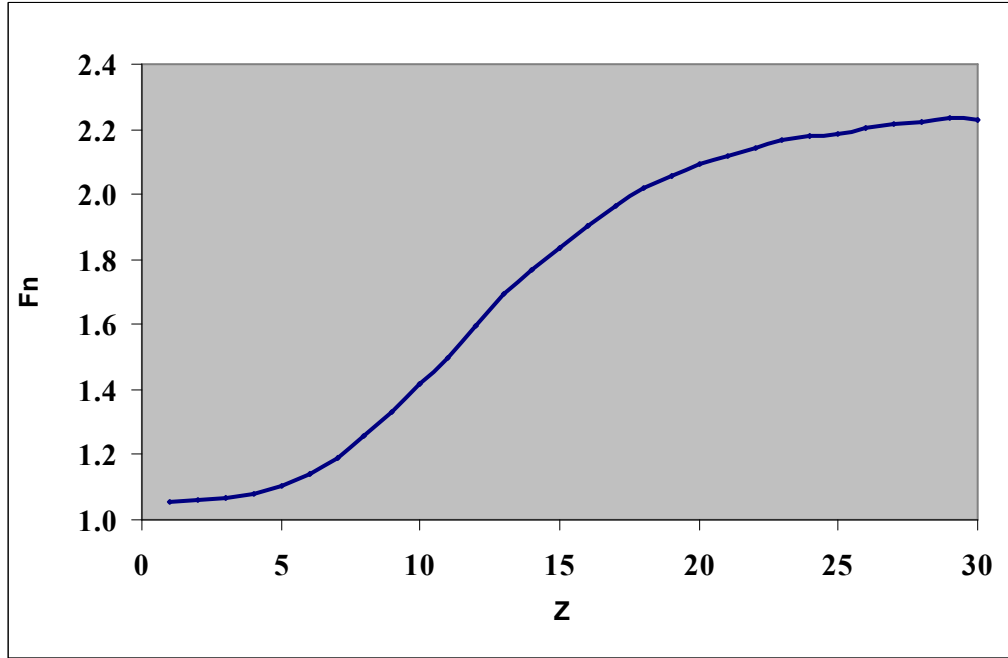


Figure 9-2: Plot of $Fn(Z)$ as function of atomic number (Z).

- Calculate ratio of linear attenuation coefficient from 80 and 140 kVp from (9-1) and (9-2) to obtain the effective atomic number of the mixture from Figure 9-2.

$$\frac{\mu_{80}}{\mu_{140}} = Fn(Z) \quad (9-8)$$

- Calculate density of the material.

$$\rho_{eff} = \frac{\mu_{80}}{C \cdot f_{100}} \quad (9-9)$$

Step 2: Find mass fractions of the three components of the mixture

- Calculate linear attenuation coefficient at 80 and 140 kVp using ρ_{eff} from Step 1

$$\mu_{80} = C \cdot \rho_{eff} \left[\left(x_1 \cdot \sum w_{80} \cdot \left(\frac{\mu}{\rho} \right)_1 \cdot dE \right) + \left(x_2 \cdot \sum w_{80} \cdot \left(\frac{\mu}{\rho} \right)_2 \cdot dE \right) + \left(x_3 \cdot \sum w_{80} \cdot \left(\frac{\mu}{\rho} \right)_3 \cdot dE \right) \right] \quad (9-10)$$

$$\mu_{140} = C \cdot \rho_{eff} \left[\left(x_1 \cdot \sum w_{140} \cdot \left(\frac{\mu}{\rho} \right)_1 \cdot dE \right) + \left(x_2 \cdot \sum w_{140} \cdot \left(\frac{\mu}{\rho} \right)_2 \cdot dE \right) + \left(x_3 \cdot \sum w_{140} \cdot \left(\frac{\mu}{\rho} \right)_3 \cdot dE \right) \right] \quad (9-11)$$

where x_1 , x_2 , x_3 are the mass coefficients of the three basis material.

- Apply conservation of mass to the three component system

$$x_1 + x_2 + x_3 = 1 \quad (9-12)$$

- Use linear attenuation coefficients from (9-1) and (9-2), and solve equations (9-8), (9-9) and (9-11) simultaneously with non-negative, non-linear least square optimization to obtain values for x_1 , x_2 , x_3 .

Step 3: Create VNC image

- Identify the amount of iodine and contrast agent in a pixel from step 2 and eliminate the iodine content to create a VNC image.

A customized algorithm comprising of Steps 1 to 3 was developed (Matlab, The Mathworks Inc., Natick, MA) to generate VNC images.

9.2.3 In-Vitro Study

All phantom and patient scans were performed using a second generation dual-source DECT scanner (Flash, Siemens Healthcare, Forchheim, Germany) employing a tin filter for removal of lower energies from the 140 kVp spectrum for improving spectral separation (Figure 9-3).

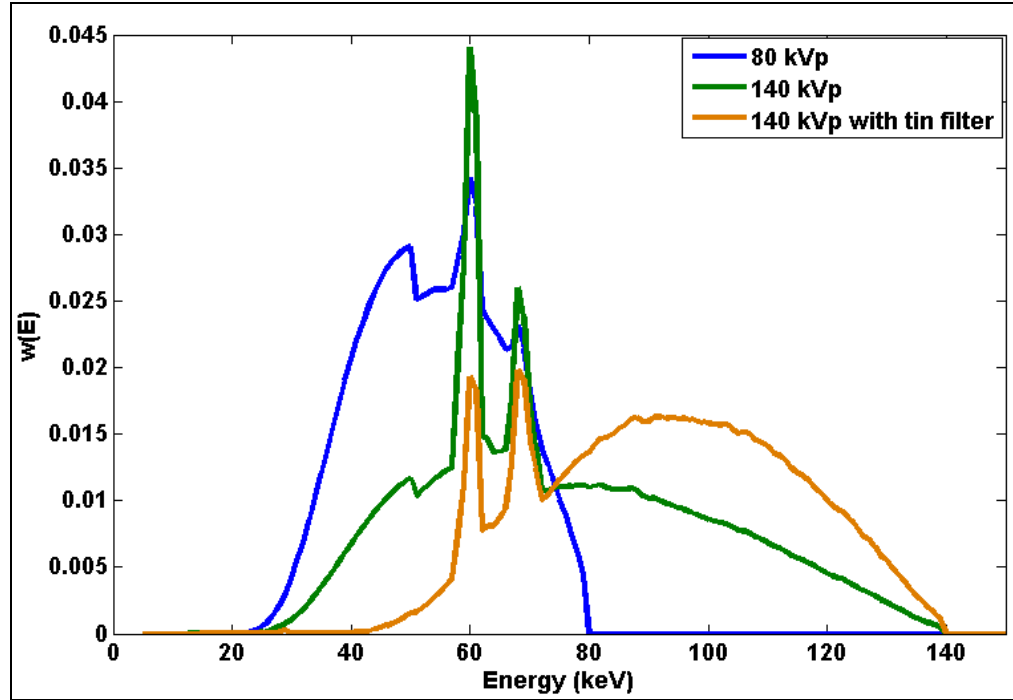


Figure 9-3: Plot of weighting function of x-ray spectrum at 80 kVp, 140 kVp and 140 kVp with tin filter as a function of energy. The tin filter applied to the 140 kVp spectrum filtered lower energies allowing better separation between the 80 and 140 kVp energies.

To validate the proposed basis spectral and basis material algorithm, phantom studies containing mixtures of water with calcium based hydroxyapatite [HA: $\text{Ca}_5(\text{PO}_4)_3(\text{OH})$] or with iodinated contrast agent were performed. A phantom containing of total of six HA inserts (QRM, Möhrendorf, Germany) and ten inserts of varying concentrations of contrast agent was developed to simulate a range of CT numbers observed clinically in patients. The HA inserts were composed of mixtures of water equivalent material and HA. The contrast inserts were made up of varying mixtures of water with iodinated contrast agent (Ultravist 240, Ultravist 300 or Ultravist 370, Berlex, Montville, NJ)

containing 240, 300 and 370 mgI/mL respectively (Table 9.1). The theoretical densities and mass fractions of each insert were known.

Insert	Iodine concentration (mgI/mL)	Total volume (mL)	Contrast volume (mL)	Water volume (mL)
1	240	10	9.7	0.3
2	240	10	9.5	0.5
3	240	10	9.3	0.7
4	300	10	9.8	0.2
5	300	10	9.6	0.4
6	300	10	9.4	0.6
7	370	10	9.8	0.2
8	370	10	9.7	0.3
9	370	10	9.6	0.4
10	-	10	0	10

Table 9.1: Composition of the ten inserts composed of aqueous contrast mixtures.

The phantom was imaged with the following parameters: tube voltage, 80 kVp (Tube A) and 140 kVp with tin filter (Tube B); effective tube current-time product, 248 mAs (Tube A) and 134 mAs (Tube B); rotation time, 0.33 sec; beam collimation, 64 x 0.6 mm; pitch, 0.2. Both 80 and 140 kVp image sets were reconstructed with 0.6 mm slice thickness and 0.6 mm slice increment using a medium-smooth kernel (D30f).

The DECT images were analyzed using the spectral analysis and material decomposition algorithm to first calculate the effective atomic number (Z_{eff}) and density (ρ_{eff}) of the imaged tissues as described in Step 1 in 9.2.1. The iodinated contrast pixels were identified and differentiated from calcium. Finally, the mass fractions of aqueous contrast solutions was computed and compared with theoretically known values.

9.2.4 In-Vivo Study

The patient-specific contrast protocols along with combined basis spectral and basis material algorithm for VNC generation were intended to be evaluated in one patient, who was imaged with a non-contrast SECT, arterial DECT and venous SECT protocol.

True non-contrast SECT—A true non-contrast scan was acquired using a non-ECG-gated helical scan prior to contrast injection according to standard SECT protocol (tube voltage, 120 kVp tube A; effective tube current–time product, 220 mAs tube A with anatomy-based modulation; rotation time, 500 milliseconds; beam collimation, 128×0.6 mm; pitch, 0.8). Images were reconstructed with 3.0-mm slice thickness and 3.0-mm slice increment with a medium-smooth kernel (B31f).

Arterial phase DECT—The study design proposed administration of patient-specific contrast protocols for arterial DECT imaging. However, from preliminary patient analysis not described here, the contrast attenuation was observed to be uniform along the length of the aorta (Figure 9-4). This is primarily due to the decreased scan time (15 s) with the second generation dual-source DECT scanner as compared to the first generation scanner (Definition, Siemens, scan time = 34 s). Hence, patient-specific injections were deemed unnecessary and optimized contrast protocols were not implemented in the patients.

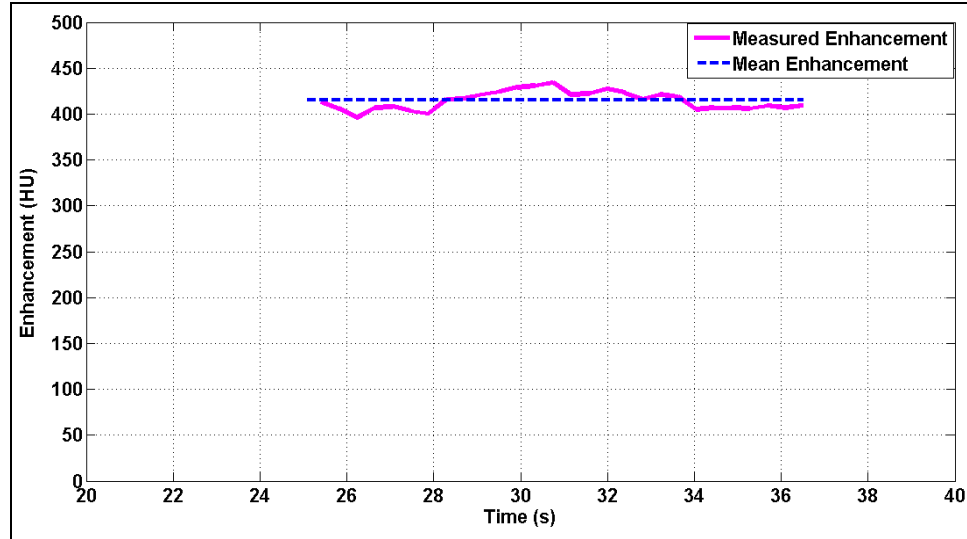


Figure 9-4: Plot of enhancement vs. time showing uniform contrast enhancement (415 ± 10 HU) in a patient imaged with a uniphasic contrast protocol and DECT scan protocol on a second generation dual-source DECT scanner.

In addition, Primak et al [142] suggested the use of 100 and 140 kVp (with additional filtration) in large patients to decrease noise and increase contrast in DECT images on the second generation dual-source DECT scanner. Hence, although the phantom scans were performed using 80 and 140 kVp with tin filter, patient scans were performed using 100 and 140 kVp with tin filter in attempt to decrease noise in patient. Therefore, for arterial DECT imaging, a routine uniphasic contrast protocol consisting of 100 mL of contrast with 30 mL saline chase was administered at 3.5 mL/s and a non-ECG gated helical acquisition was performed using the following parameters: tube voltage, 100 kVp (Tube A), 140 kVp with tin filter (Tube B); quality reference tube current-time product, 195 mAs (Tube A), 151 mAs (Tube B) with anatomic-based tube current modulation employed for each tube; rotation time, 0.28 sec; beam collimation, 64

x 0.6 mm; pitch, 0.65. Both 100 and 140 kVp image sets can be reconstructed with 3.0 mm slice thickness and 3.0 mm slice increment using a medium-smooth kernel (B31f).

Venous phase SECT—A third non-ECG-gated helical scan was obtained 5 minutes after contrast injection with standard SECT protocol (tube voltage, 120 kVp tube A; effective tube current–time product, 160 mAs tube A with anatomy-based modulation; rotation time, 500 milliseconds; beam collimation, 32×1.2 mm; pitch, 0.8). Images were reconstructed with 3.0-mm slice thickness and 3.0-mm slice increment with a medium-smooth kernel (B31f).

Image Analysis—Arterial DECT image from the patient were analyzed as described in the flow chart below (Figure 9-5) using the combined basis spectral and basis material algorithm to create VNC images. Attenuation and noise were measured in the true non-contrast, arterial 140 kVp, and VNC images. To evaluate the impact of eliminating contrast from arterial phase images with the VNC algorithm, attenuation from VNC images were compared with those from true non-contrast and arterial 140 kVp images. In addition, to assess the noise from DECT acquisition, noise from VNC was compared to true non-contrast. To evaluate the impact of VNC generation using combined basis spectral and basis material algorithm on high density substances, calcium and stent attenuation were visually compared between VNC and true non-contrast images.

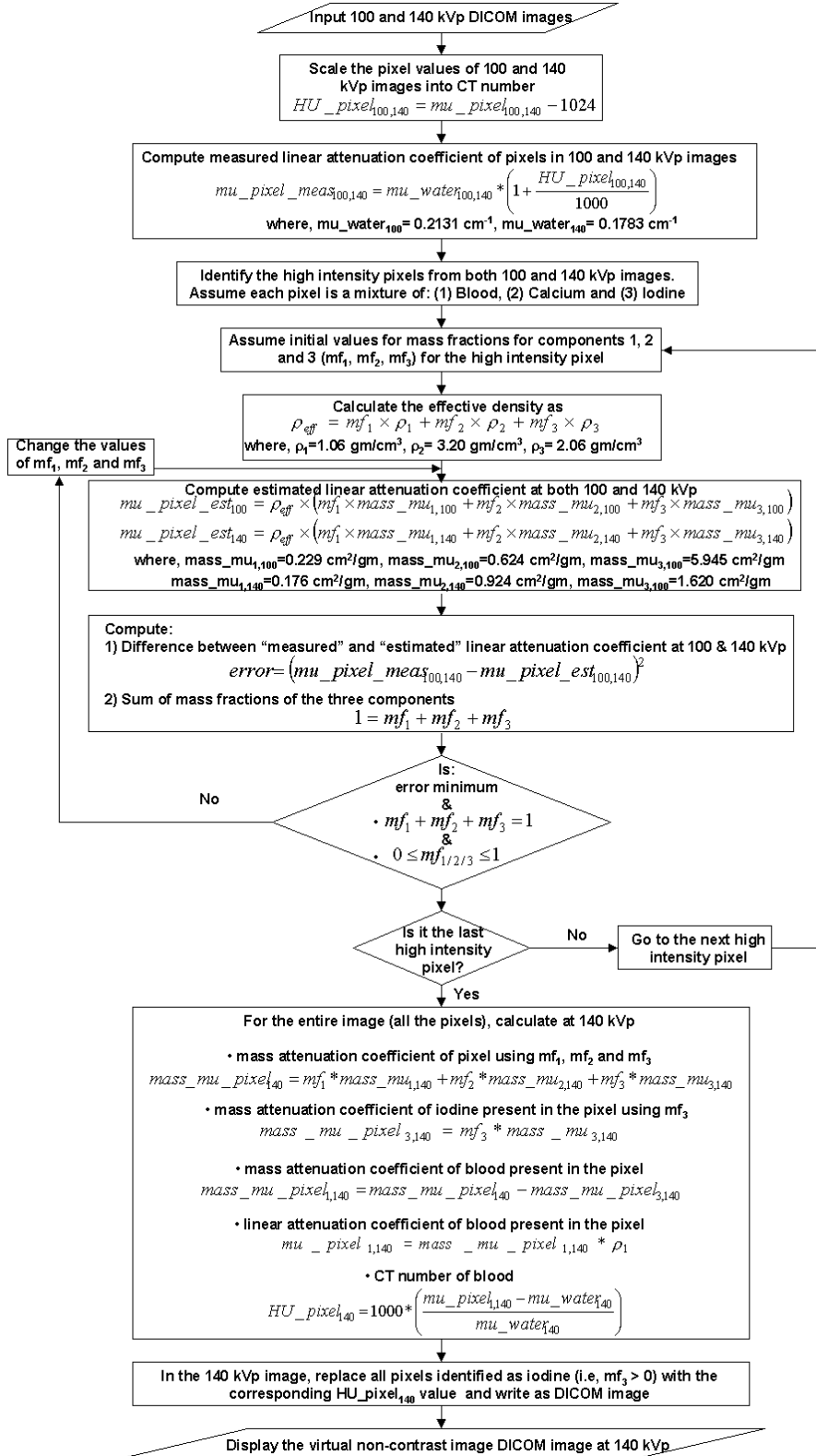


Figure 9-5: Flow chart of three-material decomposition in patients.

Finally, the effective dose in millisieverts were estimated as the product of the DLP in milligray · centimeters and a conversion coefficient, k , in mSv/(mGy · cm) [20]. The value of k is 0.014 for the chest and 0.015 for the abdomen and pelvis; the average k for a single scan encompassing all three regions is 0.015. The total effective dose for the patient in our study was estimated with the DLPs from true non-contrast SECT ($DLP_{SECT \text{ True non-contrast}}$), arterial DECT ($DLP_{DECT \text{ Arterial}}$) and venous SECT ($DLP_{SECT \text{ Venous}}$) acquisitions, as follows:

$$ED_{Total} = k \cdot (DLP_{SECT \text{ True non-contrast}} + DLP_{DECT \text{ Arterial}} + DLP_{SECT \text{ Venous}}) \quad (9-13)$$

The total effective dose with the elimination of the true non-contrast scan in the patient was also estimated:

$$ED'_{Total} = k \cdot (DLP_{DECT \text{ Arterial}} + DLP_{SECT \text{ Venous}}) \quad (9-14)$$

9.3 Results

9.3.1 In-Vitro Study

The reconstructed images acquired at 80 and 140 kVp with additional tin spectrum from the in-vitro studies are shown in Figure 9-6. The average CT numbers of calcium inserts varied from 184 to 1123 HU in 80 kVp images and from 137 to 710 in 140 kVp images. The mean CT numbers of the contrast solutions ranged from 252 to 732 HU in the 80 kVp images and from 88 to 258 HU in the 140 kVp images.

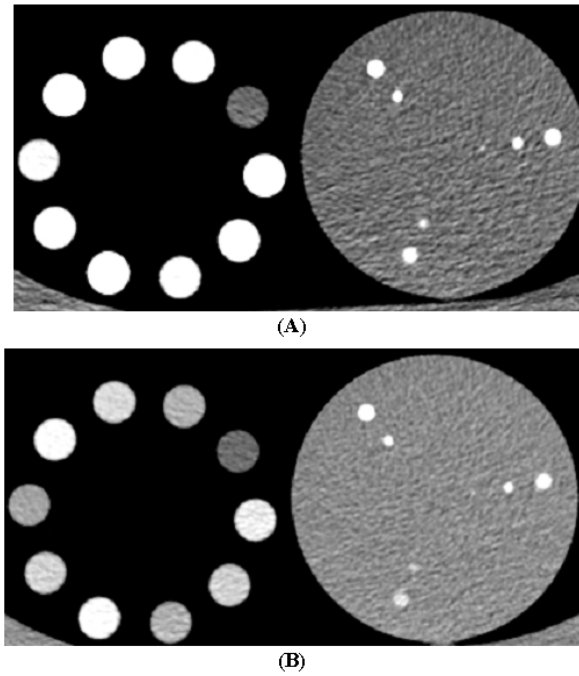


Figure 9-6: Axial images of phantom with HA cylinders and aqueous iodinated mixtures at (A) 80 kVp and (B) 140 kVp with additional tin filter.

Combined spectral and material analysis algorithm clearly differentiated calcium and iodinated pixels in the phantom studies (Figure 9-7). The mass fraction of the aqueous contrast solutions estimated using the proposed algorithm were in good agreement with known values, with a mean error of 3% (Table 9.2).

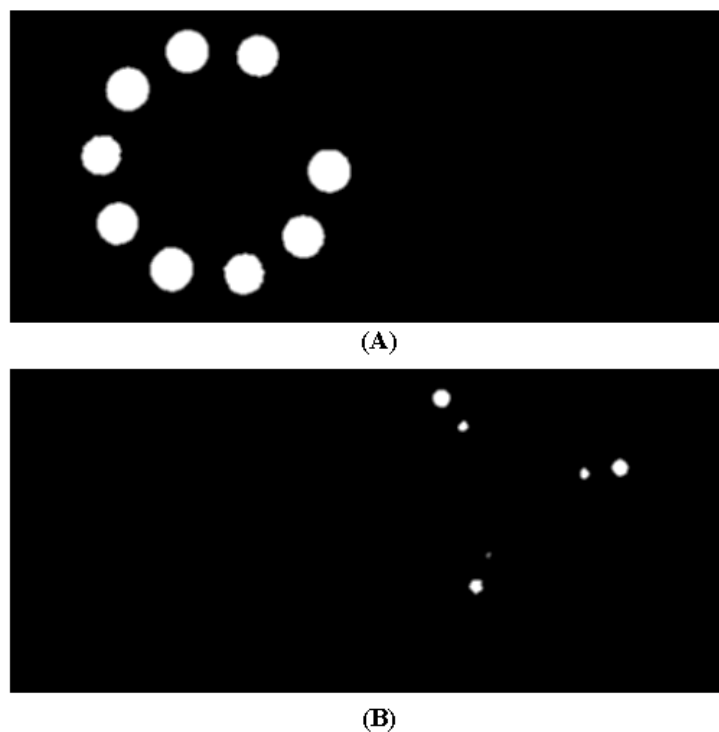


Figure 9-7: Axial images of phantom showing identification of only (A) iodine pixels in contrast agent and (B) calcium pixels in HA.

Insert	Theoretical mass fraction	Computed mass fraction	Error (%)
1	0.963	0.994	3
2	0.938	0.985	5
3	0.914	0.980	7
4	0.974	0.995	2
5	0.948	0.988	4
6	0.922	0.988	7
7	0.972	0.988	2
8	0.959	0.985	3
9	0.945	0.983	4

Table 9.2: Comparison between theoretical and calculated mass fractions of aqueous contrast mixtures.

9.3.2 In-Vivo Study

One patient (male, 67 y, 94 kg) was imaged with true non-contrast SECT, arterial DECT, and venous SECT scans. VNC images were successfully generated from the arterial DECT (100 and 140 kVp) images using the combined basis spectral and basis material algorithm. Average aortic lumen attenuation of 57 HU was measured in the VNC images as compared to 222 HU in the arterial 140 kVp and 61 HU in the true non-contrast images indicating removal of iodinated contrast and presence of unattenuated blood in VNC images (Figure 9-8).

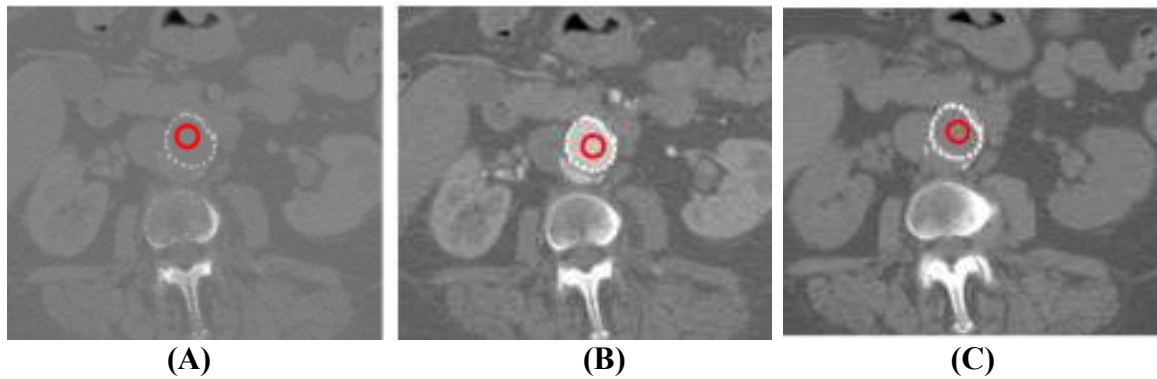
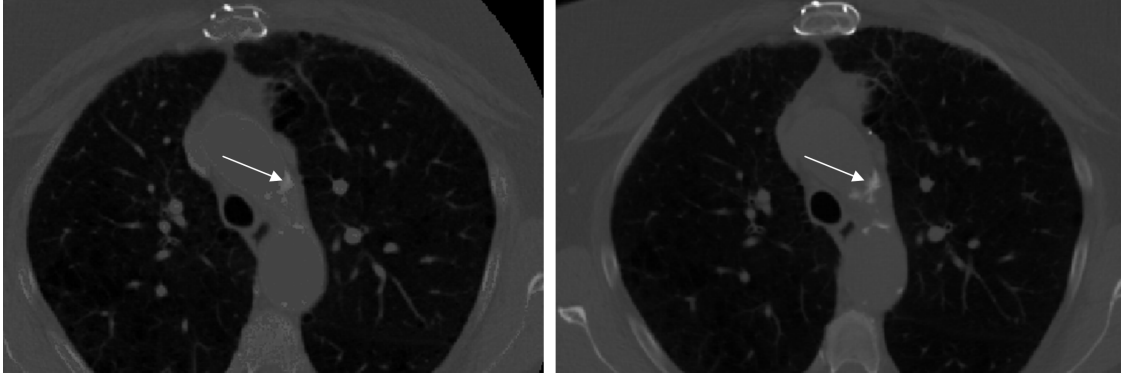


Figure 9-8: Axial images in a patient showing aortic luminal attenuation in the aorta (A) 57 HU in VNC, (B) 222 HU in arterial 140 kVp, and (C) 61 HU in true non-contrast images.

Noise from VNC images (35 HU) was higher as compared to noise from true non-contrast images (24 HU) suggesting increased noise associated with DECT acquisition. Both calcium (Figure 9-9) and stent material appeared with slightly decreased intensity in VNC images showing false identification of certain pixels of the high density materials as iodine.



(A)

(B)

Figure 9-9: Axial images in a patient showing calcium (white arrow) in (A) VNC and (B) true non-contrast images. Calcium appeared with decreased attenuation in VNC images.

The DLP from the arterial DECT acquisition (877 mGy-cm) was similar to the true non-contrast acquisition (869 mGy-cm). Elimination of a true non-contrast scan from a triple phase scan ($ED_{Total} = 35.3$ mSv) would decrease the total effective dose to 22.2 mSv (ED'_{Total}) resulting in dose savings of 37%.

9.4 Discussion

Combined spectral and material based algorithm for three-material decomposition of DECT images can be used to discriminate materials having similar high atomic numbers. Additionally, improved spectral separation using an energy selective filter to remove the low energy photons from the high energy spectrum with an energy spectrum can improve calcium-iodine separation [142]. Our study demonstrates the feasibility of differentiating iodine from calcium, and calculating mass fractions of contrast agent

mixtures accurately in phantom models. The accurate identification of contrast pixels helps to generate VNC images without contrast agent, while retaining calcium. This may help to provide description of anatomy as well as characterization of calcifications and differentiate them from contrast material from a single contrast-enhanced DECT scan.

In the in-vitro study, we used different volumes and concentrations of contrast agent in aqueous solutions in order to simulate a range of CT numbers observed clinically in patients. In some cases, the mixing resulted in similar CT numbers. For example, mixing of 9.6 mL of 300 mgI/mL with 0.4 mL of water and 9.7 mL of 370 mgI/mL with 0.3 mL of water resulted in similar CT numbers. The former mixture measured 463 and 163 HU and the later mixture measured 463 and 156 HU on 80 and 140 kVp images respectively. But, the mass fractions were identified with relative small errors (4% and 3%) respectively in each case demonstrating that combined use of spectrally separate energy spectrum for imaging and algorithm proposed in the study can accurately quantify iodine. However, these errors may be amplified in clinical scenarios; especially where the CT numbers of low attenuating contrast agent and bone may be close.

In the patient study, contrast was accurately identified and eliminated from VNC images which were similar to true non-contrast images. However, in-vivo studies showed that pixels containing tissues with high atomic numbers (stent/calcium), but low densities were falsely identified as iodine by the algorithm. Hence, these pixels appeared with decreased attenuation in VNC images. The attenuation values from VNC could not be compared to true non-contrast images as they were acquired using different tube voltages and attenuation of tissue depends on tube voltage employed for scanning.

The algorithm utilizes the measured CT numbers from the images and hence factors affecting CT numbers such as beam hardening need to be addressed in order to have accurate values. While the beam hardening artifacts can be corrected by using the basis spectral and basis material method in the pre-reconstruction space, its implementation is a time intensive task. Hence, we used the algorithm in the post-reconstruction space where the algorithm is relatively easy to implement and executes in a short amount of time.

Although noise did not impact our phantom study, it plays a critical factor in VNC generation in patients. Hence, 100 kVp and 140 kVp spectrum were employed for patient study as suggested by Primak et al [142] instead of the 80 and 140 kVp spectrum used for phantom scan. The current implementation of DECT scanner with spectrally separate x-ray energies [28] uses 100 kVp on tube A and 140 kVp with additional tin filter on tube B. Tube A has a scan field of view (SFOV) of 50 cm, while tube B has a limited SFOV of 33 cm and may result in noisy images in patients. This can increase the noise in the images causing decreased separation between low density calcium and iodine, thus allowing false identification of calcium as iodine in few pixels. Hence, employing 140 kVp with tin filter on Tube A and 100 kVp on tube B may help to decrease noise and improve segmentation of iodine to create VNC images. Another approach to decrease noise may be possible with use of energy resolving photon-counting detectors [186-188] where photons are assigned to multiple energy bins.

9.5 Conclusion

A three-material decomposition algorithm based on combined basis spectral and basis material analysis for differentiating calcium and contrast agent with DECT imaging was developed. Phantom data demonstrates the feasibility of the proposed algorithm to compute the mass fraction of contrast agent mixtures. This method can be applied clinically for the identification and removal of iodine in contrast-enhanced DECT images, allowing generation of VNC images. However, high attenuating pixels with low density values appear with decreased intensity in VNC images.

CHAPTER X

**OPTIMIZATION OF ACQUISITION AND CONTRAST-INJECTION
PROTOCOL FOR C-ARM CT IMAGING IN TRANSCATHETER AORTIC
VALVE IMPLANTATION: INITIAL EXPERIENCE IN A SWINE MODEL**

The current chapter explains the development of protocols for acquiring 3D C-arm CT images using an existing 2D C-arm system in the interventional suite. The study focuses on the feasibility of developing 3D images and their utility before, during and after transcatheter aortic valve implantation (TAVI) procedure.

10.1 Introduction

Aortic stenosis, the most common type of native valvular heart disease [40, 41] has a significant impact on cardiovascular mortality and morbidity [40, 41, 43]. Transcatheter aortic valve implantation (TAVI) has developed into a viable option for patients with aortic stenosis who are deemed high risk for surgical aortic valve replacement due to multiple comorbidities [58, 59, 61-64, 189, 190]. The valve is implanted within the native valve using transfemoral, transapical, or trans-subclavian methods. With any of these approaches, clinicians need detailed knowledge regarding the

location of the native aortic valve and the aortic anulus (AN) to place the valve accurately and prevent coronary complications, aortic regurgitation, valve embolization and conduction abnormalities. With increasing use of TAVI, the central role of periprocedural imaging has been recognized. However, the optimal imaging approach is still evolving [191]. During TAVI, conventional angiography and transesophageal echocardiography (TEE) are critical for interventional guidance. However, these modalities are limited by their 2-dimensional (2D) nature.

More recently, 3-dimensional (3D) multidetector row computed tomography (MDCT) and 3D TEE have been used in the context of TAVI to describe aortic root anatomy and orientation [11, 71, 192-194]. Availability of this 3D information appears valuable for visualization and intraprocedural guidance. However, the direct use of MDCT images in this way has been limited because of registration challenges between 3D MDCT and 2D fluoroscopic images. Rotating a C-arm system around a patient allows for acquisition of 3D C-arm CT images in the catheterization laboratory [195]. The 3D C-arm CT images can be used for overlaying on the 2D fluoroscopy images obtained from a C-arm system for guidance during TAVI. Alternatively, the 3D images from C-arm CT and preprocedural MDCT can be registered to facilitate overlay of the high definition MDCT images onto the live 2D fluoroscopic images for more accurate and safer valve positioning during TAVI. For both the procedures, it is critical to have C-arm CT images with adequate contrast opacification and optimal image quality.

C-arm CT imaging has been described in the context of endovascular repair of aortic aneurysm [158, 196, 197], ablation procedures in electrophysiology [121, 198], and other cardiac interventions [195, 199]. A recent study by Kempfert et al [170] showed the

feasibility of obtaining C-arm CT images of the aorta for stent/valve implantation during TAVI using a transapical approach. However, a systematic study exploring different C-arm CT imaging techniques and injection protocols in the context of TAVI has not yet been performed.

In this study, we sought to systematically determine optimal contrast and imaging protocols for obtaining C-arm CT images before TAVI in a swine model and to compare the resulting image measurements with those from MDCT. We then sought to evaluate the utility of overlaying 3D preprocedural MDCT images onto real-time 2D fluoroscopy images for intraprocedural guidance during TAVI, and finally to assess the feasibility of making post-TAVI measurements from C-arm CT images.

10.2 Materials and Methods

10.2.1 Animal Preparation

This study was approved by the local Institutional Animal Care and Use Committee. A total of 6 swine (average weight = 53 kg) were sedated (ketamine 10 mg/kg and xylazine 0.1-0.2 mg/kg via intramuscular injection) and prepared for TAVI. The animals were intubated and mechanically ventilated. Anesthesia was maintained with isoflurane (1 to 2.5%). During transportation between the operating room and the CT scanner, isoflurane was stopped and intravenous propofol was administered (loading dose, 3-5 mg/kg to effect). While sheaths were placed in the femoral arteries and veins to prepare for the TAVI procedure, intravenous heparin (100 to 300 U/kg) was administered to prevent thrombosis. After imaging and valve placement, the sedated animals were

sacrificed with an intravenous injection of pentobarbital sodium 390 mg/mL and phenytoin sodium 50 mg/mL.

10.2.2 Image Acquisition

10.2.2.1 Pre-TAVI

Preprocedural MDCT images were obtained with a dual-source scanner (Definition, Siemens Healthcare, Forchheim, Germany). Using an 18-gauge needle, we injected a total of 75 to 80 mL of contrast agent (Ultravist 370 mgI/mL, Berlex, Montville, NJ) at 5 mL/s for 15 to 16 s followed by 30 mL of saline (same flow rate) through a peripheral vein (Table 10.1); we monitored the ascending aorta using bolus tracking to determine the scan delay. Once a threshold of 120 Hounsfield units (HU) was reached in the ascending aorta, an electrocardiogram (ECG)-gated helical scan of the heart was performed during suspended ventilation so that data could be obtained during a breath hold with the following scan parameters: tube voltage, 120 kVp; tube current-time product per rotation, 400 mAs; rotation time, 0.33 s; beam collimation, 64×0.6 mm; and pitch, 0.4 to 0.6 (heart rate dependent). Images were reconstructed at 70% to 75% of the RR interval (heart rate dependent) with a slice thickness of 0.75 mm and a slice increment of 0.4 mm using filtered back projection with a medium smooth kernel (B26f).

During the TAVI procedure, but before valve implantation, all swine were also scanned with a C-arm CT imaging system (Axiom-Artis with syngo DynaCT, Siemens Healthcare, Forchheim, Germany). Data were obtained with different image acquisition (ungated and ECG-gated C-arm CT), cardiac rhythm (rapid pacing and normal sinus rhythm [no pacing]), and contrast injection (peripheral and aortic root) protocols. Both

ungated and ECG-gated C-arm CT protocols were acquired during suspended ventilator respiration.

C-arm CT modulates x-ray exposure to maintain a constant dose at the detector: first, by increasing the tube current-time product per pulse; and second, by increasing the tube voltage [103]. The scan parameters employed for C-arm CT imaging in this study were as follows: frame rate, 60 frames/s; detector entrance dose, 0.54 μ Gy per x-ray pulse, with automatic modulation of tube voltage from 75 to 125 kVp and tube current from 150 to 692 mAs; angular rotation, 220°; projections per rotation, 235; and scan time, 5 s/rotation.

Ungated C-arm CT data were acquired during a single spin for 5 s during normal sinus rhythm with aortic root (Method 1) or peripheral (Method 2) injection and during rapid ventricular pacing at approximately 200 beats per minute with aortic root injection (Method 3). Ungated 3D images with 0.4-mm isotropic spatial resolution were reconstructed using all of the data acquired at different angular positions (Figure 10-1A). ECG-gated C-arm CT data were obtained during 4 (2 forward and 2 backward) spins for 24 s during normal sinus rhythm with either aortic root (Method 4) or peripheral (Method 5) injection. ECG-gated 3D images with 0.4-mm isotropic spatial resolution were reconstructed from data acquired in approximately the same cardiac phase at different angular positions during the spins (Figure 10-1B). Additionally, a non-contrast, ungated C-arm CT image was acquired during normal sinus rhythm to obtain baseline attenuation values.

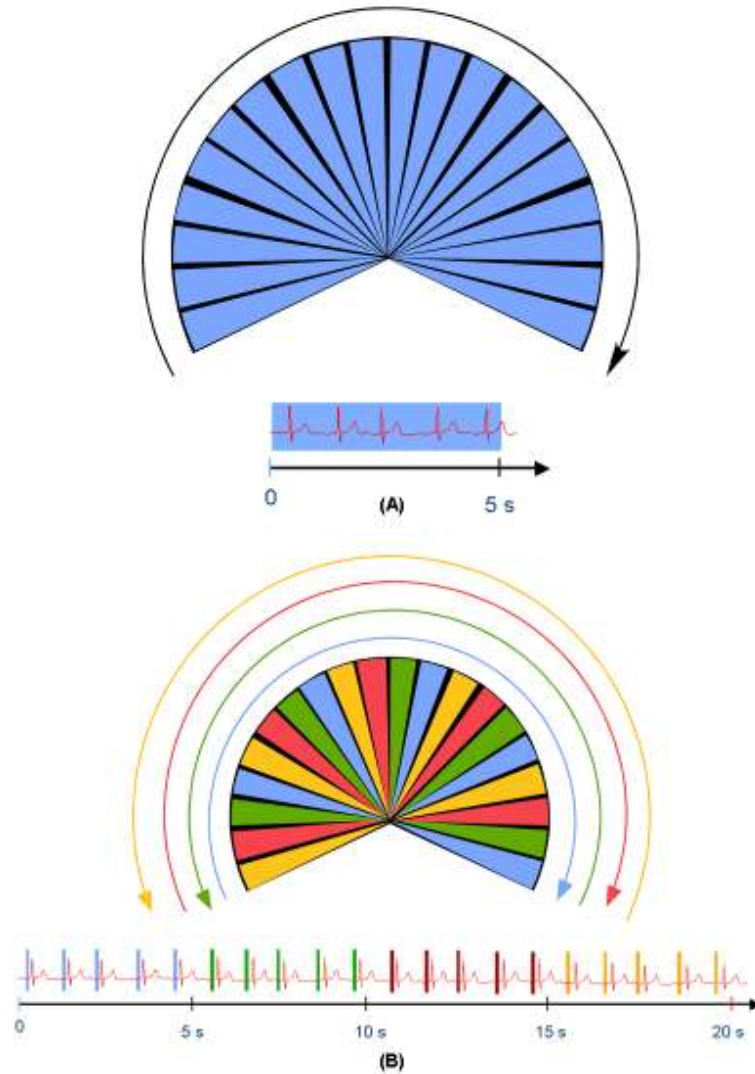


Figure 10-1: Ungated and ECG-gated C-arm CT Imaging. (A) Ungated C-arm computed tomography (CT) images reconstructed using data acquired continuously at different angular positions during a single 5-s spin. (B) Electrocardiogram (ECG)-gated C-arm CT images reconstructed from data acquired in approximately the same cardiac phase at different angular positions during 4 spins (represented by blue, green, red, and yellow) for 24-s.

Based on our previous experience [200], we injected contrast (Ultravist 370 mgI/mL) alone or mixed with saline but did not follow this injection with a saline flush. Contrast was administered to each animal via a peripheral vein with an 18-gauge needle or through direct injection into the aortic root with a standard 6-F pigtail catheter (Table 10.1). The time between the start of injection and the start of the C-arm CT scan (scan delay) was determined based on the injection site.

For ungated C-arm CT with aortic root injections (Methods 1 and 3), a total injection volume (contrast and saline) of 65 to 90 mL was administered at 10 to 15 mL/s, and images were acquired 1 to 2 s after the start of injection. For ungated C-arm CT with peripheral injection (Method 2), an undiluted contrast volume of 50 to 65 mL was injected at 6 to 7 mL/s, and the scan delay obtained from MDCT was decreased by 2 to 4 s to account for the higher flow rates (6-7 mL/s with C-arm CT vs 5 mL/s with MDCT). ECG-gated C-arm CT was acquired by administering 120 to 145 mL of contrast at 4 to 6 mL/s for 22 to 30 s either in the aortic root (Method 4) or via peripheral vein (Method 5). While 1-2 s scan delay was used for aortic root injections, the scan delay for peripheral injection was adjusted by decreasing/increasing the scan delay from MDCT as the flow rate with C-arm CT was increased/decreased in comparison to MDCT (Table 10.1) to allow sufficient time for contrast to travel from the peripheral vein to the heart [115].

Parameter	ECG-gated MDCT		ECG-gated C-arm CT		Ungated C-arm CT	
	Peripheral		Peripheral	Aortic root	Peripheral	Aortic root
Injection site						
Iodine concentration, mgI/mL	370		370	370	370	370
Total volume (contrast and saline mixture), mL	75-80		120-145	120-145	50-65	65-90
Flow rate, mL/s	5		4-6	4-6	6-7	10-15
Injection duration, s	15-16		22-30	22-30	7-9	6-7
Scan delay, s	18-26		16-28	1-2	16-22	1-2
Cardiac rhythm during imaging	Normal sinus rhythm		Normal sinus rhythm	Rapid pacing	Normal sinus rhythm	Normal sinus rhythm

Table 10.1: Contrast Injection Parameters and Cardiac Rhythm Status During ECG-gated MDCT and ECG-gated and Ungated C-arm CT Imaging.

10.2.2.2 TAVI procedure

3D MDCT images were overlaid onto 2D real-time fluoroscopy images for catheter guidance and placement of prosthetic valve during TAVI procedure. The registration of 3D MDCT images with 2D fluoroscopic images was performed using the C-arm CT images in multiple steps. First, the MDCT images acquired before TAVI were loaded into a software application (syngo InSpace, syngo X Workplace, Siemens Healthcare) to mark the AN and coronary ostia. Second, the 3D images from MDCT and C-arm CT were registered using an automatic, intensity-based registration algorithm (syngo 3D Fusion, syngo X Workplace, Siemens Healthcare). This algorithm evaluates the common characteristics between the two 3D sets and iteratively matches them based on intensity data to enable registration. Manual corrections were made when necessary to fit the image sets accurately using anatomic features or the catheter placed in the aortic root. Finally, information from image registration of the preprocedural MDCT and pre-TAVI C-arm CT were used to overlay the previously marked structures from MDCT (AN and coronary ostia) onto the real-time fluoroscopic images for guidance in placing the valve prosthesis.

10.2.2.3 Post-TAVI

The imaging protocol post-TAVI included only a single scan. The animals were scanned once with ungated C-arm CT imaging during normal sinus rhythm using aortic root injection (Method 1).

10.2.3 Image Analysis

10.2.3.1 Pre-TAVI

All contrast-enhanced MDCT and C-arm CT images acquired pre-TAVI were assessed for aortic root opacification, presence of artifacts, visibility and measurements of aortic root structures.

Aortic root opacification was evaluated quantitatively by measuring attenuation values at the level of the aortic root in all contrast-enhanced images. In addition, measurements were performed at approximately the same location in non-contrast C-arm CT images to obtain a baseline value (attenuation in the absence of contrast). Aortic root opacification was deemed sufficient in MDCT images when the attenuation measurement was greater than 250 HU. In C-arm CT images, aortic opacification was deemed sufficient when attenuation values in contrast-enhanced images were significantly higher than the baseline. However, we could not compare the attenuation measurements from C-arm CT with those from MDCT because of the different x-ray tube voltages employed in the scans: although the tube voltage is constant during a MDCT scan, the voltage varies during a C-arm CT scan.

Images were evaluated for the presence of artifacts arising from motion and/or beam hardening using a 4-point grading scale: 1 = no artifacts, with clear visibility of all aortic root structures (coronary cusps and coronary ostia); 2 = mild artifacts not interfering with visibility of aortic root structures; 3 = moderate artifacts preventing visibility of some aortic root structures; and 4 = severe artifacts impeding visibility of all aortic root structures.

The contrast-enhanced C-arm CT and MDCT images were assessed for anatomic landmarks critical for device placement and success during TAVI, including the aortic annulus (AN), sinus of Valsalva (SOV), sinotubular junction (STJ), and mid-ascending aorta (mid-AA). The number of visible coronary cusps and coronary ostia was quantified, and the images were evaluated for the presence and orientation of aortic valve calcifications. From reformatted sagittal and axial C-arm CT images, we measured the mean AN diameter (average of the minimum and maximum diameters) and the diameters of the SOV, STJ, and mid-AA, as described elsewhere [71]; these results were compared with those obtained from MDCT.

Contrast volumes used for the various C-arm CT methods were compared. The imaging method using minimal contrast volume, resulting in images with the highest attenuation measurement and lowest artifact score, and leading to measurements of aortic root structures similar to those obtained with MDCT was considered the optimal method.

MDCT images were used to predict the orientation of the aortic root relative to the body axis in X-ray angiographic projection angles perpendicular to the valve plane [10, 68, 201, 202]. The images were reformatted to a double-oblique view to correspond to X-ray angiographic images, and the angiographic projections (left anterior oblique [LAO]/right anterior oblique [RAO] and cranial/caudal) were displayed. The cranial/caudal angulations for the standard LAO 40, LAO 0, and RAO 20 angiographic projections and the LAO angulation for cranial/caudal 0 were noted [10, 68]. Similar analysis was performed for the optimal C-arm CT images to predict optimal angiographic projection angles; these results were compared with those from MDCT.

10.2.3.2 Post-TAVI

C-arm CT images acquired after TAVI were reviewed to evaluate the valve prosthesis implantation and to measure the diameters of the stent, STJ, and mid-AA and the vertical distance of the stent from the left coronary ostia.

Statistical analysis: One-way analysis of variance (ANOVA) was used to test for statistically significant differences in attenuation values among the C-arm CT methods including the non-contrast C-arm CT; artifact scores and contrast volumes among the C-arm CT methods; and pre-TAVI measurements among the C-arm CT methods and MDCT. If a significant difference was found, the Tukey test was used to make pairwise comparisons between image sets. Once the optimal C-arm CT method was determined, Bland-Altman analysis was used to assess the mean difference, 95% confidence interval, and limits of agreement between this method and MDCT for obtaining pre-TAVI diameters. A paired Student *t* test was used to compare optimal angiographic projections obtained from the optimal C-arm CT method with those obtained from MDCT. All statistical analyses were performed using StatGuideTM (version 13.32, Minitab[®] Statistical Software, State College, PA) and a *p* value <0.05 was considered statistically significant.

10.3 Results

10.3.1 Pre-TAVI

MDCT and C-arm CT scans were successfully performed in all subjects. ECG-gated helical MDCT imaging during normal sinus rhythm with peripheral contrast injection resulted in images with sufficient aortic root opacification (mean attenuation >250 HU) and without any artifacts (mean artifact score = 1.0) and served as the

reference standard (Table 10.2, Figure 10-2). C-arm CT Method 2 (ungated acquisition, sinus rhythm, peripheral injection) resulted in nonevaluable images, as the contrast bolus was missed in the aortic root during imaging. Hence, these images were removed from further analysis.

C-arm CT protocols: Ungated C-arm CT images acquired without contrast injection resulted in a baseline root attenuation value of 86 ± 10 . Mean attenuation measurements in C-arm CT images from Methods 1, 3, 4, and 5 were significantly above the baseline value, and aortic root enhancement was deemed sufficient in these images (ANOVA test, $p < 0.05$). However, the mean attenuation values among the contrast-enhanced C-arm CT protocols were not significantly different (Table 10.2; Tukey test, $p > 0.05$).

Artifact scores for Methods 1 and 4 indicated moderate artifacts, whereas scores from Methods 3 and 5 suggested only mild artifacts (Table 10.2, Figure 10-2). However, no significant differences were shown for artifact scores within the various C-arm CT protocols (Table 10.2; ANOVA test, $p > 0.05$).

The AN, SOV, STJ, and mid-AA were visible in all evaluated C-arm CT images. Out of 12 coronary ostia identified with MDCT, 2, 11, 8 and 12 were visible in C-arm CT images with Methods 1, 3, 4, and 5, respectively (Table 10.2). Out of 18 coronary cusps identified with MDCT, 16, 18, 15, and 18 were observed in C-arm CT images with Methods 1, 3, 4, and 5, respectively (Table 10.2). Calcification was not observed in the valves; hence, valve calcifications could not be evaluated.

Parameter	MDCT	C-arm CT			
		Method 1	Method 3	Method 4	Method 5
ECG gating	Yes	No	No	Yes	Yes
Cardiac rhythm status	Normal sinus rhythm	Normal sinus rhythm	Rapid pacing	Normal sinus rhythm	Normal sinus rhythm
Injection site	Peripheral	Aortic root	Aortic root	Aortic root	Peripheral
Aortic root opacification	523 ± 172 HU	1,168 ± 341	1,226 ± 216	1,005 ± 229	599 ± 222
Artifact score	1.0 ± 0	2.6 ± 0.5	2.0 ± 0.6	3.0 ± 0.8	2.2 ± 0.4
Visibility of coronary ostia	12/12	2/12	11/12	8/12	12/12
Visibility of coronary cusps	18/18	16/18	18/18	15/18	18/18

Table 10.2: Analysis of Images Obtained From ECG-gated MDCT and C-arm CT Methods. Data are expressed as mean ± SD.

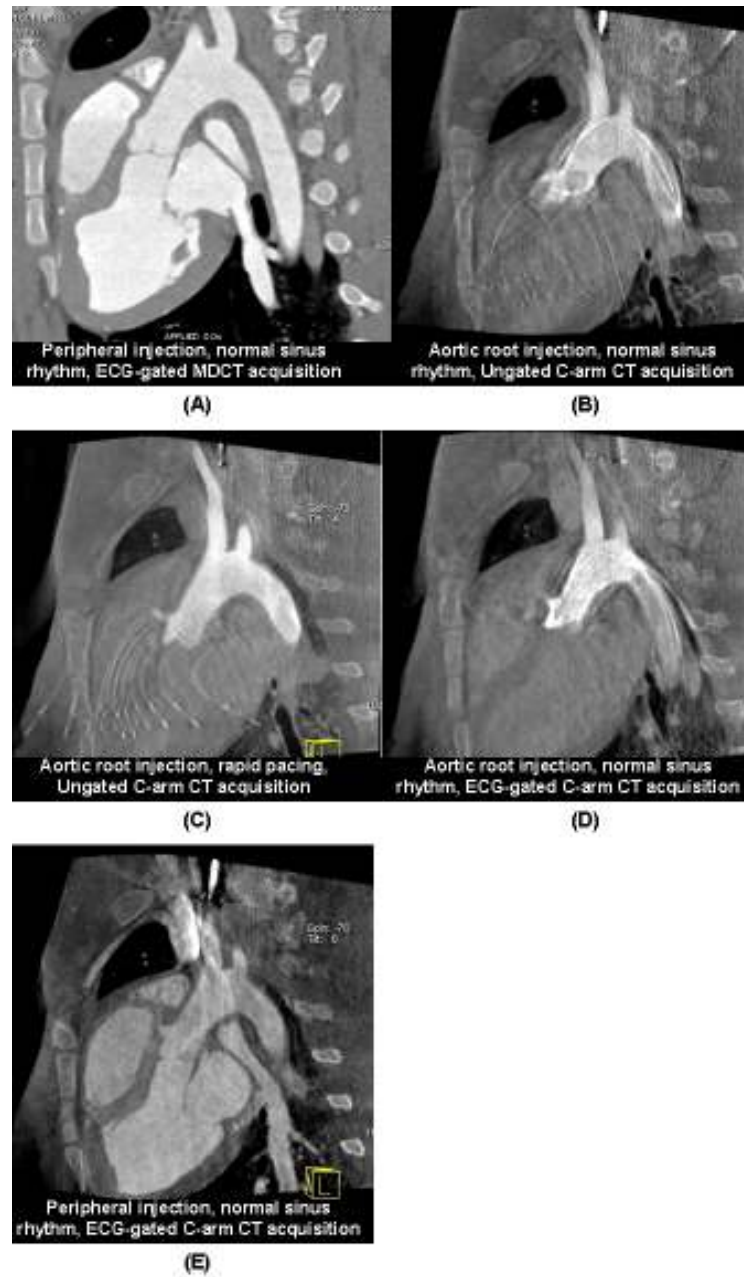


Figure 10-2: Sagittal Images Obtained From MDCT and C-arm CT Methods. (A) Multidetector row computed tomography (MDCT) image acquired with peripheral injection showing no artifacts. C-arm CT image acquired from (B) Method 1 showing moderate artifacts, (C) Method 3 showing mild artifacts, (D) Method 4 showing moderate artifacts, and (E) Method 5 showing mild artifacts.

In axial images reconstructed along the centerline from C-arm CT acquisitions obtained with aortic root injections, measurement of the AN diameter was limited, secondary to lack of contrast opacification below the valve (Figure 10-3). However, it was possible to measure the annulus in sagittal images (Figure 10-4).

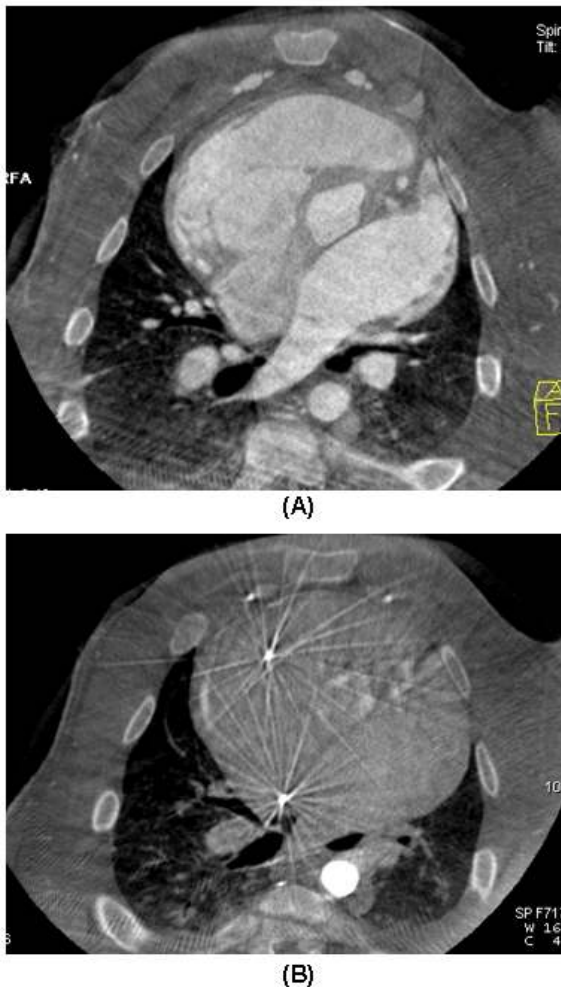


Figure 10-3: Comparison of Axial C-arm CT Images at the Level of the Aortic Annulus
Images obtained using (A) electrocardiogram (ECG)-gated C-arm computed tomography (CT) with peripheral injection and (B) ungated C-arm CT with aortic root injection. Aortic root contrast injection resulted in lack of opacification below the valve.

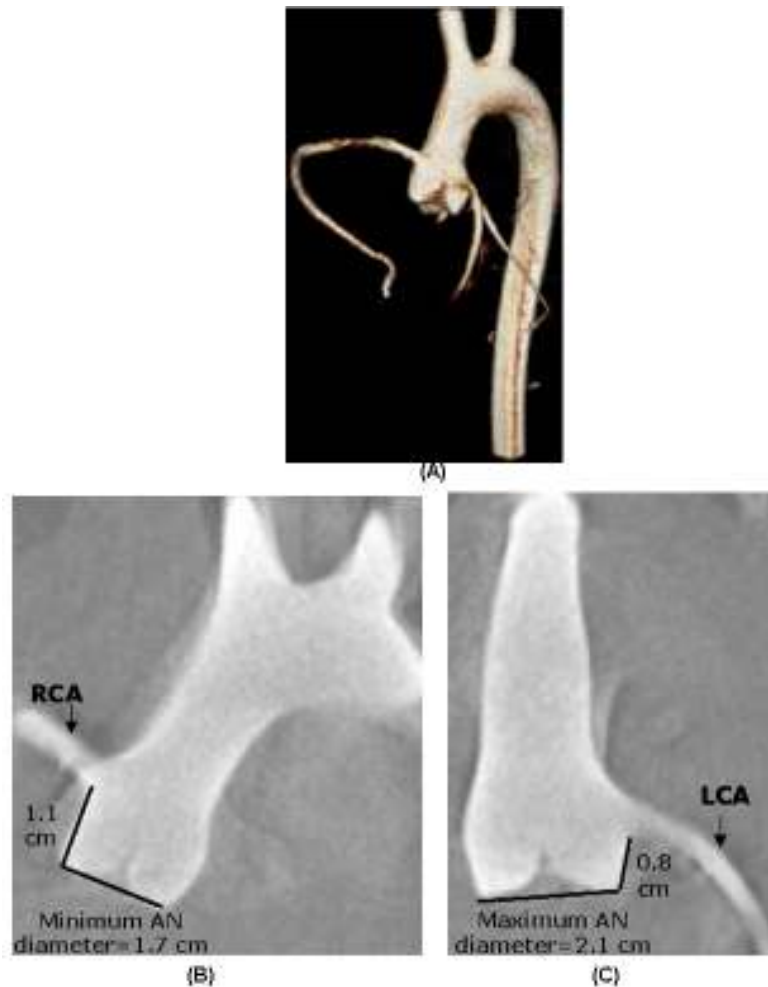


Figure 10-4: Images From Ungated C-arm CT During Rapid Pacing With Aortic Root Injection. (A) Volume-rendered computed tomography (CT) image of aortic root showing the coronary arteries. Multiplanar reformatted images of well-enhanced aortic root showing (B) vertical distance from aortic annulus (AN) to right coronary artery (RCA) along with minimum AN diameter, and (C) distance from AN to left coronary artery (LCA) along with maximum AN diameter.

Mean diameters of AN, STJ, and mid-AA measured with MDCT and C-arm CT methods were not significantly different (Table 10.3). However, the SOV diameter measured with ungated C-arm CT during normal sinus rhythm with aortic root injection

(Method 1) was significantly smaller (Tukey test, $p < 0.05$) than the diameter seen with MDCT and with the other C-arm CT protocols (Table 10.3).

Parameter	MDCT	C-arm CT			
		Method 1	Method 3	Method 4	Method 5
Average aortic annulus diameter, cm	2.1	2.1	2.0	2.1	2.1
Sinus of Valsalva diameter, cm	2.6*	2.1*	2.5	2.5	2.5
Sinotubular junction diameter, cm	2.0	2.1	1.8	1.8	1.8
Mid-ascending aorta diameter, cm	2.1	2.1	1.9	1.9	1.9
* indicates $p < 0.05$ using paired Tukey test.					

Table 10.3: Pre-TAVI aortic root measurements From MDCT Reference Images and C-arm CT Images.

On average, ungated C-arm CT imaging required significantly lower contrast volumes for aortic root injections (36 and 50 mL at 13 mL/s with Methods 3 and 1 respectively) in the study versus ECG-gated C-arm CT imaging with both peripheral and aortic root injections (133 and 135 mL at 5 mL/s with Methods 5 and 4 respectively) (Table 10.4; Tukey test, $p < 0.05$).

Parameter	Method 1	Method 3	Method 4	Method 5
Total injection volume, mL	85 ± 11	80 ± 10	135 ± 22	133 ± 24
Contrast volume, mL	50 ± 15	36 ± 13	135 ± 22	133 ± 24
Saline volume, mL	35 ± 14	44 ± 17	0 ± 0	0 ± 0
Injection flow rate, mL/s	13 ± 2	13 ± 2	5 ± 1	5 ± 1
Injection duration, s	6 ± 0	7 ± 1	27 ± 3	27 ± 3
Data are expressed as mean ± SD				

Table 10.4: Total injection volume, contrast volume, saline volume, and injection flow rate for C-arm CT methods.

Optimal C-arm CT protocol: Ungated C-arm acquisitions during rapid pacing with aortic root injection (Method 3) employed minimum contrast volume (36 mL), resulted in images with the highest attenuation value (1,226) and the lowest artifact score (2.0), and demonstrated image measurements similar to those from MDCT. The average differences of the pre-TAVI root diameters between MDCT and optimal C-arm CT lie within the Bland-Altman limits of agreement (Table 10.5). Further, there is no relationship between the average difference between the two methods and the mean pre-TAVI root measurements. These results indicate that C-arm CT Method 3 can be used to obtain pre-TAVI diameters similar to MDCT. The angiographic projections (cranial angulations for the standard LAO 40, LAO 0 and RAO 20 as well as LAO angiogram

corresponding to cranial/caudal 0 angulation) from MDCT and optimal C-arm CT were not significantly different (Table 10.5; Student t-test, $p>0.5$).

Pre-TAVI measurements			
Root measurement	Average difference	CI	Limits of agreement
AN (cm)	-0.12 ± 0.12	(0.25, 0.01)	(-0.37, 0.13)
SOV (cm)	-0.08 ± 0.14	(0.23, 0.06)	(-0.34, 0.19)
STJ (cm)	-0.17 ± 0.21	(0.72, 0.39)	(-0.59, 0.27)
mid-AA (cm)	-0.2 ± 0.22	(0.79, 0.39)	(-0.67, 0.26)
Optimal Angiographic Projections			
Projection	MDCT	Optimal C-arm CT	
LAO 40	16 ± 7	16 ± 6	
LAO 0	20 ± 7	18 ± 5	
RAO 20	18 ± 6	16 ± 4	
Cranial/caudal 0	94 ± 7	99 ± 17	
Note: Pre-TAVI measurements from MDCT and C-arm CT method were compared using Bland-Altman analysis. Average difference are expressed as mean ± SD, CI refers to the 95% confidence intervals for mean difference, and limits of agreement refer to the Bland-Altman limits. Optimal angiographic projections were compared between MDCT and optimal C-arm CT method using paired Student t-test.			

Table 10.5: Comparison of aortic root diameters and angiographic projections from optimal C-arm CT (Method 3) with MDCT.

10.3.2 TAVI Procedure

Registration of 3D MDCT with 2D fluoroscopic images for intraprocedural guidance during TAVI was successful. The TAVI procedure was performed using a transfemoral approach in the swine. The AN and coronary ostia marked on original MDCT images were also observed on 3D registered images from MDCT and C-arm CT. The identified regions of interest from MDCT were then overlaid on the 2D fluoroscopic images and were used to accurately place the valve prosthesis within the AN while avoiding the coronary ostia (Figure 10-5).

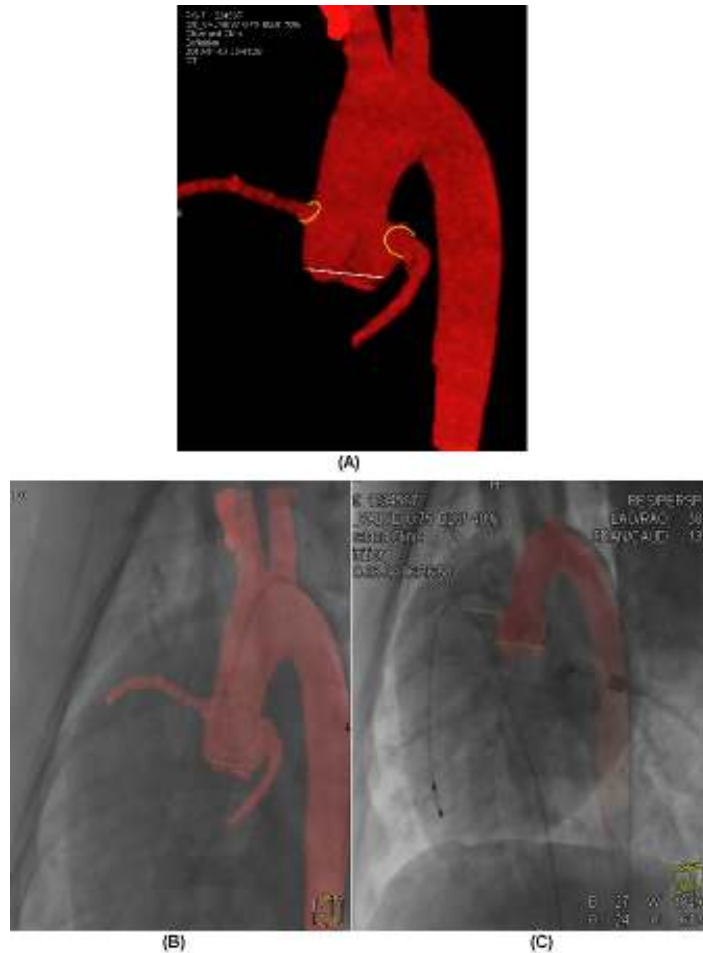


Figure 10-5: Images from MDCT Fused With Fluoroscopy. (A) 3-dimensional (3D) multidetector row computed tomography (MDCT) image with coronary ostia (yellow

lines) and aortic annulus (AN) (white line) marked. (B) Overlay of 3D MDCT images on 2-dimensional (2D) fluoroscopy image showing the catheter in the aortic root. (C) 2D image with contrast injected in the aortic root showing the AN and coronary arteries.

10.3.3 Post-TAVI

Ungated C-arm CT imaging during normal sinus rhythm using aortic root injection was successfully performed. The resulting images were evaluable with sufficient enhancement but with moderate artifacts. Ungated C-arm CT images obtained after TAVI clearly showed the valve prosthesis after implantation (Figure 10-6).

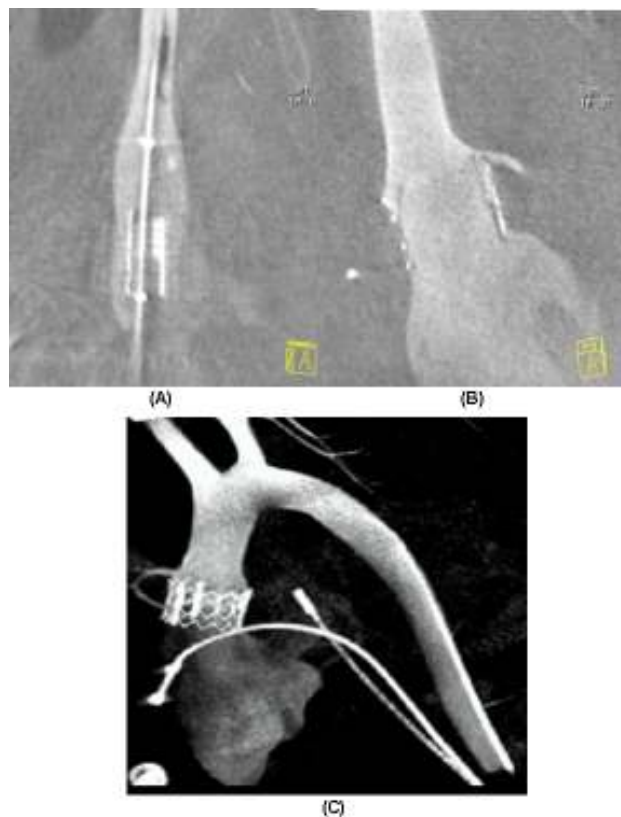


Figure 10-6: Images From Ungated C-arm CT. (A) Multiplanar reformat (MPR) C-arm CT image showing the valve and catheter before valve deployment. (B) MPR image

showing the placement of the valve without any coronary occlusions. (C) Volume-rendered image showing the valve after deployment.

The STJ and mid-AA were clearly visible in all images (average diameter, 1.8 and 1.6 cm, respectively). The mean diameter of the stent and vertical distance of the stent from the ostia were 2.2 cm and 1.6 cm, respectively.

10.4 Discussion

Our systematic comparison of contrast injection and scan acquisition protocols with C-arm CT in a swine model of TAVI demonstrated that ungated C-arm CT during rapid ventricular pacing with aortic root injection provides the optimal combination of minimal contrast, good aortic root visualization, mild artifacts, and aortic root measurements that correlate closely with those obtained by MDCT. Without rapid pacing, ungated C-arm CT imaging with aortic root injection during native sinus rhythm resulted in sufficient aortic root enhancement but was associated with moderate artifacts; gated protocols required increased contrast injection.

For patients undergoing TAVI, the optimal periprocedural imaging approach, including 3D imaging with MDCT and 3D echocardiography, is still evolving [11, 191-193]. Recently C-arm CT has also shown promise in this setting. The ability of this modality to characterize and localize valve calcifications, identify coronary ostia, and define relationships between coronary ostia and aortic leaflets may allow this technique to complement traditional 2D projection images in the catheterization lab. However, imaging protocols for this procedure have not been standardized. An imaging protocol that is effective for intraprocedural application must produce good visualization of the

aortic root with minimal contrast and reasonable radiation exposure, factors that are affected by the timing and location of contrast injection (central versus peripheral injection), acquisition protocol (ECG-gated versus ungated acquisition), and heart rate during acquisition (normal sinus rhythm versus rapid gating).

In this study, we found that an ungated C-arm CT during rapid pacing with aortic root injection could produce 3D “CT like” images with aortic root measurements similar to those seen with MDCT while using approximately the same amount of contrast as is used with conventional 2D root angiography [203]. This protocol could potentially replace preprocedural CT scans in patients with impaired renal function, for whom an imaging strategy with minimal contrast exposure is critical. Similar approaches have been described for imaging of the pelvic arteries in this population [204].

The advantage of C-arm CT lies in its ability to perform 3D acquisition in the catheterization laboratory and to integrate these 3D images directly with 2D fluoroscopic images during TAVI, allowing for accurate definition of the aortic valve plane for catheter guidance. Further, C-arm CT facilitated the registration of preprocedural 3D MDCT images with 2D fluoroscopy images during TAVI allowing accurate definition of the aortic valve plane for catheter guidance and precise placement of the valve in the plane using the transfemoral approach without occluding coronary ostia. Finally, C-arm CT images acquired post-TAVI allowed viewing of the prosthetic valve and measurement of the diameters of the stent, STJ, and mid-AA as well as the vertical distance of the stent from the left coronary ostia to ensure placement of the valve away from coronary ostia. Alternatively, C-arm CT can also be registered with preprocedural MDCT images, with critical structures marked to facilitate overlay of the MDCT images

onto the real-time fluoroscopic images for procedural guidance; this technique has recently been described in the context of TAVI [199]. Such an approach combines better soft tissue characterization from MDCT with angiography images (Figure 10-5). C-arm CT images acquired after TAVI may also allow clinicians to assess the prosthetic valve and to measure the diameters of the stent, STJ, and mid-AA as well as the vertical distance of the stent from the left coronary ostia to ensure placement of the valve away from coronary ostia (Figure 10-6).

10.4.1 Limitations

Our study is limited by its small sample size. While a recent report in human subjects used a contrast volume similar to the volume we used in Method 3 to obtain 3D C-arm CT images of the aortic root geometry [170], the applicability of our results in human subjects requires further evaluation. The swine examined in our study also did not have aortic valve calcification, which is typically seen in human patients.

In our study ungated C-arm CT acquisitions with peripheral injection (Method 2) did not provide diagnostic images, because the contrast bolus was missed during imaging. One solution may be to use a test bolus (10-20 mL) before the ungated C-arm CT scan and monitor the aortic root with low-dose fluoroscopy to estimate the transit time of contrast. The main bolus of contrast could then be injected and an ungated C-arm CT acquisition performed after the observed transit time. However, this would require an additional amount of contrast and radiation dose for the test injection and fluoroscopic scan.

In current clinical practice, repeated fluoroscopy and TEE image acquisitions are performed during the actual implantation of the valve in order to assure precise positioning. We examined feasibility and optimal acquisition protocols for C-arm CT at the time of the TAVI procedure, but prior to the actual implantation of the valve. C-arm CT acquisition during valve deployment may not be feasible, mainly because repeated imaging is limited by contrast and radiation exposure

Measuring the radiation exposure from C-arm CT is complex and only partially understood. Therefore the radiation dose resulting from the ungated and ECG-gated C-arm CT acquisitions in our study could not be described. Nevertheless, the radiation dose for ungated C-arm CT should be lower than that for ECG-gated C-arm CT because of the decreased scan time with ungated scan. Studies measuring the radiation dose for TAVI procedures with and without ungated C-arm CT imaging are needed to demonstrate whether the addition of these imaging procedures is justified by improved outcomes.

10.5 Conclusion

Ungated C-arm CT during rapid pacing with aortic root injection results in sufficient aortic root enhancement for identification of the coronary ostia and measurement of the aortic root diameters with a low contrast volume and minimal artifacts. The 3D C-arm CT images allow valve plane evaluation and aortic root measurements before TAVI, overlay of MDCT images onto 2D fluoroscopic images for guidance of valve placement during TAVI, and assessment of valve positioning after TAVI. These results, obtained in an animal model, provide guidance for future evaluation in clinical scenarios.

CHAPTER XI

DOSE ASSESSMENT WITH C-ARM CT

C-arm is increasingly used to acquire 3D C-arm computed tomography (C-arm CT) images for interventions in the cardiac catheterization lab. However, there is no standard approach to estimate the resulting radiation dose. In this chapter, the development of a methodology to obtain a C-arm CT dose metric to estimate the radiation burden with 3D C-arm acquisition is explained.

11.1 Introduction

Recently, 3D C-arm computed tomography (CT) is increasingly used in the cardiac catheterization laboratory to acquired 3D “CT like” images for procedural guidance [171, 199, 205]. C-arm CT images are obtained by rotating interventional C-arm systems mounted with flat panel detectors around the patient over a circular range of greater than 180° [104, 171]. A series of 2D projection images are acquired during the spin and 3D cone-beam algorithms are employed to reconstruct 3D images. The C-arm CT images can be used directly or registered with multidetector row CT (MDCT) images

to allow integration of 3D images with 2D real-time fluoroscopy images for procedural guidance [121, 195, 199]. However, this additional procedure results in a cost of increased radiation dose burden. Therefore, it is crucial to estimate dose to justify the addition of C-arm CT imaging during interventional procedure.

As the C-arm systems are routinely used for 2D angiography, they are equipped with dose-area product meters which estimate risk to skin exposure. Currently, these scanners do not provide any metrics which estimates dose due to the 3D acquisition. Standard CT dose index (CTDI₁₀₀) obtained using a 150 mm length phantom and 100 mm ionization chamber can be used as a dose descriptor.

$$\text{CTDI}_{100} = \frac{1}{C_z} \int_{-50\text{mm}}^{+50\text{mm}} D(z) dz \quad (11-1)$$

where C_z is the collimation of the x-ray beam used. However, recent studies showed that CTDI₁₀₀ index may not be accurate for larger collimation MDCT scanners as the maximum nominal beam width is greater than the length of the regular dose phantom and standard integration length [172, 174, 176, 206, 207]. As C-arm CT systems have a collimation of 200 mm at isocenter, the standard measuring equipment will underestimate dose. It is also essential to estimate the necessary phantom and integration length in order to measure dose integral profile from the enlarged beam. Kyriakou et al performed Monte Carlo simulations and determined that phantoms and integration lengths of 600 mm or greater are required to measure the entire dose profiles including scatter tails of the wide beam to approximate CTDI within 1% [208]. However, the availability of such long ionization chambers is limited. Hence, the purpose of the study is to determine sufficient

phantom and integration length for C-arm CT imaging and develop a methodology to obtain a metric for dose estimation in patients.

11.2 Materials and Methods

11.2.1 C-arm CT System

All phantom measurements were performed on a C-arm system (Axiom Artis, Siemens Medical Solutions, Forchheim, Germany) equipped with a 40 x 30 cm² flat panel detector. The system uses a fan angle of 19°, cone angle of 14.25°, angular rotation of 200° and collimation of 200 mm in the z-direction to acquire images. Measurements were performed by using automatic exposure control (AEC), which modulates x-ray exposure according to detector entrance dose (DED) in two steps: first by increasing the tube-current time product; second by increasing tube voltage in order to maintain the noise levels as specified by the dose at the detector [103]. Dose measurements were performed for two non-electrocardiogram-gated (ungated) cardiac C-arm CT protocols (Table 11.1).

Parameters	Protocol	
	5sDRUngated	5sDRC
Pulse width (ms)	5.0	12.5
Focus	Large	Small
Frames/s	60	30
Number of projections or frames	248	133

Table 11.1: X-ray imaging parameters used for ungated C-arm CT scan.

11.2.2 Phantom Imaging

Polymethyl methacrylate (PMMA) phantoms with 470 mm lengths and 300 mm diameter were used to make body measurements. The phantoms consist of five holes, one center and four peripheral locations, with 1 cm diameter for inserting acrylic inserts. As the C-arm system employs AEC, tube voltage may be modulated in each projection during a 3D acquisition.

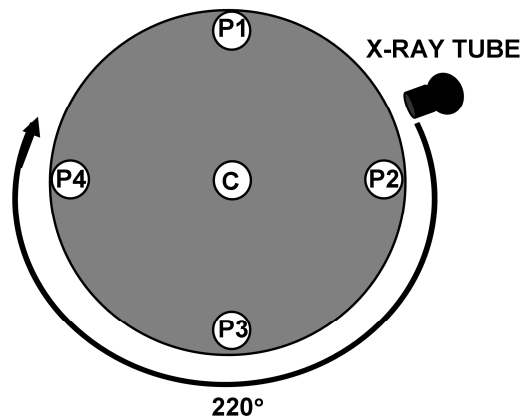


Figure 11-1: Schematic showing the center and periphery locations in a PMMA phantom.

First, in order to obtain dose measurements at constant voltage, phantom measurements were performed to find the highest possible system entrance dose required to maintain constant tube voltage during the entire scan duration. Phantom measurements were performed with different entrance dose values on a 470 mm body phantom at 90, 96, 102, 109, 117, 125 kVp, which are available to be set manually at the scanner. The entrance dose detector was modified till constant tube voltage was seen in all the projections throughout the scan, and the remaining phantom experiments were performed using this value as DED setting.

Second, dose profile measurements were performed with thermoluminescent dosimeters (TLDs) placed in a customized holder of 300 mm length placed at center and four periphery phantom locations in both the 320 and 470 mm phantoms. Dose profiles were measured for every 1 mm for 70 mm at the center and for every 10 mm for the remaining length using the two ungated C-arm CT protocols at 125 kVp. Dose profile measurements were performed to examine dependence on the phantom length. Peak dose values obtained from 320 mm phantom were normalized with those from 470 mm phantom to examine the impact of phantom length of peak dose values.

$$\text{Normalized Peak Dose} = \frac{\text{Peak Dose}_{320}}{\text{Peak Dose}_{470}} \quad (11-2)$$

Assuming phantom length of 900 mm and integration length of 300 mm are required to include complete scatter radiation tails from the 200 mm collimation of C-arm CT, a Savitzky-Golay filter was applied to the measured data and dose profiles were simulated for phantom length of 900 mm. Dose was calculated as area under dose profile curve (AUC) of 470 mm ($AUC_{470\text{-measured}}$) and 900 mm ($AUC_{900\text{-simulated}}$) phantoms and the ratio was calculated as:

$$k = \frac{AUC_{470\text{-measured}}}{AUC_{900\text{-simulated}}} \quad (11-3)$$

Phantom length of 470 mm and integration length of 300 mm were considered sufficient if $k \geq 95\%$.

Finally, dose profile integrals were measured using a 300 mm ionization chamber (Dosimax plus A HV, IBA Dosimetry GmbH, Schwarzenbruck, Germany). Imaging was performed with both the ungated C-arm CT protocols at the five locations of the 470 mm

body phantom at constant peak tube voltages (90, 96, 102, 109, 117, 125 kVp) to calculate CTDI₃₀₀ (scaled per 100 mAs) at each voltage.

$$\text{CTDI}_{300} = \frac{1}{C_z} \int_{-150\text{mm}}^{+150\text{mm}} D(z) dz \quad (11-4)$$

The central and peripheral CTDI₃₀₀ values were used to calculate the weighted-CTDI (CTDI_{w,300} scaled per 100 mAs, denoted as CTDI_w henceforth) at all tube voltages. A curve fit was applied to correlate CTDI_w with tube voltage and correlation coefficient (R²) was calculated.

$$\text{CTDI}_w = \frac{1}{3} \text{CTDI}_{c,300} + \frac{2}{3} \text{CTDI}_{p,300} \quad (11-5)$$

11.2.3 Patient Imaging

A total of 10 patient scans were performed using the ungated 5sDRC protocol employing AEC for automatic tube current-time product and tube voltage modulation. The DED dose was set to default value of 0.36 µG/pulse for patient scans. All scans were performed to register preoperative 3D MDCT images with 2D fluoroscopic images for navigating cardiovascular interventions. The power equation obtained from the dose integral phantom scans was used to estimate CTDI_w in these patients.

11.3 Results

Highest possible system entrance dose in order to maintain constant tube voltages were obtained (Table 11.2). The remaining phantom scans were performed using these entrance dose values for each tube voltage.

Tube Voltage (kVp)	Highest entrance dose ($\mu\text{G/pulse}$)
90	0.1
96	0.12
102	0.14
109	0.17
117	0.2
125	0.24

Table 11.2: Highest system entrance dose required to maintain corresponding tube voltage constant during the C-arm CT acquisition.

TLD dose profiles from the 470 mm phantom were obtained at center and all the periphery locations. Normalized peak dose values ranged from 0.97 to 0.99 indicating that peak dose value decreased less than 4% when a 320 mm phantom was used to perform dose measurements instead of a 470 mm phantom (Figure 11-2). Further, 3rd degree fit of the Savitzky-Golay filter was applied for the measured data points and k values of 98 % and $98 \pm 2\%$ were noted at center (Figure 11-3) and average of peripheral (Figure 11-4) locations. Hence, phantom length of 470 mm and integration length of 300 mm were determined sufficient for measuring the scatter tails of 200 mm collimation of C-arm system.

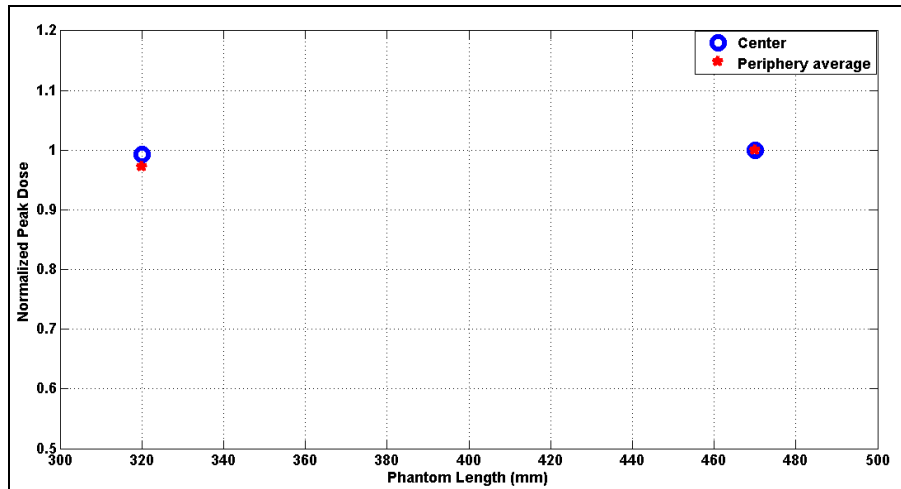


Figure 11-2: Normalized Peak Dose as a function of phantom length at center and periphery locations for the body phantom at 125 kVp. Peak dose did not vary by more than 3% when phantom length was increased from 320 to 470 mm either at the center or peripheral locations.

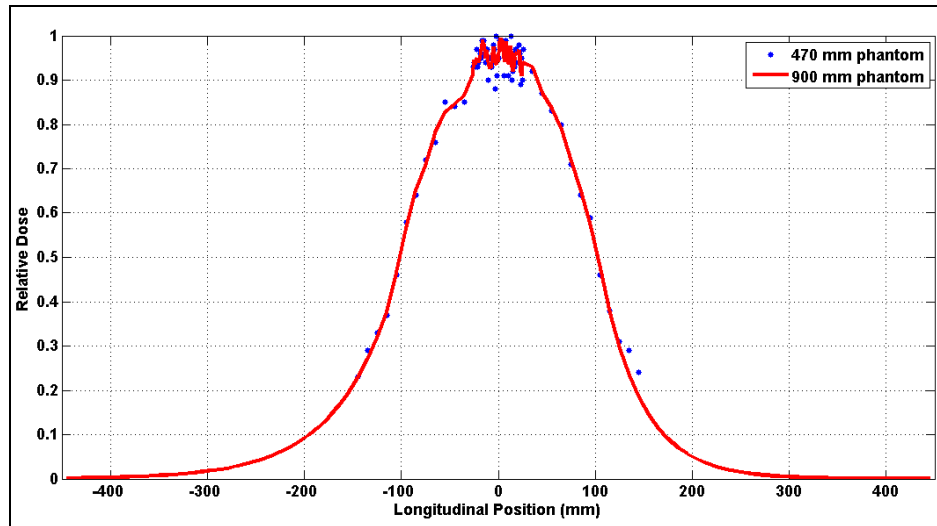


Figure 11-3: Longitudinal dose profiles using 300 mm TLDs in the body phantom at the center. Dose profiles are measured using 470 mm phantom and simulated using 900 mm phantom.

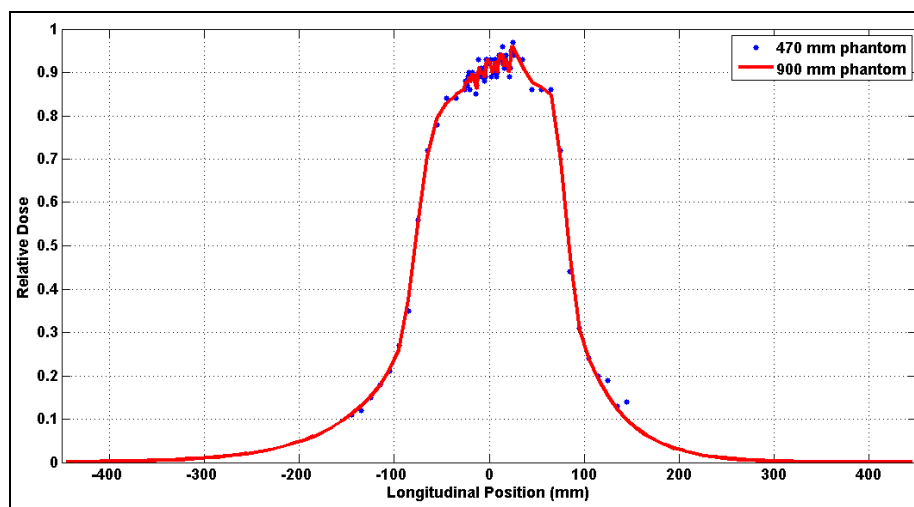


Figure 11-4: Longitudinal dose profiles using 300 mm TLDs in the body phantom at the periphery (average of four peripheral locations). Dose profiles are measured using 470 mm phantom and simulated using 900 mm phantom.

Dose profile integration values ($CTDI_w$) were obtained for the ungated C-arm CT protocols at different tube voltages (Table 11.3). Power equations correlating $CTDI_w$ and tube voltage was obtained for both the ungated C-arm CT protocols with $R^2 > 0.998$.

Tube Voltage (kVp)	$CTDI_w$ (mGy)	
	5sDRUngated	5sDRC
90	4.32	4.3
96	5.03	5.02
102	5.81	5.81
109	6.77	6.77
117	7.96	7.96
125	9.22	9.23

Table 11.3: $CTDI_w$ dose values measured at different tube voltages using 300 mm ionization chamber and 470 mm body phantom.

A total of 10 patient scans were imaged with the 5sDRC protocol with tube voltages ranging from 75-125 kVp. Application of the power equation (Figure 11-4) to patients yielded average CTDI_w of 5.48 ± 2.02 mGy.

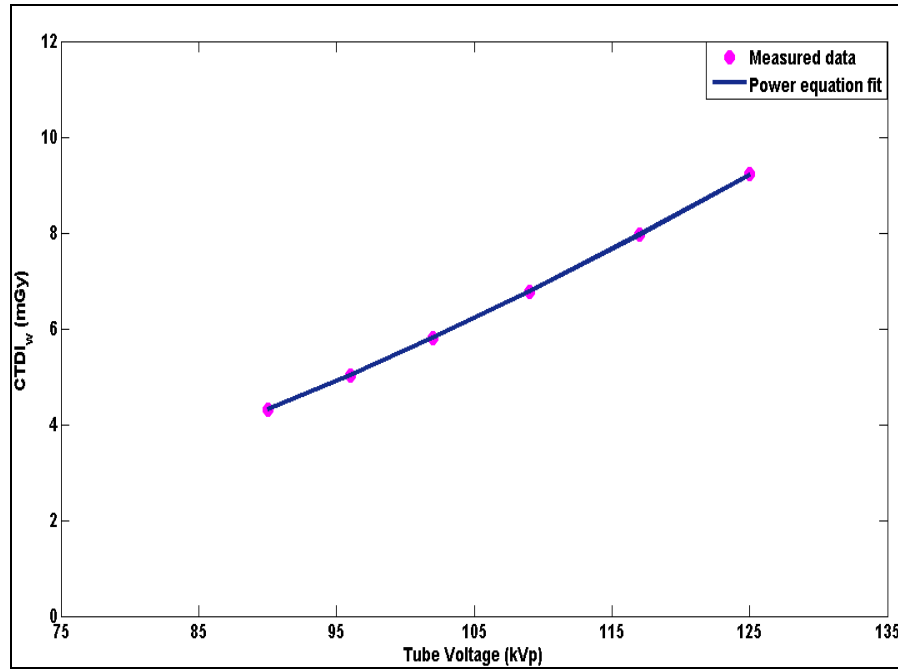


Figure 11-5: CTDI_w values calculated from weighted average of center and periphery locations for an ungated C-arm CT protocol. The power equation fit with correlation coefficient $R^2=0.99$ was used for calculating dose in patients.

11.4 Discussion

A procedure to obtain an appropriate C-arm CT dose metric in patients is required to demonstrate whether the addition of C-arm CT imaging is justified during interventional procedures. Using conventional 150 mm phantom and 100 mm integration length to calculate standard CTDI₁₀₀ underestimates dose for C-arm CT imaging due to inability to measure the direct and scatter radiation from the 200 mm collimation [172, 174, 176, 206, 207]. An approach to estimate CTDI that can be used for C-arm CT

imaging was developed in this study. Monte Carlo simulations were performed indicating that 600 mm of phantom and integration length are required to capture 99% of dose from scatter radiation [208]. However, phantom measurements supporting the observation have not been performed. Moreover, as tube voltage is modulated during a C-arm CT acquisition, care needs to be taken to estimate dose at constant tube voltage. Hence, the detector entrance dose was modified in our study in order to maintain constant tube voltage throughout the scan in our phantom experiments.

We also discuss the necessary phantom length and integration length for estimating dose with C-arm CT. Although phantom and ionization chamber of 600 mm length may be ideal, the availability of such phantoms and ionization chambers may be challenging. Multiple phantoms of same diameter can be combined to simulate a larger phantom; however a large chamber of 600 mm integration length is currently unavailable. Hence we utilized the largest commercially existing ionization chamber of 300 mm in our experiments.

The dose profile measurements showed that the peak radiation dose was underestimated by $<3\%$ with the use of a 320 mm phantom as compared to a 470 mm phantom. This indicates that the peak radiation dose did not vary significantly either at the center or periphery with change in phantom length. Hence, we assumed that peak dose values may not vary drastically for a change in phantom length beyond 470 mm phantom. Moreover, the area under curves of the dose profiles showed that 470 mm phantom estimated 98% of the dose at center and periphery locations as compared to simulated values from a 900 mm phantom. Hence, a phantom length of 470 mm and integration length of 300 mm may be sufficient to measure dose with C-arm CT. These

results are similar to the suggestions from Monte Carlo simulations showing that phantoms and integration lengths > 350 mm estimate the CTDI within a range of 5% as compared to CTDI measured with an infinite length of phantom and ionization chamber [208].

Phantom studies were performed using the determined necessary lengths to measure dose integral ($CTDI_w$) at a given set of tube voltages. A correlation to compute dose at any given tube voltage was developed and can be used to estimate radiation dose burden in patients imaged with the ungated cardiac C-arm CT protocol during interventional procedure. Dose estimates obtained for the C-arm CT protocol primarily used for registration during intervention was low (5.48 ± 2.02 mGy).

Currently, effective dose (ED) is considered as the most appropriate quantity for estimating the stochastic risk of exposure to ionizing radiation. Conversion factors to estimate dose from the CTDI values exist for MDCT imaging. However, these factors cannot be applied for C-arm CT imaging due to the partial rotation scanning resulting in inhomogeneous dose distribution as compared to MDCT. Hence, conversion factors to estimate ED are not yet available for C-arm CT.

Currently, the current use of CTDI is under discussion in the context of MDCT imaging. An alternative approach using a small chamber at the center of the phantom and scanning the entire length of phantom to measure dose profile integration or accumulated dose at the center is being proposed [209]. As there is no table translation with C-arm CT, this approach of measuring dose may not be feasible. C-arm CT imaging is similar to MDCT imaging with a large cone beam for acquiring data without any table movement [207]. A recent study by Lin et al employed a small solid state detector and moved it

linearly using a step motor over a length of 810 mm to measure the dose profile [210]. In these cases, a long ionization chamber as used in the current study can be used as an alternative. Dose measurements with greater than 300 mm length may have limitations for routine quality checks. Developing a methodology to estimate dose based on measurements from readily available 150 mm long phantoms and 100 mm ionization chambers may be pragmatic.

In conclusion, a 470 mm body phantom with 300 mm ionization chamber was sufficient to measure C-arm CT dose and develop a power equation for estimating $CTDI_w$ in patients based on applied tube voltage. Dose estimates for a C-arm CT protocol primarily used for registration during intervention was low.

CHAPTER XII

DISCUSSION AND CONCLUSION

Minimally invasive cardiovascular surgeries refer to techniques that minimize surgical trauma through smaller incisions as compared with a conventional sternotomy procedure, where the sternum is divided to access the heart and lungs. Minimally invasive cardiac surgeries represent a paradigm shift from traditional surgical techniques and have evolved as a safe and efficient treatment option with increased patient comfort and reduced complications [211, 212, 213]. Procedures ranging from coronary interventions to intracardiac interventions and including valve repair/replacement, graft placement, closure of leaks or defects are performed using smaller incisions with transcatheter approaches [191]. The aim of this thesis was to develop contrast and scan protocols for novel 3D x-ray based imaging techniques in the context of minimally invasive surgical procedures to improve preprocedural anatomical assessment, procedural guidance and postprocedural follow-up.

Transcatheter aortic valve implantation (TAVI) is a percutaneous valvular intervention procedure, and is considered a safe alternative in patients who are denied surgical valve replacement due to age, cardiovascular risk factors and comorbidities [41].

The success of TAVI relies heavily on using imaging for patient selection as well as visualization, guidance, and precise placement of valve during the procedure [214]. Typically, TAVI relies heavily on combined use of x-ray fluoroscopy with transesophageal echocardiography (TEE) or intracardiac echocardiography (ICE) for procedural guidance [60, 63, 191, 215]. However, these procedures display only a 2D image and do not provide 3D visualization. Currently, this additional anatomical information is obtained from preprocedural 3D MDCT images [10, 68, 216, 217]. 3D preprocedural MDCT images are required to characterize and localize calcifications in order to select appropriate patients for TAVI. It is also critical to understand the relationship between the coronary ostia and the aortic leaflets to prevent coronary occlusion. The 3D information routinely obtained from preprocedural MDCT has limited use directly in the cardiac catheterization lab primarily due to registration challenges between the 3D MDCT and 2D fluoroscopy images.

The modern C-arm fluoroscopy systems have the ability to acquire 3D “CT like” images in the catheterization lab during the procedure. The C-arm CT images can then be directly overlaid onto the real-time fluoroscopy images. Alternatively, 3D C-arm CT and MDCT images can be fused to facilitate display of the high contrast MDCT images on the 2D fluoroscopic images to facilitate catheter guidance and device positioning during TAVI. It is critical to obtain C-arm CT with sufficient contrast and image quality to allow overlay of either the C-arm CT or MDCT images.

Nolker et al [121] acquired C-arm CT images to compare crucial structures with MDCT and overlay the left atrium and pulmonary veins onto an electroanatomic mapping system for pulmonary vein isolation. Other studies have demonstrated the feasibility of

evaluating aortic anatomy in patients before endovascular aneurysm repair (EVAR) [218] and after EVAR to resolve endoleaks [122]. However, a systematic study exploring different C-arm CT imaging techniques and injection protocols to acquire optimal images for TAVI has not yet been performed.

As part of this thesis, feasibility of obtaining C-arm CT imaging in the context of TAVI was evaluated in a swine model. Various contrast and imaging protocols were systematically evaluated to obtain optimal scan and injection protocols for acquiring sufficient C-arm CT images. Ungated C-arm CT images acquired during rapid pacing with aortic root injection (36 mL contrast/44 mL saline mixture) were optimal for evaluation and measurement pre-TAVI. These images were employed to assess anatomy prior to placement of valve and resulted in measurements similar to those from currently used clinical standard MDCT images. Based on this study, for situations where rapid pacing cannot be performed, ungated C-arm CT imaging with aortic root injection during native sinus rhythm may be appropriate. With the ungated protocol sufficient aortic root enhancement was obtained using 50 mL of contrast, but moderate motion artifact was present. Study results also demonstrated C-arm CT images facilitate the fusion of preprocedural MDCT images with real-time 2D fluoroscopic images for intraprocedural guidance. Finally, it was shown that C-arm CT images can be acquired post-TAVI to evaluate the valve position and additionally provide diagnosis to avoid coronary occlusion complications. Although the presence of leaks after the procedure was not observed in this study, post-TAVI imaging may be useful for assessment of the location of paravalvular leaks.

The contrast and imaging protocols developed in the swine study may have to be optimized for applications in patients. Nevertheless, a recent study by Kempfert et al showed that small volumes of contrast may be sufficient even in patients to acquire C-arm CT images [170]. The optimal C-arm CT images in the current study allowed precise definition and measurement of aortic anatomy similar to MDCT. The 3D C-arm CT images were fused with 3D preprocedural contrast-enhanced cardiac MDCT images for guidance to improve safety and efficacy of the TAVI procedure itself. Although C-arm CT images can be registered with the 2D fluoroscopy images, this approach was not evaluated in the current study. Such image fusion may provide an opportunity to minimize complications related to valve placement including coronary artery occlusion, trauma to the anterior mitral leaflet or impingement of the conducting tissue due to placement of valve within the left ventricular outflow tract. In addition, the overlay of 3D images may be helpful to minimize use of multiple contrast injections and fluoroscopic scans which are typically performed in order to define the valve plane for TAVI. This may possibly reduce contrast dose and radiation exposure.

As C-arm CT is increasingly used in catheterization lab, there is a need to understand the radiation dose required during image acquisition. Currently, there is a lack of consensus regarding a C-arm CT dose metric. One option for dose estimation is the use of the standard computed tomography dose index (CTDI) employed in MDCT imaging. However, differences with C-arm CT acquisition as compared to MDCT including modulation of tube voltage, larger z-coverage and partial scanning range demand a different procedure for dose estimation from 3D C-arm CT. Imaging was performed at constant tube voltage throughout the scan in phantom experiments by increasing detector

entrance dose. The necessary phantom length and integration length for estimating dose with C-arm CT scans was also discussed. Although phantom and ionization chamber of 600 mm length may be ideal [208], the availability of such phantoms and ionization chambers is challenging. Although multiple phantoms of same diameter can be combined to simulate a larger phantom; a large chamber of 600 mm integration length is currently unavailable. Phantom measurements showed with a 300 mm integration length, peak dose values from a 300 mm phantom were similar to those from a 470 mm phantom with a maximum difference of 3%. Simulation results also showed that a 470 mm body phantom with 300 mm ionization chamber was required to measure C-arm CT dose and generate a power equation for estimating $CTDI_w$ in patients based on applied tube voltage. Dose estimates for a C-arm CT protocol primarily used for registration during intervention resulted in $CTDI_w$ of 5.48 ± 2.02 mGy on average in patients. These values indicate radiation burden from the additional C-arm CT scan was low. This approach could be used estimate dose in the pig studies as well. However, the x-ray exposure parameters used during C-arm CT pig studies were not recorded and hence, dose values could not be estimated.

MDCT imaging is routinely performed for follow-up after minimally invasive surgeries, such as endovascular aneurysm repair, a procedure for treating aortic aneurysm by placing an endograft/stent. EVAR is associated with lower morbidity and mortality rates than open surgical repair, along with reduced stay in the hospital after the procedure [38]. After stent placement, triple-phase SECT is often used to monitor patients 1 month, 6 months, and yearly [13]. Combinations of the three phases, namely the pre-contrast (non-contrast), contrast-enhanced (arterial) and post-contrast (venous) SECT images is

used to evaluate aneurysm size, stent-graft position and patency, perigraft flow (endoleaks), graft fractures/kinks, and the patency of native vessels near the graft [2, 3, 12-14]. However, this repeated imaging is associated with increased radiation dose to the patients.

An emerging approach to reduce radiation dose is the replacement of two SECT acquisitions with a single DECT acquisition [18, 19]. DECT data obtained during or after contrast agent injection can be used to create not only arterial or venous phase images, respectively, but also virtual non-contrast (VNC) images [18, 19, 22, 24]. Previous studies [18, 19] have acquired DECT data during the venous phase, but no studies to date have evaluated the feasibility of arterial phase DECT acquisition. The presence of high density iodinated contrast adjacent to other high density materials like stent or calcium and, in many cases, the non-uniformity of contrast attenuation along the length of the aorta make generation of VNC images from arterial DECT data more challenging.

An additional purpose of this work was to test the feasibility of obtaining VNC images from arterial DECT images using a dual-source DECT scanner (Definition, Siemens) and replacing routine non-contrast and arterial phase SECT images with VNC and dual-energy arterial phase images obtained in one arterial DECT acquisition. The results showed that both VNC and arterial phase images could be obtained from a single arterial DECT acquisition rather than from two separate SECT acquisitions. The attenuation of low-density tissues was similar on the dual-energy and standard SECT images, but the attenuation values of high-density materials differed significantly. Nevertheless, it was concluded that VNC and weighted-average arterial images from DECT can replace true non-contrast and arterial phase SECT images, respectively, in the

follow-up of patients who have undergone EVAR (except immediately after the procedure) to provide comparable diagnostic information with an average dose savings of 31%. Arterial phase DECT imaging has utility not only for EVAR, but for other future clinical applications. In the context of EVAR, arterial images are important for the evaluation of luminal details, in particular smaller branch vessels. In other indications for aortic imaging (aneurysm, dissection, aortitis, preoperative and postoperative evaluation), arterial phase acquisition is the clinical standard. Reliable reconstruction of VNC images from arterial DECT scans may yield information about tissue characteristics (e.g., intramural hematoma, surgical material, low-density calcium versus contrast medium) and thus elimination of the true non-contrast acquisition can help to decrease radiation dose burden in these patients.

However, the study of EVAR patients described above showed that due to limitations of the three-material decomposition algorithm, calcium and iodine were not discriminated well resulting in removal of calcium in the VNC images [183]. The current implementation of the basis three-material decomposition algorithm assumes that each voxel is composed of fat, soft tissue and iodine, and the attenuation of these materials is solved to identify and eliminate contrast pixels during VNC generation. However, as calcium is not considered as one of the three basis materials and due to the spectral overlap between the two tube voltages (80 and 140 kVp), discrimination between contrast material and calcium is challenging. The three material decomposition algorithm was improved by assuming calcium, blood and contrast as the basis materials present in each pixel and applying a combined basis spectral [77] and basis material analysis [79] to the DECT images to differentiate the components of the mixture.

Additionally, it was hypothesized that improving spectral separation between the two tube voltages would help to better differentiate and quantify tissue with similar atomic numbers like calcium and iodine with DECT. Recent study by Primak et al [142] on a second generation dual-source CT scanner (Flash, Siemens) showed that additional filtration decreased noise and increased contrast in images. Hence, we anticipated improvement in VNC generation by applying an additional filter to the higher energy x-ray spectra using the latest dual-source DECT scanner.

Difficulties in the creation of VNC images from dual-energy data acquired with first generation dual-source DECT were also attributed to non-uniform contrast enhancement along the length of the aorta. To address this issue, patient-specific modeling employing linear-time invariant concepts for optimizing contrast injection protocols was developed. However, we observed that contrast agent optimization was not required with the latest generation dual-source scanner (Flash, Siemens) as contrast attenuation along the length of the aorta was uniform in patients. This is most likely a result of shorter scan times with the latest scanner as compared to the previous generation dual-source scanner (Definition, Siemens). On average, an approximately 34 s scan time was required for DECT on the Siemens Definition CT scanner, while an average of 15 s was required on the Siemens Flash. Hence, patient-specific injections were deemed unnecessary with this new scanner.

The utility of added filtration to separate x-ray spectra and a combined basis spectral and material decomposition algorithm were evaluated in phantoms. The phantom data results showed the feasibility for differentiating calcium and contrast agent and computing the mass fraction of contrast agent mixtures. It was determined that this

method could be employed clinically for identification and removal of iodine in contrast-enhanced DECT images to generate VNC images. Therefore, the potential benefit of the improved spectral separation of low and high energies and a modified dual-energy image processing algorithm, but not patient-specific injection were further investigated in patients. One patient imaged was administered with a routine contrast injection protocol and imaged with a DECT acquisition at 100 and 140 (with tin filter) kVp on the second generation dual-source scanner and the resulting arterial images were analyzed using the new VNC processing algorithm. The luminal attenuation measurements in VNC images demonstrated adequate elimination of contrast agent.

In conclusion this project described the development of optimal imaging and contrast protocols for C-arm CT in the context of TAVI to provide data complimentary to preprocedural MDCT images and permit the registration of preprocedural images with real-time 2D fluoroscopic images for safer valve implantation during procedure. In addition, the feasibility of acquiring C-arm CT images post-TAVI to record valve position and avoid complications was demonstrated. This work also described an approach for estimating radiation dose with C-arm CT that allows direct comparison with dose estimates for MDCT. The methodology was used to estimate dose in patients imaged with C-arm CT primarily for purpose of image registration (3D MDCT with 2D fluoroscopy images) during the intervention.

Additionally, novel DECT imaging techniques were developed to image post-EVAR patients and generate virtual non-contrast images from DECT data. The results showed that both VNC and arterial phase images could be obtained from a single arterial DECT acquisition rather than from two separate SECT acquisitions and replace true non-

contrast and arterial phase SECT images, respectively, with an average dose savings of 31%. Finally, a three-material decomposition algorithm based on combined basis spectral and basis material analysis for differentiating calcium and contrast agent with DECT imaging was developed which can be used clinically to identify and remove iodine in contrast-enhanced DECT images to generate VNC images. However, pixels with high atomic number but low density were falsely identified as iodine and appear with decreased attenuation in VNC images.

The work presented in the dissertation has generated possible future developments. In the context of preprocedural planning and intraprocedural guidance, the feasibility of overlying the C-arm CT images directly for navigating minimally invasive surgeries, thus eliminating need of a preprocedural MDCT needs to be explored. Additionally, the accuracy of overlaying aortic root structures marked from 3D MDCT or C-arm CT images onto 2D fluoroscopic images needs to be quantified to see the utility of 3D images for intraprocedural guidance. The rationale of using C-arm CT images in the catheterization lab is to minimize 2D fluoroscopic acquisitions in patients. Hence, obtaining dose measurements from the entire TAVI procedure with and without C-arm CT imaging is required to understand whether the additional dose burden from C-arm CT is reducing the dose by decreasing the number of 2D fluoroscopic acquisitions.

For post-procedural imaging, the proposed patient-specific contrast protocol optimization was not required for second generation dual-source CT scanner. However, the utility of employing patient-specific protocols can still be explored with other DECT imaging techniques. Finally, the proposed combined basis spectral and basis material algorithm showed that low density calcium is still present with low intensity in VNC

images. One approach to minimize calcium loss in VNC images is to improve separation between iodine and calcium by decreasing noise in DECT arterial images. This can be possible by implementing the combined basis spectral and basis material algorithm in raw space domain.

REFERENCES

1. Akhtar NJ, Markowitz AH, Gilkeson RC. Multidetector computed tomography in the preoperative assessment of cardiac surgery patients. *Radiol Clin North Am* 2010;48:117-139
2. Duddalwar VA. Multislice CT angiography: a practical guide to CT angiography in vascular imaging and intervention. *Br J Radiol* 2004;77 Spec No 1:S27-38
3. Sundaram B, Quint LE, Patel HJ, Deeb GM. CT findings following thoracic aortic surgery. *Radiographics* 2007;27:1583-1594
4. Fleischmann D, Liang DH, Herfkens RJ. Technical advances in cardiovascular imaging. *Semin Thorac Cardiovasc Surg* 2008;20:333-339
5. Fleischmann D, Liang DH, Mitchell RS, Miller DC. Pre- and postoperative imaging of the aortic root for valve-sparing aortic root repair (V-SARR). *Semin Thorac Cardiovasc Surg* 2008;20:365-373
6. Schoenhagen P, Greenberg RK. 3-Dimensional planning of endovascular procedures with multi-detector computed tomography (MDCT): impact on procedural results and clinical outcome? *Int J Cardiovasc Imaging* 2008;24:211-213
7. Schoenhagen P, Hill A. Transcatheter aortic valve implantation and potential role of 3D imaging. *Expert Rev Med Devices* 2009;6:411-421
8. Schoenhagen P, Tuzcu EM, Kapadia SR, Desai MY, Svensson LG. Three-dimensional imaging of the aortic valve and aortic root with computed

tomography: new standards in an era of transcatheter valve repair/implantation. *Eur Heart J* 2009;30:2079-2086

9. Ueda T, Fleischmann D, Rubin GD, Dake MD, Sze DY. Imaging of the thoracic aorta before and after stent-graft repair of aneurysms and dissections. *Semin Thorac Cardiovasc Surg* 2008;20:348-357
10. Kurra V, Kapadia SR, Tuzcu EM, et al. Pre-procedural imaging of aortic root orientation and dimensions: comparison between X-ray angiographic planar imaging and 3-dimensional multidetector row computed tomography. *JACC Cardiovasc Interv* 2010;3:105-113
11. Schoenhagen P, Numburi U, Halliburton SS, et al. Three-dimensional imaging in the context of minimally invasive and transcatheter cardiovascular interventions using multi-detector computed tomography: from pre-operative planning to intra-operative guidance. *Eur Heart J* 2010
12. Bean MJ, Johnson PT, Roseborough GS, Black JH, Fishman EK. Thoracic aortic stent-grafts: utility of multidetector CT for pre- and postprocedure evaluation. *Radiographics* 2008;28:1835-1851
13. Hellinger JC. Endovascular repair of thoracic and abdominal aortic aneurysms: Pre- and postprocedural imaging. *Techniques in Vascular and Interventional Radiology* 2005;8:2-15
14. Kaufman JA, Geller SC, Brewster DC, et al. Endovascular repair of abdominal aortic aneurysms: current status and future directions. *AJR Am J Roentgenol* 2000;175:289-302

15. Brenner DJ, Elliston CD. Estimated radiation risks potentially associated with full-body CT screening. *Radiology* 2004;232:735-738
16. Brenner DJ, Hall EJ. Computed tomography--an increasing source of radiation exposure. *N Engl J Med* 2007;357:2277-2284
17. de Jong PA, Mayo JR, Golmohammadi K, et al. Estimation of cancer mortality associated with repetitive computed tomography scanning. *Am J Respir Crit Care Med* 2006;173:199-203
18. Chandarana H, Godoy MC, Vlahos I, et al. Abdominal aorta: evaluation with dual-source dual-energy multidetector CT after endovascular repair of aneurysms--initial observations. *Radiology* 2008;249:692-700
19. Stolzmann P, Frauenfelder T, Pfammatter T, et al. Endoleaks after endovascular abdominal aortic aneurysm repair: detection with dual-energy dual-source CT. *Radiology* 2008;249:682-691
20. Carmi R, Naveh G, Altman A. Material separation with dual-layer CT. In: *IEEE Nuclear Science Symposium Conference Record*, 2005:1876-1878
21. Flohr TG, McCollough CH, Bruder H, et al. First performance evaluation of a dual-source CT (DSCT) system. *European Radiology* 2006;16:256-268
22. Johnson TR, Krauss B, Sedlmair M, et al. Material differentiation by dual energy CT: initial experience. *Eur Radiol* 2007;17:1510-1517
23. Kuribayashi S. Dual energy CT of peripheral arterial disease with single-source 64-slice MDCT. *Presented at: 9th Annual International Symposium on MDCT; San Francisco, CA; 2007*

24. Graser A, Johnson TR, Chandarana H, Macari M. Dual energy CT: preliminary observations and potential clinical applications in the abdomen. *Eur Radiol* 2009;19:13-23
25. Bae KT, Tran HQ, Heiken JP. Multiphasic injection method for uniform prolonged vascular enhancement at CT angiography: pharmacokinetic analysis and experimental porcine model. *Radiology* 2000;216:872-880
26. Fleischmann D, Hittmair K. Mathematical analysis of arterial enhancement and optimization of bolus geometry for CT angiography using the discrete fourier transform. *J Comput Assist Tomogr* 1999;23:474-484
27. Numburi UD, Chatzimavroudis GP, Stillman AE, et al. Patient-specific contrast injection protocols for cardiovascular multidetector row computed tomography. *J Comput Assist Tomogr* 2007;31:281-289
28. Petersilka M, Bruder H, Krauss B, Stierstorfer K, Flohr TG. Technical principles of dual source CT. *Eur J Radiol* 2008;68:362-368
29. Gray H. *Anatomy of the Human Body*, TWENTIETH EDITION ed, 2000
30. Litmanovich D, Bankier AA, Cantin L, Raptopoulos V, Boiselle PM. CT and MRI in diseases of the aorta. *AJR Am J Roentgenol* 2009;193:928-940
31. Tatli S, Yucel EK, Lipton MJ. CT and MR imaging of the thoracic aorta: current techniques and clinical applications. *Radiol Clin North Am* 2004;42:565-585, vi
32. Boiselle PM, White CS. *New techniques in cardiothoracic imaging*. New Yor, NY: InformaHealthCare, 2007:105-126
33. Crawford ES, DeNatale RW. Thoracoabdominal aortic aneurysm: observations regarding the natural course of the disease. *J Vasc Surg* 1986;3:578-582

34. Yu T, Zhu X, Tang L, Wang D, Saad N. Review of CT angiography of aorta. *Radiol Clin North Am* 2007;45:461-483, viii
35. Greenberg RK, Chuter TA, Cambria RP, Sternbergh WC, 3rd, Fearnot NE. Zenith abdominal aortic aneurysm endovascular graft. *J Vasc Surg* 2008;48:1-9
36. Greenhalgh RM, Powell JT. Endovascular repair of abdominal aortic aneurysm. *N Engl J Med* 2008;358:494-501
37. Schermerhorn ML, O'Malley AJ, Jhaveri A, Cotterill P, Pomposelli F, Landon BE. Endovascular vs. open repair of abdominal aortic aneurysms in the Medicare population. *N Engl J Med* 2008;358:464-474
38. Drury D, Michaels JA, Jones L, Ayiku L. Systematic review of recent evidence for the safety and efficacy of elective endovascular repair in the management of infrarenal abdominal aortic aneurysm. *Br J Surg* 2005;92:937-946
39. Baumgartner H. Aortic stenosis: medical and surgical management. *Heart* 2005;91:1483-1488
40. Iung B, Baron G, Butchart EG, et al. A prospective survey of patients with valvular heart disease in Europe: The Euro Heart Survey on Valvular Heart Disease. *Eur Heart J* 2003;24:1231-1243
41. Nkomo VT, Gardin JM, Skelton TN, Gottdiener JS, Scott CG, Enriquez-Sarano M. Burden of valvular heart diseases: a population-based study. *Lancet* 2006;368:1005-1011
42. Rosamond W, Flegal K, Furie K, et al. Heart disease and stroke statistics--2008 update: a report from the American Heart Association Statistics Committee and Stroke Statistics Subcommittee. *Circulation* 2008;117:e25-146

43. Bonow RO, Carabello BA, Chatterjee K, et al. 2008 focused update incorporated into the ACC/AHA 2006 guidelines for the management of patients with valvular heart disease: a report of the American College of Cardiology/American Heart Association Task Force on Practice Guidelines (Writing Committee to revise the 1998 guidelines for the management of patients with valvular heart disease). Endorsed by the Society of Cardiovascular Anesthesiologists, Society for Cardiovascular Angiography and Interventions, and Society of Thoracic Surgeons. *J Am Coll Cardiol* 2008;52:e1-142
44. Akat K, Borggrefe M, Kaden JJ. Aortic valve calcification: basic science to clinical practice. *Heart* 2009;95:616-623
45. Goldberg SH, Elmariah S, Miller MA, Fuster V. Insights into degenerative aortic valve disease. *J Am Coll Cardiol* 2007;50:1205-1213
46. Otto CM, Kuusisto J, Reichenbach DD, Gown AM, O'Brien KD. Characterization of the early lesion of 'degenerative' valvular aortic stenosis. Histological and immunohistochemical studies. *Circulation* 1994;90:844-853
47. Cowell SJ, Newby DE, Prescott RJ, et al. A randomized trial of intensive lipid-lowering therapy in calcific aortic stenosis. *N Engl J Med* 2005;352:2389-2397
48. Novaro GM, Tiong IY, Pearce GL, Lauer MS, Sprecher DL, Griffin BP. Effect of hydroxymethylglutaryl coenzyme a reductase inhibitors on the progression of calcific aortic stenosis. *Circulation* 2001;104:2205-2209
49. Rossebø AB, Pedersen TR, Boman K, et al. Intensive lipid lowering with simvastatin and ezetimibe in aortic stenosis. *N Engl J Med* 2008;359:1343-1356

50. Shavelle DM, Takasu J, Budoff MJ, Mao S, Zhao XQ, O'Brien KD. HMG CoA reductase inhibitor (statin) and aortic valve calcium. *Lancet* 2002;359:1125-1126
51. Hammermeister KE, Sethi GK, Henderson WG, Oprian C, Kim T, Rahimtoola S. A comparison of outcomes in men 11 years after heart-valve replacement with a mechanical valve or bioprosthesis. Veterans Affairs Cooperative Study on Valvular Heart Disease. *N Engl J Med* 1993;328:1289-1296
52. Alexander KP, Anstrom KJ, Muhlbaier LH, et al. Outcomes of cardiac surgery in patients \geq 80 years: results from the National Cardiovascular Network. *J Am Coll Cardiol* 2000;35:731-738
53. Iung B, Cachier A, Baron G, et al. Decision-making in elderly patients with severe aortic stenosis: why are so many denied surgery? *Eur Heart J* 2005;26:2714-2720
54. Iung B, Vahanian A. Valvular heart diseases in elderly people. *Lancet* 2006;368:969-971
55. Mihaljevic T, Nowicki ER, Rajeswaran J, et al. Survival after valve replacement for aortic stenosis: implications for decision making. *J Thorac Cardiovasc Surg* 2008;135:1270-1278; discussion 1278-1279
56. Kapadia SR, Goel SS, Svensson L, et al. Characterization and outcome of patients with severe symptomatic aortic stenosis referred for percutaneous aortic valve replacement. *J Thorac Cardiovasc Surg* 2009;137:1430-1435
57. Varadarajan P, Kapoor N, Bansal RC, Pai RG. Clinical profile and natural history of 453 nonsurgically managed patients with severe aortic stenosis. *Ann Thorac Surg* 2006;82:2111-2115

58. Cribier A, Eltchaninoff H, Tron C, et al. Treatment of calcific aortic stenosis with the percutaneous heart valve: mid-term follow-up from the initial feasibility studies: the French experience. *J Am Coll Cardiol* 2006;47:1214-1223
59. Grube E, Laborde JC, Gerckens U, et al. Percutaneous implantation of the CoreValve self-expanding valve prosthesis in high-risk patients with aortic valve disease: the Siegburg first-in-man study. *Circulation* 2006;114:1616-1624
60. Kapadia SR, Tuzcu EM. Transcatheter aortic valve implantation. *Curr Treat Options Cardiovasc Med* 2009;11:467-475
61. Vassiliades TA, Jr., Block PC, Cohn LH, et al. The clinical development of percutaneous heart valve technology. *J Thorac Cardiovasc Surg* 2005;129:970-976
62. Walther T, Simon P, Dewey T, et al. Transapical minimally invasive aortic valve implantation: multicenter experience. *Circulation* 2007;116:1240-245
63. Webb JG, Altwegg L, Boone RH, et al. Transcatheter aortic valve implantation: impact on clinical and valve-related outcomes. *Circulation* 2009;119:3009-3016
64. Webb JG, Chandavimol M, Thompson CR, et al. Percutaneous aortic valve implantation retrograde from the femoral artery. *Circulation* 2006;113:842-850
65. Cribier A, Eltchaninoff H, Tron C, et al. Early experience with percutaneous transcatheter implantation of heart valve prosthesis for the treatment of end-stage inoperable patients with calcific aortic stenosis. *J Am Coll Cardiol* 2004;43:698-703
66. Grube E, Schuler G, Buellesfeld L, et al. Percutaneous aortic valve replacement for severe aortic stenosis in high-risk patients using the second- and current third-

- generation self-expanding CoreValve prosthesis: device success and 30-day clinical outcome. *J Am Coll Cardiol* 2007;50:69-76
67. Lichtenstein SV, Cheung A, Ye J, et al. Transapical transcatheter aortic valve implantation in humans: initial clinical experience. *Circulation* 2006;114:591-596
 68. Gurvitch R, Wood DA, Leipsic J, et al. Multislice computed tomography for prediction of optimal angiographic deployment projections during transcatheter aortic valve implantation. *JACC Cardiovasc Interv* 2010;3:1157-1165
 69. Bushberg JT, Seibert JA, Jr. EML, Boone JM. *The Essential Physics of Medical Imaging*, 2nd Edition ed: Philadelphia: Lippincott Williams & Wilkins,, 2002
 70. Schoenhagen P WR, Stillman A, Halliburton S. *Atlas and Manual of Cardiovascular Multidetector Computed Tomography*: Taylor & Francis, 2005
 71. Akhtar M, Tuzcu EM, Kapadia SR, et al. Aortic root morphology in patients undergoing percutaneous aortic valve replacement: evidence of aortic root remodeling. *J Thorac Cardiovasc Surg* 2009;137:950-956
 72. Herman GT, Lent A. Iterative reconstruction algorithms. *Comput Biol Med* 1976;6:273-294
 73. Thibault JB, Sauer KD, Bouman CA, Hsieh J. A three-dimensional statistical approach to improved image quality for multislice helical CT. *Med Phys* 2007;34:4526-4544
 74. Wang G, Yu H, De Man B. An outlook on x-ray CT research and development. *Med Phys* 2008;35:1051-1064
 75. Curry TS, Dowdey JE, Murry RE. *Christensen's Physics of Diagnostic Radiology* Malvern: Lea & Febiger, 1990

76. Kalender WA. *Computed Tomography*: Publicis Corporate Publishing, Erlangen, 2005
77. Alvarez RE, Macovski A. Energy-selective reconstructions in X-ray computerised tomography. *Physics in Medicine and Biology* 1976;21:733-744
78. McCullough EC. Photon attenuation in computed Tomography. *Medical Physics* 1975;2:307-320
79. Kalender WA, Perman WH, Vetter JR, Klotz E. Evaluation of a prototype dual-energy computed tomographic apparatus. I. Phantom studies. *Med Phys* 1986;13:334-339
80. Kelcz F, Joseph PM, Hilal SK. Noise considerations in dual energy CT scanning. *Med Phys* 1979;6:418-425
81. Flohr TG, Bruder H, Stierstorfer K, Petersilka M, Schmidt B, McCollough CH. Image reconstruction and image quality evaluation for a dual source CT scanner. *Medical Physics* 2008;35:5882-5897
82. Wu X, Langan DA, Xu D, et al. Monochromatic CT image representation via fast switching dual kVp. In: *Progress in Biomedical Optics and Imaging - Proceedings of SPIE*, 2009
83. Xu D, Langan DA, Wu X, et al. Dual energy CT via fast kVp switching spectrum estimation. In: *Progress in Biomedical Optics and Imaging - Proceedings of SPIE*, 2009
84. Zou Y, Silver MD. Analysis of fast kV-switching in dual energy CT using a pre-reconstruction decomposition technique. In: *Progress in Biomedical Optics and Imaging - Proceedings of SPIE*, 2008

85. Boll DT, Merkle EM, Paulson EK, Fleiter TR. Coronary stent patency: dual-energy multidetector CT assessment in a pilot study with anthropomorphic phantom. *Radiology* 2008;247:687-695
86. Boll DT, Merkle EM, Paulson EK, Mirza RA, Fleiter TR. Calcified vascular plaque specimens: assessment with cardiac dual-energy multidetector CT in anthropomorphically moving heart phantom. *Radiology* 2008;249:119-126
87. Taguchi K, Zhang M, Frey EC, Xu J, Segars WP, Tsui BMW. Image-domain material decomposition using photon-counting CT. In: *Progress in Biomedical Optics and Imaging - Proceedings of SPIE*, 2007
88. Kachelriess M, Ulzheimer S, Kalender WA. ECG-correlated image reconstruction from subsecond multi-slice spiral CT scans of the heart. *Med Phys* 2000;27:1881-1902
89. Ohnesorge B, Flohr T, Becker C, et al. Cardiac imaging by means of electrocardiographically gated multisection spiral CT: initial experience. *Radiology* 2000;217:564-571
90. Taguchi K, Anno H. High temporal resolution for multislice helical computed tomography. *Med Phys* 2000;27:861-872
91. Achenbach S, Ulzheimer S, Baum U, et al. Noninvasive coronary angiography by retrospectively ECG-gated multislice spiral CT. *Circulation* 2000;102:2823-2828
92. Becker CR, Ohnesorge BM, Schoepf UJ, Reiser MF. Current development of cardiac imaging with multidetector-row CT. *Eur J Radiol* 2000;36:97-103
93. Hendel RC, Patel MR, Kramer CM, et al. ACCF/ACR/SCCT/SCMR/ASNC/NASCI/SCAI/SIR 2006 appropriateness

criteria for cardiac computed tomography and cardiac magnetic resonance imaging: a report of the American College of Cardiology Foundation Quality Strategic Directions Committee Appropriateness Criteria Working Group, American College of Radiology, Society of Cardiovascular Computed Tomography, Society for Cardiovascular Magnetic Resonance, American Society of Nuclear Cardiology, North American Society for Cardiac Imaging, Society for Cardiovascular Angiography and Interventions, and Society of Interventional Radiology. *J Am Coll Cardiol* 2006;48:1475-1497

94. Hoffmann U, Nagurney JT, Moselewski F, et al. Coronary multidetector computed tomography in the assessment of patients with acute chest pain. *Circulation* 2006;114:2251-2260
95. Knez A, Becker C, Ohnesorge B, Haberl R, Reiser M, Steinbeck G. Noninvasive detection of coronary artery stenosis by multislice helical computed tomography. *Circulation* 2000;101:E221-222
96. Leber AW, Knez A, von Ziegler F, et al. Quantification of obstructive and nonobstructive coronary lesions by 64-slice computed tomography: a comparative study with quantitative coronary angiography and intravascular ultrasound. *J Am Coll Cardiol* 2005;46:147-154
97. Nieman K, Oudkerk M, Rensing BJ, et al. Coronary angiography with multi-slice computed tomography. *Lancet* 2001;357:599-603
98. Raff GL, Gallagher MJ, O'Neill WW, Goldstein JA. Diagnostic accuracy of noninvasive coronary angiography using 64-slice spiral computed tomography. *J Am Coll Cardiol* 2005;46:552-557

99. Budoff M. *Cardiac CT Imaging: Diagnosis of Cardiovascular Disease*: Springer, 2006
100. Flohr T, Ohnesorge B. Heart rate adaptive optimization of spatial and temporal resolution for electrocardiogram-gated multislice spiral CT of the heart. *J Comput Assist Tomogr* 2001;25:907-923
101. Saint-Felix D, Troussset Y, Picard C, Ponchut C, Romeas R, Rougee A. In vivo evaluation of a new system for 3D computerized angiography. *Physics in Medicine and Biology* 1994;39:583-595
102. Fahrig R, Fox AJ, Lownie S, Holdsworth DW. Use of a C-arm system to generate true three-dimensional computed rotational angiograms: preliminary in vitro and in vivo results. *AJNR Am J Neuroradiol* 1997;18:1507-1514
103. Zellerhoff M, Scholz B, Ru?hrnschopf EP, Brunner T. Low contrast 3D-reconstruction from C-arm data. In: *Progress in Biomedical Optics and Imaging - Proceedings of SPIE*, 2005:646-655
104. Kalender WA, Kyriakou Y. Flat-detector computed tomography (FD-CT). *Eur Radiol* 2007;17:2767-2779
105. Neitzel U. Status and prospects of digital detector technology for CR and DR. *Radiat Prot Dosimetry* 2005;114:32-38
106. Dawson P, Blomley MJ. Contrast media as extracellular fluid space markers: adaptation of the central volume theorem. *Br J Radiol* 1996;69:717-722
107. Fleischmann D, Rubin GD, Bankier AA, Hittmair K. Improved uniformity of aortic enhancement with customized contrast medium injection protocols at CT angiography. *Radiology* 2000;214:363-371

108. Mahnken AH, Rauscher A, Klotz E, et al. Quantitative prediction of contrast enhancement from test bolus data in cardiac MSCT. *Eur Radiol* 2007;17:1310-1319
109. Rist C, Becker CR, Kirchin MA, et al. Optimization of cardiac MSCT contrast injection protocols: dependency of the main bolus contrast density on test bolus parameters and patients' body weight. *Acad Radiol* 2008;15:49-57
110. Awai K, Hiraishi K, Hori S. Effect of contrast material injection duration and rate on aortic peak time and peak enhancement at dynamic CT involving injection protocol with dose tailored to patient weight. *Radiology* 2004;230:142-150
111. Fleischmann D, Rubin GD. Quantification of intravenously administered contrast medium transit through the peripheral arteries: implications for CT angiography. *Radiology* 2005;236:1076-1082
112. Heiken JP, Brink JA, McClennan BL, Sagel SS, Forman HP, DiCroce J. Dynamic contrast-enhanced CT of the liver: comparison of contrast medium injection rates and uniphasic and biphasic injection protocols. *Radiology* 1993;187:327-331
113. Bae KT, Tran HQ, Heiken JP. Uniform vascular contrast enhancement and reduced contrast medium volume achieved by using exponentially decelerated contrast material injection method. *Radiology* 2004;231:732-736
114. Hittmair K, Fleischmann D. Accuracy of predicting and controlling time-dependent aortic enhancement from a test bolus injection. *J Comput Assist Tomogr* 2001;25:287-294
115. Bae KT. Optimization of contrast enhancement in thoracic MDCT. *Radiol Clin North Am* 2010;48:9-29

116. Cademartiri F, Luccichenti G, Marano R, Runza G, Midiri M. Use of saline chaser in the intravenous administration of contrast material in non-invasive coronary angiography with 16-row multislice Computed Tomography. *Radiol Med (Torino)* 2004;107:497-505
117. Irie T, Kajitani M, Yamaguchi M, Itai Y. Contrast-enhanced CT with saline flush technique using two automated injectors: how much contrast medium does it save? *J Comput Assist Tomogr* 2002;26:287-291
118. Schoellnast H, Tillich M, Deutschmann MJ, Deutschmann HA, Schaffler GJ, Portugaller HR. Aortoiliac enhancement during computed tomography angiography with reduced contrast material dose and saline solution flush: influence on magnitude and uniformity of the contrast column. *Invest Radiol* 2004;39:20-26
119. Hopper KD, Mosher TJ, Kasales CJ, TenHave TR, Tully DA, Weaver JS. Thoracic spiral CT: delivery of contrast material pushed with injectable saline solution in a power injector. *Radiology* 1997;205:269-271
120. Haage P, Schmitz-Rode T, Hubner D, Piroth W, Gunther RW. Reduction of contrast material dose and artifacts by a saline flush using a double power injector in helical CT of the thorax. *AJR Am J Roentgenol* 2000;174:1049-1053
121. Nolker G, Gutleben KJ, Marschang H, et al. Three-dimensional left atrial and esophagus reconstruction using cardiac C-arm computed tomography with image integration into fluoroscopic views for ablation of atrial fibrillation: accuracy of a novel modality in comparison with multislice computed tomography. *Heart Rhythm* 2008;5:1651-1657

122. Biasi L, Ali T, Hinchliffe R, Morgan R, Loftus I, Thompson M. Intraoperative DynaCT Detection and Immediate Correction of a Type 1a Endoleak Following Endovascular Repair of Abdominal Aortic Aneurysm. *Cardiovasc Intervent Radiol* 2008
123. Mahesh M. Fluoroscopy: patient radiation exposure issues. *Radiographics* 2001;21:1033-1045
124. Shope TB, Gagne RM, Johnson GC. A method for describing the doses delivered by transmission x-ray computed tomography. *Med Phys* 1981;8:488-495
125. Rutherford RA, Pullan BR, Isherwood I. Measurement of effective atomic number and electron density using an EMI scanner. *Neuroradiology* 1976;11:15-21
126. Genant HK, Boyd D. Quantitative bone mineral analysis using dual energy computed tomography. *Invest Radiol* 1977;12:545-551
127. Avrin DE, Macovski A, Zatz LE. Clinical application of Compton and photo-electric reconstruction in computed tomography: preliminary results. *Invest Radiol* 1978;13:217-222
128. Chiro GD, Brooks RA, Kessler RM, et al. Tissue signatures with dual-energy computed tomography. *Radiology* 1979;131:521-523
129. Millner MR, McDavid WD, Waggener RG, Dennis MJ, Payne WH, Sank VJ. Extraction of information from CT scans at different energies. *Med Phys* 1979;6:70-71

130. Yu L, Liu X, McCollough CH. Pre-reconstruction three-material decomposition in dual-energy CT. In: *Progress in Biomedical Optics and Imaging - Proceedings of SPIE*, 2009
131. Heismann BJ, Leppert J, Stierstorfer K. Density and atomic number measurements with spectral x-ray attenuation method. *Journal of Applied Physics* 2003;94:2073-2079
132. Liu X, Yu L, Primak AN, McCollough CH. Quantitative imaging of element composition and mass fraction using dual-energy CT: three-material decomposition. *Med Phys* 2009;36:1602-1609
133. Nickoloff EL, Feldman F, Atherton JV. Bone mineral assessment: New dual-energy CT approach. *Radiology* 1988;168:223-228
134. Raptopoulos V, Karellas A, Bernstein J, Reale FR, Constantinou C, Zawacki JK. Value of dual-energy CT in differentiating focal fatty infiltration of the liver from low-density masses. *AJR Am J Roentgenol* 1991;157:721-725
135. Primak AN, Fletcher JG, Vrtiska TJ, et al. Noninvasive Differentiation of Uric Acid versus Non-Uric Acid Kidney Stones Using Dual-Energy CT. *Academic Radiology* 2007;14:1441-1447
136. Scheffel H, Stolzmann P, Frauenfelder T, et al. Dual-energy contrast-enhanced computed tomography for the detection of urinary stone disease. *Invest Radiol* 2007;42:823-829
137. Takahashi N, Hartman RP, Vrtiska TJ, et al. Dual-energy CT iodine-subtraction virtual unenhanced technique to detect urinary stones in an iodine-filled collecting system: a phantom study. *AJR Am J Roentgenol* 2008;190:1169-1173

138. Bacani AK, McCollough CH, Glazebrook KN, et al. Dual energy computed tomography for quantification of tissue urate deposits in tophaceous gout: help from modern physics in the management of an ancient disease. *Rheumatol Int* 2009
139. Choi HK, Al-Arfaj AM, Eftekhari A, et al. Dual energy computed tomography in tophaceous gout. *Ann Rheum Dis* 2009;68:1609-1612
140. Rutt B, Fenster A. Split-filter computed tomography: a simple technique for dual energy scanning. *J Comput Assist Tomogr* 1980;4:501-509
141. Marshall W, Hall E, Doost-Hoseini A, Alvarez R, Macovski A, Cassel D. An implementation of dual energy CT scanning. *J Comput Assist Tomogr* 1984;8:745-749
142. Primak AN, Ramirez Giraldo JC, Liu X, Yu L, McCollough CH. Improved dual-energy material discrimination for dual-source CT by means of additional spectral filtration. *Medical Physics* 2009;36:1359-1369
143. Achenbach S, Marwan M, Schepis T, et al. High-pitch spiral acquisition: a new scan mode for coronary CT angiography. *J Cardiovasc Comput Tomogr* 2009;3:117-121
144. Dewey M, Zimmermann E, Laule M, Rutsch W, Hamm B. Three-vessel coronary artery disease examined with 320-slice computed tomography coronary angiography. *Eur Heart J* 2008
145. Hameed TA, Teague SD, Vembar M, Dharaiya E, Rydberg J. Low radiation dose ECG-gated chest CT angiography on a 256-slice multidetector CT scanner. *Int J Cardiovasc Imaging* 2009

146. Rybicki FJ, Otero HJ, Steigner ML, et al. Initial evaluation of coronary images from 320-detector row computed tomography. *Int J Cardiovasc Imaging* 2008;24:535-546
147. Weigold WG, Olszewski ME, Walker MJ. Low-dose prospectively gated 256-slice coronary computed tomographic angiography. *International Journal of Cardiovascular Imaging* 2009;25:217-230
148. Doelken M, Struffert T, Richter G, et al. Flat-panel detector volumetric CT for visualization of subarachnoid hemorrhage and ventricles: preliminary results compared to conventional CT. *Neuroradiology* 2008;50:517-523
149. Doerfler A, Wanke I, Egelhof T, et al. Aneurysmal rupture during embolization with Guglielmi detachable coils: causes, management, and outcome. *AJNR Am J Neuroradiol* 2001;22:1825-1832
150. Engelhorn T, Rennert J, Richter G, Struffert T, Ganslandt O, Doerfler A. Myelography using flat panel volumetric computed tomography: a comparative study in patients with lumbar spinal stenosis. *Spine (Phila Pa 1976)* 2007;32:E523-527
151. Richter G, Engelhorn T, Struffert T, et al. Flat panel detector angiographic CT for stent-assisted coil embolization of broad-based cerebral aneurysms. *AJNR Am J Neuroradiol* 2007;28:1902-1908
152. Benndorf G, Klucznik RP, Strother CM. Images in cardiovascular medicine. Angiographic computed tomography for imaging of underdeployed intracranial stent. *Circulation* 2006;114:e499-500

153. Benndorf G, Claus B, Strother CM, Chang L, Klucznik RP. Increased cell opening and prolapse of struts of a neuroform stent in curved vasculature: value of angiographic computed tomography: technical case report. *Neurosurgery* 2006;58:ONS-E380; discussion ONS-E380
154. Engelhorn T, Struffert T, Richter G, et al. Flat panel detector angiographic CT in the management of aneurysmal rupture during coil embolization. *AJNR Am J Neuroradiol* 2008;29:1581-1584
155. Gupta V, Chugh M, Walia B, Vaishya S, Jha A. Digital subtraction angiography laboratory with inbuilt CT (DynaCT): Application during intracranial aneurysm embolization. *Neurology India* 2008;56:90-91
156. Heran NS, Song JK, Namba K, Smith W, Niimi Y, Berenstein A. The utility of DynaCT in neuroendovascular procedures. *AJNR Am J Neuroradiol* 2006;27:330-332
157. Biasi L, Ali T, Ratnam LA, Morgan R, Loftus I, Thompson M. Intra-operative DynaCT improves technical success of endovascular repair of abdominal aortic aneurysms. *J Vasc Surg* 2008
158. Biasi L, Ali T, Ratnam LA, Morgan R, Loftus I, Thompson M. A multicenter randomized trial of cryo stripping versus conventional stripping of the great saphenous vein. *J Vasc Surg* 2009;49:288-295
159. Biasi L, Ali T, Thompson M. Intra-operative dynaCT in visceral-hybrid repair of an extensive thoracoabdominal aortic aneurysm. *Eur J Cardiothorac Surg* 2008;34:1251-1252

160. Binkert CA, Alencar H, Singh J, Baum RA. Translumbal type II endoleak repair using angiographic CT. *J Vasc Interv Radiol* 2006;17:1349-1353
161. Irie K, Murayama Y, Saguchi T, et al. Dynact soft-tissue visualization using an angiographic C-arm system: initial clinical experience in the operating room. *Neurosurgery* 2008;62:266-272; discussion 272
162. Kim HC, Chung JW, An S, et al. Left inferior phrenic artery feeding hepatocellular carcinoma: angiographic anatomy using C-arm CT. *AJR Am J Roentgenol* 2009;193:W288-294
163. Kim HC, Chung JW, Park JH, et al. Transcatheter arterial chemoembolization for hepatocellular carcinoma: prospective assessment of the right inferior phrenic artery with C-arm CT. *J Vasc Interv Radiol* 2009;20:888-895
164. Meyer BC, Frericks BB, Voges M, et al. Visualization of hypervascular liver lesions During TACE: comparison of angiographic C-arm CT and MDCT. *AJR Am J Roentgenol* 2008;190:W263-269
165. Meyer BC, Witschel M, Frericks BB, et al. The value of combined soft-tissue and vessel visualisation before transarterial chemoembolisation of the liver using C-arm computed tomography. *Eur Radiol* 2009;19:2302-2309
166. Wallace MJ. C-Arm Computed Tomography for Guiding Hepatic Vascular Interventions. *Techniques in Vascular and Interventional Radiology* 2007;10:79-86
167. Lauritsch G, Boese J, Kemeth H. Towards cardiac angiographic computed tomography. In: *IEEE Nuclear Science Symposium Conference Record*, 2005:2350-2354

168. Lauritsch G, Boese J, Wigstro?m L, Kemeth H, Fahrig R. Towards cardiac C-arm computed tomography. *IEEE Transactions on Medical Imaging* 2006;25:922-934
169. Ector J, De Buck S, Nuyens D, et al. Adenosine-induced ventricular asystole or rapid ventricular pacing to enhance three-dimensional rotational imaging during cardiac ablation procedures. *Europace* 2009;11:751-762
170. Kempfert J, Falk V, Schuler G, et al. Dyna-CT during minimally invasive off-pump transapical aortic valve implantation. *Ann Thorac Surg* 2009;88:2041
171. Fahrig R, Dixon R, Payne T, Morin RL, Ganguly A, Strobel N. Dose and image quality for a cone-beam C-arm CT system. *Medical Physics* 2006;33:4541-4550
172. Boone JM. The trouble with CTDI100. *Medical Physics* 2007;34:1364-1371
173. Brenner DJ, McCollough CH, Orton CG. It is time to retire the computed tomography dose index (CTDI) for CT quality assurance and dose optimization. *Medical Physics* 2006;33:1189-1191
174. Dixon RL. A new look at CT dose measurement: beyond CTDI. *Med Phys* 2003;30:1272-1280
175. Mori S, Nishizawa K, Kondo C, Ohno M, Akahane K, Endo M. Effective doses in subjects undergoing computed tomography cardiac imaging with the 256-multislice CT scanner. *European Journal of Radiology* 2008;65:442-448
176. Nakonechny KD, Fallone BG, Rathee S. Novel methods of measuring single scan dose profiles and cumulative dose in CT. *Med Phys* 2005;32:98-109
177. Kyriakou Y, Richter G, Dorfler A, Kalender WA. Neuroradiologic applications with routine C-arm flat panel detector CT: evaluation of patient dose measurements. *AJNR Am J Neuroradiol* 2008;29:1930-1936

178. Greenberg RK, Lytle B. Endovascular repair of thoracoabdominal aneurysms. *Circulation* 2008;117:2288-2296
179. Iezzi R, Cotroneo AR, Filippone A, et al. Multidetector CT in Abdominal Aortic Aneurysm Treated with Endovascular Repair: Are Unenhanced and Delayed Phase Enhanced Images Effective for Endoleak Detection? *Radiology* 2006;241:915-921
180. Macari M, Chandarana H, Schmidt B, Lee J, Lamparello P, Babb J. Abdominal aortic aneurysm: can the arterial phase at CT evaluation after endovascular repair be eliminated to reduce radiation dose? *Radiology* 2006;241:908-914
181. Cobelli R, Zompatori M, De Luca G, Chiari G, Bresciani P, Marcato C. Clinical usefulness of computed tomography study without contrast injection in the evaluation of acute pulmonary embolism. *J Comput Assist Tomogr* 2005;29:6-12
182. Wittram C, Maher MM, Halpern EF, Shepard JA. Attenuation of acute and chronic pulmonary emboli. *Radiology* 2005;235:1050-1054
183. Numburi UD, Schoenhagen P, Flamm SD, et al. Feasibility of dual-energy CT in the arterial phase: Imaging after endovascular aortic repair. *AJR Am J Roentgenol* 2010;195:486-493
184. Tran DN, Straka M, Roos JE, Napel S, Fleischmann D. Dual-energy CT discrimination of iodine and calcium: experimental results and implications for lower extremity CT angiography. *Acad Radiol* 2009;16:160-171
185. Hubbell JH, Seltzer SM. Tables of x-ray mass attenuation coefficients and mass energy-absorption coefficients. 2004
<http://www.nist.gov/physlab/data/xraycoef/index.cfm>.

186. Roessl E, Proksa R. K-edge imaging in x-ray computed tomography using multi-bin photon counting detectors. *Phys Med Biol* 2007;52:4679-4696
187. Shikhaliev PM. Energy-resolved computed tomography: first experimental results. *Phys Med Biol* 2008;53:5595-5613
188. Halliburton SS. Recent technologic advances in multi-detector row cardiac CT. *Cardiol Clin* 2009;27:655-664
189. Leon MB, Smith CR, Mack M, et al. Transcatheter Aortic-Valve Implantation for Aortic Stenosis in Patients Who Cannot Undergo Surgery. *NEJM* 2010;363:1012-1015
190. Zajarias A, Cribier AG. Outcomes and safety of percutaneous aortic valve replacement. *J Am Coll Cardiol* 2009;53:1829-1836
191. Kapadia SR, Schoenhagen P, Stewart W, Tuzcu EM. Imaging for transcatheter valve procedures. *Curr Probl Cardiol* 2010;35:228-276
192. Messika-Zeitoun D, Serfaty JM, Brochet E, et al. Multimodal assessment of the aortic annulus diameter: implications for transcatheter aortic valve implantation. *J Am Coll Cardiol* 2010;55:186-194
193. Ng AC, Delgado V, van der Kley F, et al. Comparison of aortic root dimensions and geometries before and after transcatheter aortic valve implantation by 2- and 3-dimensional transesophageal echocardiography and multislice computed tomography. *Circ Cardiovasc Imaging* 2010;3:94-102
194. Otsuka M, Sugahara S, Nakamura M, et al. Optimal fluoroscopic view selection for percutaneous coronary intervention by multislice computed tomography. *Int J Cardiol* 2007;118:e94-96

195. Neubauer AM, Garcia JA, Messenger JC, et al. Clinical feasibility of a fully automated 3D reconstruction of rotational coronary X-ray angiograms. *Circ Cardiovasc Interv* 2010;3:71-79
196. Eide KR, Ødegaard A, Myhre HO, Lydersen S, Hatlinghus S, Haraldseth O. DynaCT during EVAR - A Comparison with Multidetector CT. *European Journal of Vascular and Endovascular Surgery* 2008
197. Rabitsch E, Celedin S, Kau T, Illiasch H, Hausegger K. Flat-panel CT as a new perinterventional imaging modality in aortic stentgraft procedures - Work in progress. *Flachdetektor-CT als ergänzende untersuchung bei der endoluminalen behandlung von thorakalen und abdominellen aortenaneurysmen - Erste klinische erfahrungen* 2008;180:127-133
198. Kriatselis C, Nedios S, Akrivakis S, et al. Intraprocedural Imaging of Left Atrium and Pulmonary Veins: A Comparison Study between Rotational Angiography and Cardiac Computed Tomography. *Pacing Clin Electrophysiol* 2010
199. Krishnaswamy A, Tuzcu EM, Kapadia SR. Three-dimensional computed tomography in the cardiac catheterization laboratory. *Catheter Cardiovasc Interv* 2010
200. Numburi UD, Kapadia SR, Schoenhagen P, Tuzcu EM, Von Roden M, Halliburton SS. Initial experience with aortic root C-arm CT during transcatheter aortic valve implantation in swine. Presented at: American Heart Association Scientific Sessions, Orlando, FL. 2009

201. John M, Liao R, Zheng Y, et al. System to guide transcatheter aortic valve implantations based on interventional C-arm CT imaging. *Med Image Comput Comput Assist Interv* 2010;13:375-382
202. Zheng Y, John M, Liao R, et al. Automatic aorta segmentation and valve landmark detection in C-arm CT: application to aortic valve implantation. *Med Image Comput Comput Assist Interv* 2010;13:476-483
203. Himbert D, Brochet E, Serfaty JM, Vahanian A. Contained aortic root rupture after transcatheter aortic valve implantation. *Eur Heart J* 2010
204. Joshi SB, Mendoza DD, Steinberg DH, et al. Ultra-low-dose intra-arterial contrast injection for iliofemoral computed tomographic angiography. *JACC Cardiovasc Imaging* 2009;2:1404-1411
205. Siewerdsen JH, Daly MJ, Bachar G, et al. Multi-mode C-arm fluoroscopy, tomosynthesis, and cone-beam CT for image-guided interventions: From proof of principle to patient protocols. In: *Progress in Biomedical Optics and Imaging - Proceedings of SPIE*, 2007
206. Brenner DJ. Is it time to retire the CTDI for CT quality assurance and dose optimization? *Medical Physics* 2005;32:3225-3226
207. Mori S, Endo M, Nishizawa K, et al. Enlarged longitudinal dose profiles in cone-beam CT and the need for modified dosimetry. *Medical Physics* 2005;32:1061-1069
208. Kyriakou Y, Deak P, Langner O, Kalender WA. Concepts for dose determination in flat-detector CT. *Physics in Medicine and Biology* 2008;53:3551-3566

209. Dixon RL, Ballard AC. Experimental validation of a versatile system of CT dosimetry using a conventional ion chamber: beyond CTDI100. *Med Phys* 2007;34:3399-3413
210. Lin PJ, Herrnsdorf L. Pseudohelical scan for the dose profile measurements of 160-mm-wide cone-beam MDCT. *AJR Am J Roentgenol* 2010;194:897-902
211. Rosengart TK, Feldman T, Borger MA, et al. Percutaneous and minimally invasive valve procedures: a scientific statement from the American Heart Association Council on Cardiovascular Surgery and Anesthesia, Council on Clinical Cardiology, Functional Genomics and Translational Biology Interdisciplinary Working Group, and Quality of Care and Outcomes Research Interdisciplinary Working Group. *Circulation* 2008;117:1750-1767
212. Kronzon I, Matros TG. Intraoperative echocardiography in minimally invasive cardiac surgery and novel cardiovascular surgical techniques. *Am Heart Hosp J* 2004;2:198-204
213. Carroll JD. The future of image guidance of cardiac interventions. *Catheter Cardiovasc Interv* 2007;70:783
214. Vahanian A, Baumgartner H, Bax J, et al. Guidelines on the management of valvular heart disease: The Task Force on the Management of Valvular Heart Disease of the European Society of Cardiology. *Eur Heart J* 2007;28:230-268
215. Masson JB, Kovac J, Schuler G, et al. Transcatheter aortic valve implantation: review of the nature, management, and avoidance of procedural complications. *JACC Cardiovasc Interv* 2009;2:811-820

216. Leipsic J, Wood D, Manders D, et al. The evolving role of MDCT in transcatheter aortic valve replacement: a radiologists' perspective. *AJR Am J Roentgenol* 2009;193:W214-219
217. Tops LF, Wood DA, Delgado V, et al. Noninvasive evaluation of the aortic root with multislice computed tomography implications for transcatheter aortic valve replacement. *JACC Cardiovasc Imaging* 2008;1:321-330
218. Nordon IM, Hinchliffe RJ, Malkawi AH, et al. Validation of DynaCT in the morphological assessment of abdominal aortic aneurysm for endovascular repair. *J Endovasc Ther* 2010;17:183-189

APPENDICES

APPENDIX 1: Matlab code for calculating patient-specific contrast protocol

```
%%%%%%%%%%%%%%%%%%%%%%%%%%%%%%%%%%%%%%%%%%%%%%%%%%%%%%%%%%%%%%%%%%%%%%%%%%
%      MAIN FUNCTION TO CALCUALTE PATIENT-SPECIFIC INJECTIONS
%%%%%%%%%%%%%%%%%%%%%%%%%%%%%%%%%%%%%%%%%%%%%%%%%%%%%%%%%%%%%%%%%%%%%%%%%%

clear all
clc

global t c len test_time test_inj test_enh start_time_test_enh
stop_time_test_enh impulse_response scan_delay scan_duration target_enh

% ENTER WEIGHT and HEIGHT
wt_lbs=input('weight in lbs =');
ht_in=input('height in inches =');

wt_kg=0.4536*wt_lbs;
ht_m= 2.54*ht_in/100;

%%%%%%%%%%%%%%%%%%%%%%%%%%%%%%%%%%%%%%%%%%%%%%%%%%%%%%%%%%%%%%%%%%%%%%%%%%
% CALCULATE PATIENT PARAMETERS: WT, HT, BMI, BSA
%%%%%%%%%%%%%%%%%%%%%%%%%%%%%%%%%%%%%%%%%%%%%%%%%%%%%%%%%%%%%%%%%%%%%%%%%%
% CALCULATE BMI & BSA
BMI=wt_kg/ht_m^2;
BSA=(sqrt(wt_kg*ht_m*100))/60;
% BSA=0.1173*wt_kg^0.6466

% Input Baseline Attenuation (HU of blood) from Control Scan
base_enh=input('baseline attenuation from control scan (HU) =');

% Input Test Bolus Data from DynaEval text document.
% matrix = input('\n enter the test enhancement curve \n');

time=matrix(1:2:length(matrix));
enh = matrix(2:2:length(matrix));

time=round(time);
temp_enh=enh-base_enh;
for i = 1:length(temp_enh)
    if temp_enh(i)<0
        temp_enh(i)=0;
    end
end

end

max_index=find(temp_enh==max(temp_enh));
min_index=find(temp_enh(1:max_index)==min(temp_enh(1:max_index)));
base_time=time(min_index(length(min_index)));
temp_time=time-base_time;
```



```

time_start=time(1);
time_stop=round(time(length(time)));
xx=time_start:1:time_stop;
% yy=interp1(time,enh,xx);
yy1 = spline(time,enh,xx);
subplot(2,1,2);
plot(time,enh,'d',xx,yy1,'--');legend('original','spline')
xlabel('Time (sec)');
ylabel('Relative Enhancement (\Delta HU)');
plot(time,enh,'d',xx,yy,'*',xx,yy1,'--');
legend('original','interp1','spline')

%%%%%%%%%%%% Input Test Injection Volume & Flow Rate %%%%%%%%%%%%%%
test_time=[0:1:60];
len=length(test_time);
test_inj_fr=input('\n test injection flow rate =');
test_inj_vol=input('\n test injection volume =');
%Calculate Cardiac Output
CO=25*r_sq*test_inj_vol/AUC*1000/60;

test_inj_dur=floor(test_inj_vol/test_inj_fr);
secondary_fr=rem(test_inj_vol,test_inj_fr);
test_inj_initial=[0 test_inj_fr*ones(1,test_inj_dur) secondary_fr];
test_inj=[test_inj_initial zeros(1,len-length(test_inj_initial))];
test_inj_vol_sum=trapz(test_time,test_inj);
fprintf('\n Contrast volume in test injection= % 2.0f ml\n',test_inj_vol_sum)

start_time_test_enh=round(time(1));
stop_time_test_enh=round(time(length(time)));
test_enh_initial=[zeros(1,start_time_test_enh) yy1];
test_enh=[test_enh_initial zeros(1,len-length(test_enh_initial))];
%%%%%%%%%%%%%%%%%%%%%%%%%%%%%%%%%%%%%%%%%%%%%%%%%%%%%%%%%%%%%%%%%%%%%%%%
% CALCULATE IMPULSE RESPONSE AND EFFECTIVE TEST INJECTION
%%%%%%%%%%%%%%%%%%%%%%%%%%%%%%%%%%%%%%%%%%%%%%%%%%%%%%%%%%%%%%%%%%%%%%%%
% CONSTRAINS FOR FINDING IMPULSE RESPONSE:
%----- BOUNDARIES -----
% 1) LOWER BOUNDARY: IMPULSE RESPONSE CANNOT BE NEGATIVE
%----- INEQUALITIES-----
% 2) IMPULSE RESPONSE FROM TIME=0 SEC TO 8 SEC IS ZERO
%%%%%%%%%%%%%%%%%%%%%%%%%%%%%%%%%%%%%%%%%%%%%%%%%%%%%%%%%%%%%%%%%%%%%%%%
lb = [zeros(1,len)]; % Set lower bounds
ub = [];

% MAKE ALL IMPULSE RESPONSE LESS THAN T=8 SECONDS EQUAL TO ZERO
for i=1:9
    Aeq(i,:)=[zeros(1,i-1) 1 zeros(1,len-i)];
end
beq=zeros(1,9)';

%%%%%%%%%%%%%%%%%%%%%%%%%%%%%%%%%%%%%%%%%%%%%%%%%%%%%%%%%%%%%%%%%%%%%%%% Initial Values for Impulse Response %%%%%%%%%%%%%%
imp_resp=[zeros(1,len)];

%-----SOLVER TO CALCULATE IMPULSE FUNCTION -----
z = fmincon(@impulsefunction,imp_resp,[],[],Aeq,beq,lb,ub,[],...
optimset('MaxFunEvals',10000));

```

```

impulse_response=z;

%-----COMPUTE CONVOLVED TEST ENHANCEMENT-----
k=1;
for j = 1:len
    l=1;
    for i = k:len
        a(i,j)=test_inj(j)*impulse_response(l);
        l=l+1;
    end
    k=k+1;
end

for i = 1:len
    tot(i)=sum(a(i,:));
end
convolved_enh=tot';

figure();
subplot(2,1,1); plot(test_time,impulse_response,'r-
',test_time,test_enh,'b*',test_time,convolved_enh,'k--');title('Test
Enhancement');legend('impulse','measured','convolved');
subplot(2,1,2); plot(test_time,test_inj,'--');title('Test Injection');
%%%%%%%%%%%%%%%%%%%%%%%%%%%%%%%%%%%%%%%%%%%%%%%%%%%%%%%%%%%%%%%%%%%%%%%%
%               END OF IMPULSE RESPONSE COMPUTATION
%%%%%%%%%%%%%%%%%%%%%%%%%%%%%%%%%%%%%%%%%%%%%%%%%%%%%%%%%%%%%%%%%%%%%%%%

%%%%%%%%%%%%%%%%%%%%%%%%%%%%%%%%%%%%%%%%%%%%%%%%%%%%%%%%%%%%%%%%%%%%%%%%
%               CALCULATE PAT-SP INJECTION
%%%%%%%%%%%%%%%%%%%%%%%%%%%%%%%%%%%%%%%%%%%%%%%%%%%%%%%%%%%%%%%%%%%%%%%%
% CONSTRAINTS FOR FINDING PAT-SP INJECTION:
%----- BOUNDARIES -----
% 1) LOWER BOUNDARY: FLOW RATES CANNOT BE NEGATIVE
% 2) UPPER BOUNDARY: FLOW RATES CANNOT BE GREATER THAN 5.5 ML/SEC
%----- INEQUALITIES-----
% 3) SUM OF TEST INJECTION >= 0
% 4) FLOW RATE OF INJECTION (i+1) <= FLOW RATE OF INJECTION(i) (i.e.,
% MONOTONOUS DECREASING INJECTION
%----- EQUALITIES-----
% 5) FLOW RATE OF TEST INJECTION AT TIME=0 SEC IS 0 ML/SEC
%%%%%%%%%%%%%%%%%%%%%%%%%%%%%%%%%%%%%%%%%%%%%%%%%%%%%%%%%%%%%%%%%%%%%%%%
fprintf('Time to Peak = %2d sec
\n',test_time(find(max(test_enh)==test_enh)));
scan_delay=input('Enter the scan delay desired =');
scan_duration=input('Enter the scan duration =');
desired_enh=input('Enter the desired enhancement level =');
target_enh=desired_enh-base_enh;

lb1 = [zeros(1,len)]; % Set lower bounds
ub1 = [0 5.5*ones(1,len-1)];

% BOUNDARY CONDITIONS
Aeq1=[1 zeros(1,len-1)];
temp_ind=2;
for i=25:len

```

```

        Aeq1(temp_ind,:)= [zeros(1,i-1) 1 zeros(1,len-i)];
        temp_ind=temp_ind+1;
    end
    beq1=zeros(1,1+length(25:len))';

temp_ind=1;
for i=2:25
    A1(temp_ind,:)= [zeros(1,i-1) -1 1 zeros(1,len-(i+1))];
    temp_ind=temp_ind+1;
end

b1=zeros(1,1+length(2:24))';

temp_time = scan_delay:1:scan_delay+scan_duration;
aa=1;
for i = scan_delay:1:scan_delay+scan_duration
    target_enh_matrix(aa)=target_enh;
    aa=aa+1;
end

initial_vals=[0 ones(1,test_inj_dur*10) zeros(1,len-1-
test_inj_dur*10)];

%-----SOLVER TO CALCULATE PATIENT-SPECIFIC INJECTION-----

z1 =
fmincon(@patspinjfunction,initial_vals,A1,b1,Aeq1,beq1,lb1,ub1,[],optim
set('MaxFunEvals',10000,'TolFun',1e-20,'TolX',1e-20));

pat_sp_inj=z1;
% calculate the diagnostic enhancement using convolution of the pat-
specific injection and impulse response
k=1;
for j = 1:len
    l=1;
    for i = k:len
        a1(i,j)=pat_sp_inj(j)*impulse_response(l);
        l=l+1;
    end
    k=k+1;
end

for i = 1:len
    tot1(i)=sum(a1(i,:));
end
diag_enh=tot1';

pat_sp_inj1=pat_sp_inj;
indices=find(pat_sp_inj1);
k=1;
for i=1:length(indices)
    if (indices(length(indices)) > 25 || indices(1)>5)
        fprintf('\n CHECK CHECK CHECK....the injection duration may be
extremely long OR the injection doesn \'\t start early ?');
    end
end

if pat_sp_inj1(indices(i))<=0.4

```

```

    pat_sp_inj1(indices(i))=0;
end

if abs(pat_sp_inj1(indices(i))-pat_sp_inj1(indices(i)-1)) <=0.6
    pat_sp_inj1(indices(i))=pat_sp_inj1(indices(i)-1);
end
end

figure();
subplot(2,1,1); plot(temp_time,
target_enh_matrix,'*',test_time,diag_enh,'r--');title('Diagnostic
Enhancement');legend('target','predicted');
subplot(2,1,2); plot(test_time,pat_sp_inj,'-',test_time,pat_sp_inj1,'-
');title('Patient Specific Injection');legend('original','modified');
fprintf('\n \n-----\n');
fprintf('\n Contrast volume in original patient-specific injection=
%3.0f ml \n Contrast volume in modified patient-specific
injection= %3.0f ml \n',sum(pat_sp_inj),sum(pat_sp_inj1));
fprintf('-----\n \n \n');

break_val=0;
pat_sp_inj_duration=find(pat_sp_inj1);
brk=1;
for i=1:pat_sp_inj_duration(length(pat_sp_inj_duration))
    if pat_sp_inj1(i+1)~=pat_sp_inj1(i)
        break_val(brk)=i+1;
        brk=brk+1;
    end
end
fprintf('|-----|');
fprintf('\n|PATIENT-SPECIFIC PROTOCOL FROM LTI MODELING | \n');
fprintf('|-----| \n');
fprintf('| PHASE | FLOW RATE (ML/S) \t VOLUME (ML) \t DURATION(S) \n');
fprintf('|-----| \n');
    % Construct phases and volumes of injection
    no_of_phases=length(break_val)-1;
    for i=1:no_of_phases
        phase_volume(i)=sum(pat_sp_inj1(break_val(i):break_val(i+1)-1));
        phase_fr(i)=pat_sp_inj1(break_val(i));
        phase_dur(i)=phase_volume(i)./phase_fr(i);
        fprintf('| %d\t\t %2.1f \t\t\t\t\t %3.0f \t\t\t\t %3.0f \t\t\t\t
| \n',i, phase_fr(i),phase_volume(i),phase_dur(i));
    end
fprintf('|-----| \n');
fprintf('| TOTAL \t\t\t\t \t\t\t\t\t %3.0f \t\t\t\t %3.0f \t
| \n',sum(pat_sp_inj1),sum(phase_dur));
fprintf('|-----| \n \n \n');

```

```

%%%%%%%%%%%%%%%%%%%%%%%%%%%%%%%%%%%%%%%%%%%%%%%%%%%%%%%%%%%%%%%%%%%%%%%%
%      FUNCTION 1: TO CALCUALTE GAMMA FIT
%%%%%%%%%%%%%%%%%%%%%%%%%%%%%%%%%%%%%%%%%%%%%%%%%%%%%%%%%%%%%%%%%%%%%%%%

function e = functionforgammafit(v)

global t c

k = v(1);
a = v(2);
b = v(3);

for i = 1:length(c)
    d(i)=k*((t(i))^a)*(exp(-t(i)/b));
end
for i=1:length(c)
    diff(i)=(c(i)-d(i))^2;
end
e=sum(diff);

%%%%%%%%%%%%%%%%%%%%%%%%%%%%%%%%%%%%%%%%%%%%%%%%%%%%%%%%%%%%%%%%%%%%%%%%
%      FUNCTION 2: TO CALCUALTE IMPULSE RESPONSE
%%%%%%%%%%%%%%%%%%%%%%%%%%%%%%%%%%%%%%%%%%%%%%%%%%%%%%%%%%%%%%%%%%%%%%%%

% THIS FUNCTION HELPS TO CALCULATE THE IMPULSE RESPONSE OF A PATIENT.
function e = impulsefunction(imp_resp)
global len test_time test_inj test_enh start_time_test_enh
stop_time_test_enh

% "INJ" IS THE DEFINITION OF TEST INJECTION FOR EVERY 1 SECOND.
% "C" IS THE DEFINITION OF THE MEASURED TEST ENHANCEMENT OBTAINED FOR
% EVERY 2 SECONDS.
% THE INITIAL VALUES OF THE IMPULSE ARE USED AND MODIFIED SUCH THAT THE
% DIFFERENCE BETWEEN CONVOLVED TEST ENHANCEMENT AND THE MEASURED TEST
% ENHANCEMENT IS ZERO.
imp=imp_resp;
k=1;

for j = 1:len
    l=1;
    for i = k:len
        imp(l)>=0;
        a(i,j)=test_inj(j)*imp(l);
        l=l+1;
    end
    k=k+1;
end

for i = 1:len
    tot(i)=sum(a(i,:));
end

```

```

diff(1:len)=0;

for i = 1:len
    diff(i)=(tot(i)-test_enh(i))^2;
end

e=sum(diff);

%%%%%%%%%%%%%%%%%%%%%%%%%%%%%%%%%%%%%%%%%%%%%%%%%%%%%%%%%%%%%%%%%%%%%%%%%%%%%%
%      FUNCTION 3: TO CALCUALTE IMPULSE RESPONSE
%%%%%%%%%%%%%%%%%%%%%%%%%%%%%%%%%%%%%%%%%%%%%%%%%%%%%%%%%%%%%%%%%%%%%%%%%%%%%%
function e = patspinjfunction(initial_vals)
global len scan_delay scan_duration target_enh impulse_response
test_time

patspinj=initial_vals;
k=1;

for j = 1:len
    l=1;
    for i = k:len
        a(i,j)=patspinj(j)*impulse_response(l);
        l=l+1;
    end
    k=k+1;
end

for i = 1:len
    tot(i)=sum(a(i,:));
end

diff(1:len)=0;
for i = scan_delay+1:1:scan_delay+scan_duration+12
    if (i>=scan_delay+1 && i<=scan_delay+scan_duration+1)
        diff(i)=(tot(i)-target_enh)^2;
    end
end

e=sum(diff);

```

APPENDIX 2: Matlab code for generating VNC image using three-material decomposition based on combined basis spectral and basis material approach.

```

%%%%%%%%%%%%%%%%%%%%%%%%%%%%%%%%%%%%%%%%%%%%%%%%%%%%%%%%%%%%%%%%%%%%%%%%%%%%%%
%      Main Function to perform 3-material decomposition based on %
%      combined basis spectral and basis material approach      %
%%%%%%%%%%%%%%%%%%%%%%%%%%%%%%%%%%%%%%%%%%%%%%%%%%%%%%%%%%%%%%%%%%%%%%%%%%%%%%

clear all;
clc;

%%%%%%%%%%%%%%%%%%%%%%%%%%%%%%%%%%%%%%%%%%%%%%%%%%%%%%%%%%%%%%%%%%%%%%%%%%%%%% Global Variables%%%%%%%%%%%%%%%%%%%%%%%%%%%%%%%%%%%%%%%%%%%%%%%%%%%%%%%%%%%%%%%%%%%%%%%%%%%%%%
global i j c rho_100_value rho_140_value fn1_100 fn2_100 fn3_100
fn1_140 fn2_140 fn3_140 fn1_100 fn2_100 fn3_100 F_value_pass
mu_tiss_meas_100_pass mu_tiss_meas_140_pass mu_tiss_meas_100_pass
mu_tiss_meas_diff_pass

%%%%%%%%%%%%%%%%%%%%%%%%%%%%%%%%%%%%%%%%%%%%%%%%%%%%%%%%%%%%%%%%%%%%%%%%%%%%%% Initializing Matrices %%%%%%%%%%%%%%%%%%%%%%%%%%%%%%%%%%%%%%%%%%%%%%%%%%%%%%%%%%%%%%%%%%%%%%%%%%%%%%%
Z_matrix = zeros(512,512);
rho_100_matrix = zeros(512,512);
rho_140_matrix = zeros(512,512);
mass_frac_water = zeros(512,512);
mass_frac_HA = zeros(512,512);
mass_frac_UV = zeros(512,512);

%%%%%%%%%%%%%%%%%%%%%%%%%%%%%%%%%%%%%%%%%%%%%%%%%%%%%%%%%%%%%%%%%%%%%%%%%%%%%%
% Read f1, f2, and F values for different Z (F vs Z curve) %
%%%%%%%%%%%%%%%%%%%%%%%%%%%%%%%%%%%%%%%%%%%%%%%%%%%%%%%%%%%%%%%%%%%%%%%%%%%%%%
file=dlmread('FvsZ_def.txt');
Z_temp=file(:,1);
f1_temp=file(:,2);
f2_temp=file(:,3);
F_temp=file(:,4);
len=length(F_temp);

%%%%%%%%%%%%%%%%%%%%%%%%%%%%%%%%%%%%%%%%%%%%%%%%%%%%%%%%%%%%%%%%%%%%%%%%%%%%%% Interpolate data for f1, f2 and F %%%%%%%%%%%%%%%%%%%%%%%%%%%%%%%%%%%%%%%%%%%%%%%%%%%%%%%%%%%%%%%%%%%%%%%%%%%%%%%
Z = 0:.001:30;
f1 = spline(Z_temp,f1_temp,Z);
f2 = spline(Z_temp,f2_temp,Z);
F= (f1./f2);
plot(Z_temp,F_temp,'*',Z,F,'-');
F= round(F.*10^4);

%%%%%%%%%%%%%%%%%%%%%%%%%%%%%%%%%%%%%%%%%%%%%%%%%%%%%%%%%%%%%%%%%%%%%%%%%%%%%% Specify paths for the two DECT images %%%%%%%%%%%%%%%%%%%%%%%%%%%%%%%%%%%%%%%%%%%%%%%%%%%%%%%%%%%%%%%%%%%%%%%%%%%%%%%

inputPath = ['C:\Documents and
Settings\numburu\Desktop\DUAL_ENERGY_FLASH\P27\'];
outputPath = ['C:\Documents and
Settings\numburu\Desktop\DUAL_ENERGY_FLASH\P27\VNC'];

```



```

%%%%%%%%%%%%%%%%%%%%%%%%%%%%%%%%%%%%%%%%%%%%%%%%%%%%%%%%%%%%%%%%%%%%%%%% Specify number of images %%%%%%%%%%%%%%%%%%%%%%%%%%%%%%%%%%%%%%%%%%%%%%%%%%%%%%%%%%%%%%%%%%%%%%%%%
total_images=input(' ');

for imageNum = 1:total_images
%-----
%                               Read the Higher kV image:
%-----

    if (i>=1 && i<10)
        inputFile = dir([inputPath 'P27.*.000' num2str(imageNum) '.*.IMA']);
    elseif (i>=10 && i<100)
        inputFile = dir([inputPath 'P27.*.00' num2str(imageNum) '.*.IMA']);
    elseif (i>=100 && i<999)
        inputFile = dir([inputPath 'P27.*. 0' num2str(imageNum) '.*.IMA']);
    end

    inputFileName = [inputPath inputFile.name];
    info_140 = dicominfo(inputFileName);
    X_140 = dicomread(info_140);

%-----
%                               Read the Lower kV image:
%-----

    if (i>=1 && i<10)
        inputFile1 = dir([inputPath 'P27.*.000' num2str(imageNum) '.*.IMA']);
    elseif (i>=10 && i<100)
        inputFile1 = dir([inputPath 'P27.*.00' num2str(imageNum) '.*.IMA']);
    elseif (i>=100 && i<999)
        inputFile1 = dir([inputPath 'P27.*.0' num2str(imageNum) '.*.IMA']);
    end

    inputFileName1 = [inputPath inputFile1.name];
    info_100 = dicominfo(inputFileName1);
    X_100= dicomread(info_100);

%%%%%%%%%%%%%%%%%%%%%%%%%%%%%%%%%%%%%%%%%%%%%%%%%%%%%%%%%%%%%%%%%%%%%%%% Calculate CT Number %%%%%%%%%%%%%%%%%%%%%%%%%%%%%%%%%%%%%%%%%%%%%%%%%%%%%%%%%%%%%%%%%%%%%%%%%

    HU140=double(X_140)-1024;
    HU100=double(X_100)-1024;
    slope=(HU140-HU100)/(140-100);
    intercept=(HU140-slope.*140);

%-----
%   APPLY MEDIAN FILTER FOR LOW AND HIGH ENERGY IMAGES
%-----

    HU_140=medfilt2(HU140,[3 3]);
    HU_100=medfilt2(HU100,[3 3]);

%-----
%   LINEAR ATTENUATION COEFFICIENT OF WATER AT LOW AND HIGH ENERGY
%-----
%%%%%%%%%%%%%%%%%%%%%%%%%%%%%%%%%%%%%%%%%%%%%%%%%%%%%%%%%%%%%%%%%%%%%%%%
% For Flash: From summation of weighting function and NIST

```

```

% database for water
%%%%%%%%%%%%%%%%%%%%%%%%%%%%%%%%%%%%%%%%%%%%%%%%%%%%%%%%%%%%%%%%%%%%%%%%
mu_water_140=0.1783;
mu_water_100=0.2131;

%-----
% CALCULATE LINEAR ATTENUATION COEFFICIENT OF IMAGES AT LOW AND HIGH %
% ENERGY
%-----
mu_tiss_meas_100=(1+HU_100/1000).*mu_water_100;
mu_tiss_meas_140=(1+HU_140/1000).*mu_water_140;
F_value=mu_tiss_meas_100./mu_tiss_meas_140;

%-----
% OBTAINING HC AND HP MAPS FROM LOW AND HIGH ENERGY DATA
%-----
%STEP 1: CALIBRATION
Hw1 = -1;
Hw2 = -1;
Ha1 = -975;
Ha2 = -907;

%STEP 2: MEASURE QUALITY FACTOR WITH 1% KI SOLUTION
Hmki1 = 167;
Hmki2 = 89;

Hki1 = abs(1000*(Hmki1-Hw1)/(Hw1-Ha1));
Hki2 = abs(1000*(Hmki2-Hw2)/(Hw2-Ha2));

% For 1% KI solution: Hkic=3; Hkip=2430
Hkic = 3;
Hkip = 2430;
% Q1 = 100*(Hki1 - Hkic)/(Hkip-Hki1);
% Q2 = 100*(Hki2 - Hkic)/(Hkip-Hki2);
Q1=0.12;
Q2=0.078;

% for segmentation
Hm1=HU_140;
Hm2=HU_100;

H1 = 1000.*(Hm1-Hw1)./(Hw1-Ha1);
H2 = 1000.*(Hm2-Hw2)./(Hw2-Ha2);

difference = H2-H1;
num1 = Q1*(1+Q2)/(Q2-Q1);
num2 = (1+Q1)/(Q2-Q1);

Hc1 = H1-difference*num1;
Hp1 = H2+difference*num2;

Hc = H1 - ((H2-H1).*(Q1*(1+Q2)/(Q2-Q1)));
Hp = H2 + ((H2-H1).*((1+Q1)/(Q2-Q1)));

figure();imshow(Hc,[]);pixval on; title('Hc Map');
figure();imshow(Hp,[]);pixval on; title('Hp Map');

```

```

%-----
% CALCULATING VARIOUS INDICES USING 100 AND 140 KVP IMAGES
%-----
% DIFFERENCE BETWEEN 100 AND 140 KVP IMAGES
diff_img=HU_100-HU_140;
figure();imshow(diff_img);pixval on; title('Diff Image');

% DUAL ENERGY INDEX IMAGE FROM 100 AND 140 KVP IMAGES
num=imsubtract(HU_100,HU_140);
den=imadd(HU_100,HU_140);
DE_ind_img=imdivide(num,den);
figure();imshow(DE_ind_img);pixval on; title('DE_ind Image');

% DUAL ENERGY RATIO IMAGE FROM 100 AND 140 KVP IMAGES
DE_ratio=HU_100./HU_140;
figure();imshow(DE_ratio);pixval on; title('Ratio Image');

%-----
% IDENTIFY HIGH DENSITY PIXELS USING (1)DIFF, (2) DUAL ENERGY INDEX,
% (3) DUAL ENERGY RATIO), (4) HC AND (5) HP INFO
%-----
CF_im_pixels= ((diff_img > 50) & (DE_ind_img > 0) & (DE_ratio > 1.5) &
(Hc > 0) & (Hp < 0));

%-----
% MARK HIGH DENSITY PIXELS IN LOW AND HIGH ENERGY IMAGES
%-----
HU_100_1=CF_im_pixels.*HU_100;
HU_140_1=CF_im_pixels.*HU_140;

%-----
% PERFORM DUAL ENERGY OPTIMIZATION FOR THE PIXELS.
%-----

for i=1:512
    for j=1:512
% PERFORM DE OPTIMIZATION ONLY FOR HIGH DENSITY PIXELS IN
        if ((HU_100_1(i,j)> 0) && (HU_140_1(i,j)> 0))

            F_temp=round(F_value(i,j)*10^4);

            if (F_temp >= 11008 && F_temp <= 40856) % for FLASH
                ind = find(F==F_temp);
                while (isempty(ind))
                    F_temp = F_temp+1;
                    ind = find(F==F_temp);
                end

                % Find effective Z and rho values
                Z_value=Z(ind(1));
                rho_100_value=mu_tiss_meas_100(i,j)/f1(ind(1));
                rho_140_value=mu_tiss_meas_140(i,j)/f2(ind(1));
            end
        end
    end
end

```

```

        else
            Z_value=0;
            rho_100_value=0;
            rho_140_value=0;
        end

fprintf('Z= %2.3f, rho_100= %2.3f, rho_140= %2.3f \n', Z_value,
rho_100_value, rho_140_value);

    % Values to be passed to the optimization function
    F_value_pass=F_value(i,j);
    mu_tiss_meas_100_pass=mu_tiss_meas_100(i,j);
    mu_tiss_meas_140_pass=mu_tiss_meas_140(i,j);

%%%%%%%%%%%%%%%%%%%%%%%%%%%%%%%%%%%%%%%%%%%%%%%%%%%%%%%%%%%%%%%%%%%%%%%% FIND MASS FRACTIONS%%%%%%%%%%%%%%%%%%%%%%%%%%%%%%%%%%%%%%%%%%%%%%%%%%%%%%%%%%%%%%%%%%%%%%%%
    if Z_value<=0
        c=0;
    elseif Z_value<10
        c=1;
    elseif Z_value >= 10
        c=1.45-(0.05*Z_value);
    end

    if (Z_value<=0)
        Z_value=0;
        rho_100_value=0;
        rho_140_value=0;
        sol(1)=0; sol(2)=0; sol(3)=0;
    else

        % fn=integral(w.(mu/rho))
        %1-blood. 2- Ca. 3- Iodine
        fn1_100=0.2541;
        fn1_140=0.2060;

        fn2_100=0.8476;
        fn2_140=0.4461;

        fn3_100=7.3119;
        fn3_140=3.9724;

        x0 = [0.1; 0.1; 0.1];    % Starting guess at the solution

        A=[-1 0 0                % A*x<=B
            0 -1 0
            0 0 -1];
        b=[0
            0
            0];
        Aeq=[1 1 1];            % Aeq*x<=Beq
        Beq=[1];

        lb=0;
        ub=1;

```

```

options = optimset('TolFun',1e-20,'MaxFunEvals',10000);
sol = fminimax(@optim3,x0,A,b,Aeq,Beq,lb,ub,[],options);

end

fprintf('mass_fraction_water= %2.4f, mass_fraction_HA= %2.4f,
mass_fraction_I= %2.4f,\n', sol(1),sol(2),sol(3));

%-----
% FOR THE PIXELS, SHOW: (1)Z MATRIX, (2) DENSITY AT LOW KVP
% 3) DENSITY AT HIGH KVP, AND MASS FRACTION OF:
% (4)WATER, (5) HYDROXYAPATITE, AND (6) IOPROMIDE
%-----

        Z_matrix(i,j)= Z_value;
        rho_100_matrix(i,j) = rho_100_value;
        rho_140_matrix(i,j) = rho_140_value;
        mass_frac_water(i,j) = sol(1);
        mass_fract_HA(i,j) = sol(2);
        mass_fract_UV(i,j) = sol(3);

        end
    end
end

figure();imshow(rho_100_matrix,[]);pixval on; title('rho 100 matrix');
figure();imshow(rho_140_matrix,[]);pixval on;title('rho 140 matrix');
figure();imshow(Z_matrix,[]);pixval on;title('Z matrix');
figure();imshow(mass_frac_water,[]);pixval on;title('mass frac water');
figure();imshow(mass_fract_HA,[]);pixval on;title('mass fract HA');
figure();imshow(VNC_im,[]);pixval on;title('VNC');
figure();imshow(mass_fract_UV,[]);pixval on;title('mass fract UV');

%-----
%                                     GENERATE VNC IMAGE
%-----
bw=mass_fract_UV > 0; % Identify pixels which contain contrast
VNC=X_140; % Initialize VNC as 140 image
VNC=((HU_140-bw.*HU_140+mass_fract_UV.*HU_140)); % Create VNC image
figure();imshow(VNC,[]);pixval on;title('VNC');
VNC_im=medfilt2(VNC,[3 3]); % Filter VNC using a median filter
figure();imshow(VNC_im,[]);pixval on;title('VNC');

dicomwrite(VNC,'VNC_CT.117_approach3.dcm',info_140);

```

```

%-----
%           FUNCTION PERFORMING 3-MATERIAL DECOMPOSITION USING
%           NON-LINEAR OPTIMIZATION
%-----
function e = optim3(x0)
    global fn1_100 fn2_100 fn3_100 fn1_140 fn2_140 fn3_140 fn1_100
    fn2_100 fn3_100 F_value_pass mu_tiss_meas_100_pass
    mu_tiss_meas_140_pass mu_tiss_meas_100_pass % c rho_100_value
    rho_140_value fn1_diff fn2_diff fn3_diff mu_tiss_meas_diff_pass

    mf1=x0(1);
    mf2=x0(2);
    mf3=x0(3);
    rho1=1.06;
    rho2=3.2;
    rho3=2.06;

    % For Three Material decomposition
    rho_eff=mf1*rho1+mf2*rho2+mf3*rho3;

    mu_tiss_calc_100=rho_eff*(mf1*fn1_100 + mf2*fn2_100 +
    mf3*fn3_100);
    mu_tiss_calc_140=rho_eff*(mf1*fn1_140 + mf2*fn2_140 +
    mf3*fn3_140);
    mu_tiss_calc_100=rho_eff*(mf1*fn1_100 + mf2*fn2_100 +
    mf3*fn3_100);
    F_value_calc= %2.4f \n', mf1, mf2, mf2, F_value, F_value_calc);

    % ERROR value
    e=(1-sum_mf)^2+(mu_tiss_calc_100-
    mu_tiss_meas_80_pass)^2+(mu_tiss_calc_140-
    mu_tiss_meas_140_pass)^2+(mu_tiss_calc_100-
    mu_tiss_meas_100_pass)^2;

end

```

APPENDIX 3: Matlab code for interpolation using Savitzky-Golay filter

```

%%%%%%%%%%%%%%%%%%%%%%%%%%%%%%%%%%%%%%%%%%%%%%%%%%%%%%%%%%%%%%%%%%%%%%%%
%           MAIN FUNCTION FOR ENTERING DATA AND APPLYING FILTER
%%%%%%%%%%%%%%%%%%%%%%%%%%%%%%%%%%%%%%%%%%%%%%%%%%%%%%%%%%%%%%%%%%%%%%%%
global x y
x=[-145,-135,-125,-115,-105,-95,-85,-75,-65,-55,-45,-35,-26,-25,-24,-
23,-22,-21,-20,-19,-18,-17,-16,-15,-14,-13,-12,-11,-10,-9,-8,-7,-6,-5,-
4,-3,-2,-
1,0,1,2,3,4,5,6,7,8,9,10,11,12,13,14,15,16,17,18,19,20,21,22,23,24,25,2
6,35,45,55,65,75,85,95,105,115,125,135,145]';

%%%%%%%%%%%%%%%%%%%%%%%%%%%%%%%%%%%%%%%%%%%%%%%%%%%%%%%%%%%%%%%%%%%%%%%%
%           SAVITZKY-GOLAY (SG) FILTER
%%%%%%%%%%%%%%%%%%%%%%%%%%%%%%%%%%%%%%%%%%%%%%%%%%%%%%%%%%%%%%%%%%%%%%%%
N = 3;           % Order of polynomial fit
F = 5;           % Window length
[b,g] = sgolay(N,F); % Calculate SG coefficients

HalfWin = ((F+1)/2) -1;
ind=1;
for n = (F+1)/2:length(x)-(F+1)/2,
    x_val(ind)=x(n);
    y_val(ind)=y(n);
    dx(ind)=x(n)-x(n-1);
    % Zero-th derivative (for smoothing the data)
    SG0(ind) = dot(g(:,1), y(n - HalfWin: n + HalfWin));
    % 1st differential of the curve
    SG1(ind) = dot(g(:,2), y(n - HalfWin: n + HalfWin));
    % 2nd differential of the curve
    SG2(ind) = 2*dot(g(:,3)', y(n - HalfWin: n + HalfWin))';
    ind=ind+1;
end

SG1_1 = SG1./dx; % Convert 1st differential into 1st derivative
SG2_1 = SG2./(dx.*dx); % Convert 2nd differential into 2nd derivative

% Extrapolate SG curve fit data for 900 mm length
% For Left Side Extrapolation
ind=1;
for i=-125:-10:-450
    al=SG0(2);
    bl=SG1_1(2)/SG0(2);
    y_left_extrap_temp(ind)=al*exp(bl*(i-x_val(2)));
    ind=ind+1;
end
x_left_extrap_temp=[-125:-10:-450];

% Reverse the matrix from -450 to -125 instead of -125 to -450

```

```

        z=length(x_left_extrap_temp);
        for i = 1:z
            x_left_extrap(z)= x_left_extrap_temp(i);
            y_left_extrap(z)= y_left_extrap_temp(i);
            z=z-1;
        end

% For Right Side Extrapolation
len=length(x_val)-1;
ind_2=1;
for i=115:10:450
    ar=SG0(len);
    br=SG1_1(len)/SG0(len);
    y_rt_extrap(ind_2)=ar*exp(br*(i-x_val(len)));
    ind_2=ind_2+1;
end
x_rt_extrap=[115:10:450];

% SG filter values
x_SG_filt=[x_left_extrap_temp(3) x_left_extrap_temp(2)
x_left_extrap_temp(1) x(2:71)' x_rt_extrap(1:4)];
y_SG_filt=[y_left_extrap_temp(3) y_left_extrap_temp(2)
y_left_extrap_temp(1) SG0(2:71) y_rt_extrap(1:4)];

% Compute errors
for i = 1:length(x)
    err1(i)=(y(i)-y_SG_filt(i))^2;
end
SSE_SG=sum(err1);
RMSE_SG=sqrt(sum(err1)/length(y));

% Final Extrapolation Values for SG filter
x_SG_filt_extrap=[x_left_extrap x(4:73)' x_rt_extrap];
y_SG_filt_extrap=[y_left_extrap SG0(2:71) y_rt_extrap];

% Find AUC for the SG filter data
AUC_SG_extrap_300mm=trapz(x_SG_filt, y_SG_filt);
AUC_SG_extrap_900mm=trapz(x_SG_filt_extrap, y_SG_filt_extrap);

plot(x,y,'b.',x_SG_filt_extrap, y_SG_filt_extrap,'r*-');
axis([-300 300 0 1]);
grid
legend('original values', 'SG Filter 3rd degree interpolation');
xlabel('Longitudinal Distance (mm)');
ylabel('Relative Dose');

```


APPENDIX 4: Modeling of Contrast Agent Injection For Coronary MDCT With Short Scan Times Utilizing Test Bolus Data

A4.1 Introduction

The technology of multi-detector computed tomography (MDCT) has evolved rapidly since its inception, resulting in continuous improvements in cardiac imaging. State-of-the-art MDCT scanners with faster rotating gantries, increased numbers of detector rows (1-3), or additional x-ray sources (4) allow imaging of the heart with very short scan times (< 6 s). These technical advances have changed the paradigm of contrast injection for cardiac imaging: optimization of contrast administration is becoming increasingly important to insure adequate enhancement during imaging (5, 6).

These short scan times allow injection of lower contrast volumes for a short duration, resulting in a narrow peak enhancement curve during the diagnostic scan. In these situations, a low-volume test bolus is used for planning injection of the main contrast bolus and data acquisition during peak enhancement (4). Currently, the only information typically gathered from a test bolus is the time to peak maximal enhancement (tPME) to compute the scan delay, despite the availability of much more data about an individual patient's response to contrast agent. Although a few modeling techniques have customized diagnostic injection using patient-specific information obtained from a test bolus and the resulting attenuation curve (7-9), these techniques were developed for an earlier generation of scanners (1- and 16-slice scanners) with longer acquisition times.

However, this type of patient-specific modeling should also allow for optimization of contrast administration with the latest scanners, as well.

The use of a test bolus to either determine timing of a standard injection or to develop a patient-specific injection relies on a correspondence between the bolus geometries of a low-volume test bolus and a high-volume main bolus. However, studies have demonstrated moderate (10) to no (11) correlation between the tPMEs for a test and main bolus, indicating that there are differences between these boluses. This discrepancy is attributed to faster dispersion of the low-volume test bolus in the venous system compared with the high-volume main bolus, a difference that can be reduced with the administration of saline immediately following the test bolus of contrast (12). Although a saline chaser is routinely included with a test bolus, its impact on delivery of the small contrast bolus has not been quantitatively evaluated.

The objectives of this study were two-fold. First, we sought to systematically evaluate the impact of saline on contrast in a test bolus injection profile and the resulting test enhancement curve characteristics, including the tPME. We then sought to determine the average volume of contrast required for short scan time (6-, 4-, 2- and 1-s) cardiac MDCT from patient-specific contrast injection protocols modeled using test bolus data.

A4.2 Materials and Methods

The local institutional review board approved this study. This study also complies with the Health Insurance Portability and Accountability Act. A total of 25 patients who were referred for contrast-enhanced cardiac MDCT were enrolled after they provided informed consent. Patient age, sex, weight, and body mass index (BMI) were recorded.

Image Acquisition

All examinations were performed with an MDCT scanner (Sensation 64; Siemens Medical Solutions, Forchheim, Germany). Contrast agent (Ultravist 370; Berlex, Montville, N.J.) was administered to each patient through an 18-gauge needle in the antecubital vein with a dual power injector (Stellant D; Medrad Inc., Pittsburgh, Pa.) in accordance with standard clinical practice at the time of the study.

A single low-dose image was obtained near the carina, and a circular region-of-interest (ROI) was drawn in the ascending aorta (AA) to determine a baseline intensity value (attenuation without contrast agent). This was followed by the administration of 2 test bolus injections: test injection A, which consisted of 20 mL of contrast injected at 4.5 mL/s, and test injection B, which consisted of 20 mL of contrast followed by 60 mL (for patients weighing < 90 kg) or 80 mL (for patients weighing \geq 90 kg) of saline administered at 4.5 mL/s. The order of the test injections was randomized, and sufficient time was allowed between injections to eliminate any potential bias resulting from residual contrast from the previous injection. From 10 s through 44 s after each injection, a test scan was performed every 2 s at the same level (near the carina), with scan parameters as follows: number of images, 18; tube voltage, 120 kVp; and tube current-time product, 40-60 mAs. The time-attenuation curves in the AA resulting from each test bolus were measured using scanner software (Syngo; Siemens Healthcare) to determine the tPME. The scan delay time (time between the start of contrast injection and the start of the main/diagnostic scan) was defined as 3 s after tPME randomly obtained either from

test injection A or B. Standard contrast and imaging protocols for the diagnostic scan were then applied.

Data Analysis

Only data from the test injections and the test scans, not the main injection and scan, were analyzed for the current study. Test bolus attenuation values (indicating enhancement caused by contrast agent injection) were obtained by subtracting the baseline intensity measured in the AA from the time-attenuation curves in the AA resulting from the test injections.

A4.2.1 Test Bolus Contrast Injection

Applying tracer kinetics, the effective flow profile of contrast in the venous system with the test injections can be estimated. Fleischmann et al (7) suggested that a patient could be assumed as a linear time-invariant (LTI) system and arterial enhancement (*enh*) could be modeled as the convolution integral of the contrast agent flow rate (*inj*) and impulse response of the patient (response to a Dirac impulse input, *imp_resp*)

$$\text{enh}(t) = \int_0^t \text{imp_resp}(\tau) \cdot \text{inj}(t - \tau) \cdot d\tau \quad (1)$$

In the discrete domain, this can be approximated as

$$\text{enh}(n) = \sum_m \text{imp_resp}(m) \cdot \text{inj}(n - m) \quad (2)$$

where *m* is the number of data points of the test bolus attenuation curve. For each patient in this study, the two test bolus attenuation curves were used to estimate the effective contrast profile (volumes and flow rates) of both test injections using customized

software (Excel Solver; Microsoft Corporation, Redmond, Wash) (described in Section 7.2.2.1). The mean differences between the programmed and effective values of contrast volume and flow rate, as well as 95% confidence intervals and Bland-Altman limits of agreement (13), were calculated for both test injections.

A4.2.2 Test Bolus Attenuation Curve Characteristics

Various indices describing test bolus attenuation curves resulting from the test injections were computed. A gamma-variate curve was fitted to each of the test bolus attenuation curves to correct for recirculation of contrast agent; curve characteristics, including peak of maximal enhancement (PME), area under the curve (AUC), mean transit time (MTT), and rise time (RT), were computed from the gamma fit (14) using customized software (Matlab; The Mathworks, Inc., Natick, Mass). All curve characteristics including tPME were compared using paired Student *t* tests. The same analysis was repeated for the heaviest patients (≥ 90 kg) exclusively. A *P* value $\leq .05$ indicated statistical significance.

A4.2.3 Prediction of Contrast Injection for Short Scan Time Cardiac Imaging

Using test bolus data, we predicted patient-specific contrast injection profiles that would achieve uniform enhancement in the heart during cardiac MDCT. Hypothesizing that saline chase will impact tPME, scan delay was determined as 2 s + tPME from test injection B in each patient. Further, a desired diagnostic enhancement of 300 HU in the heart (15) was defined for a duration of 6 s after scan delay. Optimal patient-specific contrast injection protocols were computed using the patient's impulse response and the

target diagnostic enhancement (explained in section 7.2.2.2). The total number of contrast phases and volume and flow rate of contrast for each phase were determined for each patient; average values for the 25 patients were reported. Similarly, patient-specific injection profiles were computed to achieve 300 HU for 4-, 2-, and 1-s scan durations in all of the patients using the aforementioned approach. Through the use of paired Student *t* tests with Bonferroni adjustment, contrast volumes were compared between the 6- and 4-s scan durations; the 4- and 2-s scan durations; and the 2- and 1-s scan durations. A *P* value $\leq .05/3$ (.017) indicated statistical significance.

A4.3 Results

All 25 patients (16 men, 9 women) received two test injections and a single uniphasic diagnostic injection with no cases of extravasation. Patient information is summarized in Table A4.1.

Patient Characteristic	Mean Value for Study Patients (<i>N</i> = 25)
Age (y)	59 (30-71)
Weight (kg)	96 (59-135)
Height (m)	1.77 (1.5-1.96)
Body mass index (kg/m ²)	30.7 (20.3-44)
Note.—Data are mean values, with range in parentheses.	

Table A4.1: Patient Characteristics

A4.3.1 Test Bolus Contrast Injection

The effective flow of contrast agent with test injections A and B were successfully computed for all 25 patients. Results from a typical patient are shown in Figure A4-1.

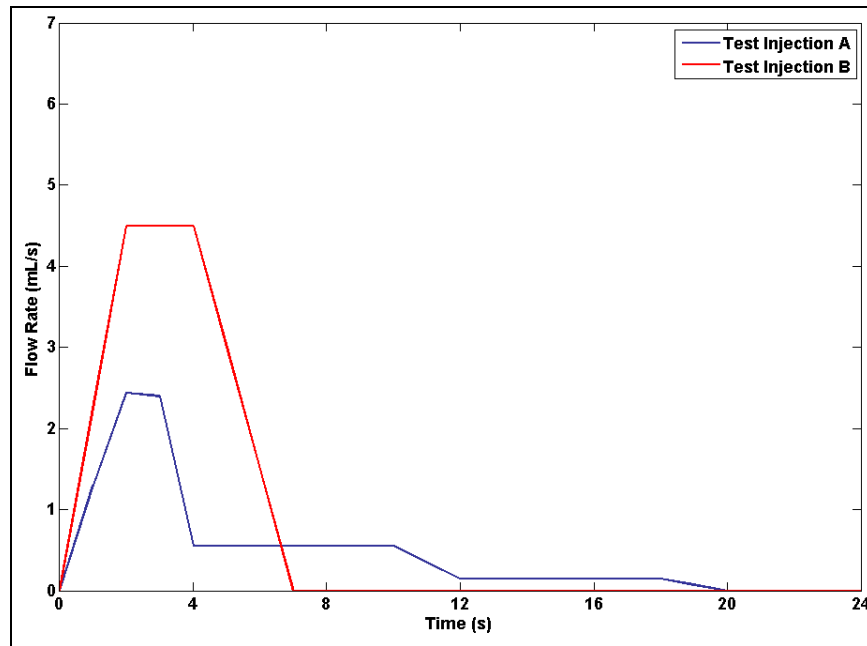


Figure A4-1: Effective flow profile of contrast agent injected with test injections A (20 mL contrast only) and B (20 mL contrast followed by saline) in 71-year-old man weighing 74 kg. Use of 60 mL saline chaser resulted in injection of the entire 20 mL of contrast at an effective rate of 4.5 mL/s; without saline, only 13 mL of contrast was delivered at a rate of 2.4 mL/s.

The injector administered 20 mL of contrast at 4.5 mL/s for both test injections. On average, however, only 13 mL of contrast was effectively delivered at 2.2 mL/s with test injection A. With the use of saline after test injection B, the entire 20 mL of contrast was injected at an effective rate of 4.4 mL/s. The mean difference, 95% confidence

interval for the mean difference, and Bland-Altman limits of agreement for volume and flow rate were smaller for test injection B than for test injection A (Table A4.2), indicating that programmed values were closer to being realized when saline was used after contrast agent in a test bolus.

	Program- med Value	Effective Value	Mean Difference	95% CI	Limits of Agreement
	Average volume of contrast (mL)				
Test injection A (20 mL contrast)	20 ± 0	13 ± 3	7.2 ± 3.4	5.8, 8.6	0.5, 13.9
Test injection B (20 mL contrast followed by 60/80 mL saline)		20 ± 1	0.4 ± 1.3	0, 0.9	0, 2.9
	Average flow rate of contrast (mL/s)				
Test injection A (20 mL contrast)	4.5 ± 0	2.2 ± 0.8	2.4 ± 0.8	2.0, 2.7	0.7, 4.0
Test injection B (20 mL contrast followed by 60/80 mL saline)		4.4 ± 0.2	0.0 ± 0.2	0, 0.1	0, 0.4
Note: Data are mean ± standard deviation for programmed, effective, and mean difference values. CI indicates the 95% confidence intervals for mean difference. Limits of agreement are the Bland-Altman limits, indicating that 95% of all individual differences in patients lie within these limits.					

Table A4.2: Impact of Saline on Contrast Volume and Flow Rate and Comparison with Values Programmed in the Injector.

A4.3.2 Test Bolus Attenuation Curve Characteristics

Injection of a saline chaser after test injection B significantly decreased tPME values in the AA (mean decrease, 1.7 s) for the entire group of patients compared with patients who received test injection A (Table A4.3). In the subset of the 11 heavy patients (weight, ≥ 90 kg), an 80-mL saline chaser reduced the average tPME by 2.7 s.

Gamma fit was successfully computed for the two test enhancement curves in all but one obese patient (BMI=42.6 kg/m²). In this patient, a gamma curve could not be fitted to the enhancement curve resulting from test injection A, so this case was eliminated from further analysis. Among the remaining 24 patients, test injection B resulted in a significantly higher PME and AUC and a shorter MTT than test injection A (Table A4.3). The same patterns were observed in the subset of heavy patients. Although the average RT was reduced with test injection B for the entire group and in the subset of heavy patients, the difference was only significant in the heavy group.

Curve Characteristics	<i>n</i>	Test Injection A -(20 mL contrast)	Test Injection B (20 mL contrast followed by 60/80 mL saline)	Mean Difference
All patients				
tPME (s)	25	21.1 ± 4.5	19.4 ± 3.5	-1.7*
PME (HU)	24	67 ± 23	151 ± 27	84*
AUC (HU-s)	24	935 ± 567	1458 ± 378	523*
MTT (s)	24	13.0 ± 14.8	10.4 ± 3.3	-2.6*
RT (s)	24	9.2 ± 6.9	8.6 ± 3.1	-0.5
Heavy patients (≥ 90 kg)				
tPME (s)	11	21.3 ± 4.8	18.5 ± 2.5	-2.7*
PME (HU)	10	61 ± 19	149 ± 25	88*
AUC (HU-s)	10	846 ± 381	1229 ± 303	383*
MTT (s)	10	13.0 ± 6.0	9.0 ± 2.3	-4.0*
RT (s)	10	9.1 ± 3.2	7.5 ± 2.1	-1.6*

Data are mean \pm standard deviation. n indicates number of patients contributing to mean values. Mean difference is the average difference in curve characteristics between test injections A and B.
tPME = time to PME, PME = peak of maximal enhancement, AUC = area under the curve, MTT = mean transit time, RT = rise time;
* Significant difference at a P value $\leq .05$ according to paired Student t test.

Table A4.3: Impact of Saline (60/80 mL) on Test Bolus Attenuation Curve Characteristics in the Ascending Aorta.

A4.3.3 Prediction of Contrast Injection for Short Scan Time Cardiac Imaging

Contrast injection profiles required to achieve the target enhancement during a 6-s (Figure A4-2), 4-s (Figure A4-3), 2-s (Figure A4-4), and 1-s (Figure A4-5) scan were predicted for all 25 patients. All patient-specific contrast profiles could generally be described as biphasic.

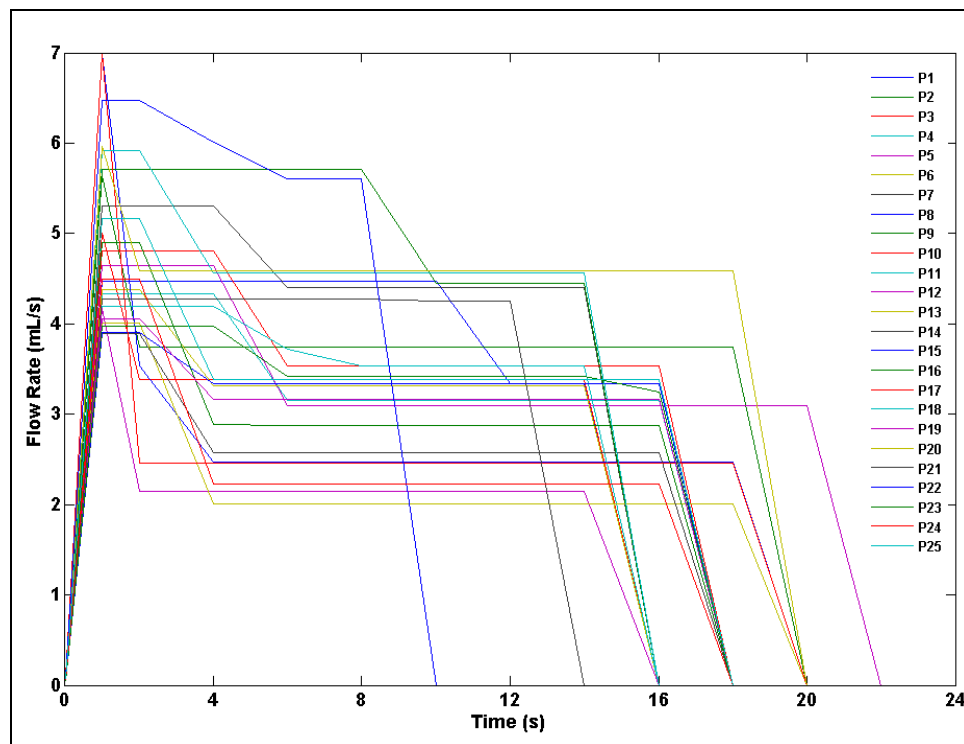


Figure A4-2: Patient-specific contrast profiles predicted to achieve a constant attenuation of 300 HU during a 6-s cardiac scan. Injections were computed for 25 patients from LTI modeling.

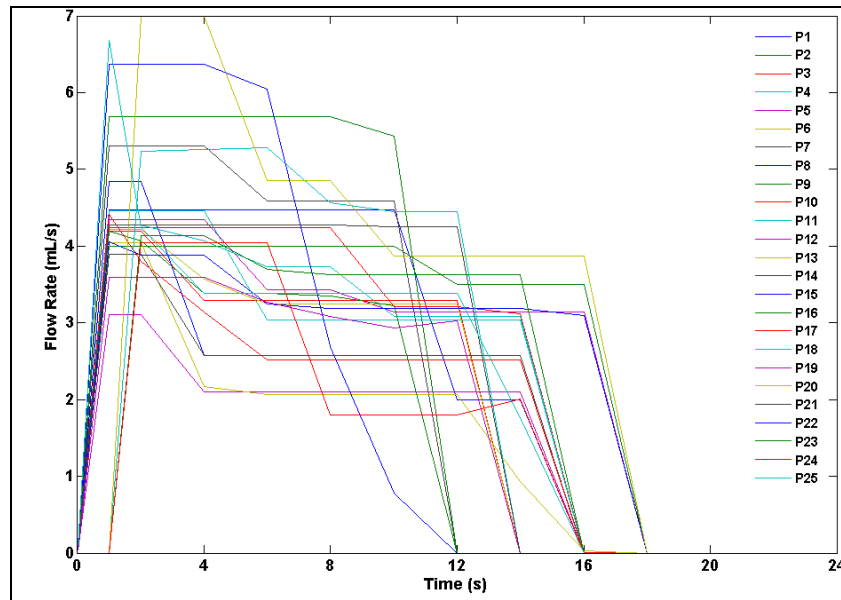


Figure A4-3: Patient-specific contrast profiles predicted to achieve a constant attenuation of 300 HU during a 4-s cardiac scan. Injections were computed for 25 patients from LTI modeling.

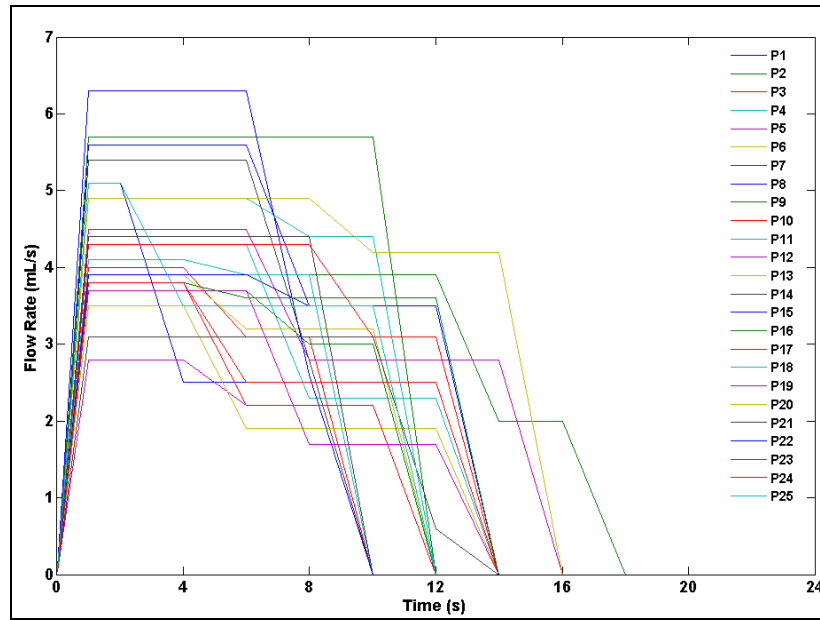


Figure A4-4: Patient-specific contrast profiles predicted to achieve a constant attenuation of 300 HU during a 2-s cardiac scan. Injections were computed for 25 patients from LTI modeling.

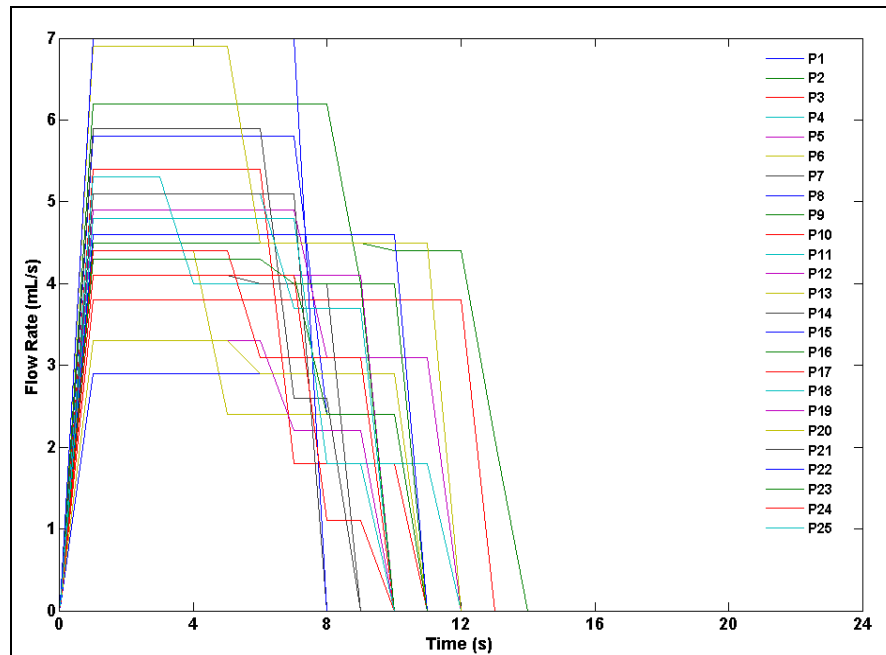


Figure A4-5: Patient-specific contrast profiles predicted to achieve a constant attenuation of 300 HU during a 1-s cardiac scan. Injections were computed for 25 patients from LTI modeling.

For a 6-s scan duration, an average volume of 23 mL injected at 4.9 mL/s for 5 s was required for phase 1, followed by an average volume of 41 mL injected at 3.5 mL/s for 12 s for phase 2 (Table A4.4). Therefore, a total volume of 64 mL of contrast injected over 17 s may be appropriate for a 6-s scan. Reduction of the scan duration from 6 to 4, 2, and 1 s resulted in a decrease of the average total contrast volume (from 64 to 55, 46, and 40 mL, respectively) and flow rate in both phase 1 (from 4.9 to 4.6, 4.3, and 4.1 mL/s, respectively) and phase 2 (from 3.5 to 3.3, 2.8, and 2.0 mL/s, respectively), with an increase in phase 1 injection duration (from 5 to 6, 8, and 8 s, respectively) and a decrease in phase 2 injection duration (from 12 to 8, 4, and 3 s, respectively) (Table A4.4; Figure A4-6 and A4-7).

	Phase 1	Phase 2	Total	<i>P</i> value
6-s scan				
Volume (mL)	23	41	64	–
Duration (s)	5	12	17	
Flow rate (mL/s)	4.9	3.5	–	
4-s scan				
Volume (mL)	29	26	55	.005*
Duration (s)	6	8	14	

Flow rate (mL/s)	4.6	3.3	—	
2-s scan				
Volume (mL)	34	12	46	.002*
Duration (s)	8	4	12	
Flow rate (mL/s)	4.3	2.8	—	
1-s scan				
Volume (mL)	34	6	40	.05
Duration (s)	8	3	11	
Flow rate (mL/s)	4.1	2.0	—	
Note.— <i>P</i> values were obtained by comparing contrast volume from a 6-s and 4-s scan, a 4-s and 2-s scan, and a 2-s and 1-s scan using 2-sided paired t tests with Bonferroni adjustment.				
* Significant difference in volume at a <i>P</i> value ≤ .017.				

Table A4.4: Average Contrast Injection Parameters for 6-, 4-, 2-, and 1-s Scan.

These differences are illustrated for 2 sample patients in Figure A4-8. The amount of contrast required reached a plateau when the scan duration decreased below 2 s (Figure A4-7 and A4-8).

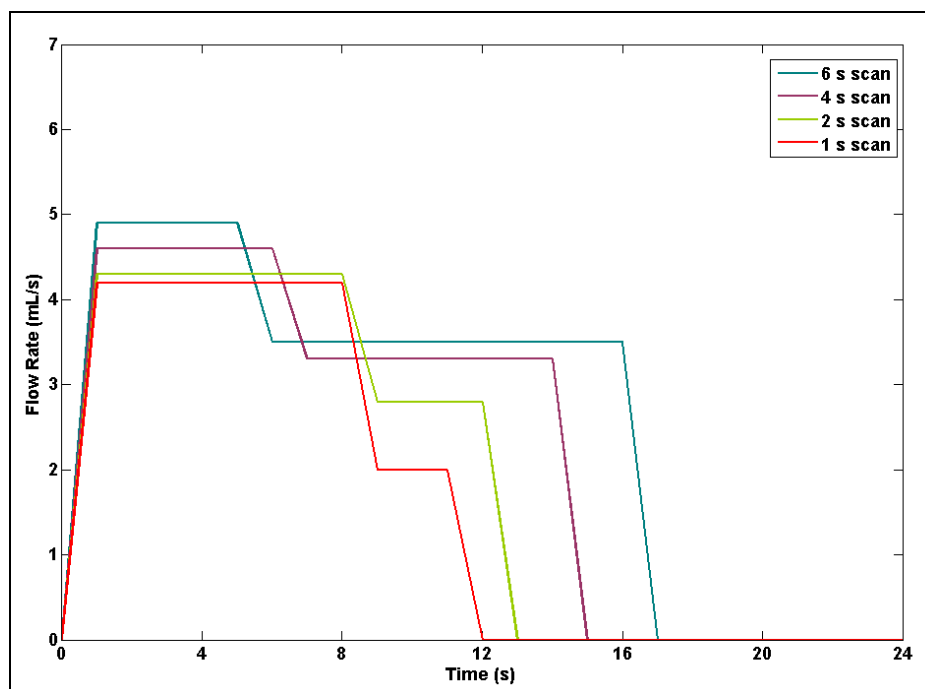


Figure A4-6: Biphasic contrast profiles obtained by averaging data from 25 patient-specific injection profiles for 6-, 4-, 2-, and 1-s cardiac scans.

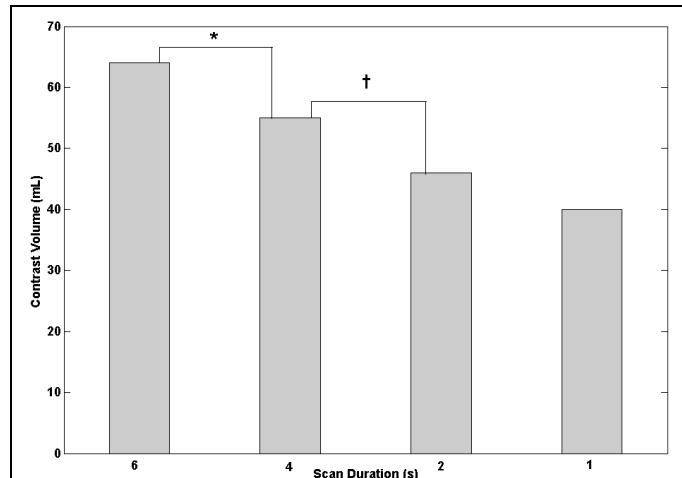


Figure A4-7: Average total contrast volumes computed from 25 patient-specific injections. Contrast volumes of 64, 55, 46, and 40 mL were required for 6-, 4-, 2-, and 1-s scans. Paired Student *t* tests with Bonferroni adjustments were used to compare average contrast volumes for 6- and 4-s scans, 4- and 2-s scans, and 2- and 1-s scans ; a *P* value < .017 indicated statistical significance. * and † indicate difference between contrast volumes was statistically significant.

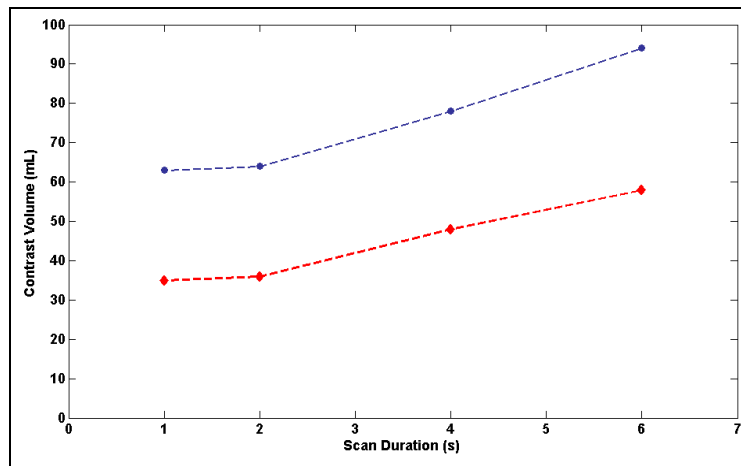


Figure A4-8: Total contrast volumes required in two sample patients for different scan durations. For 6-, 4-, 2-, and 1-s cardiac scans, a 62-year-old man 122-kg man (—●—)

required 94, 78, 64, and 63 mL of contrast, whereas a 67-year-old 85-kg man (—♦—) required 58, 48, 36, and 35 mL of contrast, respectively.

A4.4 Discussion

Latest MDCT systems allow for very short acquisition times for cardiac imaging, necessitating modification of the contrast administration routinely used with 16- and 64-slice CT scanners. In our study, contrast protocols for achieving uniform enhancement during 6-, 4-, 2-, and 1-s cardiac scans were predicted using LTI modeling. The protocols were generally biphasic, using a total of approximately 64 mL of contrast at an initial flow rate of 4.9 mL/s followed by 3.5 mL/s for a 6-s scan; while an average volume of 40 mL injected at a rate of 4.1 mL/s during phase 1 and 2.0 mL/s during phase 2 was sufficient for a 1-s scan. Although our results suggest that contrast volume can be reduced with decreasing scan time, they also indicate that a physiologic limit (16, 17) is reached when the scan duration is less than 2 s. Hence, a minimum amount of approximately 40 mL of high iodine concentration contrast agent (370 mgI/mL) is still required to achieve adequate arterial enhancement, even for subsecond cardiac imaging.

These predicted average volumes are comparable to those currently used in clinical protocols, which were determined largely through experience. Recent studies (1-4) employing fast scanners have used uniphasic contrast injections of 50 to 80 mL administered at higher flow rates (5-6 mL/s) for coronary exams ranging from less than 1 s to 4 s. Typically uniphasic injections with decreasing volumes and increasing flow rates are employed as scan times decrease, resulting in narrow peak enhancement curves with increasing peak attenuation values. Hence, uniphasic protocols may allow uniform

enhancement during very short scan durations, but only when the main scan is timed accurately during the narrow peak, avoiding the precipitous rise or fall of the enhancement curve. However, the average biphasic injections predicted by our model employ decreasing flow rates with increasing phase 1 and decreasing phase 2 injection durations (Table 4) as scan times decrease, resulting in a broader peak enhancement with constant attenuation values. With biphasic protocols, the contrast injected during phase 1 serves to achieve the target enhancement, while the contrast injected during phase 2 serves to maintain the enhancement. Moreover, the total injection duration of the modeled biphasic protocols (11-17 s) is consistent with recommendations for short duration scanning (17).

In the short term, the average contrast profiles presented here could be used to eliminate some of the guesswork in contrast administration for short-duration cardiac imaging. In the longer term, incorporation of LTI modeling into the injector and/or scanner platform could be useful for optimizing contrast load and arterial enhancement for each patient.

Developing patient-specific contrast protocols with LTI modeling requires the administration of a low-volume test bolus. In this study, we examined the impact of administering a saline chaser after injection of the test bolus of contrast. A comparison of data obtained with and without a saline chaser demonstrated that saline significantly changes the effective flow of contrast and results in smaller differences between programmed and effective contrast profiles. Saline also flushed contrast from the tubing and peripheral veins into the central blood volume; this led to an increase in PH and

AUC, which produced a better-defined test bolus attenuation curve with decreases in tPME, MTT, and RT.

These results suggest that saline should be administered when test enhancement data are used to model the main bolus geometry (7, 9), predict diagnostic enhancement (18, 19), or estimate cardiac functional parameters (20, 21). However, when test enhancement data are used simply to determine the appropriate onset of the main scan, the use of saline may not be necessary for all patients. We observed a decrease in tPME of 0.9 s with saline for patients weighing < 90 kg and a decrease in tPME of 2.7 s with saline in patients weighing \geq 90 kg. Because test data are typically acquired every 2 s, differences in tPME less than 2 s will likely have no clinical impact. Therefore, our results suggest that for CT imaging at higher flow rates, using a saline chaser is not necessary in patients weighing less than 90 kg when the test injection data (tPME) is used simply to determine the timing of data acquisition relative to injection of the main bolus. This result differs slightly from the results of an early study examining contrast injection with 16-slice cardiac CT, which described a decrease in tPME of approximately 4 s with the injection of saline following a test bolus of contrast (22). These conflicting results may be attributable to differences in flow rates between the two studies: a flow rate of 3 mL/s was used in the previous study, whereas a rate of 4.5 mL/s was used in our study.

Our study had some limitations. As lower contrast volumes are employed with shorter scan durations, the 20-mL test bolus constitutes a larger fraction of the total contrast dose administered to the patient. Decreasing the test bolus contrast volume to 10 or 5 mL may be feasible but was not examined here. Secondly, although our study demonstrated that administering saline with a test bolus is critical for modeling in all

patients and for timing in heavy patients, the amount of saline required was not definitively established. Bae et al suggested that 20 to 30 mL of saline may be sufficient to flush contrast into the central blood volume (17). However, results from Numburi et al indicate that a saline chaser of 20 mL for patients weighing < 90 kg and 40 mL for patients weighing \geq 90 kg might not be adequate for modeling main bolus injections (9). Studies by Mahnken et al (18) and Rist et al (19) found that the use of 50 mL of saline with a test bolus could successfully predict diagnostic attenuation values in the great vessels and left ventricle. Finally, although we performed LTI modeling to predict patient-specific injections, the injections were not administered to patients, and so their accuracy in achieving uniform enhancement was not evaluated. Nevertheless, previous studies (8, 9) have suggested that administration of optimized injections will provide uniform inter- and intraindividual enhancement.

In conclusion, administering saline after a low-volume test contrast bolus insures attainment of the programmed injector values, enabling LTI modeling of optimized contrast profiles for short-duration cardiac MDCT; contrast volumes of 64, 55, 46, and 40 mL were sufficient for 6-, 4-, 2-, and 1-s scans.

A4.5 References

1. Rybicki FJ, Otero HJ, Steigner ML, et al. Initial evaluation of coronary images from 320-detector row computed tomography. *Int J Cardiovasc Imaging* 2008; 24:535-546.
2. Hameed TA, Teague SD, Vembar M, Dharaiya E, Rydberg J. Low radiation dose ECG-gated chest CT angiography on a 256-slice multidetector CT scanner. *Int J Cardiovasc Imaging* 2009.
3. Weigold WG, Olszewski ME, Walker MJ. Low-dose prospectively gated 256-slice coronary computed tomographic angiography. *International Journal of Cardiovascular Imaging* 2009; 25:217-230.
4. Achenbach S, Marwan M, Ropers D, et al. Coronary computed tomography angiography with a consistent dose below 1 mSv using prospectively electrocardiogram-triggered high-pitch spiral acquisition. *Eur Heart J* 2009.
5. Bae KT. Optimization of contrast enhancement in thoracic MDCT. *Radiol Clin North Am* 2010; 48:9-29.
6. Cademartiri F, Palumbo A, Maffei E, et al. Tips and tricks in Multislice CT coronary angiography. *Acta Biomed* 2008; 79:65-72.
7. Fleischmann D, Hittmair K. Mathematical analysis of arterial enhancement and optimization of bolus geometry for CT angiography using the discrete fourier transform. *Journal of Computer Assisted Tomography* 1999; 23:474-484.

8. Fleischmann D, Rubin GD, Bankier AA, Hittmair K. Improved uniformity of aortic enhancement with customized contrast medium injection protocols at CT angiography. *Radiology* 2000; 214:363-371.
9. Numburi UD, Chatzimavroudis GP, Stillman AE, et al. Patient-specific contrast injection protocols for cardiovascular multidetector row computed tomography. *J Comput Assist Tomogr* 2007; 31:281-289.
10. Kaatee R, Van Leeuwen MS, De Lange EE, et al. Spiral CT angiography of the renal arteries: should a scan delay based on a test bolus injection or a fixed scan delay be used to obtain maximum enhancement of the vessels? *J Comput Assist Tomogr* 1998; 22:541-547.
11. Platt JF, Reige KA, Ellis JH. Aortic enhancement during abdominal CT angiography: correlation with test injections, flow rates, and patient demographics. *AJR Am J Roentgenol* 1999; 172:53-56.
12. Cademartiri F, van der Lugt A, Luccichenti G, Pavone P, Krestin GP. Parameters affecting bolus geometry in CTA: a review. *J Comput Assist Tomogr* 2002; 26:598-607.
13. Bland JM, Altman DG. Statistical methods for assessing agreement between two methods of clinical measurement. *Lancet* 1986; 1:307-310.
14. Blomley MJ, Dawson P. Bolus dynamics: theoretical and experimental aspects. *Br J Radiol* 1997; 70:351-359.
15. Becker CR, Hong C, Knez A, et al. Optimal contrast application for cardiac 4-detector-row computed tomography. *Invest Radiol* 2003; 38:690-694.

16. Hallett RL, Fleischmann D. Tools of the trade for CTA: MDCT scanners and contrast medium injection protocols. *Tech Vasc Interv Radiol* 2006; 9:134-142.
17. Bae KT. Intravenous contrast medium administration and scan timing at CT: considerations and approaches. *Radiology* 2010; 256:32-61.
18. Mahnken AH, Rauscher A, Klotz E, et al. Quantitative prediction of contrast enhancement from test bolus data in cardiac MSCT. *Eur Radiol* 2007; 17:1310-1319.
19. Rist C, Becker CR, Kirchin MA, et al. Optimization of cardiac MSCT contrast injection protocols: dependency of the main bolus contrast density on test bolus parameters and patients' body weight. *Acad Radiol* 2008; 15:49-57.
20. Mahnken AH, Henzler D, Klotz E, Hennemuth A, Wildberger JE, Gunther RW. Determination of cardiac output with multislice spiral computed tomography: a validation study. *Invest Radiol* 2004; 39:451-454.
21. Raman SV, Tran T, Simonetti OP, Sun B. Dynamic computed tomography to determine cardiac output in patients with left ventricular assist devices. *J Thorac Cardiovasc Surg* 2009; 137:1213-1217.
22. Becker. The use of contrast media in cardiac CT. *Applied Radiology* 32 (12 SUPPL.), pp. 50-54 2003.